Relativistic Theory of the Interaction of Two-Dimensional Materials with Moving Charged Particles

by

Kamran Akbari

A thesis
presented to the University of Waterloo
in fulfillment of the
thesis requirement for the degree of
Doctor of Philosophy
in
Applied Mathematics

Waterloo, Ontario, Canada, 2019

Examining Committee Membership

The following served on the Examining Committee for this thesis. The decision of the Examining Committee is by majority vote.

External Examiner: Dr. George W. Hanson
Professor,
Department of Electrical Engineering and Computer Science,
College of Engineering and Applied Science,
University of Wisconsin-Milwaukee,
3200 N. Cramer St. Milwaukee, Wisconsin, USA 53211

Internal-External Member: Dr. Amir Hamed Majedi
Professor,
Department of Electrical Engineering, Faculty of Engineering,
University of Waterloo
200 University Avenue West, Waterloo, ON, Canada N2L 3G1

Internal Member: Dr. Raymond G. McLenaghan
Professor Emeritus,
Department of Applied Mathematics, Faculty of Mathematics,
University of Waterloo
200 University Avenue West, Waterloo, ON, Canada N2L 3G1

Internal Member: Dr. Mohammad Kohandel
Associate Professor,
Department of Applied Mathematics, Faculty of Mathematics,
University of Waterloo
200 University Avenue West, Waterloo, ON, Canada N2L 3G1

Supervisor(s): Dr. Zoran L. Miskovic
Professor,
Department of Applied Mathematics, Faculty of Mathematics,
University of Waterloo
200 University Avenue West, Waterloo, ON, Canada N2L 3G1

I hereby declare that I am the sole author of this thesis. This is a true copy of the thesis, including any required final revisions, as accepted by my examiners.

I understand that my thesis may be made electronically available to the public.

Abstract

Prompted by the recent surge of interest in integrating atomically thin layers of conducting materials into nanophotonic and nanoplasmonic devices; we propose, in this thesis, a theoretical framework to analyze the interaction of externally moving charged particles with two-dimensional (2D) materials. The interactions of 2D materials with externally moving charged particles in the context of electron energy loss spectroscopy (EELS) has become a very popular experimental technique for exploring the plasmon excitations in 2D layered specimens over a broad range of frequencies. On the other hand, the technological need for a stable and tunable source of terahertz (THz) radiation has inspired researchers to explore the electromagnetic radiation from a family of 2D materials, induced by their interaction with fast charged particles.

We present a fully relativistic analysis of the energy loss of a charged particle traversing such layers. We distinguish between two contributions to this process: (i) the energy deposited in the layers in the form of electronic excitations (Ohmic losses), which include excitation of 2D plasmon polariton (PP) modes, and (ii) the energy emitted in the far-field region in the form of transition radiation. Owing to the proposed theoretical framework, we study various structures consisting of isotropic and anisotropic conducting and semiconducting sheets with different trajectories of the incident charged particles, including single and multiple parallel layers of graphene under normal incidence of charged particles and single-layer graphene and phosphorene under oblique incidence, in broad ranges of frequency, incident particle's speed, and its angle of incidence relative to the layers.

Suitable models for the 2D conductivity of each layer are chosen to represent: (a) excitation of the Dirac PP (DPP) mode in doped graphene in the THz range, (b) interband transitions in graphene in the range from infrared to ultraviolet frequencies, and (c) hyperbolic plasmon modes in doped phosphorene at the THz to mid-infrared frequencies. Among other findings, we observe that, for multilayer graphene, strong asymmetries arise in the Ohmic losses and in the radiation spectra with respect to the direction of motion of the incident particle. These asymmetries are explained by hybridization taking place between DPPs in different layers, which is found to be strongly affected by the interlayer distances and the differences in the doping densities of those layers.

In addition, we explore the possibility of exciting the so-called transverse plasmon mode in graphene as well as the directionality of exciting anisotropic plasmons in phosphorene by an obliquely incident charged particle. Our findings may help in the ongoing studies of plasmon excitations in 2D materials via EELS, as well as in exploring the possibility of designing a THz radiation source using an electron beam.

Acknowledgements

I would like to thank all my commitee/examination members who kindly took the responsibility of being part of my education and improvment during my Ph.D. program. Also, I would like to acknowledge special thanks to my supervisor, Dr. Miskovic, who has been a great mentor and friend to me for the whole period of my Ph.D. study. Finally, I would like to warmly thank my parents, family, and friends for all their support, patience, and company.

Dedication

To my parents, family and friends. To humanity, freedom and equality.

Table of Contents

List of Figures

Chapter 1

Introduction

In the first chapter of the thesis we introduce the problem under consideration. We motivate the readers of the thesis by explaining the overall idea of the thesis and how we are going to approach the problem while providing a thorough review of the literature. We offer all aspects of the importance of the thesis containing the theoretical, experimental, application-minded and technological and also the educational viewpoints. Next, we present the general organization of the thesis by listing the content and the management of the building blocks of the chapters.

1.1 Motivation and literature review

The emergence of two-dimensional (2D) crystals that took place in recent years has been regarded as a platform that may impact future photonic science and electronic technologies. Ever since the discovery of graphene in 2004 [1], unique optical properties of 2D materials have enabled many important device applications in nanophotonics and nanoplasmonics. In comparison with the common three-dimensional photonic materials, such as noble metals or silicon, 2D materials exhibit many exceptional features, including: (1) quantum confinement in the direction perpendicular to the 2D material, (2) naturally passivated surfaces without any dangling bonds, making it easy to integrate 2D materials with photonic structures such as waveguides and cavities, (3) the capability of constructing vertical heterostructures using different 2D materials without the conventional "lattice mismatch" issue since layers with different lattice constants in such heterostructures are only weakly bonded by the van der Waals forces, (4) the ability of strong interaction with light despite being atomically thin, and (5) the capability of operating in a very wide range of the electromagnetic (EM) frequency spectrum because of their diverse electronic properties [2, 3, 4, 5, 6].

Initially, graphene has attracted enormous amount of interest in plasmonic and optoelectronic research owing to its low-energy electronic band structure being akin to the massless Dirac fermions, its high carrier mobility, and the dynamic tunability of its doping density. However, graphene suffers the lack of a band gap, which is a serious limitation for its use in electronic devices. In the wake of the initial excitement about graphene, the need for a direct band gap in the electronic band structure has lead researchers to study other 2D materials, such as transition metal dichalcogenides [7, 8] and various monoelemental 2D crystals termed Xene (X = Si, Ge, Sn,...) [9]. The advent of these new 2D materials also opened the possibility to integrate different 2D materials together in layered structures to provide novel heterostructure applications [5]. Nevertheless, relatively low carrier mobility in these materials, in comparison to graphene, has been recognized as a considerable setback [10].

The invention of phosphorene in 2014 by exfoliation from black phosphorus (BP) [11, 10, 12, 13] – one of the four known allotropes of phosphorus that shows semiconducting properties, a thickness-dependent (i.e., highly tunable) band gap, strong in-plane anisotropy (particularly the anisotropy of electric conductance), and high carrier mobility– offers improvements for many technological concerns regarding the above mentioned 2D materials. Structurally, BP is similar to graphite and other layered (van derWaals) materials, comprised of 2D sheets that are vertically stacked with respect to one another. However, unlike graphite, the in-plane bonding in BP occurs via sp^3 hybridization and, accordingly, phosphorene does not form an atomically flat sheet like graphene, but rather a puckered honeycomb-structured layer (Fig. 5.1). Owing to this unique topological structure and the resulting differences between the armchair (AC) and the zigzag (ZZ) directions, many properties of phosphorene display strong in-plane anisotropy with respect to those two principal directions. Particularly, this anisotropy is markedly manifested in a large difference in the effective electron and hole masses along the AC and ZZ directions [14].

Determining the EM response of 2D materials and, in particular, graphene and phosphorene is of great significance for their potential applications in nanophotonics and nanoplasmonics. Optical properties of 2D layered materials have been extensively investigated using photon irradiation, both from the experimental and theoretical viewpoints. Currently associated to optical spectroscopies and techniques, surface plasmons were first observed in electron energy loss experiments, where energetic free electrons interact with the plasmon fields losing defined amounts of energy [15, 16]. As regards the plasmonic properties of 2D materials, electron energy loss spectroscopy (EELS) has become one of the most widely used analytical techniques that measures the dynamic polarization of a 2D material by a fast electron beam in a broad range of frequencies [17]. Such technique also allows one to study the dispersion relation of plasmon modes and their relation with the stopping of the incident particle [18].

Experimentally, by performing EELS in a modern scanning transmission electron microscope (STEM), one can obtain structural information about the target with spatial resolution down to

the atomic scale [17, 18], while simultaneously probing its collective electronic modes [19], detecting the cathodoluminescence (CL) light emission from the target [18, 20] and performing angle-resolved measurements of transition radiation (TR) from it [21]. The experimental setting of a STEM which allows for measurements of CL light emission from the material, can also be applied to the TR detection [18, 20, 22]. In particular, angle-resolved measurements of CL can be used within STEM experiments to distinguish between TR and incoherent CL, which often appears in the form of, e.g., luminescence from various materials [21, 23]. In addition, a number of experiments have been carried out using different energetic electron sources to generate EM radiation from graphene [24, 25, 26], increasing the interest in studying the coupling between moving electrons, plasmons and radiation fields. In that context, electron beam irradiation of graphene has been recently explored for its prospects to fill in technological gap regarding the lack of radiation sources at terahertz (THz) frequencies [27].

Nowadays, EELS benefits from the high spatial and energetic resolutions available in STEMs, allowing new insights in the study of plasmons, e.g., the mapping of plasmon modes at a nanoscopic scale [28, 29]. Whereas only the long-wavelength region is accessible in experiments probing nanostructures with incident photons, EELS can scan an extended range in the reciprocal space to cover both the long- and short-wavelength regimes of the dynamic response of those structures. Furthermore, it is possible to obtain momentum-resolved energy loss spectra in the low ultraviolet (UV) range, including the range $0 - 2$ eV which was usually inaccessible due to the presence of a zero-loss peak [30]. Even spatial mapping of plasmon modes in graphene and graphene-related nanostructures has been accomplished in recent works [19, 31]. Accordingly, EELS has been the main experimental technique for investigating electronic excitations in graphene over a broad range of frequencies and wavenumbers [32]. In particular, the high energy peak structures occurring at about 4 eV and 14 eV in the EELS of graphene have been studied in detail, both experimentally and theoretically, for free-standing single-layer graphene (SLG) and multilayer graphene (MLG) structures [33, 34, 35, 36, 37, 38, 39]. Although nonretarded calculations in the theoretical studies of EELS have reproduced the experimental data for graphene quite successfully [33, 40], a quantitative assessment of the importance of the relativistic correction was undertaken in a broad range of the electron energy losses to elucidate the role of retardation effects in energy loss spectra [9, 41] and to investigate the significance of TR in such experiments [22, 42, 43].

Studying interactions of the fast, externally moving charged particles with 2D materials is not only important in the context of EELS. We note that free-electron interactions with 2D targets were recently studied in several other contexts [24, 44, 45, 46, 47, 48, 49]. In particular, such interactions play a possibly important role in an effort towards designing a stable, highly tunable source of THz to infrared (IR) and even X-ray radiation. In that respect, there have been several recent proposals to use EM radiation from graphene induced by a fast electron beam,

moving either parallel (aloof scattering) [25, 50, 51] or perpendicular to graphene [52] and also cyclotron electron beam [26]. It has been shown that, depending on the trajectory of external particles with respect to graphene, various parameters such as the velocity of the particles may be used as additional tuning parameters, besides the chemical potential in graphene, for creating radiation at various frequencies [25, 50]. Moreover, the opportunity that EM radiation can be measured in a STEM equipped for the detection of CL light from the target material [53], opens the possibility of studying the low-energy losses beyond the detection limit through the emitted radiation patterns.

Considering the isotropy of graphene's (or, in general, isotropic 2D materials') polarization by a normally incident electron beam, graphene-based radiative applications are expected to offer relatively isotropic radiation patterns in all spatial directions. This intuitive argument calls for attention to study interactions of an external charged particle with a strongly anisotropic sheet, such as phosphorene, in the retarded regime. In particular, using an oblique incidence of the charged particle could reveal how the more exotic collective modes in anisotropic 2D materials may affect the energy loss spectra of the incident particle and the directional patterns of the emitted EM radiation from the target. Finally, to further motivate our study here, we mention that the systematic study of radiative and nonradiative losses is known to provide insight into the limitations that may arise in the fundamental physical properties of plasmonic systems, for example plasmon propagation lengths in nanoparticles [54].

In this thesis, we present fully relativistic calculations of the energy loss spectra in the THz to UV frequency range, generated by STEM electrons at different trajectories of incidence passing through a single-layer or multilayer structure of 2D materials. We establish a theoretical framework to analyze the interaction of fast moving charged particles with single- or multilayer conducting sheets with an arbitrary number of parallel monolayers, taking the retardation effects into account. In the case of multilayer structures, we assume that the layers are well separated so that the only interaction between their electronic systems is due to EM fields. Our approach is, essentially, to solve the corresponding macroscopic Maxwell's equations within the dielectric response formalism with adequate boundary or matching conditions [55, 56].

The inputs to this theoretical framework are two-fold: (1) the external current density associated to the motion of the external charged particles, which, in turn, can be related to the straight-line trajectory of the motion with respect to the plane of the 2D materials and the speed of the motion and (2) the induced current density associated to the dynamical response of the 2D materials which is dependent on the response model of the conducting sheets. Assuming a straight-line trajectory, we neglect the recoil of the incident charged particle and, accordingly, we neglect its bremsstrahlung. Thereby, focusing on various ranges of frequency, we use the appropriate optimal models of the response of each monolayer which will be validated for each structure under consideration. However, this analysis is essentially independent of the model

used for the response of the layers.

We elucidate two contributions to the total energy loss of the external particles: the Ohmic loss in 2D materials (conducting sheets) and the EM energy emitted in the far-field region in the form of TR, a purely relativistic phenomenon which is characteristic of the passage of a charge through an interface. We further show that Ohmic loss is related to excitation of the plasmon polaritons (PPs) which is the excitation of the valence electrons in each monolayer, as well as to generation of the Joule heat due to decay of those PPs in the presence of dissipative processes in the conducting sheets. While TR contributes only inside the light cone, with frequencies $\omega > ck$ (with c, ω, and k being the speed of light, operating frequency, and the in-plane wavenumber, respectively), the Ohmic energy loss has finite contributions both within and outside the light cone ($\omega \lessgtr ck$).

1.2 Organization of the thesis

This thesis is comprised of six chapters and two appendices. The first chapter is dedicated to the introductory concepts such as motivation, literature review, etc. The last chapter is dedicated to the general conclusion of the thesis, suggestions and probable future research projects concerning the thesis. Each chapter of 2-5 begins with a short section in the form of an abstract where we give the gist of the chapter and is followed by an *Introduction* section devoted to motivating the readers for the specifics of the chapter and the general structure of it. In the *Theory* section, then, we give the formulation of the proposed problem followed by the *Results and discussion* section where we show several quantitative aspects of the problem and discuss them, and ultimately each chapter will be wrapped up by a *Concluding remarks* section.

The overall content of the thesis is as follows: in Chapters 2, 3, 4 and 5 we present the formalism of the relativistic interaction of fast charged particles with 2D materials in order to analyze the transfer of energy between the external particles and 2D materials. In Chapter 2 we apply our formalism to a multilayer structure consisting of isotropic conducting sheets identified by scalar conductivities, under normal incidence of external charged particles. In such a case we consider graphene with a scalar conductivity model. The results of this chapter are published in three ISI journal papers [57, 58, 59]. In Chapter 3 we apply our formalism to a single-layer structure consisting of an isotropic conducting sheet identified by a tensorial conductivity model interacting with charged particles moving on a parallel trajectory. The model system in this chapter is again graphene. The results of this chapter are published in an ISI journal paper [60].

In Chapter 4 we apply our formalism to a single-layer structure consisting of an isotropic conducting sheet identified by a tensorial conductivity, under oblique incidence of external charged

particles. The model system here is graphene with a tensorial conductivity. The results of this chapter are published in an ISI journal paper [61]. In Chapter 5 we apply our formalism to a single-layer structure consisting of an anisotropic conducting sheet identified by a tensorial conductivity, under oblique incidence of external charged particles. The model system is single-layer BP, also known as phosphorene with a tensorial conductivity. The results of this chapter are published in a conference proceeding [62] and will be submitted shortly to an ISI journal. Ultimately, the thesis becomes complete by the concluding aspects of the research presented in the thesis in Chapter 6.

Unless otherwise stated, Gaussian units of electrodynamics are used throughout the thesis [63]. The reader should also note that the subsequent chapters are written in a self-contained form, so that some general definitions and equations will appear repeatedly in each chapter. This avoids the reader going back and forth among chapters for similar definitions. Likewise, each chapter contains its own set of introduced acronyms.

Chapter 2

Energy Loss and Transition Radiation in Multilayer Graphene Traversed by Fast Charged Particles under Normal Incidence

We present a fully relativistic formulation of the energy loss of charged particles traversing a multilayer graphene structure under normal incidence. We focus on the terahertz (THz) frequency range and we assume a large enough separation d between the layers to neglect any electronic interaction among them, such as interlayer electron hopping or formation of excitons. We use the Drude model for two-dimensional (2D) conductivity of each layer to describe hybridization between Dirac plasmon polaritons (DPPs) in different layers. We distinguish two types of contributions to the external charged particles energy loss: the energy deposited in graphene layers in the form of electronic excitations (Ohmic loss), which include the excitation of DPPs, and the energy that is emitted in the form of transition radiation. We study in detail the contribution of each layer to the Ohmic loss and analyze the directional decomposition of the radiation emitted in the half-spaces defined by the graphene planes.

Firstly, we apply the formalism to the case of two spatially separated layers, probed by an energetic electron and allowing for different doping density in each layer by defining an asymmetry parameter in the THz frequency range. By increasing the interlayer distance and changing the relative doping densities in graphene layers, we find surprisingly strong asymmetries in both the directional and layer-wise decompositions with respect to the direction of motion of the external charged particles.

A modal decomposition is also performed in the limit of vanishing damping in graphene, exposing quite intricate roles of bonding and antibonding hybridization between DPPs in Ohmic

losses. We obtain the probability density of exciting the hybridized DPP (HDPP) modes that result from the coupling of the layers, and we also calculate the average number of HDPPs excited by the external charged particles traversing the two parallel graphene layers. We analyze the effect of different parameters, such as the interlayer distance, the incident particle velocity, and the asymmetry in doping densities. In particular, we find a cusp-like behaviour for nearly equal conductivities, that indicates a high sensitivity of the system to slight variations in doping densities.

Secondly, we analyze the energy loss channels for a fast charged particle traversing a multilayer graphene (MLG) structure with N layers under normal incidence. Focusing on a THz range of frequencies, and assuming equally doped graphene layers, we describe hybridization of graphene's DPPs. Performing a layer decomposition of Ohmic energy losses, which include excitation of those HDPPs, we have found for $N = 3$ that the middle HDPP eigenfrequency is not excited in the middle layer due to symmetry constraint, whereas the excitation of the lowest HDPP eigenfrequency produces a Fano resonance in the graphene layer that is first traversed by the charged particle. While the angular distribution of transition radiation emitted in the far-field region also shows asymmetry with respect to the traversal order by the incident charged particle at supra-THz frequencies, the integrated radiative energy loss is surprisingly independent of both d and N for $N \leq 5$, which is explained by a dominant role of the outer graphene layers in transition radiation.

We have further found that the integrated Ohmic energy loss in optically thin MLG scales as $\propto 1/N$ at sub-THz frequencies, which is explained by exposing the role of dissipative processes in graphene at low frequencies. Finally, prominent peaks are observed at supra-THz frequencies in the integrated Ohmic energy loss for MLG structures that are not optically thin. The magnitude of those peaks is found to scale with N for $N \leq 2$, while their shape and position replicate the peak in a double-layer graphene ($N = 2$), which is explained by arguing that plasmon hybridization in such MLG structures is dominated by electromagnetic interaction between the nearest-neighbor graphene layers.

2.1 Introduction

The study of plasmons in graphene is the subject of a vast experimental and theoretical effort in the last years, due to its remarkable properties that make it preferable to other plasmonic materials like noble metals [64, 65, 66, 67]. Researchers have explored its capabilities taking advantage of the long plasmon lifetimes, low losses [68], high spatial confinement, and versatile tunability [69, 70], together with the large electro-optical response provided by its two-dimensional (2D)

geometry and peculiar electronic structure [71]. Graphene-based devices are designed for applications in optoelectronics [64, 72, 73], solar cells [74, 75], sensing of gases and molecules [76, 77, 78, 79], photocatalysis [80, 81], terahertz (THz) technology [82], etc. Also, the fine biocompatibility of graphene makes it an admirable candidate for applications in biotechnology and medical sciences [83, 84]. From a fundamental point of view, the simplicity of its atomic structure as well as the definiteness and richness regarding its electronic structure, makes graphene an excellent material to test methods for modeling emerging new phenomena of other low-dimensional systems [85, 86, 87].

Although the optical response of graphene presents pronounced spectral features at frequencies in the ultraviolet (UV) range ($\sim$ $2-30$ eV, the so-called π and $\sigma+\pi$ plasmons) [35, 38, 39, 88], it is in the THz to infrared (IR) [89] region (with frequencies <1 eV) where it stands out for the aforementioned applications. In this regime, heavily doped graphene supports the so-called Dirac plasmon, originated in intraband π-electron excitations [90, 91]. A distinct property of this plasmon is the high tunability of frequencies, which can be controlled by altering the chemical potential through external gates in a relatively simple manner [69, 70], a unique feature not applicable in the higher energy regime. The associated plasmon polariton shows strong confinement in the direction perpendicular to graphene and propagates along it for relatively long distances [92].

Tunable plasmons have been detected also in a variety of graphene nanostructures, like ribbons, nanodisks, rings, and others [93], which add localization properties in the plane of the layers. Nevertheless, extended graphene remains a central topic for theoretical as well as experimental investigation of graphene, both monolayered and multilayered, isolated or combined with other materials and heterostructures [68, 94, 95, 96, 97], and even in nonparallel configurations [98]. Furthermore, stacks of multiple graphene layers, which are typically separated by distances in excess of some 10 nm, have shown great promise for nanophotonic and nanoplasmonic applications due to hybridization taking place between Dirac plasmons in individual layers, which may be tuned by controlling their doping densities [99, 100, 101]. Over the past several years, growing effort has been invested in developing optoelectronic devices using layered structures that contain stacks of multiple layers of graphene [100, 102, 103, 104, 105, 106, 107]. Other examples of applications of multilayer graphene (MLG) structure include radiation absorbers at sub-THz frequencies [108] and ultrasensitive THz biosensors [109, 110]. Graphene layers in such applications are usually well separated, so that the only interaction between their electronic systems is due to EM fields.

Both experimental and theoretical investigations of the collective electron excitation modes in doped graphene have played important roles over the past decade in the subfield of photonics research concerned with the range of frequencies from THz to mid-infrared (MIR) [66, 82, 111]. While the main effort of research in this area is aimed at designing optoelectronic and plasmonic

devices with optimal functionalities, interactions of graphene with externally moving charged particles have also attracted substantial interest in recent years, e.g., in the context of using electron energy loss spectroscopy (EELS) to explore plasmonic properties of both single-layer graphene (SLG) and MLG in the $\sim 2-30$ eV range of frequencies [35, 38, 32]. On the other hand, joining the global effort to design a stable, highly tunable source of THz radiation, there have been several recent proposals to use EM radiation from graphene induced by a fast electron beam, moving normal to graphene [52], where the electron velocity may be used as tuning parameter.

In a recent article [42], the authors presented fully relativistic calculations of the energy loss spectra in the THz to UV frequency range, generated by a scanning transmission electron microscope (STEM) electrons at normal incidence passing through a SLG. The research was performed in order to elucidate the role of retardation effects in EELS, Ohmic losses and transition radiation (TR) from doped graphene probed by a fast electron in a STEM, where it is shown that the retardation effects are of significant importance at low frequency range. In that context, it may be worthwhile mentioning that the experimental setting of a STEM allows for measurements of cathodoluminescence light emission from a target [18, 20], which could be adapted to perform angle-resolved measurements of TR from graphene [21].

Motivated by [42], in this chapter we generalize the theoretical framework to MLG with an arbitrary number of parallel sheets. We assume that graphene layers are well separated so that the only interaction between their electronic systems is due to EM fields. As mentioned before, in the THz to infrared range, the graphene π electrons participate in low energy intraband excitations, giving rise to Dirac plasmons (or sheet plasmons), which can couple with EM waves to generate Dirac plasmon polaritons (DPPs) that propagate along the graphene sheet. As a result, a key novel mechanism arises in the optical response of such MLG based devices due to strong hybridization among the DPP modes of individual graphene layers, which opens the possibility of using the geometric design of such structures to achieve eigenmodes with various dispersion relations and oscillator strengths in the THz to MIR frequency range.

In our theory, we solve the corresponding Maxwell's equations within the dielectric response formalism with adequate boundary conditions [55, 56]. As mentioned before, we next elucidate two contributions to the total energy loss of the external particle: the Ohmic losses in graphene and the EM energy emitted in the far-field region in the form of TR. We further show that Ohmic losses are related to excitation of the DPPs in graphene, as well as to generation of the Joule heat due to decay of those DPPs in the presence of dissipative processes in graphene. Focusing on the THz range, we use the Drude model of conductivity and apply our model to, initially, double-layer graphene (DLG) [99] and then to MLG, onto which a ~ 100 keV electron beam impinges perpendicularly. We emphasize that we do not consider a bilayer graphene in the sense of two electronically-coupled layers [94]. Besides calculations of the total Ohmic and radiative energy

loss spectra, we also derive a layer-wise decomposition of the Ohmic losses and a directional decomposition of the radiation emitted in the upper and lower half-spaces.

It is worth mentioning that, theoretical investigation of MLG structures was initially concerned with plasmon hybridization in DLG, first studied by Hwang and Das Sarma [99], followed by other authors [112, 113, 114]. The dispersion of a DPP mode in an SLG is well described in [42] considering the retardation effects. The presence of a second graphene layer (even at a relatively large distance) produces hybridization of the single-layer DPPs giving rise to new modes with essentially different frequencies (low-energy bonding and high-energy antibonding modes [101]), which depend on the physical parameters of the coupled system, such as the interlayer distance and the asymmetry in doping densities [99, 105, 106, 115]. The interplay of these parameters may be the key to optimize the performance of such system in a particular design. Hence, relative roles of the bonding and antibonding hybridization modes in the two graphene layers are elucidated by developing a modal decomposition for Ohmic losses in the limit of vanishing dissipation in graphene. Furthermore, in addition to the case of graphene layers with equal conductivities, we also study an inherently asymmetric structure with two graphene layers having different conductivities due to doping with different densities of charge carriers. We analyze the dependence of the Ohmic loss spectra and the angular distribution of the emitted radiation with parameters such as the interlayer distance and the relative doping density.

This analysis is essentially independent of the model used for the conductivity of the layers. Generally speaking, the conductivity σ of a graphene layer is a complex function of frequency ω (and wavevector k, if we consider a non-local response model). The real part $\Re\{\sigma\}$ accounts for dissipative effects, while the imaginary part $\Im\{\sigma\}$ corresponds to reactive phenomena, including the excitation of plasmons. As stated before, the Ohmic contribution to the energy loss includes both the excitation and the subsequent decay of plasmons through an explicit dependence on $\Re\{\sigma\}$. For the modal decomposition, we adopt a conductivity model with zero damping (i.e. $\Re\{\sigma\} = 0$ for each layer), hence disregarding dissipative effects and focusing on the fundamental aspects of the excitation of plasmons. Using the aforementioned relativistic formulation, we analyze the production of plasmons in a two-layered graphene system, with an emphasis on the role played by the external parameters that can be adjusted in an experiment. Finally, for both symmetrically and asymmetrically doped DLGs, we give an analysis of the average number of plasmons excited by the swift external electron.

Plasmon hybridization in MLG systems with $N \geq 2$ layers was theoretically studied by Zhu *et al.* [116], Stauber [101], and Rodrigo *et al.* [106], among other authors. Those authors have found that, for an MLG with N layers, there exist N hybridized DPP (HDPP) modes with eigenfrequencies $\omega_j(k)$, for $j = 1, 2, \ldots, N$, where k is an in-plane wavenumber. The spread among those frequencies was found to generally increase with decreasing interlayer distance(s), so that the highest-lying hybrid mode with frequency, say, ω_N merges with the light line, $\omega = ck$,

at long wavelengths and approached the typical $\omega_N \propto \sqrt{k}$ dependence of a 2D electron gas at shorter wavelengths [91], whereas the remaining $N-1$ hybrid modes with lower frequencies exhibit quasi-acoustic dispersions at long wavelengths [116]. Thus, while the highest mode is always strongly affected by retardation effects at the wavelengths of interest in the THz range [117], the lower lying modes are pushed further below the light line $\omega = ck$ by decreasing interlayer distance, and are therefore less affected by retardation.

Several applications of MLG rely on the properties of the highest HDPP mode in optically thin structures, such that their thickness is much smaller than the characteristic wavelength of that mode. In that limit one may represent the conductivity of an MLG as a sum of conductivities of independent graphene layers [100, 105, 106, 107, 109, 110]. As a result, it was shown that an optically thin MLG may exhibit considerably higher effective doping density than in an SLG, which could give rise to a larger oscillator strength, as well as a higher eigenfrequency of its highest HDPP mode in comparison to the DPP mode in a SLG [106]. On the other hand, there has also been an increasing interest in the past several years to exploit dispersion relations associated with the acoustic plasmon modes in graphene for various applications [95, 118]. For example, it was recently shown that radiation sources could be developed at THz frequencies based on excitation of the low-frequency quasi-acoustic HDPP hybrid modes in an MLG by an electron beam moving parallel to graphene at a moderate speed [95, 118]. We remark that such acoustic modes can be produced, not only in an MLG structure with electronically decoupled graphene sheets [99, 101, 116], as discussed above, but also in an SLG in the presence of a nearby metal gate [118], or in a structure that combines those two designs, namely, an MLG on a conducing substrate [95].

With all the above mentioned intricacies regarding the dispersion relations and oscillator strengths of the HDPP modes in MLG structures, and in view of a diverse range of their applications, we expose some new features of MLG at THz frequencies when such structures are traversed by a fast external charged particle. Since we are interested in the limit of extremely long wavelengths associated with those frequencies, we adopt the Drude model, which was shown to describe rather well the DPP mode in a doped graphene by means of an in-plane optical conductivity [119, 43]. Specifically, in this work we analyze the effects of the number of layers N and the interlayer distance on the energy loss of a fast charged particle traversing the MLG, as well as the resulting TR from those layers in the THz range of frequencies. We only consider a somewhat idealized system represented by a stack of graphene layers suspended in free space in order to emphasize the role of plasmon hybridization between graphene layers by eliminating screening, or possible additional hybridization with collective modes due to the presence of a substrate or dielectric spacer layers [115]. By choosing such a system we also focus on TR from graphene layers, while eliminating Cherenkov radiation in a substrate [51], as well as TR arising when the charged particle traverses a dielectric boundary.

Regarding the results of N-layer problem, for DLG we find strong asymmetries with respect to the order in which graphene layers are traversed by the external charged particle that are manifested in the angular distributions of TR in the half-spaces defined by the DLG, as well as in the amounts of energy deposited in individual graphene layers, which mostly goes into the excitation of two HDPP modes. Those asymmetries were found to be accentuated by increasing interlayer distance and by increasing asymmetry between the doping densities of the two graphene layers in a DLG. Next, we add the number N of layers as a critically important parameter for all MLG structures, and investigate how the above mentioned physical observations change with N in the range $1 \leq N \leq 5$ for equally doped graphene layers with a broad range of interlayer distances.

The chapter is organized as follows: in the *Theory* section (2.2) we give a derivation of the EM fields and define probability densities for various energy losses for the general case of N graphene layers. We apply this theory to the case of two graphene layers providing a more detailed analysis, for which we study a modal decomposition of plasmon excitation probability and average number of plasmons. The *Results and Discussion* section (2.3) is divided in two parts, dedicated to DLG layers with equal conductivities and different conductivities, and MLG with more than two layers with equal conductivities. For the case of DLG we also investigate the effects of changing damping rates and external particle's velocity for both cases of equal and different conductivies. That section is followed by the *Concluding remarks* section (2.4).

2.2 Theory

We consider a structure with N parallel graphene layers with large area placed in the planes $z = z_l$ with $l = 1, 2, \ldots, N$ in a three-dimensional Cartesian coordinate system with coordinates $\mathbf{R} = \{\mathbf{r}, z\}$, where $\mathbf{r} = \{x, y\}$, as shown in Fig. 2.1. We shall assume in our calculations that the structure is placed in vacuum in order to be able to neglect any other sources of radiation or dissipation, apart from those pertaining to the graphene layers.

2.2.1 Self-consistent solution for the induced electromagnetic fields

By the symmetry of the structure, we find it convenient to use the electric Hertz vector $\mathbf{\Pi}(\mathbf{R}, t)$ to describe the electric and magnetic fields generated by the external and induced currents in the system. Assuming that the system is always invariant under time translation to prevent the alteration of the material properties, we employ the Fourier transform pair with respect to time

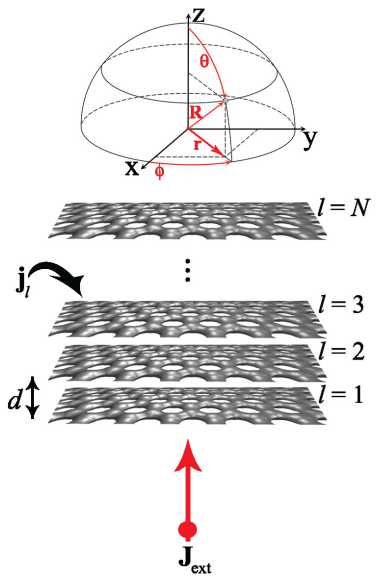

Figure 2.1: Geometry of the structure for probing the multilayer specimen by an electron under normal incidence in STEM.

and frequency so that we can express the Hertz vector via

$$\mathbf{\Pi}(\mathbf{R},t)=\int_{-\infty}^{\infty}\frac{d\omega}{2\pi}\,\mathrm{e}^{-i\omega t}\mathbf{\Pi}(\mathbf{R},\omega). \tag{2.1}$$

Then, in an infinite medium described by a frequency dependent relative dielectric constant $\epsilon_d(\omega)$ and relative permeability $\mu_d(\omega)$ the electric field and the magnetic field may be obtained from [120]

$$\begin{aligned}\mathbf{B}(\mathbf{R},\omega)&=-i\frac{\omega}{c}\epsilon_d(\omega)\mu_d(\omega)\,\boldsymbol{\nabla}\times\mathbf{\Pi}(\mathbf{R},\omega),\\ \mathbf{E}(\mathbf{R},\omega)&=\boldsymbol{\nabla}\boldsymbol{\nabla}\cdot\mathbf{\Pi}(\mathbf{R},\omega)+\frac{\omega^2}{c^2}\epsilon_d(\omega)\mu_d(\omega)\mathbf{\Pi}(\mathbf{R},\omega),\end{aligned} \tag{2.2}$$

respectively, where c is the speed of light in vacuum.

Assuming translational invariance inside each graphene layer, we may perform a 2D spatial Fourier transform with respect to the 2D materials' in-plane coordinates ($\mathbf{r}=\{x,y\}\rightarrow\mathbf{k}=\{k_x,k_y\}$ with $\mathbf{k}$ being the in-plane wavevector), enabling us to express the Hertz vector as

$$\mathbf{\Pi}(\mathbf{R},\omega)=\iint\frac{d^2\mathbf{k}}{(2\pi)^2}\,\mathrm{e}^{i\mathbf{k}\cdot\mathbf{r}}\,\mathbf{\Pi}(\mathbf{k},z,\omega). \tag{2.3}$$

This vector may be decomposed into two contributions as $\mathbf{\Pi} = \mathbf{\Pi}_{\rm ext} + \mathbf{\Pi}_{\rm ind}$, resulting from the external charged particle and the currents induced in graphene layers, see Fig. 2.1. In the presence of a charge current with density $\mathbf{J}(\mathbf{k}, z, \omega)$ the Hertz vector in vacuum (i.e., setting $\epsilon_d(\omega) = \mu_d(\omega) = 1$), is obtained by solving the equation [120]

$$\left(\frac{\partial^2}{\partial z^2} - q^2\right) \mathbf{\Pi}(\mathbf{k}, z, \omega) = -\frac{4\pi i}{\omega}\, \mathbf{J}(\mathbf{k}, z, \omega), \tag{2.4}$$

where $q^2 = k^2 - k_0^2$ with $k = \sqrt{k_x^2 + k_y^2}$ and $k_0 = \omega/c$. This equation implies that the Hertz vector is in the direction of the current density (in the absence of any scattering condition) and may be solved for arbitrary current density $\mathbf{J}$ as

$$\mathbf{\Pi}(\mathbf{k}, z, \omega) = \int_{-\infty}^{+\infty} dz'\, G_{\Pi 0}(\mathbf{k}, z - z', \omega)\, \mathbf{J}(\mathbf{k}, z', \omega), \tag{2.5}$$

where $G_{\Pi 0}(k, z, \omega)$ is the scalar retarded Green's function (GF) [63, 121] for the components of the Hertz vector in vacuum (subscript 0 implies the homogenius medium), obtained in Appendix A:

$$G_{\Pi 0}(k, z, \omega) = \frac{2\pi i}{\omega q} \mathrm{e}^{-q|z|}, \tag{2.6}$$

with the field dependency on the z coordinate governed by

$$q(k, \omega) = \begin{cases} \frac{|\omega|}{c}\sqrt{\left(\frac{ck}{\omega}\right)^2 - 1} \equiv \alpha(k, \omega), & |\omega| < ck \\ -i\frac{\omega}{c}\sqrt{1 - \left(\frac{ck}{\omega}\right)^2} \equiv -i\kappa(k, \omega), & |\omega| > ck. \end{cases} \tag{2.7}$$

Here, we have defined $\alpha = \sqrt{k^2 - k_0^2}$ as the inverse decay length of evanescent fields outside the light cone representing the solutions of Eq. (2.4) in the near-field region that are localized around the conducting layer when $|\omega| < ck$ and $\kappa = \mathrm{sign}(\omega)\sqrt{k_0^2 - k^2}$ as the wavenumber of traveling wave inside the light cone representing the radiative waves propagating in the far-field region as $|z| \to \infty$ when $|\omega| > ck$ in directions perpendicular to graphene layers, respectively.

Considering the external particle to be a point charge Ze that moves along the z-axis with constant velocity $\mathbf{v} = \hat{\mathbf{z}} v$ (enabling us to neglect its braking radiation), where $\hat{\mathbf{z}}$ is a unit vector in the direction of that axis, one may write the external volume charge density as $\rho_{\rm ext}(\mathbf{R}, t) = Ze\, \delta^{(2)}(\mathbf{r})\, \delta(z - vt)$ and the corresponding current density as $\mathbf{J}_{\rm ext}(\mathbf{R}, t) = \mathbf{v}\rho_{\rm ext}(\mathbf{R}, t)$. Thus, the Fourier transform of the current density due to the external charge is given via

$$\mathbf{J}_{\rm ext}(\mathbf{k}, z, \omega) = Ze\, \mathrm{e}^{iQz}\, \hat{\mathbf{z}}, \tag{2.8}$$

where $Q = \omega/v$. This external current density inserted in Eq. (2.5) yields the corresponding Hertz vector as

$$\mathbf{\Pi}_{\text{ext}}(\mathbf{k}, z, \omega) = \frac{i}{\omega} A(k, \omega)\, \mathbf{J}_{\text{ext}}(\mathbf{k}, z, \omega), \tag{2.9}$$

with the auxiliary amplitude

$$A(k, \omega) = \frac{4\pi}{q^2 + Q^2}. \tag{2.10}$$

Using standard vector relations in Eq. (2.2), one may retrieve from $\mathbf{\Pi}_{\text{ext}}$ the usual expressions for electric and magnetic fields associated with a uniformly moving point charge in free space [63, 120].

Defining $\mathbf{j}_l(\mathbf{k}, \omega)$ as the in-plane current in the lth graphene layer, which arises due to dynamic polarization of charge carriers in that layer, we may express the total induced current in the system in terms of a sum involving Dirac's delta functions as

$$\mathbf{J}_{\text{ind}}(\mathbf{k}, z, \omega) = \sum_{l=1}^{N} \delta(z - z_l)\, \mathbf{j}_l(\mathbf{k}, \omega). \tag{2.11}$$

We assume that the lth graphene layer is characterized by its own equilibrium density of charge carriers, n_l, giving rise to an in-plane, scalar conductivity $\sigma_l(k, \omega)$, which may be generally dependent on both the wavenumber $k = \sqrt{k_x^2 + k_y^2}$ and frequency ω. Then, the polarization current in that layer may be expressed by the 2D Ohm's law as $\mathbf{j}_l(\mathbf{k}, \omega) = \sigma_l(k, \omega)\mathbf{E}_{||}(\mathbf{k}, z_l, \omega)$, where $\mathbf{E}_{||}(\mathbf{k}, z_l, \omega)$ is the tangential, or the in-plane component of the total electric field evaluated at $z = z_l$. Equation (2.11) allows us to express the total induced Hertz vector as

$$\begin{aligned} \mathbf{\Pi}_{\text{ind}}(\mathbf{k}, z, \omega) &= \frac{i}{\omega}\frac{2\pi}{q} \sum_{l=1}^{N} e^{-q|z - z_l|} \mathbf{j}_l(\mathbf{k}, \omega) \\ &= \frac{i}{\omega}\frac{2\pi}{q} \sum_{l=1}^{N} \mathrm{e}^{-q|z - z_l|} \sigma_l(k, \omega) \mathbf{E}_{||}(\mathbf{k}, z_l, \omega). \end{aligned} \tag{2.12}$$

Notice that the components of this vector are parallel to the graphene layers, $\mathbf{\Pi}_{\text{ind}}(\mathbf{k}, z, \omega) = \mathbf{\Pi}_{||}(\mathbf{k}, z, \omega) = \hat{\mathbf{k}}\Pi_{||}(\mathbf{k}, z, \omega)$, where $\hat{\mathbf{k}}$ is a unit vector in the direction of $\mathbf{k}$, whereas the z component of the Hertz vector is entirely due to the external charged particle, $\mathbf{\Pi}_{\text{ext}}(\mathbf{k}, z, \omega) = \hat{\mathbf{z}}\Pi_z(\mathbf{k}, z, \omega)$, where

$$\Pi_z(\mathbf{k}, z, \omega) = \frac{i}{\omega} Ze\, A(k, \omega)\, \mathrm{e}^{iQz}. \tag{2.13}$$

Using the vector relations between the electric field and the Hertz vector expressed in Eq. (2.2), we may express components of the total electric field in directions parallel to the graphene layers as

$$\mathbf{E}_{||}(\mathbf{k},z,\omega)=\left(\frac{\omega^2}{c^2}-\mathbf{k}\,\mathbf{k}\cdot\right)\mathbf{\Pi}_{||}(\mathbf{k},z,\omega)+i\mathbf{k}\frac{\partial}{\partial z}\Pi_z(\mathbf{k},z,\omega). \tag{2.14}$$

We insert Eq. (2.12) for $\mathbf{\Pi}_{||}$ in Eq. (2.14), multiply by $\hat{\mathbf{k}}\cdot$ and set $z=z_l$, to obtain a system of algebraic equations for the in-plane, longitudinal components of the total electric field, $E_{||}=\hat{\mathbf{k}}\cdot\mathbf{E}_{||}$, in all layers,

$$E_{||}(\mathbf{k},z_l,\omega)\left(1+\frac{2\pi i}{\omega}q\,\sigma_l\right)+\frac{2\pi i}{\omega}q\sum_{l'=1,l'\neq l}^{N}\sigma_{l'}\mathrm{e}^{-q|z_l-z_{l'}|}E_{||}(\mathbf{k},z_{l'},\omega)=-ik\frac{Ze}{v}A\,\mathrm{e}^{iQz_l}, \tag{2.15}$$

having a solution that gives a self-consistent set of values for $E_{||}(\mathbf{k},z_l,\omega)$. Now, this system of equations may be further written in a matrix form as $\underline{\underline{\boldsymbol{\epsilon}}}\,\underline{\mathbf{E}}=\underline{\mathbf{b}}$, where the $N\times N$ matrix $\underline{\underline{\boldsymbol{\epsilon}}}$ has its components defined by

$$\epsilon_{ll'}=\begin{cases}1+i\frac{2\pi}{\omega}q\sigma_l & \text{if}\quad l=l'\\ i\frac{2\pi}{\omega}q\sigma_{l'}\mathrm{e}^{-q|z_l-z_{l'}|} & \text{if}\quad l\neq l',\end{cases} \tag{2.16}$$

whereas vectors $\underline{\mathbf{E}}$ and $\underline{\mathbf{b}}$ have their components defined by $E_l\equiv E_{||}(\mathbf{k},z_l,\omega)$ and $b_l=\mathcal{A}\,\mathrm{e}^{iQz_l}$ with $\mathcal{A}\equiv -ikA\frac{Ze}{v}$, respectively. Then, the solution of the system, $\underline{\mathbf{E}}=\underline{\underline{\boldsymbol{\epsilon}}}^{-1}\underline{\mathbf{b}}$, may be inserted back into Eq. (2.12) to obtain an expression for $\Pi_{||}(\mathbf{k},z,\omega)=\hat{\mathbf{k}}\cdot\mathbf{\Pi}_{\mathrm{ind}}$,

$$\Pi_{||}(\mathbf{k},z,\omega)=\frac{2\pi i}{q\omega}\sum_{l=1}^{N}\sigma_l\mathrm{e}^{-q|z-z_l|}E_l, \tag{2.17}$$

which finally gives from Eq. (2.14)

$$E_{||}(\mathbf{k},z,\omega)=-\frac{2\pi i}{\omega}q\sum_{l=1}^{N}\sigma_l\mathrm{e}^{-q|z-z_l|}E_l+\mathcal{A}\mathrm{e}^{iQz}. \tag{2.18}$$

In a similar manner, the z component of the total electric field, $E_z=\hat{\mathbf{z}}\cdot\mathbf{E}$, may be evaluated as

$$\begin{aligned}E_z(\mathbf{k},z,\omega)&=\frac{\partial}{\partial z}\left(i\mathbf{k}\cdot\mathbf{\Pi}_{||}+\frac{\partial}{\partial z}\Pi_z\right)+\frac{\omega^2}{c^2}\Pi_z\\&=\frac{2\pi}{\omega}k\sum_{l=1}^{N}\sigma_l\,\mathrm{e}^{-q|z-z_l|}\,E_l\,\mathrm{sign}(z-z_l)+i\omega AZe\left(\frac{1}{c^2}-\frac{1}{v^2}\right)\mathrm{e}^{iQz}.\end{aligned} \tag{2.19}$$

Having obtained $\mathbf{\Pi}_{\rm ind}$, one may use standard vector relations, Eq. (2.2), to express the induced electric and magnetic fields as [42, 120]

$$\mathbf{E}_{\rm ind}(\mathbf{k},z,\omega) = -\hat{\mathbf{k}}\frac{2\pi iq}{\omega}\sum_{l=1}^{N}\sigma_l\,\mathrm{e}^{-q|z-z_l|}E_l + \hat{\mathbf{z}}\frac{2\pi k}{\omega}\sum_{l=1}^{N}\sigma_l\,\mathrm{e}^{-q|z-z_l|}E_l\,\mathrm{sign}(z-z_l), \tag{2.20}$$

$$\mathbf{H}_{\rm ind}(\mathbf{k},z,\omega) = -\frac{2\pi}{c}\left(\hat{\mathbf{z}}\times\hat{\mathbf{k}}\right)\sum_{l=1}^{N}\sigma_l\,\mathrm{e}^{-q|z-z_l|}E_l\,\mathrm{sign}(z-z_l), \tag{2.21}$$

with "sign" being the signum function.

Once the components of the electric field are identified, the derivations of the probability densities for the total energy losses of the external charged particle, the Ohmic energy losses, and radiative energy losses become straightforward. For instance, for the radiative energy losses one requires the z component of the complex Poynting vector in the Fourier domain, which is given by

$$\hat{\mathbf{z}}\cdot\left[\mathbf{E}_{\rm ind}(\mathbf{k},z,\omega)\times\ \mathbf{H}^{*}_{\rm ind}(\mathbf{k},z,\omega)\right] = \frac{(2\pi)^2}{\omega c}\kappa\sum_{l=1}^{N}\sum_{l'=1}^{N}\sigma_l\,\sigma^{*}_{l'}\mathrm{e}^{i\kappa(|z-z_l|-|z-z_{l'}|)}E_l\,E^{*}_{l'}\,\mathrm{sign}\,(z-z_{l'}). \tag{2.22}$$

Moreover, the eigenvalues of the system in Eq. (2.15) yield N eigenfrequencies $\omega_j(k)$, with $j=1,2,\ldots,N$, of the HDPP modes, satisfying $0<\omega_j(k)<ck$. It should also be noted that we assume that the electron systems in graphene layers are not spin polarized, e.g., by the presence of an external magnetic field [122], and we neglect the effects of spin-orbit coupling on the Dirac plasmon, which are deemed to be small in graphene [101].

2.2.2 Energy loss probability densities

The energy balance of the system composed of the incident particle traversing a number of graphene layers gives the condition $W_{\rm ext}+W_{\rm Ohm}+W_{\rm rad}=0$, where $W_{\rm ext}<0$ is the total energy lost by the external charged particle, $W_{\rm Ohm}>0$ is the Ohmic energy deposited in the graphene layers, and $W_{\rm rad}>0$ is the electromagnetic energy radiated in the far-field region. We use appropriate Physical definitions for each term to deduce expressions for the corresponding probability densities while upholding the conservation of the total energy. Each of these energy contributions may be further suitably decomposed into Physically motivated and/or experimentally observable components.

We define $W_{\rm ext}$ as the total work done by the induced electric field on the external charge,

$$W_{\rm ext} = \int_{-\infty}^{+\infty} dt \iiint d^3\mathbf{R}\, \mathbf{J}_{\rm ext}(\mathbf{R},t) \cdot \mathbf{E}_{\rm ind}(\mathbf{R},t). \tag{2.23}$$

Switching to Fourier transforms and invoking the parity properties of $\sigma_l(k,\omega)$, $A(k,\omega)$ and $q(k,\omega)$ as functions of frequency enables us to write Eq. (2.23) in a form, which defines a joint probability density that the external charge will lose an energy $\hbar\omega \geq 0$ (at zero temperature) and suffer a change in the momentum $\hbar\mathbf{k}$ perpendicular to its trajectory, $F_{\rm ext}(k,\omega)$, via

$$W_{\rm ext} \equiv -\iint d^2\mathbf{k} \int_0^{+\infty} d\omega\, \omega\, F_{\rm ext}(k,\omega), \tag{2.24}$$

where

$$F_{\rm ext}(k,\omega) = \frac{1}{4\pi^3\omega} \sum_{l=1}^{N} \Re\left\{\sigma_l E_l \mathcal{A}^* \mathrm{e}^{-iQz_l}\right\} \tag{2.25}$$

can be evaluated upon substitution of the solution of the system of equations in Eq. (2.15) for E_l.

In a similar manner, we may write the total Ohmic energy loss in all graphene layers in terms of the total electric field $\mathbf{E}$ as

$$\begin{aligned} W_{\rm Ohm} &= \int_{-\infty}^{+\infty} dt \iiint d^3\mathbf{R}\, \mathbf{J}_{\rm ind}(\mathbf{R},t) \cdot \mathbf{E}(\mathbf{R},t) \\ &\equiv \iint d^2\mathbf{k} \int_0^{+\infty} d\omega\, \omega\, F_{\rm Ohm}(k,\omega), \end{aligned} \tag{2.26}$$

where we have defined $F_{\rm Ohm}(k,\omega)$ as the corresponding joint probability density. In principle, it may be possible to observe the Ohmic losses in individual graphene layers, so it makes sense to define a layer-wise decomposition of the total Ohmic loss as $W_{\rm Ohm} = \sum_{l=1}^{N} W_{{\rm Ohm},l}$, with the Ohmic loss in the lth layer given by

$$W_{{\rm Ohm},l} \equiv \iint d^2\mathbf{k} \int_0^{+\infty} d\omega\, \omega\, F_{{\rm Ohm},l}(k,\omega), \tag{2.27}$$

where the corresponding probability density for Ohmic loss in the lth layer is

$$F_{{\rm Ohm},l}(k,\omega) = \frac{1}{4\pi^3\omega} |E_l|^2 \ \Re\left\{\sigma_l\right\}. \tag{2.28}$$

Thus, the total probability density for Ohmic losses may also be written as a layer decomposition, $F_{\rm Ohm}(k,\omega) = \sum_{l=1}^{N} F_{{\rm Ohm},l}(k,\omega)$.

Finally, we obtain the total electromagnetic energy radiated in the far-field from the flux of Poynting vector due to induced electric and magnetic fields taken over a large closed surface S enclosing all graphene layers,

$$\begin{aligned} W_{\rm rad} &= \frac{c}{4\pi}\int_{-\infty}^{+\infty} dt \oiint_S dS\,\hat{\mathbf{n}}\cdot[\mathbf{E}_{\rm ind}(\mathbf{R},t)\times\ \mathbf{H}_{\rm ind}(\mathbf{R},t)] \\ &\equiv \iint d^2\mathbf{k}\int_0^{+\infty} d\omega\,\omega\,F_{\rm rad}(k,\omega), \end{aligned} \tag{2.29}$$

where $F_{\rm rad}(k,\omega)$ is the corresponding joint probability density. We may represent the surface S by two (infinite) planes at $z=\pm\infty$, so that $dS = d^2\mathbf{r}$ and $\hat{\mathbf{n}} = \pm\hat{\mathbf{z}}$. Then, the total radiated energy may be written as the sum $W_{\rm rad} = W_{\rm rad}^{\uparrow} + W_{\rm rad}^{\downarrow}$, involving contributions in the upper half-space ($\uparrow$) and the lower half-space ($\downarrow$), with

$$W_{\rm rad}^{\uparrow\downarrow} \equiv \iint d^2\mathbf{k}\int_0^{+\infty} d\omega\,\omega\,F_{\rm rad}^{\uparrow\downarrow}(k,\omega), \tag{2.30}$$

where we have defined the corresponding probability densities of the radiation losses as

$$F_{\rm rad}^{\uparrow\downarrow}(k,\omega) = \frac{\kappa}{\omega^2\,(2\pi)^2}\sum_{l=1}^{N}\sum_{l'=1}^{N}\Re\left\{\sigma_l\,\sigma_{l'}^{*}\mathrm{e}^{\mp i\kappa(z_l-z_{l'})}E_l\,E_{l'}^{*}\right\}. \tag{2.31}$$

Thus, the total probability density for the radiation energy losses may also be written as a directional decomposition, $F_{\rm rad}(k,\omega) = F_{\rm rad}^{\uparrow}(k,\omega) + F_{\rm rad}^{\downarrow}(k,\omega)$.

We emphasize that the function $F_{\rm rad}(k,\omega)$ for radiative losses is non-zero only for frequencies above the light line, $\omega > ck$, whereas external and Ohmic losses may generally occur at all frequencies, $\omega > 0$. Thus, the functions $F_{\rm ext}(k,\omega)$ and $F_{\rm Ohm}(k,\omega)$ for external and Ohmic losses have non-zero contributions both below *and* above the light line, which may be accordingly defined via

$$F_{\rm ext}(k,\omega) = \begin{cases} F_{\rm ext}^{<}(k,\omega), & \omega < ck \\ F_{\rm ext}^{>}(k,\omega), & \omega > ck, \end{cases} \tag{2.32}$$

and

$$F_{\rm Ohm}(k,\omega) = \begin{cases} F_{\rm Ohm}^{<}(k,\omega), & \omega < ck \\ F_{\rm Ohm}^{>}(k,\omega), & \omega > ck. \end{cases} \tag{2.33}$$

Hence, in that sense, one may write the conservation of energy with respect to the frequency ranges as $F_{\rm ext}^{<}(k,\omega) = F_{\rm Ohm}^{<}(k,\omega)$ and $F_{\rm ext}^{>}(k,\omega) = F_{\rm Ohm}^{>}(k,\omega) + F_{\rm rad}(k,\omega)$, outside and inside the light cone, respectively. It should be stressed, however, that the probability density

$F^{>}_{\rm Ohm}(k,\omega)$ in the second line of Eq. (2.33) is not associated with any radiation, even though that contribution to Ohmic losses covers the region of frequencies above the light line.

In various electron energy loss spectroscopies it is often of interest to study quantities after performing integration over the momentum transfer, so that for each joint probability density function $F_L(k,\omega)$, we define an associated total integrated probability density as

$$P_{\rm L}(\omega) = \frac{1}{\hbar^2}\iint d^2\mathbf{k}\, F_{\rm L}(k,\omega), \tag{2.34}$$

where $\mathrm{L} = \mathrm{ext}, \mathrm{Ohm}, \mathrm{rad}$. In the case of Ohmic and radiation losses, one may also express the corresponding integrated densities in terms of layer-wise and directional decompositions, $P_{\rm Ohm}(\omega) = \sum_{l=1}^{N} P_{{\rm Ohm},l}(\omega)$ and $P_{\rm rad}(\omega) = P^{\uparrow}_{\rm rad}(\omega) + P^{\downarrow}_{\rm rad}(\omega)$, respectively.

Any differences between the radiation emitted in the upper and the lower half-spaces would be most feasibly observed in the joint spectral density and the angular distribution, $\mathcal{S}(\theta,\omega)$, defined so that the total radiation energy loss is written as

$$W_{\rm rad} \equiv \iint d^2\hat{\Omega} \int_0^{\infty} d\omega\, \mathcal{S}(\theta,\omega), \tag{2.35}$$

where $d^2\hat{\Omega} = \sin\theta d\theta d\phi$ is the element of solid angle in spherical coordinates ($0 \le \theta \le \pi$ and $0 \le \phi < 2\pi$, see Fig. 2.1), with the angle θ defining the direction of radiation with respect to the z-axis. One may express the joint spectral density and the angular distribution of radiation as

$$\mathcal{S}(\theta,\omega) = \frac{\omega^3}{c^2}\,|\cos\theta| \times \begin{cases} F^{\uparrow}_{\rm rad}\left(\dfrac{\omega}{c}\sin\theta,\omega\right), & 0 \le \theta \le \pi/2 \\ F^{\downarrow}_{\rm rad}\left(\dfrac{\omega}{c}\sin\theta,\omega\right), & \pi/2 \le \theta \le \pi. \end{cases} \tag{2.36}$$

The relation between the joint spectral density and the angular distribution of radiation and the corresponding joint momentum and energy loss density, given in Eq. (2.36), may be obtained by writing $\mathbf{k} = \{k_x, k_y\} = \frac{\omega}{c}\sin\theta\,\{\cos\phi, \sin\phi\}$, so that $d^2\mathbf{k} = dk_x dk_y = \frac{\omega^2}{c^2}\sin\theta|\cos\theta| d\theta d\phi$, $k = \frac{\omega}{c}\sin\theta$, and $\kappa = \frac{\omega}{c}|\cos\theta|$. Thus, one finds for the integrated probability density of radiation in the upper and lower half-spaces

$$P^{\uparrow\downarrow}_{\rm rad}(\omega) = \frac{1}{\hbar^2}\iint d^2\mathbf{k}\, F^{\uparrow\downarrow}_{\rm rad}(k,\omega) = \frac{1}{\omega}\iint\limits_{\vee,\wedge} d^2\hat{\Omega}\, \mathcal{S}(\theta,\omega), \tag{2.37}$$

where the last integral over solid angle goes over $0 \le \theta \le \pi/2$ (region $\vee$) or $\pi/2 \le \theta \le \pi$ (region $\wedge$).

2.2.3 Conductivity model

We note that our theory may be implemented for any 2D material, which can be described by a scalar conductivity $\sigma(k,\omega)$. In order to be specific, we adopt here a Drude model for optical conductivity of doped graphene, but note that conclusions of this work are applicable to any 2D conductive system exhibiting low-energy intraband electronic excitations that may be described by a Drude-type model [91]. Our interest in doped graphene stems from the fact that it supports the technologically interesting Dirac plasmon in the THz to IR frequency range [82], which is well reproduced by the Drude model [66, 119]. At the same time, this range of frequencies implies that we work in an extreme long-wavelength limit, for which Novko *et al.* showed that *ab initio* calculations of graphene conductivity give a Drude model as a correct $k \to 0$ limit at low frequencies [43]. We further assume that distances between graphene layers in our work are large enough that the electronic band structure of each layer is not affected by the presence of other layers, so that the optical conductivity of each layer may be adequately described by a Drude model under sufficient graphene doping [101]. The validity of this assumption was demonstrated in experiments performed by Yan *et al.* on the IR plasmonic devices with stacks of graphene layers separated by 20 nm thick spacers [100].

The general form of a Drude model for optical conductivity of graphene is given by

$$\sigma(\omega) = i\frac{v_B}{\pi}\frac{v_F k_F}{\omega + i\gamma}, \tag{2.38}$$

where $v_B = e^2/\hbar \approx c/137$ is the Bohr velocity, $v_F \approx c/300$ is the Fermi speed of graphene's π electron bands, $k_F = \sqrt{\pi|n|}$ is the Fermi wavenumber in a graphene layer doped with the charge carrier density n, and γ is phenomenological damping rate, which we let $\gamma \to 0^+$ in the limit of vanishing dissipation. This model is accurate enough for the range $k \ll \omega/v_F \ll k_F$ [91].

In the THz range, it is convenient to work with nondimensionalized wavenumber and frequency, defined as $\overline{k} = k/k_c$ and $\overline{\omega} = \omega/\omega_c$, respectively, where $k_c = e^2 v_F k_F/(\hbar c^2)$ and $\omega_c = ck_c$ [42]. We note that for the doping density of $|n| = 2.36 \times 10^{13}$ cm^{-2}, with the corresponding Fermi energy of $\varepsilon_F = \hbar v_F k_F \approx 0.57$ eV that is easily achieved in experiments with MLG, one obtains $\lambda_c = 2\pi/k_c \approx 300$ μm and $\nu_c = \omega_c/(2\pi) \approx 1$ THz. Thus, defining the reduced conductivity by $\overline{\sigma} = \sigma/c$, the Drude model gives

$$\overline{\sigma}(\overline{\omega}) = \frac{i}{\pi}\frac{1}{\overline{\omega} + i\overline{\gamma}}, \tag{2.39}$$

where $\overline{\gamma} = \gamma/\omega_c$ is the reduced damping rate.

Considering the Drude model in relation (2.38), the difference in the conductivities of the graphene layers can be spotted in the differences in the doping densities and damping rates of

the layers. A symmetric MLG structure is the one in which all the layers have the same doping densities, n, and damping rates, γ. In contrast, in an asymmetric MLG structure, graphene layers have, in general, different doping densities, n_l's and damping rates γ_l's. While for the MLG with $N > 2$ we shall only analyze the symmetric structure, for the special case of DLG we shall consider both symmetric and asymmetric structures under analysis.

Clearly, the Drude model neglects nonlocal effects in the graphene's conductivity, which may become critical for theoretical modeling of the quasi-acoustic HDPP modes in an MLG [101, 114, 116, 118]. Namely, the lowest-lying of those modes may be pushed close to the boundary line $\omega = v_F k$ of the continuum of the low-energy, single electron excitations within graphene's π electron bands [91]. Defining the reduced distance between graphene layers as $\overline{d} = k_c d$ (assuming equally spaced layers), one may use Eq. (9) in Ref. [116] to show that the condition $\overline{d} \gg (v_F/c)^2$ guarantees that the dispersions of the lowest-lying HDPPs are well above the line $\omega = v_F k$, thereby rendering the Drude model adequate for all HDPP modes in an MLG. In order to test the role of nonlocal effects, we have performed calculations using a wavenumber dependent conductivity based on the random-phase approximation given in Ref. [123]. We have found no difference in comparison with the results obtained from the Drude model in Eq. (2.39), even down to $\overline{d} = 10^{-5}$. We adopt here the range of interlayer distances $10^{-3} \leq \overline{d} \leq 1$, corresponding to the physical distances of 48 nm $\lesssim d \lesssim$ 48 μm for the doping density of $|n| = 2.36 \times 10^{13}$ cm^{-2}. We note that, even for the shortest distance of $d = 48$ nm considered in this work, which is comparable to distances used in the experiments in Refs. [100, 105], one may safely assume that graphene layers are electronically decoupled and their only interaction is due to the EM fields.

It should be mentioned that theoretical modeling of optical experiments using MLG at THz frequencies often invokes an approximation that the conductivity of N equally doped graphene layers is given by $\sigma_N(\omega) = N\sigma(\omega)$, where $\sigma(\omega)$ is the optical conductivity of an SLG [100, 105, 107]. This approximation is expected to work well if the interlayer distances are not too large, so that the MLG may be considered as optically thin, but also not too small, so that the graphene layers are electronically decoupled. The validity of this approximation was confirmed in experiments using plasmonic devices with two graphene layers separated by an 80 nm polymer layer [105], stacks of up to $N = 5$ graphene layers separated by 20 nm thick spacers [100], periodic lattices of graphene nanoribbons in two parallel planes a distance 1 nm apart [106], and even stacks of randomly oriented graphene layers with $d \sim 0.3$ nm [107]. Accordingly, in the subsequent sections, we shall test the range of applicability of the above approximation for optically thin MLG by using an analytical result obtained in Ref. [42] for the integrated Ohmic energy loss in an SLG, $P_{\rm Ohm}^{\rm SLG}[\sigma(\omega), \omega]$, where the conductivity of an SLG is replaced by $\sigma_N(\omega) = N\sigma(\omega)$.

2.2.4 Two graphene layers

We apply the general formulation of the problem for N layers to the case of two parallel graphene layers with distance d between them. Letting $z_{1,2} = \mp\frac{d}{2}$, we solve the system of equations in Eq. (2.15) for $E_{1,2}$ and obtain expressions for joint probability densities. Limiting our focus to $N = 2$ for such a case, the matrix $\underline{\underline{\epsilon}}$ in Eq. (2.16) becomes

$$\underline{\underline{\epsilon}} = \begin{bmatrix} 1 + i\frac{2\pi}{\omega} q\sigma_1 & i\frac{2\pi}{\omega} q\sigma_2 \mathrm{e}^{-qd} \\ i\frac{2\pi}{\omega} q\sigma_1 \mathrm{e}^{-qd} & 1 + i\frac{2\pi}{\omega} q\sigma_2 \end{bmatrix}. \tag{2.40}$$

Then, the solution of the matrix equation $\underline{\underline{\epsilon}}\ \underline{\mathbf{E}} = \underline{\mathbf{b}}$ may be written as $E_l = \mathcal{A}\,\tilde{E}_l\,\mathrm{e}^{iQz_l}$ with $l = 1, 2$, where the dimensionless in-plane electric fields are given by

$$\tilde{E}_{1,2} = \frac{1}{\Delta}\left[1 + i\frac{2\pi}{\omega} q\sigma_{2,1}\left(1 - \mathrm{e}^{-qd}\,\mathrm{e}^{\pm iQd}\right)\right], \tag{2.41}$$

with $\Delta \equiv \det\left(\underline{\underline{\epsilon}}\right)$ being the determinant of the matrix in Eq. (2.40). Thus, using this solution for $E_{1,2}$ in Eqs. (2.25), (2.28) and Eq. (2.31) gives our final results for probability densities for various contributions to the energy loss in the case of two graphene layers. One may then use the expressions for $E_{1,2}$ obtained from Eq. (2.41) to explicitly verify that the conservation of energy is expressed in terms of the probability densities as $F_{\mathrm{ext}}(k,\omega) = F_{\mathrm{Ohm}}(k,\omega) + F_{\mathrm{rad}}(k,\omega)$.

To facilitate further discussion, we give here explicit expressions for F_{Ohm} and F_{rad} in the case of graphene layers with equal conductivities (symmetric DLG). Noticing that the radiative losses are non-zero only for frequencies above the light line, $\omega > ck$, we obtain

$$F_{\mathrm{rad}}(k,\omega) = \frac{|\mathcal{A}|^2}{4\pi^3\omega}\frac{2\pi}{\omega}\kappa\,|\sigma|^2\left\{\frac{[1-\cos(Qd)]\,[1-\cos(\kappa d)]}{\left|1+\frac{2\pi}{\omega}\kappa\sigma\left(1-\mathrm{e}^{i\kappa d}\right)\right|^2} + \frac{[1+\cos(Qd)]\,[1+\cos(\kappa d)]}{\left|1+\frac{2\pi}{\omega}\kappa\sigma\left(1+\mathrm{e}^{i\kappa d}\right)\right|^2}\right\}. \tag{2.42}$$

On the other hand, Ohmic losses may generally occur at all frequencies, $\omega > 0$. Defining the probability densities for Ohmic losses above the light line and below the light line as in Eq. (2.33), we obtain

$$F^{>}_{\mathrm{Ohm}}(k,\omega) = \frac{|\mathcal{A}|^2}{4\pi^3\omega}\Re\{\sigma\}\left\{\frac{1-\cos(Qd)}{\left|1+\frac{2\pi}{\omega}\kappa\sigma\left(1-\mathrm{e}^{i\kappa d}\right)\right|^2} + \frac{1+\cos(Qd)}{\left|1+\frac{2\pi}{\omega}\kappa\sigma\left(1+\mathrm{e}^{i\kappa d}\right)\right|^2}\right\}, \tag{2.43}$$

and

$$F^{<}_{\mathrm{Ohm}}(k,\omega) = \frac{|\mathcal{A}|^2}{4\pi^3\omega}\Re\{\sigma\}\left\{\frac{1-\cos(Qd)}{\left|1+i\frac{2\pi}{\omega}\alpha\sigma\left(1-\mathrm{e}^{-\alpha d}\right)\right|^2} + \frac{1+\cos(Qd)}{\left|1+i\frac{2\pi}{\omega}\alpha\sigma\left(1+\mathrm{e}^{-\alpha d}\right)\right|^2}\right\}. \tag{2.44}$$

We finally note that, in the non-retarded regime, we let $c \to \infty$ so that both $F_{\rm rad}(k,\omega) \to 0$ and $F^{>}_{\rm Ohm}(k,\omega) \to 0$, whereas the total energy loss of the external charged particle becomes $F^{NR}_{\rm ext}(k,\omega) = F^{<}_{\rm Ohm}(k,\omega)$, with $F^{<}_{\rm Ohm}$ given in Eq. (2.44) where we set $\alpha(k,\omega) \to k$ and $\mathcal{A} \to -ik\,\frac{Ze}{v}\,A^{NR}$ with $A^{NR} = 4\pi/\left(\frac{\omega^2}{v^2}+k^2\right)$. The non-retarded integrated probability density is then

$$P^{NR}_{\rm ext}(\omega) = \frac{2\pi}{\hbar^2}\int_0^{+\infty} dk\,k\,F^{NR}_{\rm ext}(k,\omega). \tag{2.45}$$

We next show that both the Ohmic and radiative losses exhibit an asymmetry with respect to the direction of motion of the external charge particle, i.e., the corresponding decompositions of those two types of losses depend on the sign of the external charge particle's velocity component along the z-axis. This is best illustrated by considering the special case of the symmetric structure consisting of two graphene layers with equal conductivities. In that case, we may write the probability densities for Ohmic losses in the layers 1 and 2 as

$$F_{\rm Ohm,1,2}(k,\omega) = \frac{|\mathcal{A}|^2}{4\pi^3\omega}\Re\{\sigma\}\left[\frac{1-\cos(Qd)}{2\,|\lambda_-|^2}+\frac{1+\cos(Qd)}{2\,|\lambda_+|^2}\mp\sin(Qd)\Im\left\{\frac{1}{\lambda_-^*\lambda_+}\right\}\right], \tag{2.46}$$

and the probability densities for radiative losses in the upper/lower half-spaces as

$$F^{\uparrow\downarrow}_{\rm rad}(k,\omega) = \frac{|\mathcal{A}|^2}{4\pi^3\omega}\frac{2\pi}{\omega}\kappa\,|\sigma|^2\left[\frac{1-\cos(Qd)}{2\,|\lambda_-|^2}\,(1-\cos(\kappa d))+\frac{1+\cos(Qd)}{2\,|\lambda_+|^2}\,(1+\cos(\kappa d))\right.$$
$$\left.\pm\sin(Qd)\sin(\kappa d)\Re\left\{\frac{1}{\lambda_-^*\lambda_+}\right\}\right], \tag{2.47}$$

where $\lambda_\mp = 1 + i\frac{2\pi}{\omega}q\sigma\left(1\mp e^{-qd}\right)$ are the eigenvalues of a 2×2 matrix, which defines the system of equations in Eq. (2.15) upon setting $\sigma_1 = \sigma_2 = \sigma$. Clearly, asymmetries arise in the layer-wise decomposition of Ohmic losses and in the directional decomposition of radiative losses from the last terms in Eqs. (2.46) and (2.47), respectively. Those terms will be canceled out when we evaluate the total Ohmic and the total radiative losses as $F_{\rm Ohm} = F_{\rm Ohm,1} + F_{\rm Ohm,2}$ and $F_{\rm rad} = F^{\downarrow}_{\rm rad} + F^{\uparrow}_{\rm rad}$, respectively.

Going back to a more general case of two graphene layers with different conductivities, $\sigma_1 \neq \sigma_2$, we emphasize that the function $F_{\rm rad}(k,\omega)$ for radiative losses is non-zero only for frequencies above the light line, $\omega > ck$, whereas Ohmic losses may generally occur at all

frequencies, $\omega > 0$. Conductivity of each graphene layer has both a dissipative part, $\Re\{\sigma_l\}$, and a reactive part, $\Im\{\sigma_l\}$, which are generally different from zero. While the collective oscillations of charge carriers in each graphene layer or, equivalently, the excitation of its DPP gives rise to $\Im\{\sigma_l\} > 0$, scattering of those carriers on phonons, charged impurities or atomic-size defects in graphene gives rise to $\Re\{\sigma_l\} > 0$, signalling the existence of several possible decay channels for the DPPs. Referring to the result obtained by $F_{\mathrm{Ohm},l}(k,\omega) = \frac{1}{4\pi^3\omega}\,|E_l|^2\ \Re\{\sigma_l\}$, one may assert that the Ohmic losses describe both the process of plasmon excitation in graphene layers and the decay of those plasmons, which ultimately generates Joule heat at all frequencies whenever $\Re\{\sigma_l\} > 0$.

In an idealized case of clean graphene layers at zero temperature, and at frequencies well separated from the phonon frequencies, it is worthwhile considering a theoretical limit of vanishing dissipation, $\Re\{\sigma_l\} \to 0^+$, when no heat is generated in those layers. It may be then shown that the function in the second line of Eq. (2.33) vanishes, $F^{>}_{\mathrm{Ohm}}(k,\omega) \to 0$, leaving the radiation to be the only cause of energy losses of the external charged particle at frequencies $\omega > ck$, governed by a probability density $F_{\mathrm{rad}}(k,\omega)$, which turns out to be only marginally affected by reduction of dissipation in graphene layers. On the other hand, it may also be shown that, by taking the limit $\Re\{\sigma_l\} \to 0^+$, the function in the first line of Eq. (2.33) does not vanish, but is rather reduced to a new function, $F^{<}_{\mathrm{Ohm}}(k,\omega) \to F_{\mathrm{pl}}(k,\omega)$, which we define as the probability density for exciting collective modes that result from hybridization of the DPPs in two graphene layers. We will later outline a procedure showing that, in the limit of vanishing dissipation, $\Re\{\sigma_l\} \to 0^+$, the total probability density of plasmon excitations may be expressed in the form of a modal decomposition, $F_{\mathrm{pl}}(k,\omega) = F^{-}_{\mathrm{pl}}(k,\omega) + F^{+}_{\mathrm{pl}}(k,\omega)$, with the function $F^{\mp}_{\mathrm{pl}}(k,\omega)$ containing a Dirac's delta function that involves a dispersion relation for the bonding/antibonding hybridized mode.

The dispersion relations for those modes may be found by letting $\Re\{\sigma_1\} = \Re\{\sigma_2\} \to 0^+$ in a 2×2 matrix defining the system of equations in Eq. (2.15). Solving an eigenvalue problem with that matrix yields two eigenvalues, given by

$$\lambda_{\mp} = 1 + i\frac{2\pi}{\omega}\alpha\left(\sigma_m \mp \sqrt{\sigma_d^2 + \sigma_1\sigma_2\,\mathrm{e}^{-2\alpha d}}\right), \tag{2.48}$$

where $\sigma_m = \frac{\sigma_1+\sigma_2}{2}$ and $\sigma_d = \frac{\sigma_2-\sigma_1}{2}$, and $\alpha(k,\omega) \equiv \sqrt{k^2 - \left(\frac{\omega}{c}\right)^2}$. Those eigenvalues have real-valued zeros in the (k,ω) plane only for frequencies below the light line, $0 < \omega < ck$, i.e., when $\alpha(k,\omega)$ is real-valued. Note that the square root in Eq. (2.48) is purely imaginary in the limit of vanishing dissipation, and it should be taken with the same sign as the sign of the reactive part of graphene conductivities, $\Im\{\sigma_{1,2}\}$. By solving the equations $\lambda_{\mp}(k,\omega) = 0$ defined via Eq. (2.48) we obtain two dispersion relations, $\omega = \omega_{\mp}(k)$, for two hybridized DPP modes in

graphene layers, where the signs $\mp$ correspond to the low-energy bonding and the high-energy antibonding coupling between the layers, respectively [99, 100]. Since those dispersion relations are located below the light line, excitation of long-lived bonding and antibonding DPP modes is the only cause of energy loss of the external charged particle at frequencies $\omega < ck$ in the limit of vanishing dissipation in graphene, governed by the probability density $F_{\mathrm{pl}}(k,\omega)$.

According to Eq. (2.38), the Drude model for optical conductivity of the lth graphene layer, with $l = 1, 2$, is given by

$$\sigma_l(\omega) = i\frac{v_B}{\pi}\frac{v_F k_{F,l}}{\omega + i\gamma_l}, \tag{2.49}$$

where $k_{F,l} = \sqrt{\pi|n_l|}$ is the Fermi wavenumber in the lth graphene layer, and γ_l is phenomenological damping rate, which we let $\gamma_l \to 0^+$ in the limit of vanishing dissipation.

In the case of DLG with generally different conductivities, it is convenient to introduce reduced wavenumber and reduced frequency, $\overline{k} = k/k_c$ and $\overline{\omega} = \omega/\omega_c$, respectively, with $k_c = v_B v_F\left(k_{F,1} + k_{F,2}\right)/\left(2c^2\right)$ and $\omega_c = ck_c$. The system also needs to be characterized by the ratio $\rho = k_{F,1}/k_{F,2} = \sqrt{|n_1/n_2|}$, where $l = 1$ stands for the "lower" layer and $l = 2$ stands for the "upper" layer with respect to the direction of the z-axis. Thus, defining the reduced conductivities by $\overline{\sigma}_l = \sigma_l/c$, we may write

$$\overline{\sigma}_1(\overline{\omega}) = \frac{i}{\pi}\frac{2\rho}{\rho+1}\frac{1}{\overline{\omega} + i\overline{\gamma}_1} \quad \text{and} \quad \overline{\sigma}_2(\overline{\omega}) = \frac{i}{\pi}\frac{2}{\rho+1}\frac{1}{\overline{\omega} + i\overline{\gamma}_2}, \tag{2.50}$$

where $\overline{\gamma}_l = \gamma_l/\omega_c$ are the reduced damping rates.

Upon switching to reduced units and setting $\overline{\gamma}_1 = \overline{\gamma}_2 = 0$ in Eq. (2.50), it may be shown that the equations $\lambda_{\mp}(k,\omega) = 0$ become equivalent to $\overline{\omega}^2 - 2\overline{\alpha}\left[1 \mp \mathcal{R}(\overline{\alpha})\right] = 0$, where $\overline{\alpha} = \sqrt{\overline{k}^2 - \overline{\omega}^2}$ and

$$\mathcal{R}(\overline{\alpha}) = \sqrt{\left(\frac{\rho-1}{\rho+1}\right)^2 + \frac{4\rho\,\mathrm{e}^{-2\overline{\alpha}\overline{d}}}{(\rho+1)^2}}, \tag{2.51}$$

with $\overline{d} = k_c d$. Solving those equations in the region below the light line, $0 < \overline{\omega} < \overline{k}$, gives the dispersion relations of the bonding/antibonding modes in reduced units, $\overline{\omega} = \overline{\omega}_{\mp}(\overline{k})$.

Modal decomposition of plasmon excitation

Considering the case of two graphene layers with different conductivities, we take the limit of vanishing dissipation in both layers, $\Re\{\sigma_{1,2}\} \to 0$, which gives rise to two HDPP modes with

the dispersion relations localized in the range of frequencies below the light line, $\omega < ck$. Thus, we may start from an expression for the probability density for total energy loss of the external charged particle at frequencies $\omega < ck$, and obtain an expression for the total probability density for excitation of those modes according to $F_{\rm ext}(k,\omega) = F^{<}_{\rm Ohm}(k,\omega) \rightarrow F_{\rm pl}(k,\omega)$. We wish to express this probability density in the form of a modal decomposition, $F_{\rm pl}(k,\omega) = F^{-}_{\rm pl}(k,\omega) + F^{+}_{\rm pl}(k,\omega)$, corresponding to excitations of the bonding and antibonding modes, respectively.

Note that the eigenvectors of the matrix $\underline{\underline{\epsilon}}$ in Eq. (2.40) corresponding to the eigenvalues $\lambda_{\mp}$, given in Eq. (2.48), may be written as

$$\underline{\mathbf{u}}_{\mp} = N_{\mp} \begin{bmatrix} \sigma_2 \, \mathrm{e}^{-\alpha d} \\ \sigma_d \mp \sqrt{\sigma_d^2 + \sigma_1 \sigma_2 \, \mathrm{e}^{-2\alpha d}} \end{bmatrix}, \tag{2.52}$$

where $N_{\mp}$ are normalization factors. Using eigenvalue decomposition, we have $\underline{\underline{\boldsymbol{\epsilon}}} = \underline{\underline{\mathbf{U}\boldsymbol{\Lambda}\mathbf{U}}}^{-1}$, where $\underline{\underline{\mathbf{U}}} = \begin{bmatrix} \underline{\mathbf{u}}_{-} & \underline{\mathbf{u}}_{+} \end{bmatrix}$ and $\underline{\underline{\boldsymbol{\Lambda}}} = \mathrm{diag}\,[\lambda_{-} \;\; \lambda_{+}]$. Thus, one may express the longitudinal components of the in-plane electric fields in graphene layers, $E_l \equiv \hat{\mathbf{k}} \cdot \mathbf{E}_{||}(\mathbf{k}, z_l, \omega)$ with $l = 1, 2$ as a modal decomposition $\underline{\mathbf{E}} = \underline{\underline{\boldsymbol{\epsilon}}}^{-1} \underline{\mathbf{b}} = \underline{\underline{\mathbf{U}\boldsymbol{\Lambda}}}^{-1} \underline{\underline{\mathbf{U}}}^{-1} \underline{\mathbf{b}}$. If we write $E_l = \mathcal{A} \, \tilde{E}_l \, \mathrm{e}^{iQz_l}$, we obtain the dimensionless variables $\tilde{E}_l$ as

$$\tilde{E}_{1,2} = \frac{C^{-}_{1,2}}{\lambda_{-}} + \frac{C^{+}_{1,2}}{\lambda_{+}}, \tag{2.53}$$

where

$$C^{\mp}_{1} = \frac{1}{2} \left(1 \mp \frac{\sigma_2 \mathrm{e}^{-\alpha d} \mathrm{e}^{i\frac{\omega}{v}d} - \sigma_d}{\sqrt{\sigma_d^2 + \sigma_1 \sigma_2 \, \mathrm{e}^{-2\alpha d}}} \right), \tag{2.54}$$

$$C^{\mp}_{2} = \frac{1}{2} \left(1 \mp \frac{\sigma_1 \mathrm{e}^{-\alpha d} \mathrm{e}^{-i\frac{\omega}{v}d} + \sigma_d}{\sqrt{\sigma_d^2 + \sigma_1 \sigma_2 \, \mathrm{e}^{-2\alpha d}}} \right). \tag{2.55}$$

Note that the expression in Eq. (2.53) is fully equivalent to that in Eq. (2.41). Recall that the dispersion relations, $\omega = \omega_{\mp}(k)$, of the bonding/antibonding modes are obtained from the zeros of the the eigenvalues $\lambda_{\mp}(k,\omega)$, given in Eq. (2.48), in the limit of vanishing dissipation in graphene layers.

Using the above solution for the in-plane longitudinal electric fields $E_{1,2}$ in Eq. (2.25) gives

$$F_{\rm ext}(k,\omega) = \frac{|\mathcal{A}|^2}{4\pi^3 \omega} \Re \left\{ \sigma_1 \tilde{E}_1 + \sigma_2 \tilde{E}_2 \right\} \longrightarrow F^{-}_{\rm pl}(k,\omega) + F^{+}_{\rm pl}(k,\omega), \tag{2.56}$$

where the joint probability densities for excitation of the bonding/antibonding modes,

$$F^{\mp}_{\rm pl}(k,\omega) = \frac{|\mathcal{A}|^2}{4\pi^3 \omega} \, \Re \left\{ \frac{1}{\lambda_{\mp}} \left[\sigma_m \mp \frac{\sigma_d^2 + \sigma_1 \sigma_2 \mathrm{e}^{-\alpha d} \cos\left(\frac{\omega}{v} d\right)}{\sqrt{\sigma_d^2 + \sigma_1 \sigma_2 \mathrm{e}^{-2\alpha d}}} \right] \right\} \Bigg|_{\Re\{\sigma_1\} = \Re\{\sigma_2\} \rightarrow 0^{+}}, \tag{2.57}$$

ultimately result in the expression given by

$$F_{\rm pl}^{\mp}(k,\omega) = F_c \frac{\beta^2\left(\overline{\omega}^2+\overline{\alpha}^2\right)}{\left(\overline{\omega}^2+\overline{\alpha}^2\beta^2\right)^2}\left\{1\mp\frac{1}{\mathcal{R}(\overline{\alpha})}\left[\left(\frac{\rho-1}{\rho+1}\right)^2+\frac{4\rho\,\mathrm{e}^{-\overline{\alpha}\overline{d}}}{(\rho+1)^2}\cos\left(\frac{\overline{\omega}}{\beta}\overline{d}\right)\right]\right\} \times\delta\left(\overline{\omega}^2-2\overline{\alpha}\left[1\mp\mathcal{R}(\overline{\alpha})\right]\right), \tag{2.58}$$

where $F_c \equiv 4(Ze)^2/\left(\pi\omega_c^2 k_c\right)$ and $\beta \equiv v/c$. As with the other contributions to energy losses, we may use the above result in Eq. (2.34) to define the integrated probability densities, $P_{\rm pl}^{\mp}(\omega)$, for exciting the bonding and antibonding modes per unit interval of frequency. Note that integration of $F_{\rm pl}^{\mp}(\overline{k},\overline{\omega})$ over $\overline{k}$ (or $\overline{\alpha}$) is greatly aided by the presence of the Dirac's delta function in Eq. (2.58), which is peaked along the dispersion relation $\overline{\omega}=\overline{\omega}_{\mp}(\overline{k})$ for those two modes.

Average number of plasmons

Based on the interpretation of $P_{\rm pl}^{\mp}(\omega)$ as the probability density for exciting the hybridized DPP modes per unit energy, we can evaluate the average numbers of the bonding and antibonding modes as [124]

$$\begin{aligned}\nu_{\mp} &= \hbar\int_0^{\infty} d\omega\, P_{\rm pl}^{\mp}(\omega)\\ &= 8\frac{v_B}{c}\int_0^{\infty} d\overline{\omega}\int_{\overline{\omega}}^{\infty} d\overline{k}\,\overline{k}\,\overline{F}_{\rm pl}^{\mp}\left(\overline{k},\overline{\omega}\right),\end{aligned} \tag{2.59}$$

where we switched to reduced quantities and defined $\overline{F}_{\rm pl}^{\mp}=F_{\rm pl}^{\mp}/F_c$, with $F_{\rm pl}$ given in Eq. (2.58). Interchanging the order of integration in Eq. (2.59), using the Dirac's delta function,

$$\delta\left(\overline{\omega}^2-2\overline{\alpha}\left[1\mp R(\overline{\alpha})\right]\right)=\frac{\delta\left(\overline{\omega}-2\overline{\alpha}\left[1\mp R(\overline{\alpha})\right]\right)}{2\left|\overline{\omega}\right|},$$

and changing the variable $\overline{k}$ to $\overline{\alpha}=\sqrt{\overline{k}^2-\overline{\omega}^2}$, we finally obtain for the average numbers of the excited modes

$$\begin{aligned}\nu_{\mp} &= 8\frac{v_B}{c}\int_0^{\infty} d\overline{\omega}\int_0^{\infty} d\overline{\alpha}\,\overline{\alpha}\,\overline{F}_{\rm pl}^{\mp}\left(\overline{\alpha},\overline{\omega}\right)\\ &= 4\frac{v_B}{c}\int_0^{\infty} d\overline{\alpha}\,\overline{\alpha}\,\frac{\overline{\alpha}^2+\overline{\omega}^2}{\overline{\omega}\beta^2\left(\frac{\overline{\omega}^2}{\beta^2}+\overline{\alpha}^2\right)^2}\\ &\quad\times\left\{1\mp\frac{1}{\mathcal{R}(\overline{\alpha})}\left[\left(\frac{\rho-1}{\rho+1}\right)^2+\frac{4\rho\,\mathrm{e}^{-\overline{\alpha}\overline{d}}}{(\rho+1)^2}\cos\left(\frac{\overline{\omega}}{\beta}\overline{d}\right)\right]\right\}\Bigg|_{\overline{\omega}=\sqrt{2\overline{\alpha}[1\mp\mathcal{R}(\overline{\alpha})]}},\end{aligned} \tag{2.60}$$

with $\mathcal{R}\left(\overline{\alpha}\right)$ defined in Eq. (2.51). As one can easily verify, the average number of plasmons is symmetric with respect to $\rho = 1$, showing that the production of plasmons in each mode is independent of the direction of motion of the incident electron. In the following section we assess this expression for different values of the involved parameters.

We note that the corresponding analytical expression for the DPP in a single-layer graphene may be obtained by replacing the expression in curly brackets in Eq. (2.60) by unity, and substituting $\overline{\omega} = \sqrt{2\overline{\alpha}}$. On the other hand, the non-retarded results for $\nu_{\mp}$ are obtained from Eq. (2.60) by transforming the variable $\overline{\alpha} \to \overline{k}$ with the same range of integration, $0 \leq \overline{k} < \infty$, and by replacing the numerator $\overline{k}^2 + \overline{\omega}^2$ in the first quotient in the integrand of that equation by $\overline{k}^2$.

It is necessary to comment that we ignore any electromechanical interactions between doped graphene layers, including van der Waals and Casimir forces, and assume that the distance between them remains constant in the course of the charged particle traversal. Also, note that, with the use of the Drude conductivity model given in Eq. (2.39), in the limit of vanishing dissipation, each (non-interacting) layer supports a single-layer Dirac plasmon, with dispersion relation [42]

$$\left(\omega_{SL}^{l}\right)^2 = 2\left(v_F k_{F,l}\right)^2 \left[-\left(\frac{v_B}{c}\right)^2 + \sqrt{\left(\frac{v_B}{c}\right)^4 + \left(\frac{v_B}{v_F}\frac{k}{k_{F,l}}\right)^2} \right] . \tag{2.61}$$

The single-layer Dirac plasmons are electrodynamically coupled when the interlayer distance $d = |z_1 - z_2|$ is finite, giving rise to two hybridized DPP modes with dispersions $\omega = \omega_{\mp}(k)$, which can be identified as bonding and antibonding modes (for the case $\sigma_1 = \sigma_2 = \sigma$ they are symmetric and antisymmetric). We assume that the distance between graphene layers is bounded below, such that $d\, k_{F,l} \gg \hbar v_F / e^2$, allowing us to neglect the effects of the intraband single-electron excitation continuum on the hybridized plasmon dispersions. For typical doping densities, this condition also guarantees that direct electron coupling, or electron tunneling between graphene layers may be neglected as well. Remember that the "asymmetry parameter" ρ characterizes any difference between the doping densities. Hence the case $\rho = 1$ corresponds to equal conductivities, and any $\widetilde{\rho} = 1/\rho$ is equivalent to reversing the order of the layers.

2.3 Results and Discussion

While the formalism developed in the preceding sections can be directly applied to multiple layers of any 2D material described by a scalar conductivity [3], it may also be readily generalized to anisotropic 2D materials [125]. However, in this chapter, we are primarily interested

in graphene based layered structures of interest for possible applications in photonic and plasmonic devices that operate in the THz to IR range of frequencies. For this purpose it suffices to adopt the Drude model in Eq. (2.38), which is accurate enough for doped graphene satisfying $k \ll \omega/v_F \ll k_F$ [91], or in terms of the reduced variables, $\frac{v_F}{c}\overline{k} \ll \overline{\omega} \ll \frac{c}{v_B}$ [42].

2.3.1 Double-layer graphene

For two graphene layers, one of the most important parameters is the interlayer distance d, which we define in reduced units as $\overline{d} = k_c d$ and take it to vary in the range of values $10^{-3} \leq \overline{d} \leq 1$. Our calculations are designed to illustrate interferences due to retardation effects, which may give rise to asymmetries in: (a) directional decomposition of the radiation emitted in the upper and lower half-spaces, (b) layer-wise decomposition of the Ohmic losses in graphene, and (c) modal decomposition of the plasmon excitation probability density for the bonding and antibonding modes. We analyze what roles are played in those interference effects by the distance d and the ratio $\rho = k_{F,1}/k_{F,2} = \sqrt{|n_1|/|n_2|}$ defining asymmetry between the doping densities of the two graphene layers.

At the same time, we keep the damping rates in graphene layers fixed at a given value $\overline{\gamma}_l = 0.1$, except when discussing the dispersion relations of HDPP modes and the corresponding modal decomposition. In addition, we assume the external particle to be an electron ($Z = 1$) and keep its (reduced) speed fixed at the value $\beta = v/c = 0.5$, corresponding to a typical electron velocity in STEM. The effects of variation in the $\overline{\gamma_l}$ and β values are illustrated separately.

Equal conductivities

In this subsection we study the case of two graphene layers with equal doping densities ($\rho = 1$), and hence equal conductivities, $\sigma_1 = \sigma_2 = \sigma(\omega)$, described by the Drude model in Eq. (2.38).

Figure 2.2 shows dispersion relations for the bonding and antibonding modes using reduced units for frequency and wavenumber, $\overline{\omega}$ and $\overline{k}$. Results for the retarded case are shown in panel (a) by pairs of solid lines of different colors for different $\overline{d}$ values, while the corresponding results for the non-retarded case are shown in panel (b) by pairs of the dashed lines using the same colors, whereas the corresponding dispersion curve for single graphene layer is shown by a black line in each panel. One notices that the effect of retardation is to push the dispersion curves for both modes $\overline{\omega}_{\mp}$ below the light line, which is represented by the dotted line $\overline{\omega} = \overline{k}$ in Fig. 2.2. The two eigenfrequencies $\overline{\omega}_{\mp}(\overline{k})$ are seen in Fig. 2.2 to always straddle the dispersion relation for single graphene layer, given by $\overline{\omega}_{\text{single}} = \sqrt{2\left(-1+\sqrt{1+\overline{k}^2}\right)}$. While for $\overline{d} \to \infty$ we

find that $\overline{\omega}_{\mp} \to \overline{\omega}_{\rm single}$, the separation between $\overline{\omega}_{\mp}$ increases with decreasing interlayer distance, where the long wavelength limit is particularly interesting. Namely, when $kd = \overline{k}\,\overline{d} \ll 1$, we find for antibonding mode $\overline{\omega}_{+} \sim 2\sqrt{-2+\sqrt{4+\overline{k}^2}}$, corresponding to a single graphene layer with a doubled Fermi wavenumber, whereas the bonding mode exhibits a quasi-acoustic dispersion given by $\overline{\omega}_{-} \sim \sqrt{\frac{2\overline{d}}{1+2\overline{d}}}\,\overline{k}$. It is interesting that the dispersion of this mode is not affected by retardation for small inter-graphene distances, $\overline{d} \ll 1$, in which case we obtain in non-reduced units $\omega_{-} \sim \sqrt{2k_F d v_F v_B}\,k$. Accordingly, one can see in the two panels of Fig. 2.2 that the bonding mode dispersion relations $\overline{\omega} = \overline{\omega}_{-}(\overline{k})$ in the retarded and non-retarded cases are almost the same for $\overline{d} \leq 0.1$. On the other hand, it is observed that, generally, the bonding mode frequency $\omega_{-}(k)$ is much more affected by variations in the interlayer distance d than the antibonding mode frequency $\omega_{+}(k)$.

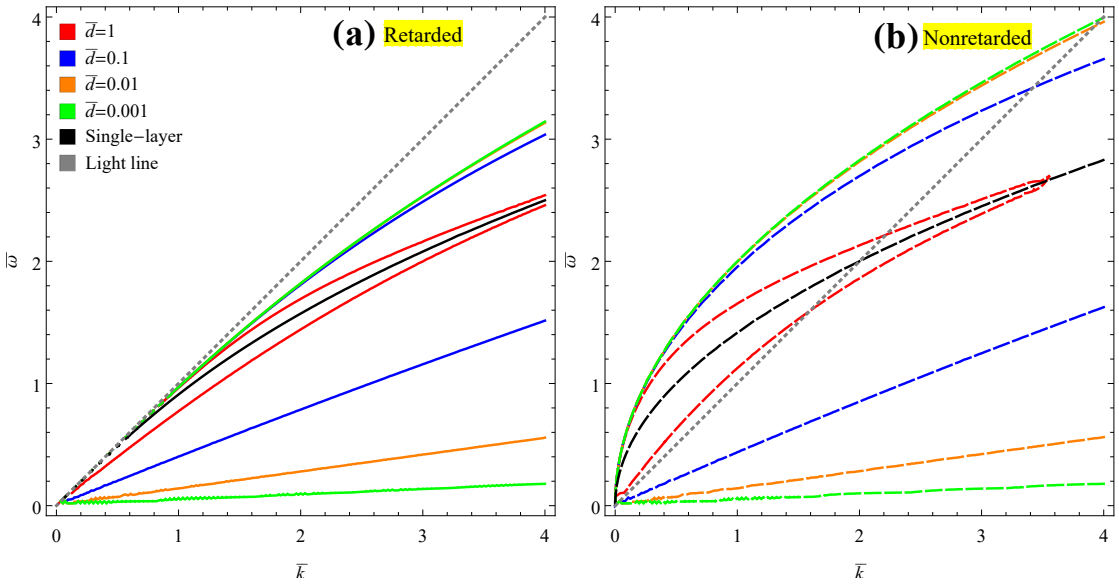

Figure 2.2: Dispersion curves for double-layer graphene with equal conductivities for several interlayer distances $\overline{d}$ in comparison with single-layer dispersion. Solid lines in panel (a) show retarded regime and dashed lines in panel (b) show non-retarded regime.

It is expected that, for sufficiently small distances and/or sufficiently small doping densities of graphene layers, the bonding mode will be subjected to strong Landau damping in the continuum of the intraband, single particle excitations of graphene's π electrons, which take place at frequencies $\omega < v_F k$ [91]. Thus, the condition for Landau damping of the bonding mode, $\omega_{-}(k) < v_F k$, may be expressed as $k_F d < \frac{1}{2}\frac{v_F}{v_B} \approx 0.23$. However, this regime is

not of interest in the present context because inclusion of the Landau damping due to single-particle excitations in graphene would require using a more elaborate model for its conductivity, $\sigma(k,\omega)$, which goes beyond the scope of the present chapter. In terms of the reduced distance between graphene layers, the condition for Landau damping of the bonding mode amounts to $\overline{d} < \frac{1}{2}\left(\frac{v_F}{c}\right)^2 \approx 5.6\times 10^{-6}$, so the range of inter-graphene distances we have chosen in the interval $0.001 \leq \overline{d} \leq 1$ eliminates the need to consider this regime and, at the same time, maintains the range of confidence in Drude model.

In Fig. 2.3 we show the joint probability densities for (a) Ohmic losses, $\overline{F}_{\rm Ohm}(\overline{k},\overline{\omega})$, and (b) radiation losses, $\overline{F}_{\rm rad}(\overline{k},\overline{\omega})$, as functions of the reduced frequency and wavenumber, $\overline{\omega}$ and $\overline{k}$, for an illustrative case of the reduced interlayer distance $\overline{d} = 0.1$. The color coding for those functions is based on reduced units using the normalization factor $F_c = 4\left(Ze\right)^2/\left(\pi\omega_c^2 k_c\right)$. Also shown are the dispersion relations for the bonding and antibonding modes with eigenfrequencies $\overline{\omega}_{\mp}(\overline{k})$ for two graphene layers (white solid lines), the dispersion curve for single graphene layer (black dashed line) with eigenfrequency $\overline{\omega}_{\rm single}$, and the light line (gray dashed line) $\overline{\omega} = \overline{k}$.

It is obvious from the panel (a) of Fig. 2.3 that the peak values of $\overline{F}_{\rm Ohm}(\overline{k},\overline{\omega})$ closely follow the dispersion curves for bonding and antibonding DPP modes, indicating that Ohmic energy losses of the external electron mostly go to excitations of those modes. However, the finiteness of $\overline{\gamma}$ causes a significant fraction of Ohmic losses to go to generating Joule heat in the layers, as is indicated by the red regions below *and* above the light line in Fig. 2.3(a), around small $\overline{\omega}$ and $\overline{k}$ values. When the damping rate is reduced, the energy losses due to the Joule heating are reduced, leaving the excitation of long-lived bonding and antibonding DPP modes as the only contribution to the Ohmic losses in the limit $\gamma \to 0^+$. In that limit, $\overline{F}_{\rm Ohm}(\overline{k},\overline{\omega})$ in Fig. 2.3(a) would be represented by a weighted superposition of two Dirac's delta functions located at the dispersion relations $\overline{\omega} = \overline{\omega}_{\mp}(\overline{k})$. On the other hand, in the panel (b) of Fig. 2.3 one notices that $\overline{F}_{\rm rad}(\overline{k},\overline{\omega})$ exhibits a relatively broad spectrum of radiation energy losses, which are strictly located above the light line, $\overline{\omega} > \overline{k}$. Those losses are not strongly affected by reduction of the damping rate, and they remain finite in the limit of vanishing dissipation in graphene.

Figure 2.4 displays joint probability densities for radiation and Ohmic losses, $\overline{F}_{\rm rad}(\overline{k},\overline{\omega})$ (dash-dotted lines) and $\overline{F}_{\rm Ohm}(\overline{k},\overline{\omega})$ (dashed lines), respectively, which we show in reduced units using the normalization factor $F_c = 4(Ze)^2/\left(\pi\omega_c^2 k_c\right)$. We show cross sections of those functions with $\overline{k} = 1$ (panel (a)) and $\overline{k} = 2$ (panel (b)) for several interlayer distances in the interval $0.01 \leq \overline{d} \leq 1$ using lines of different colors, and compare them with the results for $\overline{F}_{\rm rad}(\overline{k},\overline{\omega})$ and $\overline{F}_{\rm Ohm}(\overline{k},\overline{\omega})$ (black lines) for single graphene layer. One notices in Fig. 2.4 that the Ohmic losses are dominated by two peaks at frequencies $\overline{\omega} < \overline{k}$, with the lower-frequency peak located near the bonding mode eigenfrequency $\overline{\omega}_{-}(\overline{k})$ and the higher-frequency peak located near the antibonding mode eigenfrequency $\overline{\omega}_{+}(\overline{k})$. While the positions of those peaks are controlled by

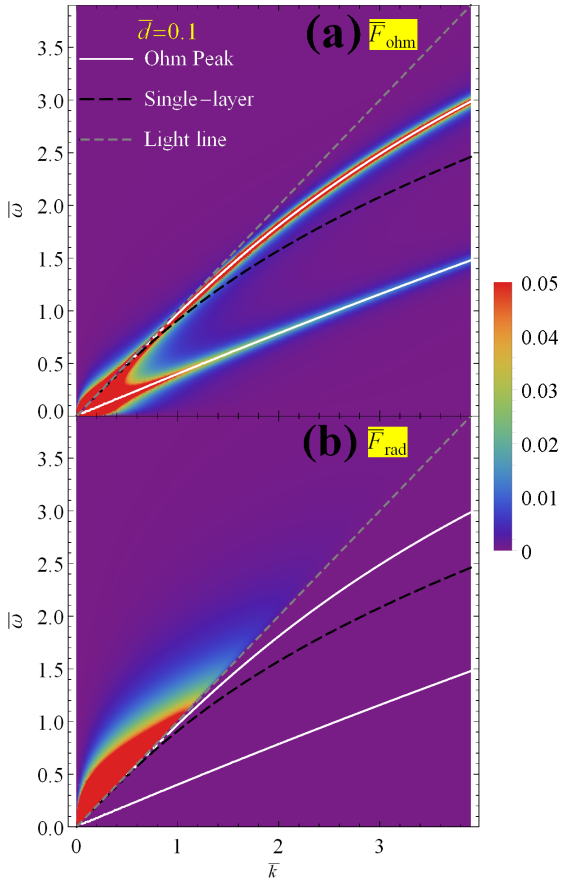

Figure 2.3: (a) The total Ohmic, $\overline{F}_{\rm Ohm}(\overline{k},\overline{\omega})$, and (b) the total radiative, $\overline{F}_{\rm rad}(\overline{k},\overline{\omega})$, joint probability densities for two graphene layers having equal conductivities with the damping rate $\overline{\gamma} = 0.1$, for interlayer distance $\overline{d} = 0.1$, and the reduced electron speed $\beta \equiv v/c = 0.5$. Results are shown in reduced units using the normalization factor $F_c = 4(Ze)^2/(\pi\omega_c^2 k_c)$. Also shown are the dispersion relations for the bonding and antibonding modes with eigenfrequencies $\overline{\omega}_{\mp}(\overline{k})$ for two graphene layers (white solid lines), the dispersion curve for single graphene layer (black dashed line) with eigenfrequency $\overline{\omega}_{\rm single} = \sqrt{2\left(-1+\sqrt{1+\overline{k}^2}\right)}$, and the light line (gray dashed line) $\overline{\omega} = \overline{k}$.

the interlayer distance $\overline{d}$ in a manner that is expected from Fig. 2.2, we find that the magnitude of the peak at $\overline{\omega}_-(\overline{k})$ decreases, and the magnitude of the peak at $\overline{\omega}_+(\overline{k})$ increases with decreasing interlayer distance. There is also a small, broadly distributed contribution of Ohmic losses at frequencies $\overline{\omega} > \overline{k}$, which seems to decrease in magnitude with decreasing interlayer distance. However, the region of frequencies $\overline{\omega} > \overline{k}$ is dominated by a broad spectrum of radiation losses, exhibiting complicated dependence on the interlayer distance due to oscillatory behavior implied by the terms involving $\cos(\kappa d)$ in Eq. (2.42). Such dependence is emphasized for large interlayer distances, whereas the radiation losses are practically independent of the interlayer distance for $\overline{d} \leq 0.1$.

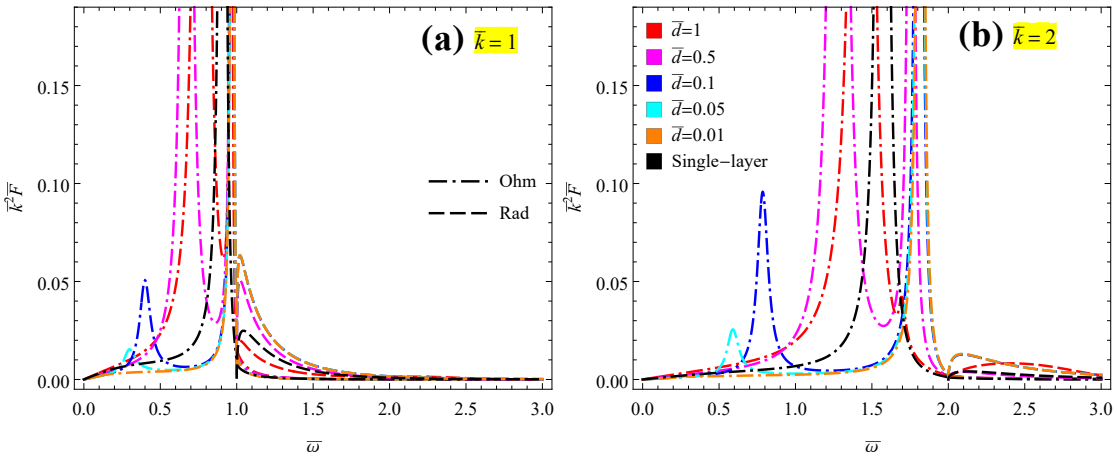

Figure 2.4: Ohmic (dot-dashed lines) and radiative (dashed lines) joint probability densities for two wavenumbers, (a) $\overline{k} = 1$ and (b) $\overline{k} = 2$, and for several inter-graphene distances $\overline{d}$. Colored curves show results for double-layer graphene, while the black curves are for single-layer graphene. Other parameters are $\overline{\gamma} = 0.1$ and $\beta = 0.5$.

In Fig. 2.5 we show layer-wise decomposition of the joint probability density for Ohmic losses in the lower graphene layer, $\overline{F}_{\mathrm{Ohm},1}(\overline{k},\overline{\omega})$ (green solid lines) and the upper graphene layer, $\overline{F}_{\mathrm{Ohm},2}(\overline{k},\overline{\omega})$ (blue dotted lines), respectively. Also shown are the results for the total Ohmic losses, $\overline{F}_{\mathrm{Ohm}}(\overline{k},\overline{\omega}) = \overline{F}_{\mathrm{Ohm},1}(\overline{k},\overline{\omega}) + \overline{F}_{\mathrm{Ohm},2}(\overline{k},\overline{\omega})$, in those two layers (red dot-dashed lines), as well as for the Ohmic loss in a single graphene layer (black dot-dashed lines). Results are shown in reduced units for $\overline{k} = 1$ and for several $\overline{d}$ values. One notices that most of the Ohmic losses in both graphene layers occur within the peaks located near the frequencies $\overline{\omega}_\mp$ corresponding to the bonding and antibonding modes, respectively. It is seen that the total Ohmic loss, $\overline{F}_{\mathrm{Ohm}}(\overline{k},\overline{\omega})$, as well as the layer losses, $\overline{F}_{\mathrm{Ohm},1,2}(\overline{k},\overline{\omega})$, contain contributions from the peak at $\overline{\omega}_-(\overline{k})$ with a magnitude that decreases, and from the peak at $\overline{\omega}_+(\overline{k})$ with a magnitude that increases with

decreasing inter-layer distance $\overline{d}$. What is interesting here is that there is an asymmetry between $\overline{F}_{\mathrm{Ohm},1}$ and $\overline{F}_{\mathrm{Ohm},2}$ such that the Ohmic losses are generally larger in the lower than in the upper layer. This asymmetry stems from the interference terms in Eq. (2.46), which contain a factor $\sin(\omega d/v)$, explaining why the asymmetry diminishes with decreasing $\overline{d}$ values. We note that the two peaks in the total Ohmic losses, $\overline{F}_{\mathrm{Ohm}}$, represent a broadened version of the total probability density for plasmon excitations, $\overline{F}_{\mathrm{pl}} = \overline{F}^{-}_{\mathrm{pl}} + \overline{F}^{+}_{\mathrm{pl}}$, with the Dirac delta functions in Eq. (18) being broadened due to finite damping rate $\overline{\gamma} = 0.1$ used in Fig. 2.5.

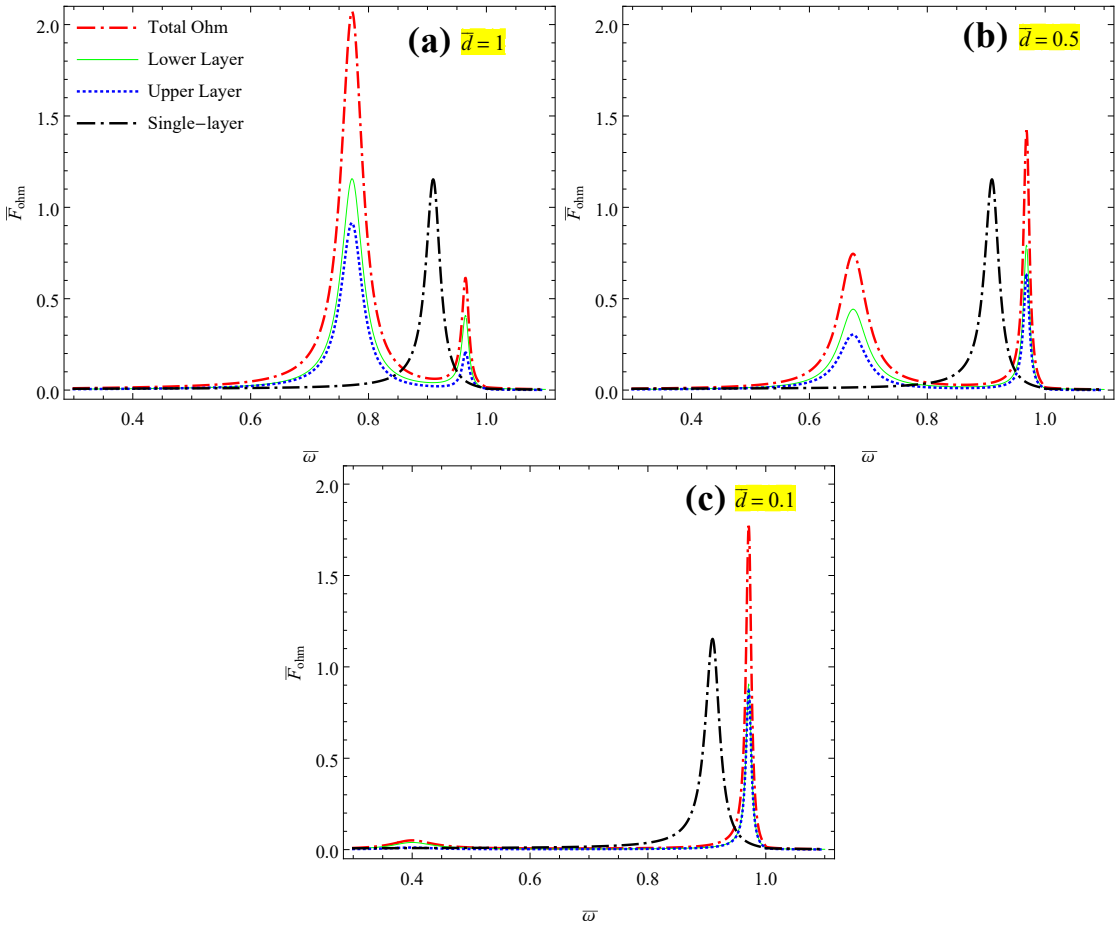

Figure 2.5: Layer-wise decomposition of Ohmic joint probability density for double-layer graphene at three interlayer distances, (a) $\overline{d} = 1$, (b) $\overline{d} = 0.5$, and (c) $\overline{d} = 0.1$, in comparison with single-layer Ohmic joint probability density, with $\overline{k} = 1$, $\overline{\gamma} = 0.1$ and $\beta = 0.5$.

In Fig. 2.6 we show the directional decomposition of the joint probability density for radiation

losses in the lower half-space, $\overline{F}^{\downarrow}_{\rm rad}(\overline{k},\overline{\omega})$ (green solid lines) and upper half-space, and $\overline{F}^{\uparrow}_{\rm rad}(\overline{k},\overline{\omega})$ (blue dotted lines), respectively. Also shown are the results for the corresponding total radiation losses in both half-spaces, $\overline{F}_{\rm rad}(\overline{k},\overline{\omega}) = \overline{F}^{\downarrow}_{\rm rad}(\overline{k},\overline{\omega}) + \overline{F}^{\uparrow}_{\rm rad}(\overline{k},\overline{\omega})$ (red dashed lines), which are compared to the total radiation losses for single graphene layer (black dashed lines). Results are shown in reduced units for $\overline{k} = 1$ and for several $\overline{d}$ values. One notices an asymmetry in the decomposition with more radiation going into the upper half-space than into the lower half-space, which is pronounced for larger interlayer distances and vanishes for decreasing distances. However, for different values of $\overline{k}$, it may happen that we see a different scenario, i.e., with more radiation going in the lower half-space. This asymmetry stems from the interference terms in

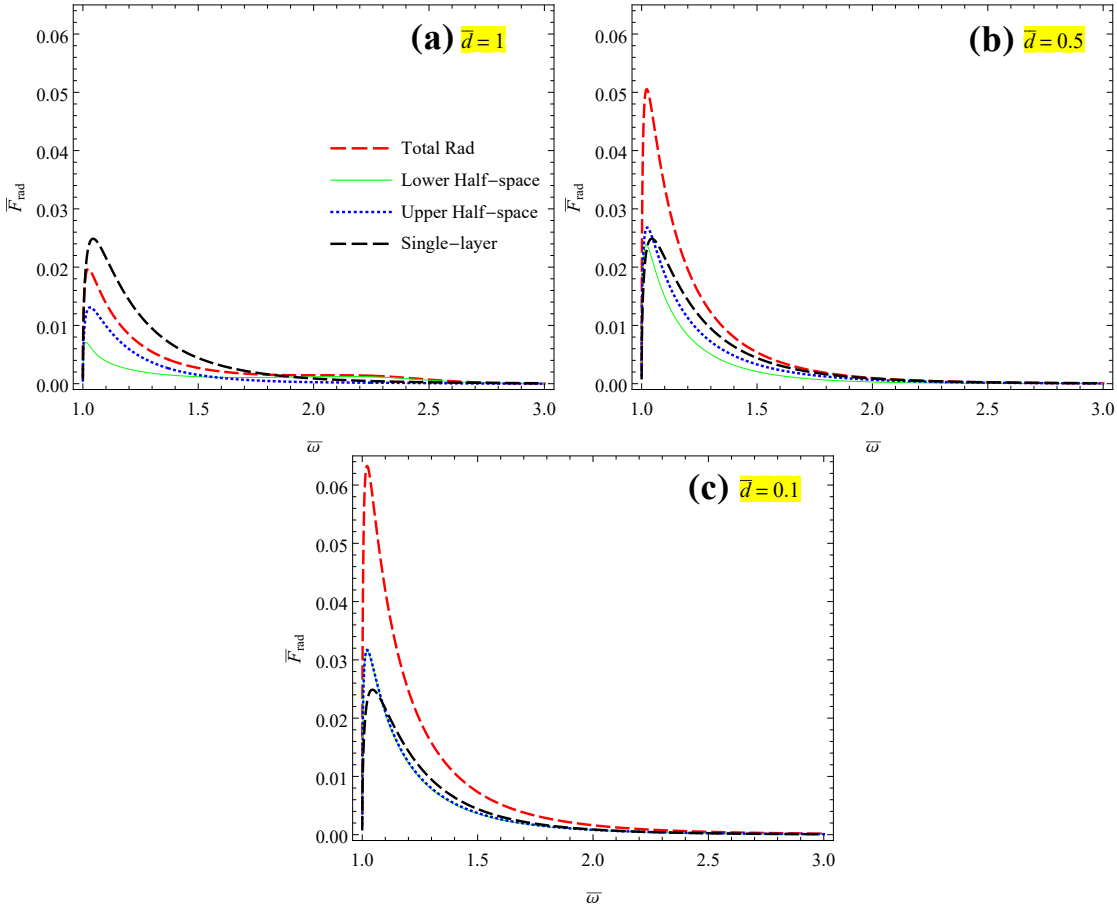

Figure 2.6: Directional decomposition of radiative joint probability density for double-layer graphene at three interlayer distances, (a) $\overline{d} = 1$, (b) $\overline{d} = 0.5$, and (c) $\overline{d} = 0.1$, in comparison with single-layer radiative joint probability density, with $\overline{k} = 1$, $\overline{\gamma} = 0.1$, and $\beta = 0.5$.

Eq. (2.47), which contain a factor $\sin(\kappa d)\sin(\omega d/v)$, explaining why the asymmetry diminishes with decreasing $\overline{d}$ values. (We remark that, in the case of a single graphene layer there is no such asymmetry [42].) It is interesting that the total radiation from two graphene layers may be smaller than that from a single-layer (at large distances), as well as larger than the total radiation from a single-layer (at shorter distances). In the latter case, the radiation in the upper *or* lower half-spaces from two graphene layers seems to be comparable to the total radiation from a single-layer.

Changing the interlayer distance $\overline{d}$ brings rich variety of effects due to retardation in both the dispersion relations $\overline{\omega} = \overline{\omega}_{\mp}(\overline{k})$, and the probability densities $\overline{F}_{\rm Ohm}(\overline{k},\overline{\omega})$ and $\overline{F}_{\rm rad}(\overline{k},\overline{\omega})$. Figure 2.7 shows such effects in the radiation spectra, which should be readily observable by using angle-resolved measurements of TR of double-layer graphene in STEM [20, 21, 23]. In this figure the angular distribution of the joint spectral density of radiation emitted from two graphene layers, $\overline{\mathcal{S}}(\theta,\overline{\omega})$, is plotted as function of the angle θ relative to the direction of motion of the external electron, for several values of the radiation frequency $\overline{\omega}$. Results are shown using reduced units for the spectral density with normalization factor $\mathcal{S}_c = (Ze)^2/c$, for two interlayer distances, (a) $\overline{d} = 0.1$ and (b) $\overline{d} = 1$. One sees typical "butterfly" patterns of TR, with no noticeable difference between contributions to the upper and lower half-spaces for the shorter distance $\overline{d} = 0.1$, similar to the case of single-layer graphene [42]. On the other hand, there is quite large asymmetry between the angular distributions of radiation emitted in the upper and lower half-spaces at the longer distance $\overline{d} = 1$, which is particularly emphasized with increasing frequencies. This asymmetry results from the interference terms in Eq. (2.47), which contain the factor $\sin(\omega d/v)\sin(\kappa d) = \sin\big(\overline{\omega}\overline{d}/\beta\big)\sin\big(\overline{\omega}\overline{d}\cos(\theta)\big)$, explaining the retardation origin of the asymmetry, as well as why the asymmetry is diminished when $\overline{\omega}\overline{d} \ll 1$.

In the panel (a) of Fig. 2.8 we show the integrated probability densities for the total energy loss of the external electron, $\overline{P}_{\rm ext}(\overline{\omega})$ (solid lines), total Ohmic loss, $\overline{P}_{\rm Ohm}(\overline{\omega})$ (dash-dotted lines), and the total radiation loss, $\overline{P}_{\rm rad}(\overline{\omega})$ (dashed lines). Results are displayed in reduced units using the normalization factor $P_c = \frac{4}{\pi}\frac{v_B}{c}\frac{1}{\hbar\omega_c}$, for several values of the inter-graphene distance in the interval $0.001 \leq \overline{d} \leq 1$. While those three functions were computed from their respective definitions, we remark that each set of curves in Fig. 2.8(a) upholds the conservation of energy in the sense $\overline{P}_{\rm ext}(\overline{\omega}) = \overline{P}_{\rm Ohm}(\overline{\omega}) + \overline{P}_{\rm rad}(\overline{\omega})$. One notices that $\overline{P}_{\rm ext}(\overline{\omega})$ is almost completely determined by the Ohmic losses $\overline{P}_{\rm Ohm}(\overline{\omega})$ for frequencies $\overline{\omega} > 1$, where the main channel of the total energy loss of the external charged particle is due to excitation of the HDPP modes, see Fig. 2.3. On the other hand, radiation losses $\overline{P}_{\rm rad}(\overline{\omega})$ are comparable to the Ohmic losses when $\overline{\omega} \sim 1$, and they become a dominant contribution to $\overline{P}_{\rm ext}(\overline{\omega})$ for $\overline{\omega} \lesssim 0.1$.

It is interesting to see in Fig. 2.8(a) that there is almost no dependence on the interlayer distance in radiation losses, $\overline{P}_{\rm rad}(\overline{\omega})$, indicating that integration of the angular distributions shown

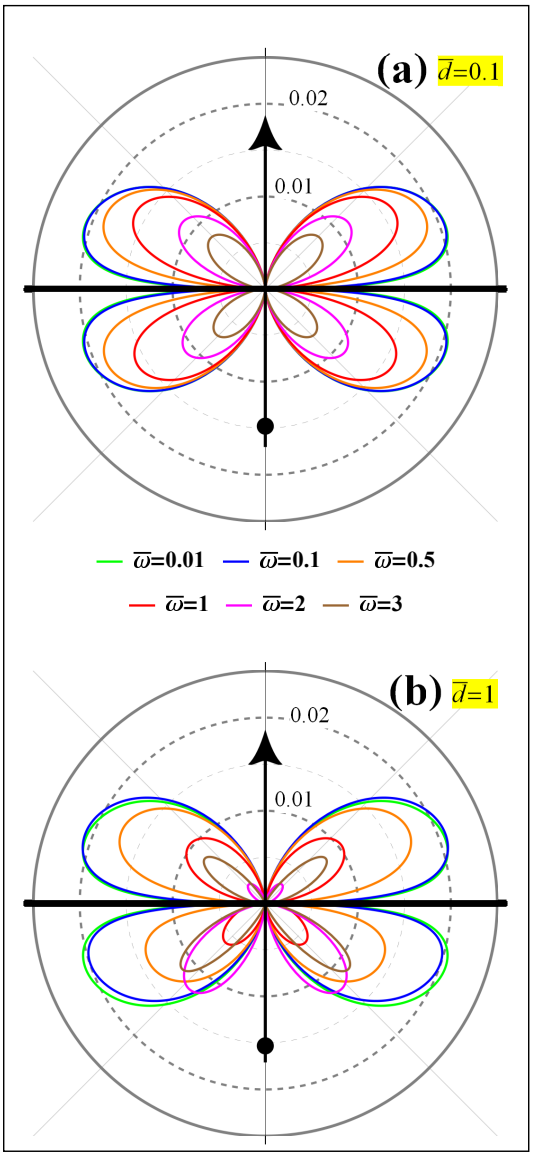

Figure 2.7: Angular joint probability density $\overline{\mathcal{S}}(\theta, \overline{\omega})$, normalized using the factor $\mathcal{S}_c = (Ze)^2/c$, for two graphene layers having equal conductivities with the damping rate $\overline{\gamma} = 0.1$, for the reduced electron speed $\beta = 0.5$, and for two interlayer distances: (a) $\overline{d} = 0.1$ and (b) $\overline{d} = 1$, and for several reduced frequencies $\overline{\omega}$. A strong directional asymmetry arises between the radiation emitted in the upper and lower half-spaces for the larger interlayer distance.

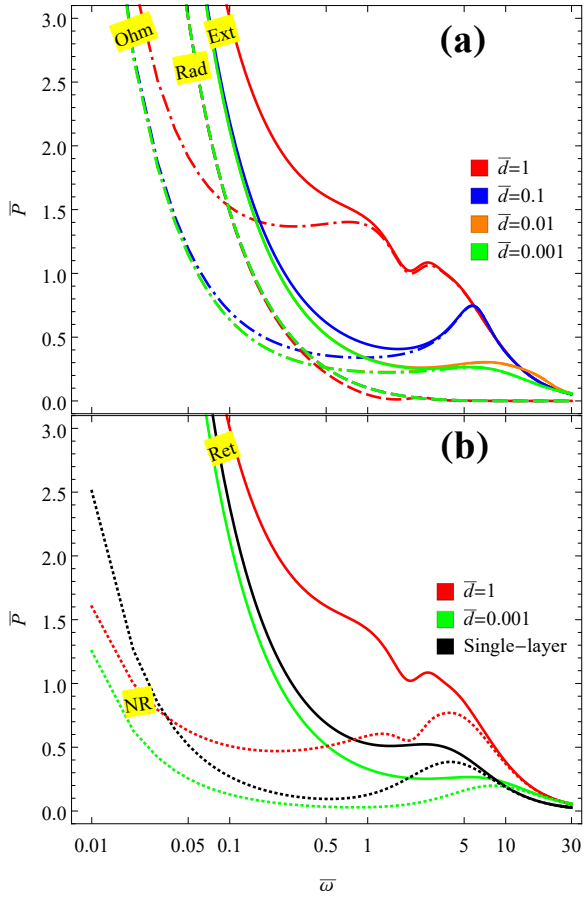

Figure 2.8: (a) Integrated probability density $\overline{P}$ is shown in reduced units using the normalization factor $P_c = \frac{4}{\pi}\frac{v_B}{c}\frac{1}{\hbar\omega_c}$ as a function of the reduced frequency $\overline{\omega}$ for the total energy loss of the external charged particle, $\overline{P}_{\rm ext}\left(\overline{\omega}\right)$ (solid lines), the total Ohmic loss, $\overline{P}_{\rm Ohm}\left(\overline{\omega}\right)$ (dot-dashed lines), and the total radiative loss, $\overline{P}_{\rm rad}\left(\overline{\omega}\right)$ (dashed lines) for several interlayer distances, $\overline{d} = 1$, 0.1, 0.01, and 0.001. (b) The results for $\overline{P}_{\rm ext}\left(\overline{\omega}\right)$ in two graphene layers at the distances $\overline{d} = 0.001$ and 1, as well as those for $\overline{P}_{\rm ext}\left(\overline{\omega}\right)$ in single graphene layer (solid lines) are compared with the corresponding results obtained in the nonretarded limit (dotted lines). For both panels: $\overline{\gamma} = 0.1$ and $\beta = 0.5$.

in Fig. 2.7 over a full range of angles $0 \leq \theta \leq \pi$ removes the dependence on $\overline{d}$. This may be traced to the presence of factors $[1 \mp \cos(\kappa d)]$ in Eq. (2.47), which exhibit strong oscillations as functions of κ (and k) for large d values. When integration over k is performed in $F_{\rm rad}(k,\omega)$ to obtain $P_{\rm rad}(\omega)$, then the d–dependence that would result from the nearby factors $[1 \mp \cos(\omega d/v)]$ in Eq. (2.47) is washed out. On the other hand, the integrated Ohmic losses in Fig. 2.8(a), $\overline{P}_{\rm Ohm}(\overline{\omega})$, show rather strong dependence on the interlayer distance in the range $\overline{d} \geq 0.1$. This may be explained by absence of any factors exhibiting strong oscillations as a function of k in Eq. (2.46). Then, the factors $[1 \mp \cos(\omega d/v)]$, which are present in that equation, survive integration over k in $F_{\rm Ohm}(k,\omega)$, giving rise to strong interference effects in the resulting distribution of Ohmic losses $P_{\rm Ohm}(\omega)$ for two graphene layers at a large distance.

In the panel (b) of Fig. 2.8 we compare the results for $\overline{P}_{\rm ext}(\overline{\omega})$ including retarded effects with the nonretarded case, $\overline{P}^{NR}_{\rm ext}(\overline{\omega}) \equiv \overline{P}^{NR}_{\rm Ohm}(\overline{\omega})$, for two graphene layers at the distances $\overline{d} = 0.001$ and $\overline{d} = 1$, as well as for a single graphene layer. One sees that the effects of retardation are quantitatively relevant for Ohmic losses at frequencies $\overline{\omega} < 10$, giving rise to a significant increase in magnitude of $\overline{P}_{\rm Ohm}(\overline{\omega})$ in comparison to $\overline{P}^{NR}_{\rm Ohm}(\overline{\omega})$. When combined with the radiation losses, this increase amounts to $\overline{P}_{\rm ext}(\overline{\omega}) \gg \overline{P}^{NR}_{\rm ext}(\overline{\omega})$ for $\overline{\omega} \lesssim 1$. On the other hand, one sees in Fig. 2.8(b) that the results for two graphene layers with short separation of $\overline{d} = 0.001$ exhibit energy losses that are quite similar to those for single graphene layer, both in the retarded and nonretarded cases, whereas two layers with larger separation of $\overline{d} = 1$ exhibit substantially larger energy losses in both cases.

From Fig. 2.8 one may conclude that interesting interference effects arise in the Ohmic losses of two graphene layers at large distances. For example, a curious peak-and-valley structure develops in $\overline{P}_{\rm Ohm}(\overline{\omega})$ in the retarded case for $\overline{d} = 1$ in the interval of frequencies $1 \lesssim \overline{\omega} \lesssim 5$, which degenerates in a structure with two peaks in the nonretarded case. Hence, it is worthwhile analyzing separate Ohmic losses in each graphene layer. In addition, recalling the strong asymmetries observed in Fig. 2.7(b) for $\overline{d} = 1$ at higher frequencies, it appears also worthwhile analyzing the angle-integrated energy losses due to radiation emitted in the upper and the lower half-spaces. Accordingly, we show in Fig. 2.9 the integrated probability density of the total energy loss of the external electron, $\overline{P}_{\rm ext}(\overline{\omega})$, along with the layer-wise decomposition of the integrated probability density for Ohmic losses in the lower and upper graphene layers, $\overline{P}_{\rm Ohm,1}(\overline{\omega})$ and $\overline{P}_{\rm Ohm,2}(\overline{\omega})$, and the directional decomposition of the integrated probability density for radiation losses in the upper and lower half-spaces, $\overline{P}^{\uparrow}_{\rm rad}(\overline{\omega})$ and $\overline{P}^{\downarrow}_{\rm rad}(\overline{\omega})$, for two interlayer distances, (a) $\overline{d} = 1$ and (b) $\overline{d} = 0.1$.

It is interesting to see in Fig. 2.9 that there is almost no asymmetry between $\overline{P}^{\uparrow}_{\rm rad}(\overline{\omega})$ and $\overline{P}^{\downarrow}_{\rm rad}(\overline{\omega})$, which are obtained by integrating the angular distributions shown in Fig. 2.7 over two ranges of angles, $0 \leq \theta \leq \pi/2$ and $\pi/2 \leq \theta \leq \pi$, respectively. The fact that the asymmetry

seen in the angular distributions shown in Fig. 2.7(b) for $\overline{d} = 1$ has disappeared upon integration may be traced to the same reason as the lack of dependence on the interlayer distance $\overline{d}$ in the total radiative losses, $\overline{P}_{\rm rad}(\overline{\omega}) = \overline{P}^{\uparrow}_{\rm rad}(\overline{\omega}) + \overline{P}^{\downarrow}_{\rm rad}(\overline{\omega})$. Namely, the presence of the factor $\sin(\kappa d)$ in the interference terms in Eq. (2.47) gives rise to strong oscillations as a function of κ (and k), which will largely diminish contributions of those terms upon integration of $\overline{F}^{\uparrow\downarrow}_{\rm rad}(k, \overline{\omega})$ over k.

On the other hand, one sees in Fig. 2.9 that $\overline{P}_{\rm Ohm,1}(\overline{\omega})$ and $\overline{P}_{\rm Ohm,2}(\overline{\omega})$ exhibit relatively large differences for $\overline{\omega} \lesssim 1$ with increasing $\overline{d}$ values, resulting from the interference terms with the factor $\sin(\omega d/v)$ in Eq. (2.46), which survives integration of $F_{\rm Ohm,1,2}(k, \omega)$ over k. It is interesting that $\overline{P}_{\rm Ohm,2}(\overline{\omega}) < \overline{P}_{\rm Ohm,1}(\overline{\omega})$ at $\overline{\omega} \lesssim 1$ for both interlayer distances in Fig. 2.9, showing that lower graphene layer absorbs more Ohmic losses than the upper layer at low frequencies. Moreover, there are some other interesting features in Ohmic losses of individual graphene layers at high frequencies, $\overline{\omega} \gtrsim 1$. For example, it appears that the peak-and-valley structure seen in $\overline{P}_{\rm ext}(\overline{\omega})$ in the interval of frequencies $1 \lesssim \overline{\omega} \lesssim 5$ in Fig. 2.9(a) for $\overline{d} = 1$ results from partial cancelation of a local minimum in $\overline{P}_{\rm Ohm,1}(\overline{\omega})$ and a local maximum in $\overline{P}_{\rm Ohm,2}(\overline{\omega})$. This effect also explains the double-peak structure seen in the total Ohmic loss, $\overline{P}_{\rm Ohm}(\overline{\omega}) = \overline{P}_{\rm Ohm,1}(\overline{\omega}) + \overline{P}_{\rm Ohm,2}(\overline{\omega})$, in Fig. 2.8(a) for $\overline{d} = 1$. Likewise, even though $\overline{P}_{\rm ext}(\overline{\omega})$ exhibits a single peak near $\overline{\omega} = 5$ in Fig. 2.8(b) for $\overline{d} = 0.1$, Ohmic losses of individual layers, $\overline{P}_{\rm Ohm,1,2}(\overline{\omega})$, show somewhat unexpected features at frequencies $\overline{\omega} > 5$.

We have shown that dominant contributions to the joint probability densities for Ohmic losses in both the lower and upper graphene layers, $\overline{F}_{\rm Ohm,1}(\overline{k}, \overline{\omega})$ and $\overline{F}_{\rm Ohm,2}(\overline{k}, \overline{\omega})$, are contained in two peak regions centered at the frequencies $\overline{\omega}_{\mp}$ corresponding to the bonding and antibonding DPP modes. Relative weights describing the participation of these modes in the Ohmic losses in each graphene layer strongly depend on the interlayer distance d. Accordingly, it is worthwhile to take the limit of vanishing damping rates in graphene layers and to evaluate the modal decomposition of the integrated probability density for Ohmic energy losses in *both* graphene layers. Such decomposition gives the probability densities, $\overline{P}^{-}_{\rm pl}(\overline{\omega})$ and $\overline{P}^{+}_{\rm pl}(\overline{\omega})$, for exciting the bonding and antibonding DPP modes per unit frequency, respectively. As a result, we reveal below in Fig. 2.10 that oscillations arise in the modal decomposition, which may shed light on the features observed at large frequencies in the total Ohmic losses $\overline{P}_{\rm Ohm}(\overline{\omega})$ in Fig. 2.8, and in their layer components $\overline{P}_{\rm Ohm,1,2}(\overline{\omega})$ in Fig. 2.9.

In Fig. 2.10 we show the modal decomposition of the probability density for plasmon excitations, $\overline{P}_{\rm pl}(\overline{\omega}) = \overline{P}^{-}_{\rm pl}(\overline{\omega}) + \overline{P}^{+}_{\rm pl}(\overline{\omega})$, for (a) $\overline{d} = 1$ and (b) $\overline{d} = 0.1$. Results are shown in reduced units using the normalization factor $P_c = \frac{4}{\pi}\frac{v_B}{c}\frac{1}{\hbar\omega_c}$. One notices strong oscillations in the components $\overline{P}^{\mp}_{\rm pl}(\overline{\omega})$ at large frequencies, which nevertheless superimpose into a rather smooth frequency dependence of the total probability density for plasmon excitation, $\overline{P}_{\rm pl}(\overline{\omega})$, in that range. The origin of these oscillations may be explained by setting $\rho = 1$ in the expressions

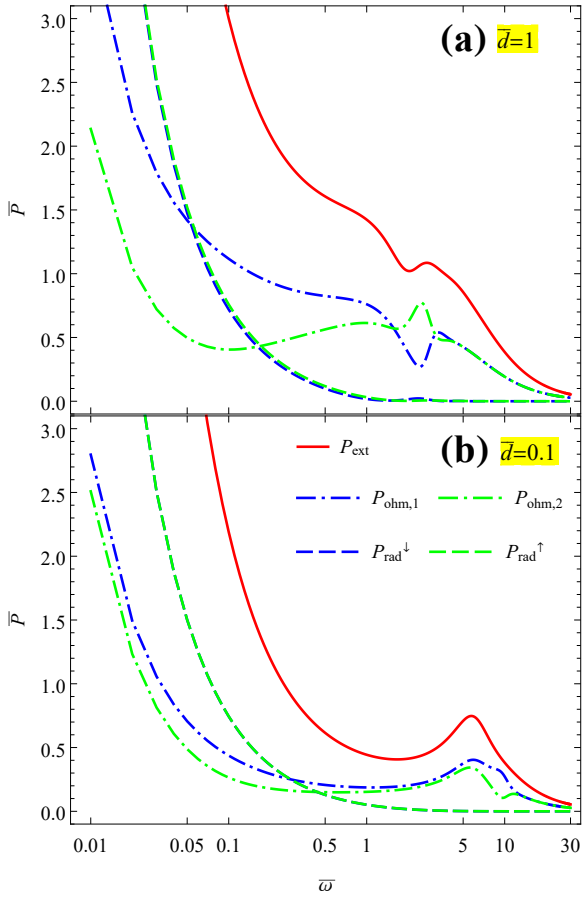

Figure 2.9: A layer-wise decomposition of the integrated Ohmic energy losses, $\overline{P}_{\mathrm{Ohm},1,2}(\overline{\omega})$, and a directional decomposition of the integrated radiative losses, $\overline{P}_{\mathrm{rad}}^{\uparrow\downarrow}(k,\overline{\omega})$, are shown in reduced units for two graphene layers at the distances: (a) $\overline{d}=1$ and (b) $\overline{d}=0.1$. The Ohmic decomposition (dot-dashed lines) shows strong asymmetry with respect to the direction of motion for increasing $\overline{d}$, while the radiation decomposition (dashed lines) shows no such asymmetry. Also shown are the results for the total integrated energy loss of the external charged particle, $\overline{P}_{\mathrm{ext}}(\overline{\omega})$, (solid lines). All results are obtained with $\overline{\gamma}=0.1$ and $\beta=0.5$.

within curly brackets in Eq. (2.58), giving factors $1 \mp \cos(\omega d/v) = 1 \mp \cos\big(\overline{\omega}\overline{d}/\beta\big)$, which survive upon integrating $F_{\rm pl}^{\mp}(k,\omega)$ over k to obtain $P_{\rm pl}^{\mp}(\omega)$. The onset of these oscillations around the frequency $\overline{\omega} \sim \pi\beta/\overline{d}$ seems to give rise to the features observed in Ohmic losses at high frequencies in Fig. 2.9. For example, referring to Fig. 2.10(a), one may ascertain that the double peak seen in $\overline{P}_{\rm Ohm}(\overline{\omega})$ in Fig. 2.8(a) for $\overline{d} = 1$, which is a result of coupling of the external electron to the bonding and antibonding modes, is accompanied by an interference that gives rise to the peak-and-valley structure seen in $\overline{P}_{\rm ext}(\overline{\omega})$ in Figs. 2.8(a) and 2.9(a) for $\overline{d} = 1$. On the other hand, referring to Fig. 2.10(b), one may ascertain that the main peak seen near $\overline{\omega} = 5$ in both $\overline{P}_{\rm ext}(\overline{\omega})$ and $\overline{P}_{\rm Ohm}(\overline{\omega})$ in Fig. 2.8(a) for $\overline{d} = 0.1$ predominantly originates from the antibonding mode, whereas features seen in $\overline{P}_{\rm Ohm,1,2}(\overline{\omega})$ at $\overline{\omega} > 5$ in Fig. 2.9(b) for $\overline{d} = 0.1$ are the signature of interferences between the bonding and antibonding modes.

By comparison of $\overline{P}_{\rm pl}(\overline{\omega})$ in Fig. 2.10 with the function $\overline{P}_{\rm Ohm}(\overline{\omega})$ for $\overline{d} = 1$ and 0.1 in Fig. 2.8(a), one may assert that the total integrated Ohmic losses at frequencies $\overline{\omega} \gtrsim 1$ are dominated by the excitation of both the bonding and antibonding DPP modes. Further comparison reveals that the plasmon excitation probability densities in Fig. 2.10 approach constant values at low frequencies, $\overline{\omega} < 1$, in contrast to the behavior of the Ohmic losses in Figs. 2.8 and 2.9, which grow in magnitude with decreasing $\overline{\omega}$. This difference is a consequence of the fact that the integrated probability densities for Ohmic losses in Figs. 2.8 and 2.9 were calculated with finite damping rate of $\overline{\gamma} = 0.1$, whereas the plasmon excitation probability densities in Fig. 2.10 are calculated in the limit of vanishing damping rates. Accordingly, the competition between the Ohmic and radiation losses seen in Figs. 2.8 and 2.9 at frequencies $\overline{\omega} \lesssim 1$ is strongly affected by increasing the damping rates in graphene layers, which ultimately leads to deposition of the Joule heat in those layers at such frequencies, as discussed in Fig. 2.3.

Finally, regarding the role of the interlayer distance in Fig. 2.10, it is interesting to note that $\overline{P}_{\rm pl}^{-}(\overline{\omega})$ and $\overline{P}_{\rm pl}^{+}(\overline{\omega})$ settle at different constant values at low frequencies, $\overline{\omega} < 1$. In particular, the probability density of exciting the antibonding mode at such frequencies, $\overline{P}_{\rm pl}^{+} \approx 0.2$, is not affected by the value of $\overline{d}$, whereas the bonding mode is excited with a probability density that strongly depends on $\overline{d}$, which goes from $\overline{P}_{\rm pl}^{-} < \overline{P}_{\rm pl}^{+}$ for $\overline{d} = 0.1$ to $\overline{P}_{\rm pl}^{-} > \overline{P}_{\rm pl}^{+}$ for $\overline{d} = 1$. This may be related to the strong sensitivity of the bonding mode eigenfrequency $\overline{\omega}_{-}(\overline{k})$ on variations in the interlayer distance. On the other hand, we recall the relation $\overline{P}_{\rm Ohm,2}(\overline{\omega}) < \overline{P}_{\rm Ohm,1}(\overline{\omega})$ between the integrated Ohmic energy losses in the lower and upper graphene layers, seen in Fig. 2.9 at frequencies $\overline{\omega} \lesssim 1$ for both $\overline{d} = 1$ and 0.1, which primarily results from the interference terms with $\sin(\omega d/v)$ in Eq. (2.46). Therefore, it appears that the interlayer distance plays different, and somewhat intricate roles in the modal decomposition of plasmon excitation probability and the layer-wise decompositions of Ohmic losses at sub-THz frequencies.

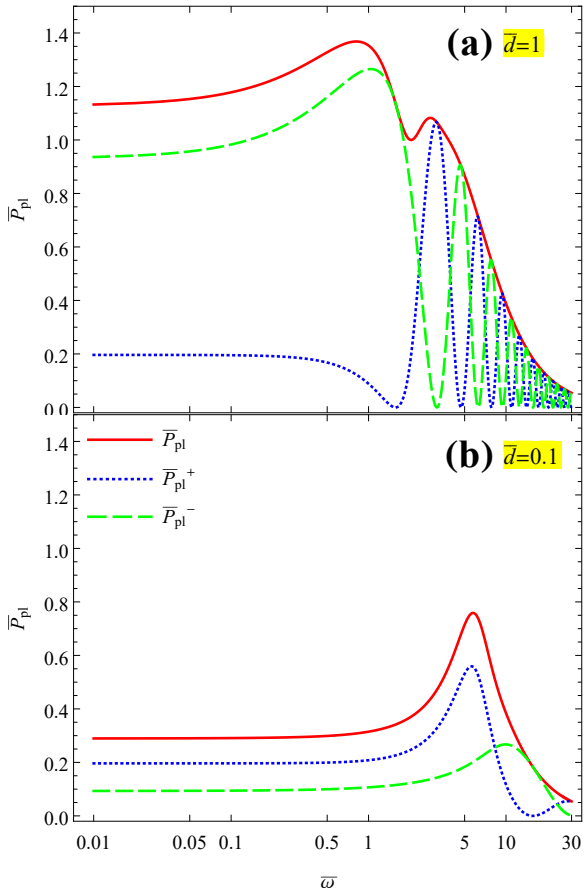

Figure 2.10: Modal decomposition of the integrated probability density for plasmon polariton excitations in two graphene layers having equal conductivities with zero damping, $\overline{\gamma} = 0$, for two interlayer distances: (a) $\overline{d} = 1$ and (b) $\overline{d} = 0.1$. The reduced speed of the external electron is $\beta = 0.5$. The blue dotted lines label excitations of the bonding and the green dashed lines label excitations of the antibonding modes, while the red solid lines show the total excitation probabilities.

The effect of damping rate $\overline{\gamma}$. As we have already mentioned in our discussion, variations in the damping rate seem to exhibit much weaker effects on radiative losses than on Ohmic losses, at least for the reduced damping rates $\overline{\gamma} \lesssim 0.1$. We show in Fig. 2.11 the effects of damping on the joint probability densities for both Ohmic contribution, $\overline{F}_{\rm Ohm}(\overline{k},\overline{\omega})$ (dot-dashed lines), and radiative contribution, $\overline{F}_{\rm rad}(\overline{k},\overline{\omega})$ (dashed lines), with $\overline{k}=1$ for three different $\overline{\gamma}$ values and two interlayer distances, $\overline{d}=1$ and 0.1. One sees that the effect of increasing damping rate on Ohmic energy losses is to broaden and reduce the height of the two peaks, which occur near frequencies $\overline{\omega}_{\mp}$ corresponding to the bonding and antibonding modes, respectively. This effect of broadening is more pronounced for the lower-energy bonding mode $\overline{\omega}_{-}$ than for the antibonding mode $\overline{\omega}_{+}$. In particular, for the highest damping rate of $\overline{\gamma}=1$ shown in Fig. 2.11, the two peaks tend to

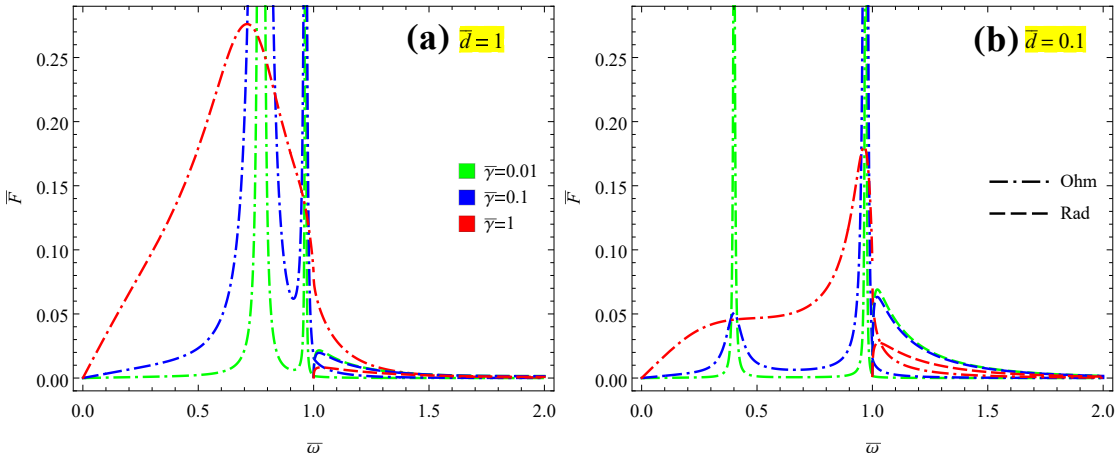

Figure 2.11: Ohmic (dot-dashed lines) and radiative (dashed lines) joint probability densities for two interlayer distances, (a) $\overline{d}=1$ and (b) 0.1, and for three damping rates, $\overline{\gamma}=0.01$, 0.1, and 1, with $\overline{k}=1$ and $\beta=0.5$.

merge into one broad structure, which is peaked near the frequency $\overline{\omega}_{-}$ for $\overline{d}=1$ and near the frequency $\overline{\omega}_{+}$ for $\overline{d}=0.1$. For frequencies above the light line, $\overline{\omega}>\overline{k}=1$, one may observe that the Ohmic contribution is almost proportional to $\overline{\gamma}$ because there are no resonant frequencies in that range and the only parameter, which can influence the Ohmic losses there is the damping ratio. At the same time, radiative losses are seen in Fig. 2.11 to decrease with increasing $\overline{\gamma}$ and increasing $\overline{d}$, so that for very large damping rates, Ohmic energy losses may become completely dominant over the radiation losses at $\overline{\omega}>\overline{k}=1$ in the case of large interlayer distances.

In order to understand the effect of damping over full range of wavenumbers, we show in Fig. 2.12 the integrated probability densities for the total energy loss of the external charged particle, $\overline{P}_{\rm ext}(\overline{\omega})$ (solid lines), along with the Ohmic, $\overline{P}_{\rm Ohm}(\overline{\omega})$ (dot-dashed lines), and radiative,

$\overline{P}_{\rm rad}(\overline{\omega})$ (dashed lines) contributions for $\overline{d} = 1$ and 0.1 and for several damping rates. We see that both the Ohmic and radiative energy losses are mostly affected by changing damping rates at the sub-THz frequencies, $\overline{\omega} \lesssim 1$, showing opposite trends. It is interesting that, with the Ohmic losses increasing, and the radiative losses decreasing with increasing $\overline{\gamma}$, the total energy loss of the external charged particle shows relatively weak dependence on damping rate, especially in the range $\overline{\gamma} \leq 0.1$. It is also remarkable that the radiative energy losses are quite weakly dependent on damping rate in the range $\overline{\gamma} \leq 0.1$.

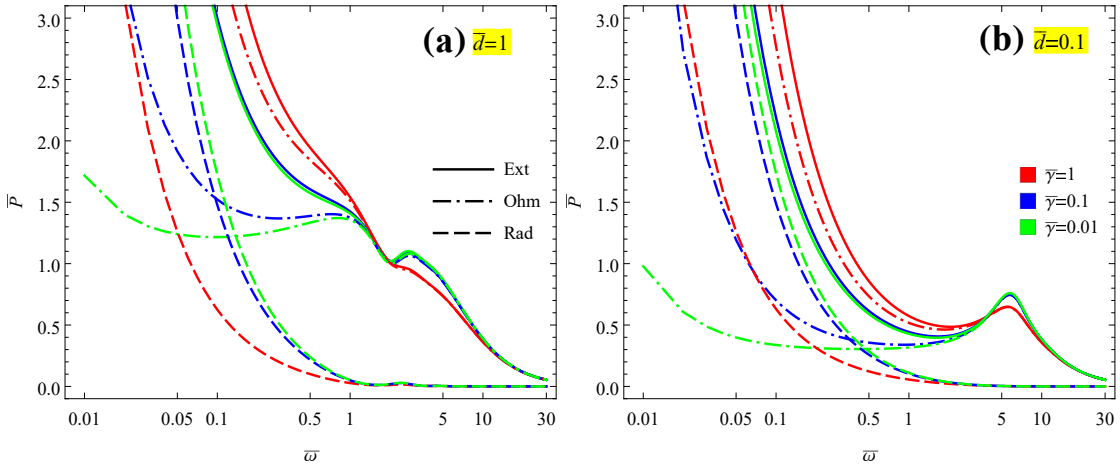

Figure 2.12: Integrated probability density for the total energy loss of external particle (solid lines), Ohmic loss (dot-dashed lines) and radiative loss (dashed lines) for two interlayer distances, (a) $\overline{d} = 1$ and (b) 0.1, and for three damping rates, $\overline{\gamma} = 0.01$, 0.1, and 1, with $\beta = 0.5$.

Finally, in Fig. 2.13 we discuss the effects of different damping rates on the angular distribution of the joint spectral density of radiation emitted from two graphene layers, $\overline{\mathcal{S}}(\theta, \overline{\omega})$, as a function of the angle θ relative to the direction of motion of the external electron, for several values of the radiation frequency $\overline{\omega}$. Results are shown for the interlayer distance $\overline{d} = 1$ using reduced units for the spectral density with normalization factor $\mathcal{S}_c = (Ze)^2/c$. The cases of reduced damping rates $\overline{\gamma} = 1$ and $\overline{\gamma} = 0.01$ shown in Fig. 2.13 should be compared with those shown in Fig. 2.7(b) for $\overline{\gamma} = 0.1$ with the interlayer distance $\overline{d} = 1$. As in that figure, we also see here quite large asymmetry between the angular distributions of radiation emitted in the upper and lower half-spaces, which is particularly emphasized with increasing frequency. It is interesting that the asymmetry shows similar redistribution of the radiation emitted in the upper and lower half-spaces for all three damping rates for $\overline{\omega} \gtrsim 1$, while for the lower frequency range the patterns tend to be symmetric, but differently shaped for different $\overline{\gamma}$ values. In general, the overall intensity of radiation decreases with increasing damping rates.

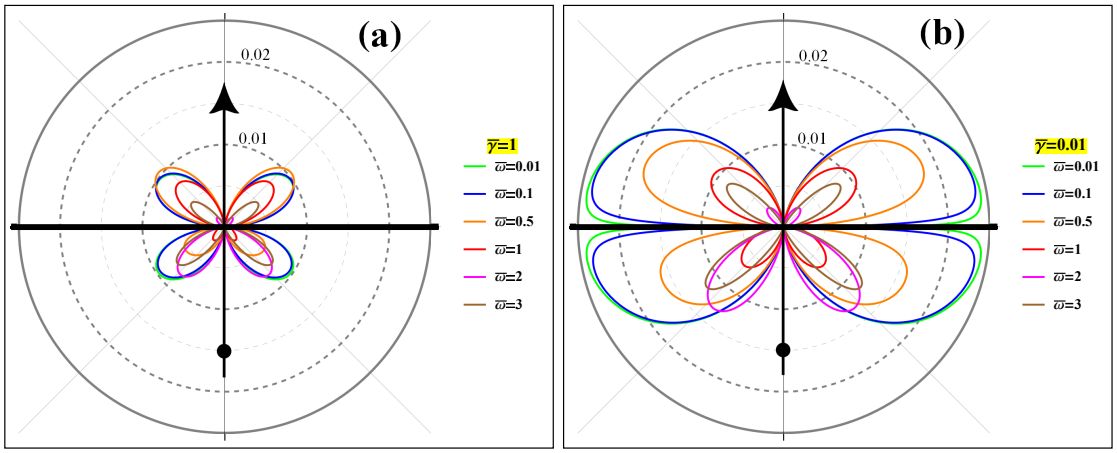

Figure 2.13: Angular distribution of the joint spectral density of radiation losses, $\overline{\mathcal{S}}(\theta,\overline{\omega})$, for two damping rates, (a) $\overline{\gamma}=1$ and (b) $\overline{\gamma}=0.01$, and for several emission frequencies $\overline{\omega}$. The other parameters are fixed at $\overline{d}=1$ and $\beta=0.5$. (The case for $\overline{\gamma}=0.1$ is shown in Fig. 2.3(b).)

The effect of charged particle's speed. Figure 2.14 shows the effect of $\beta=v/c$ on joint probability densities for Ohmic energy losses, $\overline{F}_{\rm Ohm}(\overline{k},\overline{\omega})$ (dot-dashed lines) and the radiative energy losses, $\overline{F}_{\rm rad}(\overline{k},\overline{\omega})$ (dashed lines), with $\overline{k}=1$ and $\overline{\gamma}=0.1$, and for two interlayer distances, $\overline{d}=1$ and 0.1. One sees that the peak near the lower-energy bonding mode, $\overline{\omega}_-$, decreases in magnitude with increasing speed, while the peak near the higher-energy antibonding mode, $\overline{\omega}_+$, seems to show the opposite trend. These effects obviously depend on the interlayer distance, and it is remarkable that, for the distance $\overline{d}=1$ the higher-energy peak near $\overline{\omega}_+$ disappears at the lowest speed shown in Fig. 2.14, $\beta=0.3$. At the same time, radiative energy losses at frequencies $\overline{\omega}>\overline{k}=1$ are seen to strongly increase with increasing charged particle speed, as expected, at a rate that is higher for the shorter interlayer distance $\overline{d}=0.1$.

In Fig. 2.15 we show the integrated probability densities for the total energy loss of the external charged particle, $\overline{P}_{\rm ext}(\overline{\omega})$ (solid lines), along with the Ohmic, $\overline{P}_{\rm Ohm}(\overline{\omega})$ (dot-dashed lines), and radiative, $\overline{P}_{\rm rad}(\overline{\omega})$ (dashed lines) contributions for $\overline{\gamma}=0.1$ and two interlayer distances, $\overline{d}=1$ and 0.1, and for several external particle speeds. We see that the total losses $\overline{P}_{\rm ext}(\overline{\omega})$, which are completely determined by the Ohmic losses $\overline{P}_{\rm Ohm}(\overline{\omega})$ at frequencies $\overline{\omega}\gtrsim 5$, decrease in magnitude with increasing speed in that range of frequencies. On the other hand, both the Ohmic losses $\overline{P}_{\rm Ohm}(\overline{\omega})$ and the radiative losses $\overline{P}_{\rm rad}(\overline{\omega})$ increase with increasing speed at frequencies $\overline{\omega}\lesssim 5$.

Finally, we show in Fig. 2.16 the angular distribution of the reduced joint spectral density of emitted radiation, $\overline{\mathcal{S}}(\theta,\overline{\omega})$, as a function of the angle θ for several values of the radiation

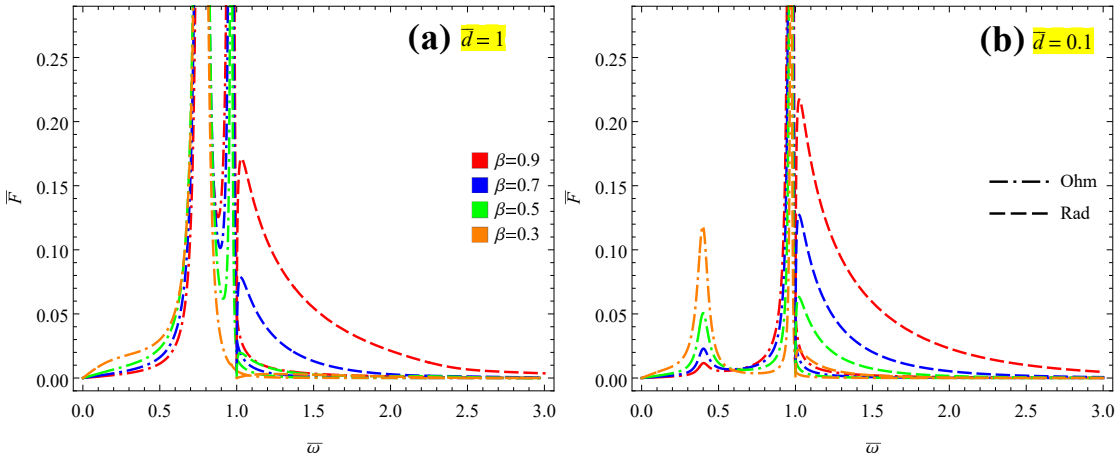

Figure 2.14: Ohmic (dot-dashed lines) and radiative (dashed lines) joint probability densities for two interlayer distances, (a) $\overline{d} = 1$ and (b) 0.1, and for four external particle speeds, $\beta = 0.3$, 0.5, 0.7, and 0.9, with $\overline{k} = 1$ and $\overline{\gamma} = 0.1$.

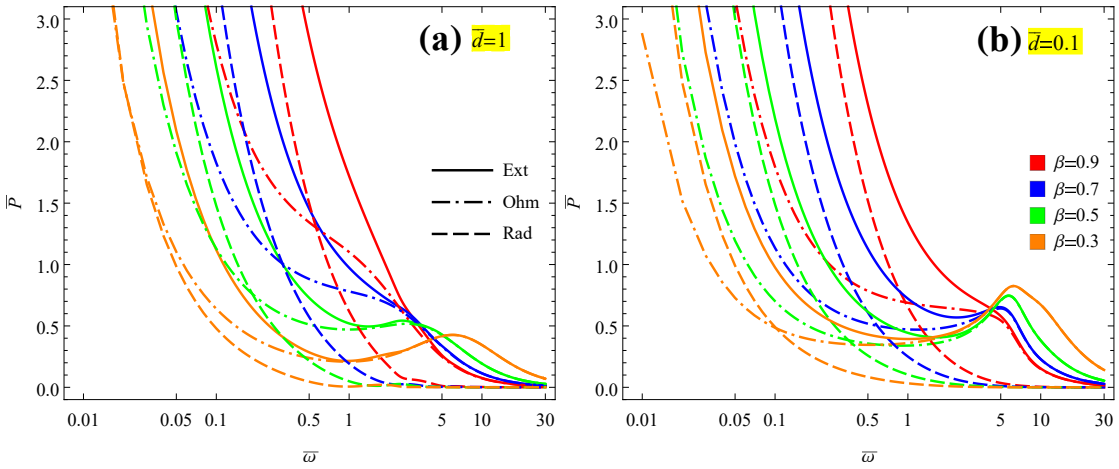

Figure 2.15: Integrated probability density for the total energy loss of external particle (solid lines), Ohmic loss (dot-dashed lines) and radiative loss (dashed lines) for two interlayer distances, (a) $\overline{d} = 1$ and (b) 0.1, and for four external particle speeds, $\beta = 0.3$, 0.5, 0.7, and 0.9, with $\overline{\gamma} = 0.1$.

frequency $\overline{\omega}$, with $\overline{d} = 1$ and $\overline{\gamma} = 0.1$. Results are shown for the relative speeds $\beta = 0.3$, 0.7 and 0.9, which should be compared with those shown in Fig. 2.7(b) for $\beta = 0.5$. One notices

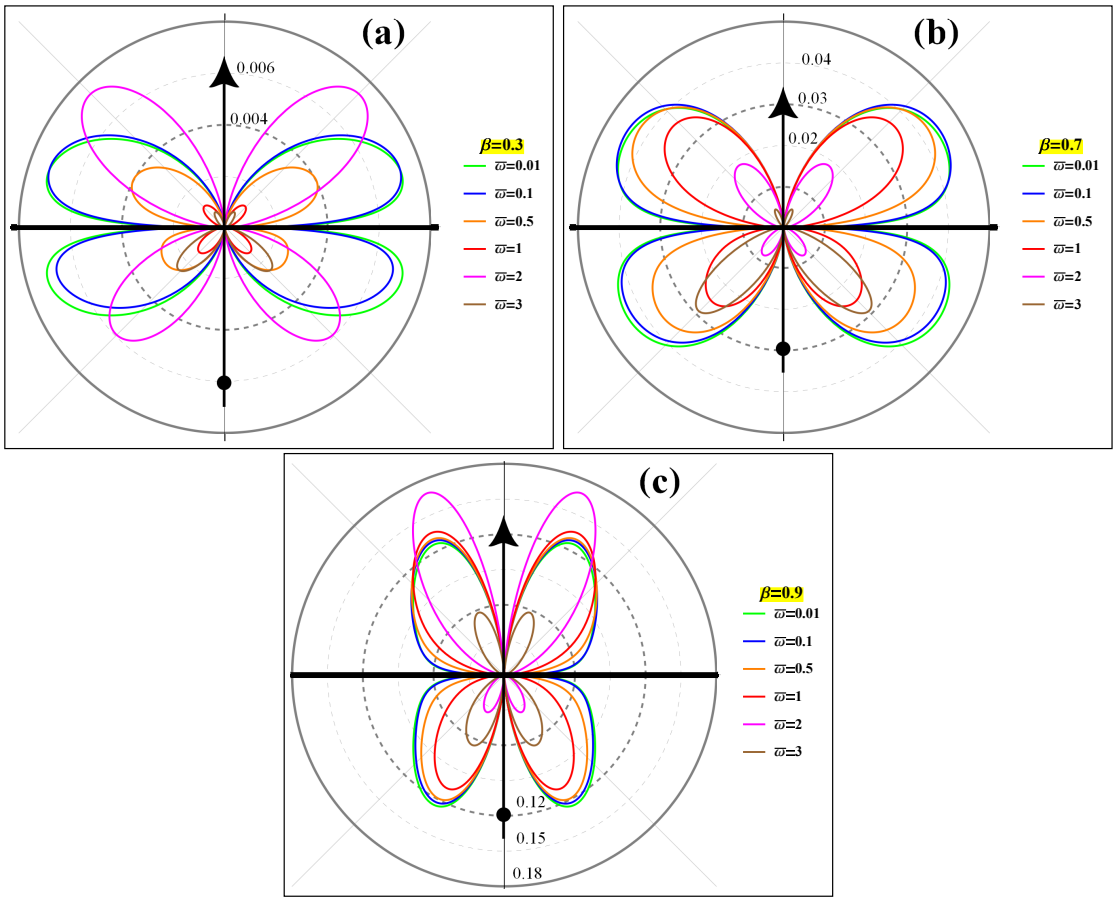

Figure 2.16: Angular distribution of the joint spectral density of radiation losses, $\overline{\mathcal{S}}(\theta, \overline{\omega})$, for three external particle speeds, $\beta = 0.3$, 0.7, and 0.9, and for several emission frequencies $\overline{\omega}$. The other parameter are fixed at $\overline{d} = 1$ and $\overline{\gamma} = 0.1$. (The case for $\beta = 0.5$ is shown in Fig. 2.7(b).)

a strong distortion of the "butterfly" pattern towards the trajectory of the external particle with increasing speed, similar to the case of single-layer graphene [42]. However, the asymmetry in radiation patterns from two graphene layers is seen at higher frequencies for all speeds, with an interesting re-distribution of intensity, which is most likely due to the interference terms in Eq. (2.47), containing the factor $\sin(\omega d/v)\sin(\kappa d) = \sin\big(\overline{\omega}\overline{d}/\beta\big)\sin\big(\overline{\omega}\overline{d}\cos(\theta)\big)$.

Average number of plasmons. We have seen that the modal decomposition of integrated probability density for plasmon excitations, $\overline{P}_{\rm pl}(\overline{\omega}) = \overline{P}^{-}_{\rm pl}(\overline{\omega}) + \overline{P}^{+}_{\rm pl}(\overline{\omega})$, exhibits intricate effects of the interlayer distance $\overline{d}$, which differently affects the bonding and antibonding modes. Here we show in Fig. 2.17 the average numbers of those two modes, $\nu_{\mp}$, obtained by integrating $\overline{P}^{\mp}_{\rm pl}(\overline{\omega})$ over all frequencies, as functions of the interlayer distance $\overline{d}$ for several external particle speeds, $\beta = v/c = 0.3$, 0.5, and 0.7. Besides the results for ν_{-} (solid lines) and ν_{+} (dashed lines), obtained from the fully retarded Eq. (2.60), we also show in Fig. 2.17 the corresponding results for ν_{-} (dot-dashed lines) and ν_{+} (dotted lines) obtained in the nonretarded limit of that equation. One notices a surprisingly strong effect of increasing interlayer distance, which promotes the bonding mode from a suppressed mode at short distances to a dominant mode at large distances. At the same time, the antibonding mode, which dominates at short distances in a manner

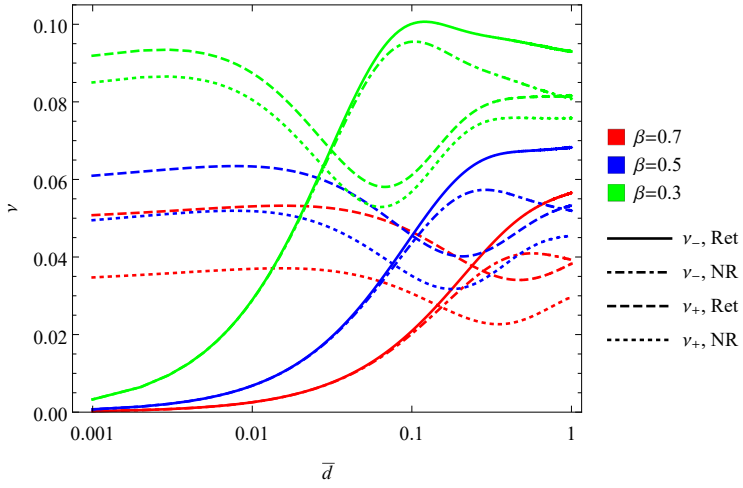

Figure 2.17: Average numbers of DPP's for the bonding mode, ν_{-}, and antibonding mode, ν_{+}, versus inter-graphene distance $\overline{d}$, for several external particle speeds $\beta = v/c$. Results for the retarded case (Ret), obtained from Eq. (2.60) with $\rho = 1$, are compared with those obtained in the nonretarded (NR) limit.

corresponding to the limit of two graphene layers being merged into single-layer, undergoes a dip in the range of intermediate distances, where a crossing with the bonding mode occurs (at $\overline{d} \approx 0.032$, 0.1, and 0.24 for the three particle speeds β), but the antibonding mode regains a weight comparable to the bonding mode at large interlayer distances. Figure 2.17 further shows that relative weights of excitation of the bonding and antibonding modes may also be efficiently controlled by the particle's speed. While the number of the antibonding mode ν_{+} does not vary too much in the full range of speeds and interlayer distances shown in this figure, one notices a suppression of the number of the bonding mode ν_{-} with increasing charged particle speed, which

is particulary strong at short distances, $\overline{d} \lesssim 0.1$. On the other hand, the increase of ν_- with $\overline{d}$ seems to saturate at large interlayer distances.

Different conductivities

In the previous subsection we have analyzed asymmetries, which arise in the Ohmic energy losses and radiation spectra with respect to the direction of the external particle trajectory, for a symmetric structure consisting of two graphene layers with equal conductivities. In this subsection we focus on a structure that is inherently asymmetric due to different doping densities of two graphene layers, $|n_1| \neq |n_2|$, which we parameterize by the ratio $\rho = k_{F,1}/k_{F,2} = \sqrt{|n_1|/|n_2|}$ as quotient of the Fermi wavenumbers $k_{F,1}$ and $k_{F,2}$ (or doping densities) in the lower and upper graphene layers, when viewed relative to the direction of motion of the external charged particle. Some of the results shown in this subsection will exhibit an asymmetry with respect to changing the ratio from a value $\rho > 1$ to $1/\rho$, which is equivalent to changing the direction of motion of the external charged particle, while other results will not exhibit such asymmetry. Accordingly, whenever a set of results for some $\rho > 1$ cannot be distinguished from results for the corresponding value $1/\rho$, we shall only discuss a range of values $\rho \geq 1$. Otherwise, we shall show results for both $\rho > 1$ *and* the corresponding $1/\rho$ values.

Figures in this subsection discuss various effects following, roughly, the same progression as in the previous subsection, which was devoted to two graphene layers with equal conductivities. In some figures in this subsection, which have multiple panels, results for the value $\rho = 1$ are excluded if they replicate results shown in the previous subsection. For example, panels (a) with $\rho = 0.1$ and (b) with $\rho = 10$ in Fig. 2.20 should be compared with panel (a) with $\overline{d} = 1$ of Fig. 2.5 for $\rho = 1$. Likewise, panels (a) with $\rho = 0.1$ and (b) with $\rho = 10$ in Fig. 2.21 should be compared with panel (a) with $\overline{d} = 1$ of Fig. 2.5 for $\rho = 1$. In Figures 2.19, 2.20, and 2.21 we assume that graphene layers have equal damping rates, $\overline{\gamma}_1 = \overline{\gamma}_2 = \overline{\gamma}$, whereas in Fig. 2.24 we also allow those rates to take different values in different graphene layers.

In Fig. 2.18 we show the dispersion relations for the bonding and antibonding hybridized modes with eigenfrequencies $\overline{\omega}_-$ (lower groups of colored lines) and $\overline{\omega}_+$ (upper groups of colored lines), respectively. Results are shown for the retarded (solid lines in panels (a) and (c)) and nonretarded (dashed lines in panels (b) and (d)) cases, for two inter-graphene distances, $\overline{d} = 0.1$ (panels (a) and (b)) and $\overline{d} = 1$ (panels (c) and (d)), and for several values of the asymmetry ratio $\rho \geq 1$. The effects of changing distance $\overline{d}$ seen in Fig. 2.18 are similar to those observed in Fig. 2.2 for the case $\rho = 1$. For fixed value of $\overline{d}$, one can see that the separation between the two modes $\overline{\omega}_\mp$ increases with increasing asymmetry ratio ρ. Particularly sensitive to this asymmetry is the bonding mode, where the dispersion curves for $\overline{\omega}_-$ are seen to be strongly lowered by

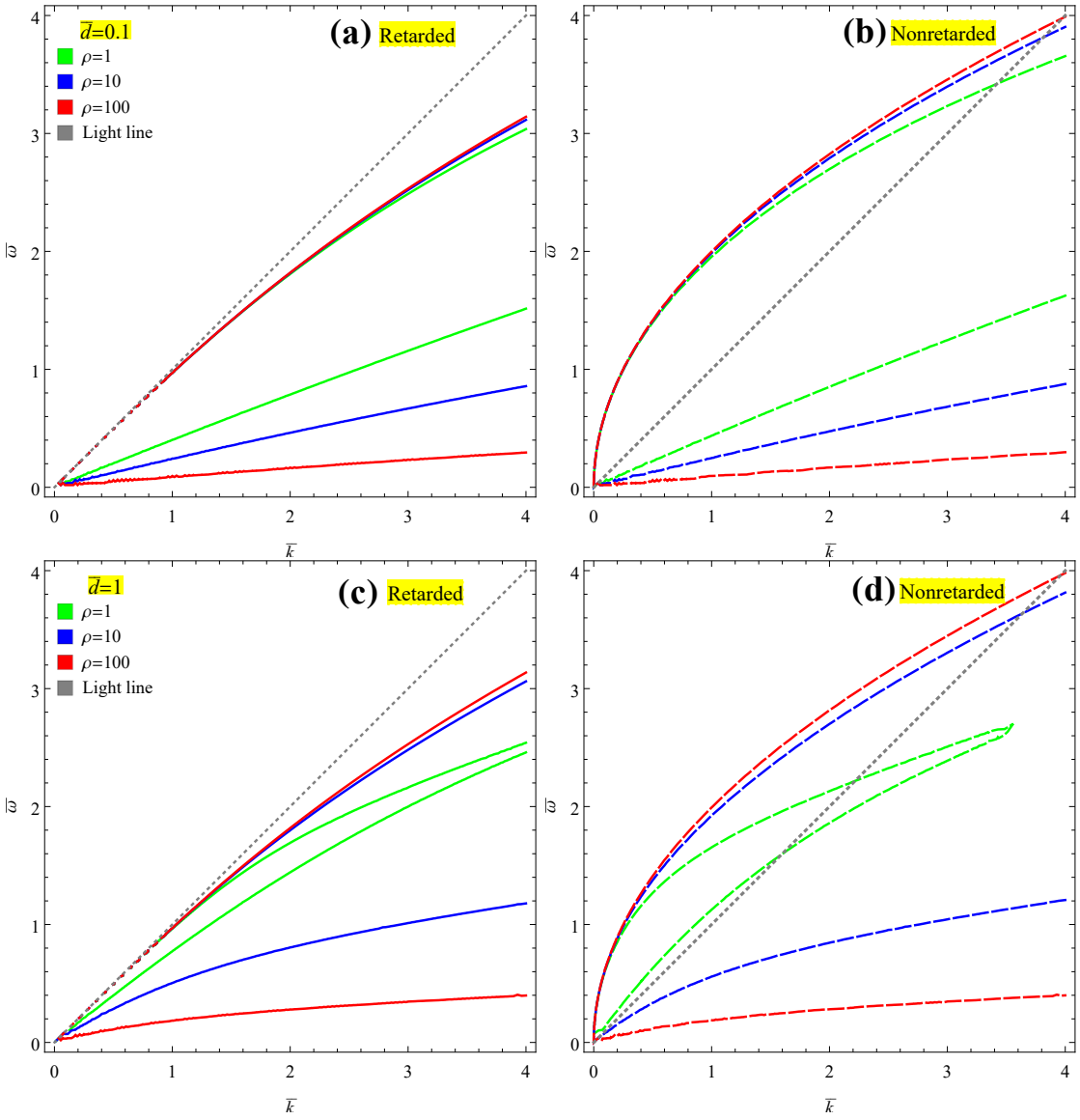

Figure 2.18: Dispersion curves for double-layer graphene with different conductivities for two interlayer distances, (a) and (b) $\overline{d} = 0.1$, (c) and (d) $\overline{d} = 1$. Solid lines in the left panels show the retarded case and dashed lines in the right panels show the nonretarded case for three values of the asymmetry ratio, $\rho = 1$, 10, and 100.

increasing ρ values, while the dispersion curves for the antibonding mode tend to gather close to each other and close to the light line as ρ increases. In the limit of long wavelengths, when $kd = \overline{k}\,\overline{d} \ll 1$, we find that the antibonding mode follows the dispersion relation given in reduced units by $\overline{\omega}_+ \sim 2\sqrt{-2+\sqrt{4+\overline{k}^2}}$, which is independent of the ratio ρ and corresponds to a single graphene layer with the effective Fermi wavenumber $k_F = k_{F,1} + k_{F,2}$. On the other hand, the long wavelength limit gives for the bonding mode a quasi-acoustic dispersion $\overline{\omega}_- \sim \sqrt{\frac{8\rho\overline{d}}{(1+\rho)^2+8\rho\overline{d}}}\,\overline{k}$, which in the limit of short distances, $\overline{d} \ll 1$, becomes independent of retardation effects and is given in nonreduced units by $\omega_- \sim \sqrt{2k_{F,h}dv_Fv_B}\,k$, where $k_{F,h} = 2k_{F,1}k_{F,2}/\left(k_{F,1}+k_{F,2}\right)$ is the harmonic mean of the Fermi wavenumbers in the two graphene layers.

Figure 2.19 displays the joint probability densities for radiation and Ohmic losses, $\overline{F}_{\rm rad}(\overline{k},\overline{\omega})$ (dashed lines) and $\overline{F}_{\rm Ohm}(\overline{k},\overline{\omega})$ (dot-dashed lines), respectively, which we show in reduced units using the normalization factor $F_c = 4(Ze)^2/\left(\pi\omega_c^2 k_c\right)$. We show the results for the cross sections of those functions with $\overline{k} = 1$ for two values of the inter-graphene distance, $\overline{d} = 1$ (panel (a)) and $\overline{d} = 0.1$ (panel (b)) and for several values of the asymmetry ratio $\rho \geq 1$. One notices in

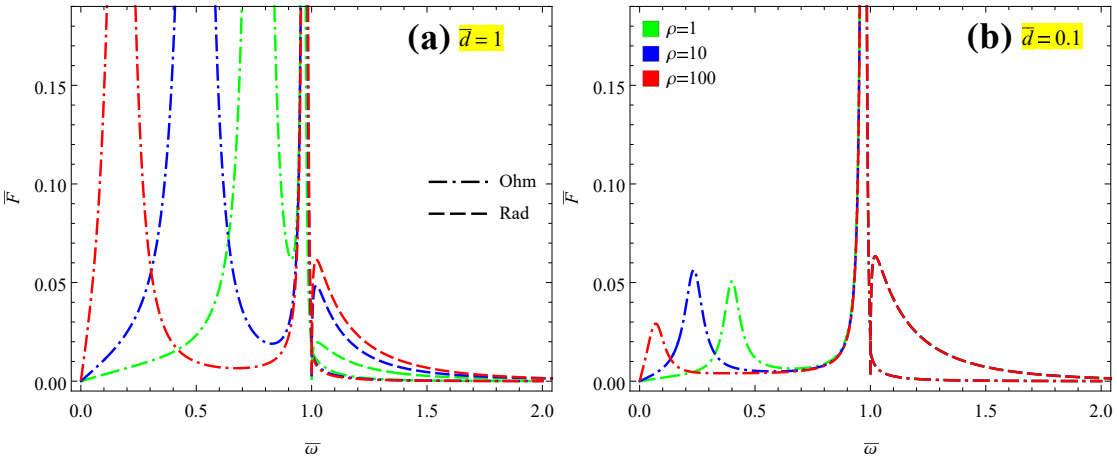

Figure 2.19: Ohmic (dot-dashed lines) and radiative (dashed lines) joint probability densities for two inter-graphene distances, (a) $\overline{d} = 1$ and (b) $\overline{d} = 0.1$, and for three asymmetry ratios, $\rho = 1$, 10, and 100, with $\overline{k} = 1$, $\overline{\gamma} = 0.1$ and $\beta = 0.5$.

Fig. 2.19 that the Ohmic losses are dominated by two peaks at frequencies $\overline{\omega} < \overline{k}$, with positions that are controlled by the ratio ρ in a manner that is expected from the behavior of the dispersion curves in Fig. 2.18, namely, the peak at $\overline{\omega}_+$ is barely affected by changing the ρ value, whereas the position of the peak at $\overline{\omega}_-$ decreases with increasing ρ. The shift of the peak at $\overline{\omega}_-$ increases,

and its amplitude decreases by decreasing the inter-graphene distance $\overline{d}$. On the other hand, the energy losses at frequencies $\overline{\omega} > \overline{k}$ are dominated by the radiation losses, which are not affected by the changing ρ values for the shorter distance $\overline{d} = 0.1$, but increase in magnitude with increasing ρ when the inter-graphene distance takes larger value, $\overline{d} = 1$.

In Fig. 2.20 we show layer-wise decomposition of the joint probability density for Ohmic losses in the lower and upper graphene layers, $\overline{F}_{\mathrm{Ohm},1}(\overline{k},\overline{\omega})$ (green solid lines) and $\overline{F}_{\mathrm{Ohm},2}(\overline{k},\overline{\omega})$ (blue dotted lines), respectively, as well as the total Ohmic losses in those two layers, $\overline{F}_{\mathrm{Ohm}}(\overline{k},\overline{\omega}) = \overline{F}_{\mathrm{Ohm},1}(\overline{k},\overline{\omega}) + \overline{F}_{\mathrm{Ohm},2}(\overline{k},\overline{\omega})$ (dot-dashed lines). Results are shown in reduced units for $\overline{k} = 1$ and $\overline{d} = 1$ and for two values of the asymmetry ratio, $\rho = 0.1$ (panel (a)) and $\rho = 10$ (panel (b)). As in Fig. 2.5, one notices that the most Ohmic losses in Fig. 2.20 occur in the peaks located near the frequencies $\overline{\omega}_{\mp}$ corresponding to the bonding and antibonding modes. In particular, we recall that in the panel (a) of Fig. 2.5 with $\overline{d} = 1$ and $\rho = 1$, Ohmic losses were generally larger in the lower layer than in the upper layer, but both the bonding and antibonding modes made comparable contributions to the Ohmic losses in both layers. However, we see in Fig. 2.20

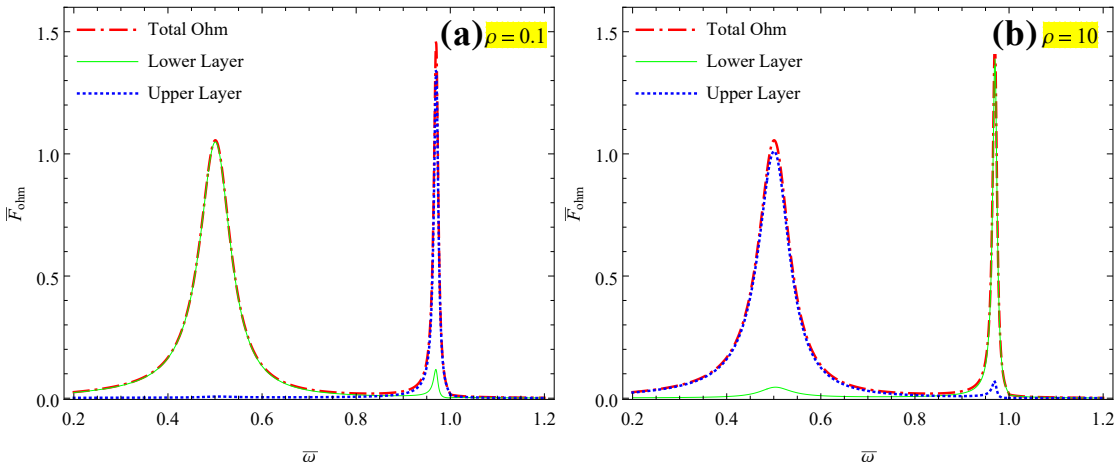

Figure 2.20: Layer-wise decomposition of Ohmic joint probability density for double-layer graphene at the distance $\overline{d} = 1$ for two asymmetry ratios, (a) $\rho = 0.1$ and (b) $\rho = 10$, with $\overline{k} = 1$, $\overline{\gamma} = 0.1$, and $\beta = 0.5$.

some important differences, namely, for $\rho = 0.1$ Ohmic losses in the lower layer occur mostly in the bonding mode, while the Ohmic losses in the upper layer occur mostly in the antibonding mode. The roles of graphene layers are largely reversed in the case $\rho = 10$, but the distribution of weights coming from the bonding and antibonding modes to Ohmic losses in those layers is not completely symmetrical when going from $\rho = 0.1$ to $\rho = 10$. Notwithstanding this small asymmetry due to the direction of charged particle motion, one may conclude that, when there is

large difference in doping densities of the two graphene layers, it is the layer with higher concentration of charge carriers that absorbs Ohmic losses predominantly in the antibonding mode with the peak at the frequency $\overline{\omega}_+$, while the layer with lower concentration absorbs Ohmic losses predominantly in the bonding mode with the peak at the frequency $\overline{\omega}_-$. We remark that this is only true for the wavenumber $\overline{k} = 1$, and the conclusion may change for other wavenumbers.

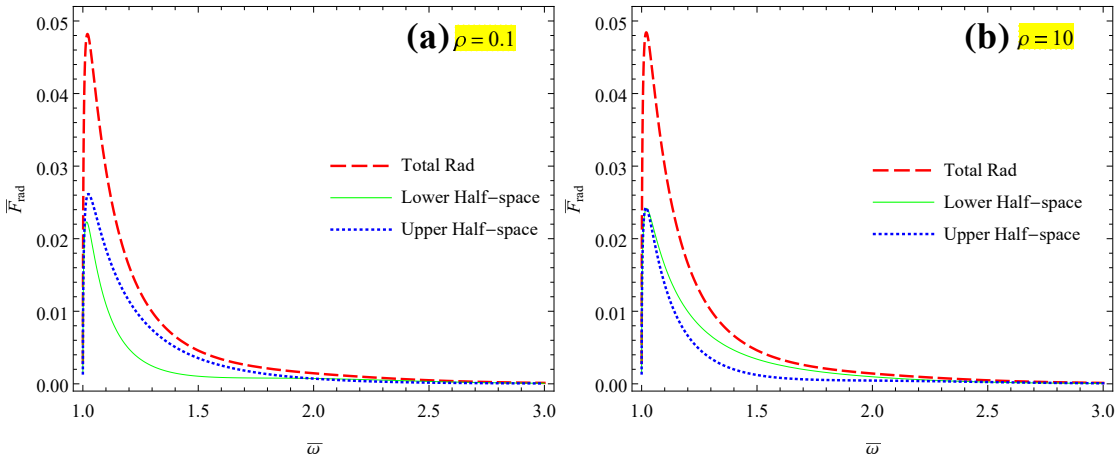

Figure 2.21: Directional decomposition of radiative joint probability density for double-layer graphene at the distance $\overline{d} = 1$ for two asymmetry ratios, (a) $\rho = 0.1$ and (b) $\rho = 10$, with $\overline{k} = 1$, $\overline{\gamma} = 0.1$, and $\beta = 0.5$.

In Fig. 2.21 we show the directional decomposition of the joint probability density for radiation losses in the lower and upper half-spaces, $\overline{F}^{\downarrow}_{\rm rad}(\overline{k}, \overline{\omega})$ (solid lines) and $\overline{F}^{\uparrow}_{\rm rad}(\overline{k}, \overline{\omega})$ (dotted lines), respectively, as well as the total radiation losses in both half-spaces, $\overline{F}_{\rm rad}(\overline{k}, \overline{\omega}) = \overline{F}^{\downarrow}_{\rm rad}(\overline{k}, \overline{\omega}) + \overline{F}^{\uparrow}_{\rm rad}(\overline{k}, \overline{\omega})$ (dashed lines) . Results are shown in reduced units for $\overline{k} = 1$ and $\overline{d} = 1$ and for two values of the asymmetry ratio, $\rho = 0.1$ (panel (a)) and $\rho = 10$ (panel (b)). We recall that in the panel (a) of Fig. 2.5 with $\overline{d} = 1$ and $\rho = 1$, there was significantly more radiation emitted in the upper than in the lower half-space for $\overline{k} = 1$. The situation is similar in the case $\rho = 0.1$ in Fig. 2.21, but is reversed in the case $\rho = 10$ in this figure. While there is no complete reversal of contributions of the upper and lower half-spaces when going from $\rho = 0.1$ to $\rho = 10$, one may conclude that, for the wavenumber $\overline{k} = 1$, more radiation is emitted into the half-space next to the graphene layer with higher concentration of charge carriers. Of course, this conclusion may be different for other $\overline{k}$ vales and other ρ values.

Figure 2.22 displays angular distribution of the joint spectral density of radiation losses, $\overline{\mathcal{S}}(\theta, \overline{\omega})$, which we show in reduced units using the normalization factor $\mathcal{S}_c = (Ze)^2 / c$ for $\overline{d} = 1$ at fixed frequency $\overline{\omega} = 1$, for several values of the asymmetry ratio in the range $0.01 \leq \rho \leq 100$.

Notice that the curve with $\rho = 1$ is reproduced from Fig. 2.7(b) for $\overline{\omega} = 1$ in order to recall that there exists an asymmetry between the radiation patterns emitted in the upper and lower half-spaces. While that figure showed substantial variability of the patterns for different $\overline{\omega}$ values due to oscillating terms in Eq. (2.47), we see in Fig. 2.22 that, for fixed $\overline{\omega} = 1$ and fixed $\overline{d} = 1$, there also exists great variability with ρ in the asymmetry of the emitted radiation patterns, especially in the interval $0.1 \leq \rho \leq 10$.

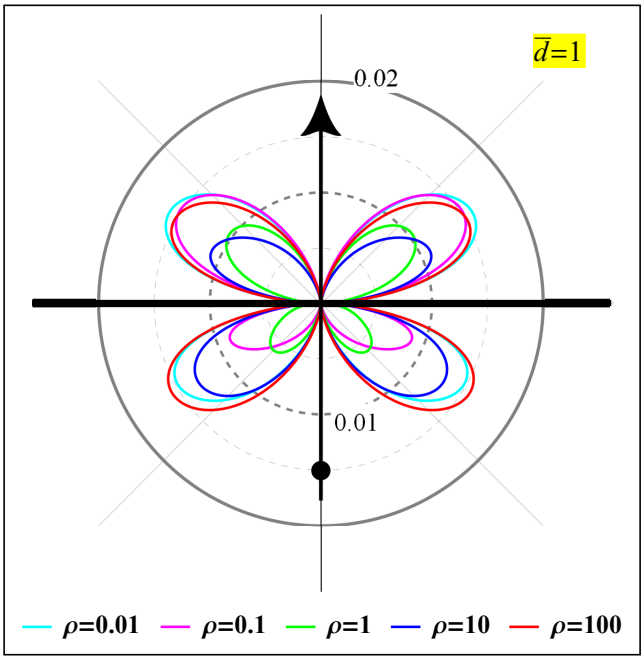

Figure 2.22: Angular distribution of the joint spectral density of radiation losses, $\overline{S}(\theta, \overline{\omega})$, at fixed frequency $\overline{\omega} = 1$, for two graphene layers at a distance $\overline{d} = 1$, having equal damping rates, $\overline{\gamma}_1 = \overline{\gamma}_2 = 0.1$, but different doping densities giving rise to several values of the asymmetry ratio ρ. The reduced speed of the external electron is $\beta = 0.5$.

Furthermore, it should be noted in Fig. 2.22 that the emitted spectra in the upper and lower half-spaces are not completely reversed when going from $\rho = 0.1$ to $\rho = 10$, which points to an interesting interplay of the inherent asymmetry of a structure with $\rho \neq 1$ and the asymmetry due to retardation effects upon changing the direction of motion of the charged particle. On the other hand, it seems that the asymmetry between the spectra emitted in the upper and lower half-spaces is significantly reduced when either $\rho = 0.01$ or $\rho = 100$, corresponding to situations when one graphene layer is almost removed from the structure on the account of having a negligibly small charge carrier density compared to the other layer. Finally, it is worthwhile to remark that,

similarly to the trends discussed in Fig. 2.7(a), the asymmetry with respect to varying the ratio ρ is also diminished when $\overline{\omega}\overline{d} \ll 1$. This describes a situation where the two graphene layers are almost blended into a single layer with an effective Fermi wavenumber $k_F = k_{F,1} + k_{F,2}$ [42].

Figure 2.23 displays the integrated probability densities for the total energy losses of the external electron, $\overline{P}_{\rm ext}(\overline{\omega})$ (solid lines), total Ohmic losses, $\overline{P}_{\rm Ohm}(\overline{\omega})$ (dash-dotted lines), and the total radiation losses, $\overline{P}_{\rm rad}(\overline{\omega})$ (dashed lines), which we show in reduced units using the normalization factor $P_c = \frac{4}{\pi}\frac{v_B}{c}\frac{1}{\hbar\omega_c}$ for (a) $\overline{d} = 1$ and (b) $\overline{d} = 0.1$, and for three values of the asymmetry ratio, $\rho = 1$, 10 and 100. Note that each set of curves upholds the conservation of energy in the sense $\overline{P}_{\rm ext}(\overline{\omega}) = \overline{P}_{\rm Ohm}(\overline{\omega}) + \overline{P}_{\rm rad}(\overline{\omega})$. One notices in the panel (a) of Fig. 2.23 a progression of peak structures in $\overline{P}_{\rm ext}(\overline{\omega})$, which grow in magnitude and move to lower frequencies with increasing ρ values. When $\rho = 1$ and 10, those structures are related to Ohmic losses, $\overline{P}_{\rm Ohm}(\overline{\omega})$, which dominate at frequencies $\overline{\omega} \gtrsim 1$, whereas radiation losses, $\overline{P}_{\rm rad}(\overline{\omega})$, are comparable to the Ohmic losses when $\overline{\omega} \sim 0.1$ and become dominant for $\overline{\omega} \lesssim 0.1$. On the other hand, when $\rho = 100$ in Fig. 2.23(a), a peak in $\overline{P}_{\rm Ohm}(\overline{\omega})$ that occurs at a frequency $0.1 < \overline{\omega} < 0.5$, is converted to a shoulder in $\overline{P}_{\rm ext}(\overline{\omega})$ in the same frequency interval owing to the presence of a strongly increasing $\overline{P}_{\rm rad}(\overline{\omega})$ at decreasing frequencies. In the case of a shorter interlayer distance $\overline{d} = 0.1$ in Fig. 2.23(b), the peak structures that arise from $\overline{P}_{\rm Ohm}(\overline{\omega})$ are moved to higher frequencies, so that the effects of radiation losses are not so prominent in the features observed in $\overline{P}_{\rm ext}(\overline{\omega})$. It is interesting to observe in Fig. 2.23(a) that the total energy losses of the external electron, as well as the Ohmic losses, decrease in magnitude with increasing ρ at frequencies $\overline{\omega} \gtrsim 2$, whereas the opposite is true for those losses at frequencies $\overline{\omega} \lesssim 0.5$. Similar observations are made in Fig. 2.23(b), but for frequencies $\overline{\omega} \gtrsim 5$ and $\overline{\omega} \lesssim 1$, respectively.

Finally, it is noteworthy in Fig. 2.23 that the integrated radiation energy losses, $\overline{P}_{\rm rad}(\overline{\omega})$, do not show any appreciable dependence on the value of the asymmetry ratio ρ or on the interlayer distance $\overline{d}$. This is similar to observations made in Fig. 2.8(a) regarding the $\overline{d}$–dependence of $\overline{P}_{\rm rad}(\overline{\omega})$. Our calculations for directional decomposition of the radiation losses (not shown) also confirm that the integrated probability densities for radiation losses in the upper and lower half-spaces, $\overline{P}^{\uparrow}_{\rm rad}(\overline{\omega})$ and $\overline{P}^{\downarrow}_{\rm rad}(\overline{\omega})$, do not show any appreciable dependence on ρ or $\overline{d}$, similar to the observations made in Fig. 2.9(a).

Later, in Fig. 2.25, we further analyze the effects of the asymmetry ratio ρ in the layer-wise decomposition of the integrated probability density for Ohmic energy losses, $\overline{P}_{\rm Ohm}(\overline{\omega}) = \overline{P}_{\rm Ohm,1}(\overline{\omega}) + \overline{P}_{\rm Ohm,2}(\overline{\omega})$, and find much larger differences between contributions from the lower and upper graphene layers for values $\rho \neq 1$ when $\overline{d} = 1$ than differences observed in Fig. 2.9(a) for $\rho = 1$. This is further elucidated by analyzing modal decomposition of the probability density for plasmon excitations, $\overline{P}_{\rm pl}(\overline{\omega}) = \overline{P}^{-}_{\rm pl}(\overline{\omega}) + \overline{P}^{+}_{\rm pl}(\overline{\omega})$, which reveals an intricate interplay between the effects of increasing interlayer distance $\overline{d}$ and variations in the asymmetry ratio ρ in Ohmic

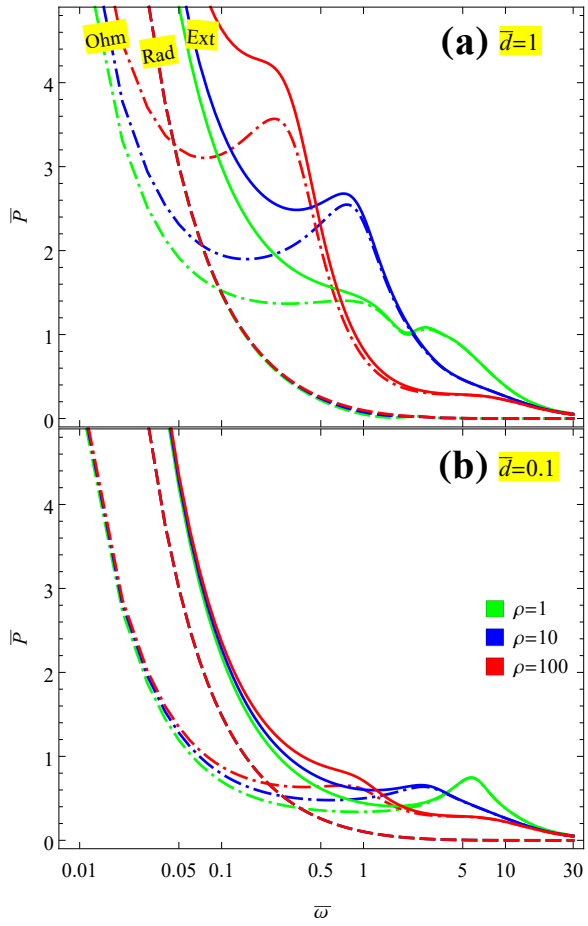

Figure 2.23: Integrated probability densities for the total energy losses of the external electron, $\overline{P}_{\rm ext}(\overline{\omega})$ (solid lines), total Ohmic losses, $\overline{P}_{\rm Ohm}(\overline{\omega})$ (dot-dashed lines), and the total radiation losses, $\overline{P}_{\rm rad}(\overline{\omega})$ (dashed lines), are shown in reduced units for two graphene layers with equal damping rates, $\overline{\gamma}_1 = \overline{\gamma}_2 = 0.1$, at distances: (a) $\overline{d} = 1$ and (b) $\overline{d} = 0.1$, for three values of the asymmetry ratio, $\rho = 1$, 10 and 100. The reduced speed of the external electron is $\beta = 0.5$.

losses at frequencies $\overline{\omega} \gtrsim 1$.

The effect of asymmetry in damping rates on integrated Ohmic losses. Another issue of interest is to analyze the situation when the lower and upper graphene layers have different damping rates, $\overline{\gamma}_1$ and $\overline{\gamma}_2$, respectively. In Fig. 2.24 we show the total integrated probability density for Ohmic energy losses, $\overline{P}_{\rm Ohm}(\overline{\omega})$ (dot-dashed lines), along with its layer-wise decomposition into the lower and upper graphene layers, $\overline{P}_{\rm Ohm,1}(\overline{\omega})$ (dashed lines) and $\overline{P}_{\rm Ohm,2}(\overline{\omega})$ (dotted lines), respectively. Results are shown for the inter-graphene distance $\overline{d} = 1$ and for three asymmetry ratios, $\rho = 0.1$, 1 and 10, using two asymmetric combinations of damping rates: $\overline{\gamma}_1 = 0.5$ and $\overline{\gamma}_2 = 0.1$ (red lines) and $\overline{\gamma}_1 = 0.1$ and $\overline{\gamma}_2 = 0.5$ (blue lines). One notices in the panel (b) of Fig. 2.24 that, for the case of graphene layers with equal doping densities, $\rho = 1$, the asymmetry in damping rates gives surprisingly large effects in the layer-wise decomposition of Ohmic losses at frequencies $\overline{\omega} \lesssim 2$. In particular, one sees that the graphene layer with higher damping rate absorbs more energy at frequencies $0.1 \lesssim \overline{\omega} \lesssim 2$ (see the difference between the blue and red dashed lines, as well as the difference between the blue and red dotted lines), whereas the opposite is true at frequencies $\overline{\omega} \lesssim 0.05$. At the same time, one sees in Fig. 2.24(b) that there is no big difference between the total integrated Ohmic energy losses, $\overline{P}_{\rm Ohm}(\overline{\omega})$, for the two asymmetric combinations of damping rates.

We next consider the cases of asymmetric doping densities with $\rho = 0.1$ and $\rho = 10$, shown in the panels (a) and (c) of Fig. 2.24, respectively. One sees somewhat larger differences between the total Ohmic losses, $\overline{P}_{\rm Ohm}(\overline{\omega})$, for the two asymmetric combinations of damping rates, which are remarkably reversed when going from $\rho = 0.1$ to $\rho = 10$, i.e., the red and blue dot-dashed lines approximately reverse the roles in the panels (a) and (c). On the other hand, the reversal between the red and blue lines in the panels (a) and (c) for the layer-wise decomposition of Ohmic losses is much more complicated. Namely, one can only observe reversal between the curves describing Ohmic losses in a graphene layer with higher doping density and lower damping rates, i.e., the red dashed and dotted curves in panel (a) look very similar to the blue dotted and dashed curves in panel (b), respectively.

We finally note that our calculations (not shown here) imply that there are no substantial effects of the asymmetry in the damping rates in the directional decomposition of integrated radiative energy losses.

The effects of interlayer distance and doping asymmetry on the layer-wise and modal decompositions. In Fig. 2.25 we show the total integrated probability density for Ohmic energy losses, $\overline{P}_{\rm Ohm}(\overline{\omega})$ (dash-dotted lines), along with its layer-wise decomposition into the lower and

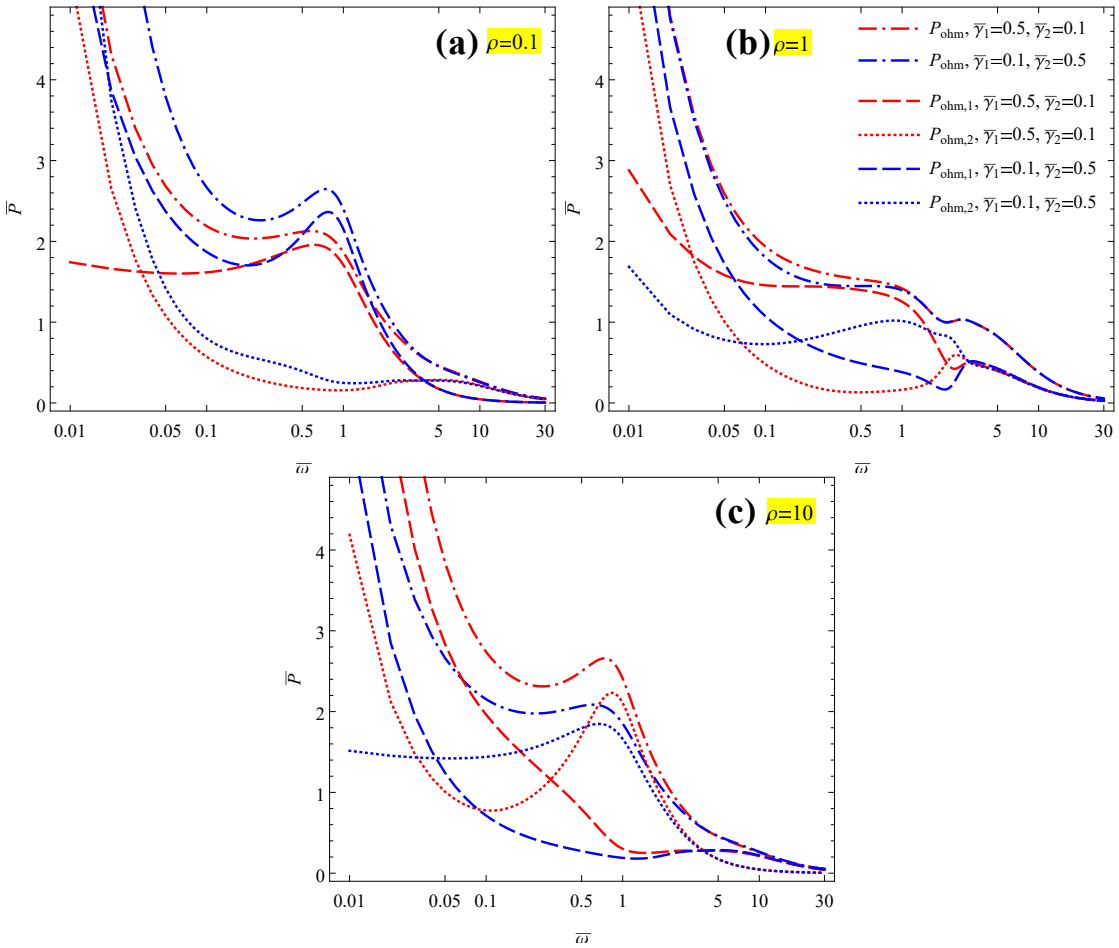

Figure 2.24: Layer-wise decomposition of the integrated probability density for Ohmic energy losses in double-layer graphene at the distance $\overline{d} = 1$ for three asymmetry ratios for doping density, (a) $\rho = 0.1$, (b) $\rho = 1$, and (c) $\rho = 10$, and for several asymmetric combinations of the damping rates $\overline{\gamma}_1$ and $\overline{\gamma}_2$, with $\beta = 0.5$.

upper graphene layers, $\overline{P}_{\mathrm{Ohm},1}(\overline{\omega})$ (dashed lines) and $\overline{P}_{\mathrm{Ohm},2}(\overline{\omega})$ (dotted lines), respectively. Results are shown for the interlayer distances (a) $\overline{d} = 1$ and (b) $\overline{d} = 0.1$, and for three asymmetry ratios, $\rho = 0.1$, 1 and 10. (Notice that the curves for $\rho = 1$ are reproduced from Figs. 2.8 and 2.9 for the sake of comparison.) One sees in Fig. 2.25 that, while there is practically no difference between the curves for the total Ohmic losses $\overline{P}_{\mathrm{Ohm}}(\overline{\omega})$ with $\rho = 0.1$ and $\rho = 10$, there are large differences between the contributions from the lower and upper graphene layers for those two ρ values when $\overline{d} = 1$ in panel (a), and much smaller differences when $\overline{d} = 0.1$ in panel (b). This points to a possibly very important role played by the asymmetry ratio ρ in the $\overline{d}$–dependence of interference terms determining the layer-wise decomposition of Ohmic losses.

When $\rho = 0.1$ in Fig. 2.25(a), Ohmic losses in the lower layer are dominated by a massive peak in $\overline{P}_{\mathrm{Ohm},1}(\overline{\omega})$ at $\overline{\omega} \approx 1$, while the upper layer is characterized by a large increase in $\overline{P}_{\mathrm{Ohm},2}(\overline{\omega})$ at low frequencies, $\overline{\omega} \lesssim 0.05$. The roles of the lower and upper layers are reversed when $\rho = 10$ in Fig. 2.25(a), but this reversal is completely symmetrical only for $\overline{\omega} > 1$, whereas a strong asymmetry remains for frequencies $\overline{\omega} \lesssim 1$. This residual asymmetry with respect to reversal of the direction of motion of the external electron in the case of graphene layers with different doping densities has the same origin as the asymmetry seen between the curves for $\overline{P}_{\mathrm{Ohm},1}(\overline{\omega})$ and $\overline{P}_{\mathrm{Ohm},2}(\overline{\omega})$ with $\rho = 1$, showing that a graphene layer with given doping density absorbs more Ohmic losses at frequencies $\overline{\omega} \lesssim 1$ when it is first traversed by the external electron than when it is traversed last, as discussed in Fig. 2.9. Similar conclusions may be deduced from Fig. 2.25(b), but with the main peak in $\overline{P}_{\mathrm{Ohm}}(\overline{\omega})$ with $\rho = 0.1$ and $\rho = 10$ being moved to a frequency $\overline{\omega} \approx 2$, and with much weaker residual asymmetry when going from $\rho = 0.1$ to $\rho = 10$ at $\overline{\omega} \lesssim 1$.

A progress towards better understanding of the roles of graphene layers with different doping densities in Fig. 2.25 is provided by analyzing the modal decomposition of the probability density for plasmon excitations in Fig. 2.26 below. Namely, it is revealed in that figure that the peaks seen in $\overline{P}_{\mathrm{Ohm}}(\overline{\omega})$ at $\overline{\omega} \approx 1$ in Fig. 2.25(a) and $\overline{\omega} \approx 2$ in Fig. 2.25(b) are related to the bonding DPP mode. This leads us to an assertion that the layer with lower doping density absorbs Ohmic losses predominantly via excitations of the bonding DPP mode. This assertion was previously verified in the Fig. 2.20 by analyzing the layer-wise decomposition of the joint probability density for Ohmic energy losses in the lower and upper graphene layers, $\overline{F}_{\mathrm{Ohm},1}(\overline{k},\overline{\omega})$ and $\overline{F}_{\mathrm{Ohm},2}(\overline{k},\overline{\omega})$ for $\rho \neq 1$. It was shown in Fig. 2.20 that graphene layer with higher doping density absorbs Ohmic energy predominantly within a peak centered at higher frequency close to $\overline{\omega}_+$ for antibonding mode, while the layer with lower doping density absorbs Ohmic energy predominantly within a peak centered at lower frequency close to $\overline{\omega}_-$ for bonding mode.

Finally, in Fig. 2.26 we show the modal decomposition of the probability density for plasmon excitations of the bonding and antibonding modes, $\overline{P}_{\mathrm{pl}}(\overline{\omega}) = \overline{P}^{-}_{\mathrm{pl}}(\overline{\omega}) + \overline{P}^{+}_{\mathrm{pl}}(\overline{\omega})$, with the

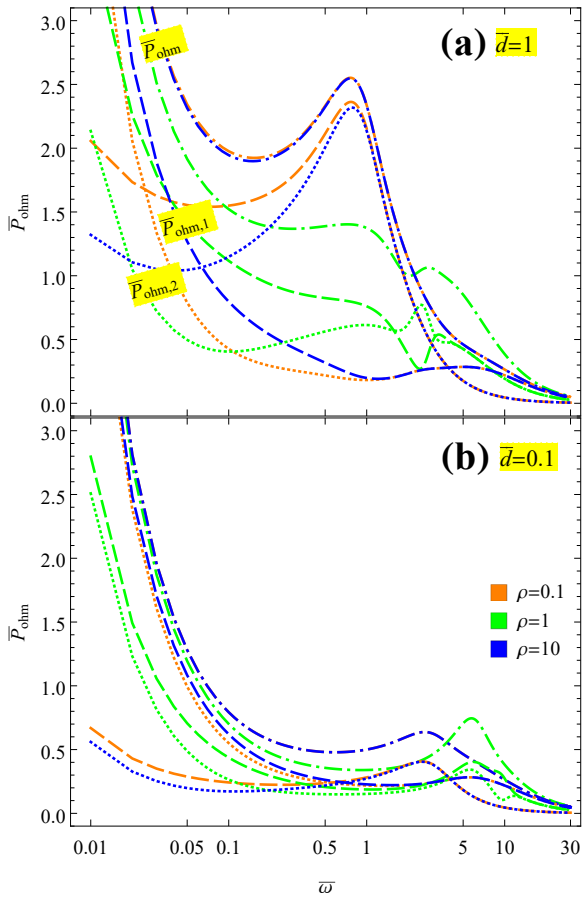

Figure 2.25: The total integrated probability density for Ohmic energy losses, $\overline{P}_{\mathrm{Ohm}}(\overline{\omega})$ (dot-dashed lines), along with its layer-wise decomposition into the lower and upper graphene layers, $\overline{P}_{\mathrm{Ohm},1}(\overline{\omega})$ (dashed lines) and $\overline{P}_{\mathrm{Ohm},2}(\overline{\omega})$ (dotted lines), respectively. Results are shown for two graphene layers with equal damping rates, $\overline{\gamma}_1 = \overline{\gamma}_2 = 0.1$, at two distances, (a) $\overline{d} = 1$ and (b) $\overline{d} = 0.1$, for three asymmetry ratios, $\rho = 0.1$, 1 and 10. The reduced speed of the external electron is $\beta = 0.5$.

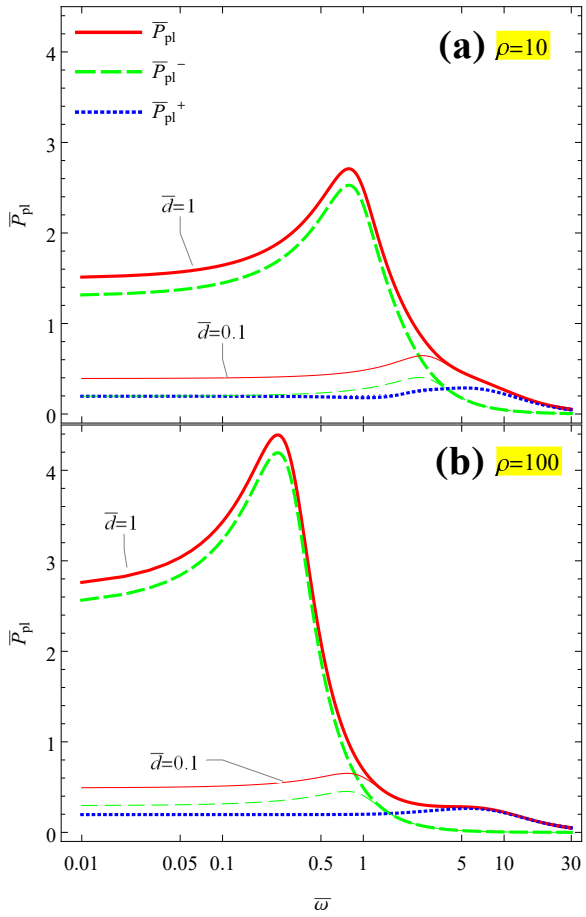

Figure 2.26: Modal decomposition of the integrated total probability density (solid red lines) for plasmon polariton excitations of the bonding (green dashed lines) and antibonding (blue dotted lines) modes, $\overline{P}_{\rm pl}(\overline{\omega}) = \overline{P}_{\rm pl}^{-}(\overline{\omega}) + \overline{P}_{\rm pl}^{+}(\overline{\omega})$, for two graphene layers with zero damping rates and the asymmetry ratios (a) $\rho = 10$ and (b) $\rho = 100$, for two interlayer distances, $\overline{d} = 1$ (thick lines) and $\overline{d} = 0.1$ (thin lines). The reduced speed of the external electron is $\beta = 0.5$.

asymmetry ratios (a) $\rho = 10$ and (b) $\rho = 100$, for two interlayer distances, $\overline{d} = 1$ and $\overline{d} = 0.1$. Results are shown in reduced units using the normalization factor $P_c = \frac{4}{\pi}\frac{v_B}{c}\frac{1}{\hbar\omega_c}$. Results in Fig. 2.26 should be compared with those in Fig. 2.10 for $\rho = 1$, recalling that the limit of zero damping in graphene layers, $\overline{\gamma} = 0$, was used in both figures. Whereas $\overline{P}^{\mp}_{\rm pl}(\overline{\omega})$ in Fig. 2.10 for $\rho = 1$ showed strong oscillations at frequencies $\overline{\omega} > \pi\beta/\overline{d}$, such oscillations are suppressed in Fig. 2.26 for $\rho \neq 1$. This may be explained by referring to the expression in the square brackets in Eq. (18), showing that the oscillatory term with the factor $\cos(\overline{\omega}d/\beta)$ will be suppressed whenever $\rho + \frac{1}{\rho} - 2 \gg 1$, i.e., when the asymmetry ratio is sufficiently different from unity. Suppression of oscillations for $\rho \neq 1$ explains why the curves for $\overline{P}_{\rm Ohm,1,2}(\overline{\omega})$ with $\rho \neq 1$ in Fig. 2.25 do not exhibit intricate features seen in the curves with $\rho = 1$ at frequencies $\overline{\omega} \sim \pi\beta/\overline{d}$.

On the other hand, one notices in Fig. 2.26 that the probability density for the antibonding mode, $\overline{P}^{+}_{\rm pl}(\overline{\omega})$, is practically independent of both the interlayer distance $\overline{d}$ and the asymmetry ratio ρ, whereas the density for the bonding mode, $\overline{P}^{-}_{\rm pl}(\overline{\omega})$, increases in magnitude with both increasing $\overline{d}$ and increasing ρ. This is in close correlation with observations made in Figs. 2.2 and 2.18 regarding the dispersion relations for those two modes, with the bonding mode found to be much more sensitive to variations in both $\overline{d}$ and ρ than the antibonding mode.

Moreover, it is seen in Fig. 2.26 that the total probability density for plasmon excitations $\overline{P}_{\rm pl}(\overline{\omega})$ is dominated by a peak in $\overline{P}^{-}_{\rm pl}(\overline{\omega})$, occurring at a frequency $\overline{\omega}$ that decreases with increasing $\overline{d}$ and increasing ρ. Comparing the curves for $\overline{P}_{\rm pl}(\overline{\omega})$ in Fig. 2.26(a) with the curves for $\overline{P}_{\rm Ohm}(\overline{\omega})$ with $\rho = 0.1$ or $\rho = 10$ in Fig. 2.25, one may assert that the total integrated Ohmic losses in the latter figure are dominated by the excitation of both hybridized DPP modes at frequencies $\overline{\omega} \gtrsim 0.5$, whereas differences at $\overline{\omega} \lesssim 0.1$ stem from the fact that $\overline{P}_{\rm Ohm}(\overline{\omega})$ in Fig. 2.25 was calculated with finite damping rate of $\overline{\gamma} = 0.1$. In particular, the peaks in $\overline{P}_{\rm pl}(\overline{\omega})$ in Fig. 2.26(a) with $\rho = 10$, which occur at $\overline{\omega} \approx 1$ for $\overline{d} = 1$ and $\overline{\omega} \approx 2$ for $\overline{d} = 0.1$, correspond to the peaks in $\overline{P}_{\rm Ohm}(\overline{\omega})$ in Fig. 2.25 for $\rho = 0.1$ and $\rho = 10$, and they clearly originate from excitation of the bonding mode.

These conclusions should be contrasted with conclusions regarding the features seen in $\overline{P}_{\rm Ohm}(\overline{\omega})$ in Fig. 2.25 for $\rho = 1$, which have different origins. We recall that analyzing the results in Figs. 4 and 5 in terms of the modal decompositions in Fig. 2.10 revealed that the peak-and-valley in $\overline{P}_{\rm Ohm}(\overline{\omega})$ in Fig. 2.25(a) for $\rho = 1$ originates as an interference between the bonding and antibonding modes, whereas the peak near $\overline{\omega} = 5$ in $\overline{P}_{\rm Ohm}(\overline{\omega})$ in Fig. 2.25(b) for $\rho = 1$ originates from excitation of the antibonding mode. This shows that there is a strong interplay between the effects of interlayer distance $\overline{d}$ and the asymmetry ratio ρ in Ohmic losses at frequencies $\overline{\omega} \gtrsim 1$.

Average number of plasmons. In the previous section we have extensively analyzed the plasmon excitation for two graphene layers in the case $\rho = 1$, i.e., for layers with equal conductivities. In the present subsection we extend this study to the case of different conductivities, $\rho \neq 1$.

Using the expression obtained in the previous section in Eq. (2.60), we plot in Fig. 2.27 the contribution $\nu_{\mp}$ of each mode as a function of ρ for different values of $\bar{d}$. We compare the results from the fully retarded expression in Eq. (2.60) with nonretarded results obtained in the limit $c \to \infty$. One notices that the retardation affects primarily the antibonding mode, which is not strongly dependent on the interlayer distance, except when $\rho \approx 1$. On the other hand, the bonding mode does not show effects of retardation at distances $\bar{d} < 1$, but it is strongly promoted by increasing interlayer distance for the asymmetric ratio in the interval $0.1 \lesssim \rho \lesssim 10$, in which range the retardation effects also become remarkable.

It is interesting that all curves in Fig. 2.27 exhibit a cusp-like dependence on the asymmetry ratio when $\rho \to 1$. This indicates that even small variations of nominally equal doping densities can cause significant variations in the number of excited plasmons. Nevertheless, we note that the abrupt structure is wiped out when adding the modes to obtain the total average number of plasmons, as shown in Fig. 2.28 for the cases $\bar{d} = 0.1$ and $\bar{d} = 1$.

A close inspection of Eq. (2.60) makes it evident that the oscillatory term in the integrand is damped by the exponential function $e^{-\alpha d}$ when $\rho \neq 1$. In the limit $\rho \to 1$, the exponential is cancelled out and the oscillatory term prevails at all frequencies. To illustrate this, we plot in Fig. 2.29 the integrated probability of exciting plasmons $P_{\rm pl} \propto \int dk\, kF_{\rm pl}(k,\omega)$ as a function of frequency for $\rho = 1$ and $\rho = 0.99$. It is clear that the behaviour at $\rho = 1$ is the result of the highly oscillatory integrand, which disappears with a relatively small variation of ρ.

Finally, in Fig. 2.30 we explore the behaviour of the average number of excited plasmons as a function of the interlayer distance for three cases of ρ, considering equal and different conductivities. For each ρ we choose three values of the incident velocity, $\beta = 0.3$, 0.5 and 0.7. Notice that the case $\rho = 1$ has been considered in Fig. 2.17. For the cases with $\rho \neq 1$, we observe that the relative behaviour of the modes is maintained, with the bonding mode passing from negligible values at small distances to be dominant over the antibonding mode by increasing $\bar{d}$. Nevertheless, the structure shown by the antibonding mode for $\rho = 1$, with a pronounced minimum at intermediate distances, is smoothed for $\rho \neq 1$ and tends to disappear for layers with very different conductivities. On the other hand, when the particle velocity increases, the average number of excited plasmons diminishes for each mode, as expected.

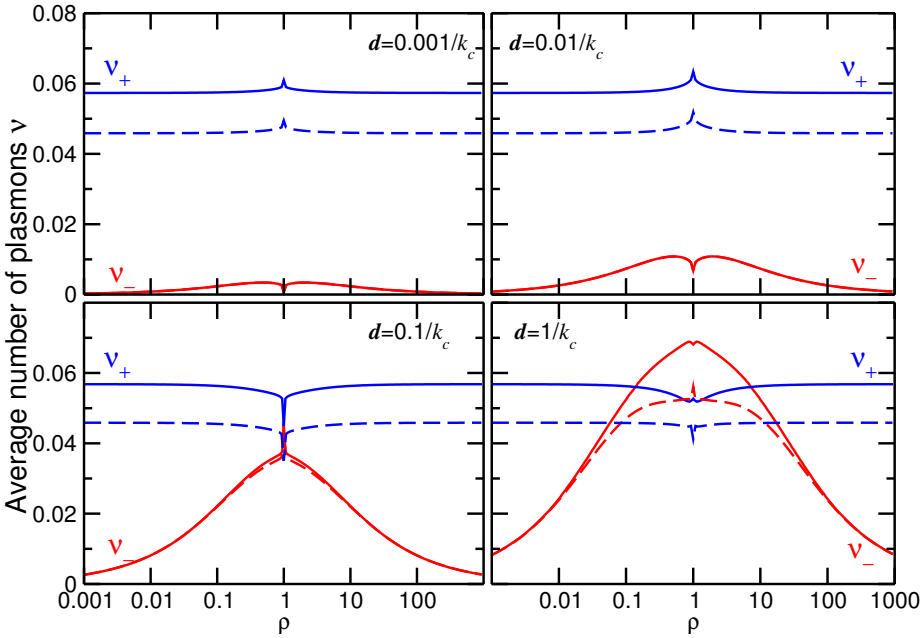

Figure 2.27: Average numbers of DPPs at the bonding mode, ν_- (red, continuous), and antibonding mode, ν_+ (blue, continuous), versus asymmetry parameter ρ for several interlayer distances d. The external particle speed is $\beta = v/c = 0.5$. Results are compared with nonretarded results, obtained from Eq. (2.60) in the limit $c \to \infty$ (dashed lines).

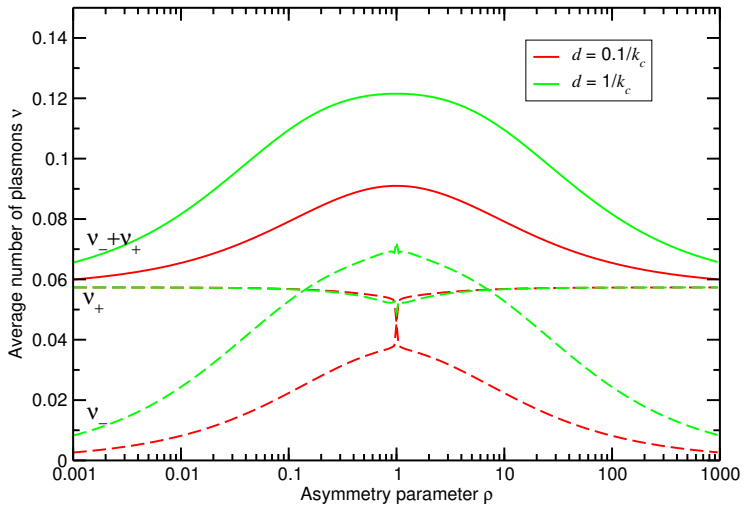

Figure 2.28: Total average number of plasmons obtained summing both contributions, $\nu = \nu_- + \nu_+$, for $\overline{d} = dk_c = 0.1$ (solid red line) and $\overline{d} = dk_c = 1$ (solid green line), with the particle speed $\beta = v/c = 0.5$, showing the cancellation of the cusp-like behaviour. The two pairs of dashed lines with matching colors show the individual numbers of plasmons ν_- and ν_+.

2.3.2 Multilayer graphene

In the previous subsection we have shown that there are strong effects of variations in the charged particle speed v and the damping rate γ on both the Ohmic and radiation energy losses in a DLG, showing much more variety than in the case of an SLG due to the presence of two HDDPs in the case of DLG [42]. Moreover, we have found strong effects due to differences in doping densities of graphene layers in a DLG. However, in order to decrease the size of the parameter space in this subsection, we keep the reduced particle speed fixed at $\beta = v/c = 0.5$ (corresponding to a typical electron energy in a STEM) and the reduced damping rate fixed at $\overline{\gamma} = 0.05$, while assuming that all graphene layers are doped with equal densities. For the same reason, we assume equal spacing d between the nearest graphene layers in an MLG. Thus, with the conductivity of each layer being described by Eq. (2.39), we concentrate on the effects of variations in the number of layers N and the interlayer distance d for the energy loss and radiation spectra when a fast charged particle traverses an MLG.

In Fig. 2.31, we use reduced units to show the joint probability densities of the total Ohmic energy loss, $\overline{F}_{\rm Ohm}(\overline{k},\overline{\omega}) = F_{\rm Ohm}(\overline{k},\overline{\omega})/F_c$ (panel a), and the total radiation energy loss, $\overline{F}_{\rm rad}(\overline{k},\overline{\omega}) = F_{\rm rad}(\overline{k},\overline{\omega})/F_c$ (panel b), where $F_c = 4(Ze)^2/\left(\pi\omega_c^2 k_c\right)$, as well as the dispersion curves for three HDPP modes, $\overline{\omega} = \overline{\omega}_j(\overline{k})$, with $j = 1, 2$ and 3 (panel c), for a three-layer graphene (TLG)

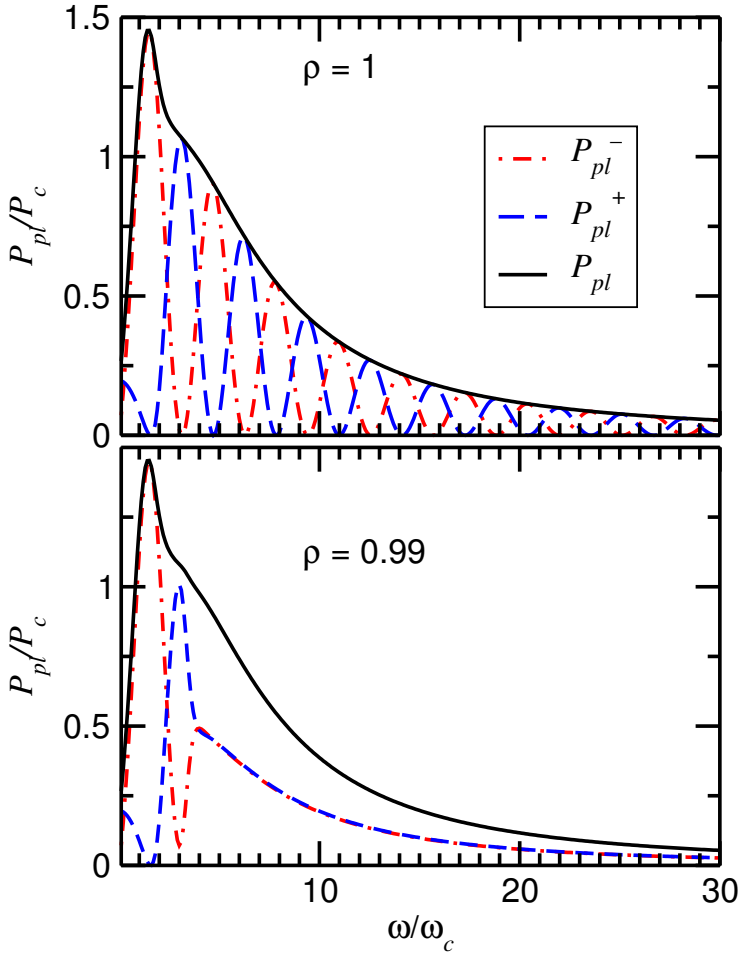

Figure 2.29: Modal decomposition of the integrated probability of exciting plasmons, $P_{\rm pl} = P_{\rm pl}^{-} + P_{\rm pl}^{+}$, shown in reduced units using $P_c = \frac{4}{\pi}\frac{v_B}{c}\frac{1}{\hbar\omega_c}$, for $\overline{d} = dk_c = 1$, $\beta = v/c = 0.5$, and two values of the asymmetry parameter, $\rho = 1$ and $\rho = 0.99$.

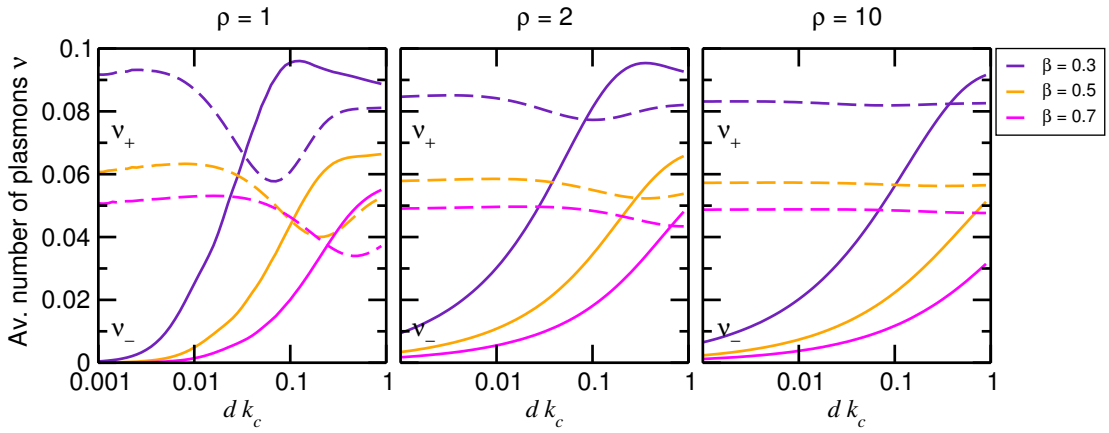

Figure 2.30: Average number of plasmons $\nu_{\mp}$ as a function of the reduced interlayer distance $\overline{d} = dk_c$ for asymmetry parameters $\rho = 1$, 2, and 10. Bonding modes $(-)$ are plotted with continuous lines, while antibonding $(+)$ modes are plotted with dashed lines. The reduced particle speeds are $\beta = 0.3$ (indigo lines); $\beta = 0.5$ (orange lines); $\beta = 0.7$ (magenta lines).

structure with $\overline{d} = 0.1$. Besides the exact dispersion curves, for the sake of comparison we also show in Fig. 2.31(c) three approximations to the exact dispersion curves, $\overline{\omega} = \overline{\omega}_j^{\rm appr}(\overline{k})$, which will be introduced later, as well as the DPP dispersion curve for an SLG with $\overline{\omega}_{\rm SLG}(\overline{k}) = \sqrt{2\left(-1+\sqrt{1+\overline{k}^2}\right)}$.

By comparison with the panel (c), it is clear that the main contribution to the Ohmic energy loss in panel (a) of Fig. 2.31 occurs predominantly in the regions close to the three HDPP dispersion curves. Those regions exhibit different amounts of broadening, such that the largest width occurs along the middle dispersion curve, $\overline{\omega} = \overline{\omega}_2(\overline{k})$, and the smallest width occurs along the lowest dispersion curve, $\overline{\omega} = \overline{\omega}_1(\overline{k})$. One notices that the three broadened curves merge in Fig. 2.31(a), giving rise to a relatively broad and structureless background of Ohmic energy loss in a region of very small $\overline{\omega}$ and $\overline{k}$ values, which is a consequence of finite damping rate that governs dissipative processes at low frequencies. It should be stressed that, even though part of this background extends above the light line, $\overline{\omega} > \overline{k}$, the associated processes do not give rise to any radiation, but rather produce Joule heat that remains in graphene. On the other hand, we display in the panel (b) of Fig. 2.31 the energy loss density due to the TR, which is seen to be broadly distributed in a region that is located strictly above the light line.

In the panel (c) of Fig. 2.31, one notices that all three dispersion curves lie below the light line, $\overline{\omega} = \overline{k}$, and that the highest dispersion exhibits a transition to the $\overline{\omega}_3 \propto \sqrt{\overline{k}}$ form, whereas

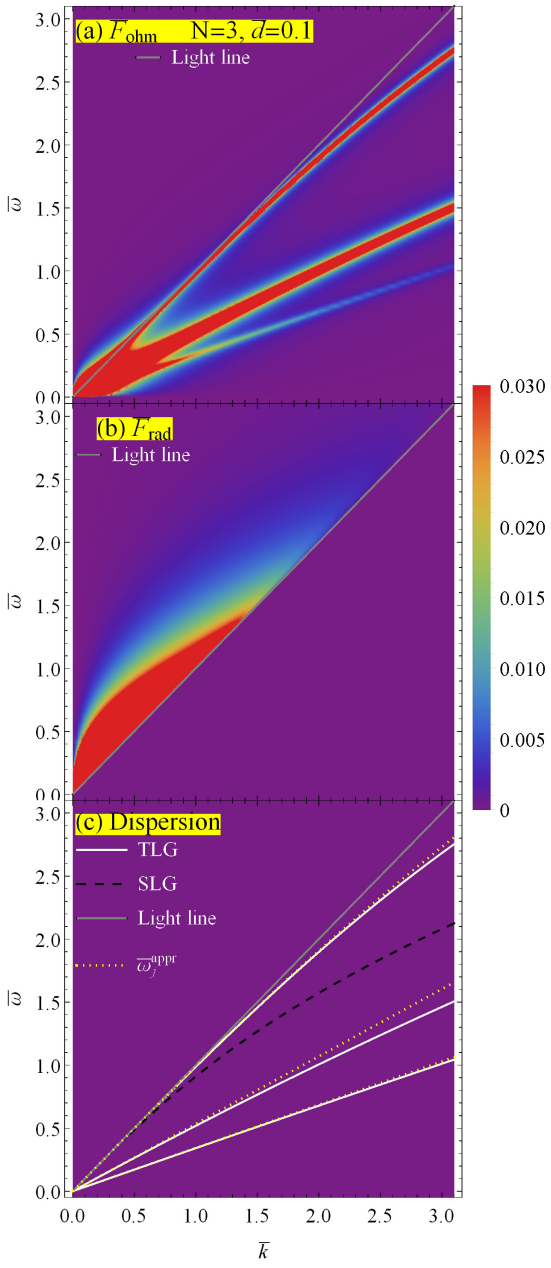

Figure 2.31: The total Ohmic energy loss density, $\overline{F}_{\rm Ohm} = F_{\rm Ohm}/F_c$ (panel a), and the total radiative energy loss density, $\overline{F}_{\rm rad} = F_{\rm rad}/F_c$ (panel b), are displayed in reduced units with $F_c = 4(Ze)^2/(\pi\omega_c^2 k_c)$, as functions of the reduced wavenumber $\overline{k} = k/k_c$ and the reduced frequency $\overline{\omega} = \omega/\omega_c$, for a three-layer graphene with reduced interlayer distance $\overline{d} = k_c d = 0.1$. Panel (c) displays with white solid lines the dispersion curves for three hybridized Dirac plasmon polariton modes, $\overline{\omega} = \overline{\omega}_j(\overline{k})$ for $j = 1, 2, 3$, along with the corresponding long-wavelength approximations (white dotted lines), a dispersion curve for single-layer graphene (black dashed line), and the light line $\overline{\omega} = \overline{k}$ (gray solid line).

the two lower lying curves exhibit quasi-acoustic dispersions. Besides the dispersion curves with the exact eigenfrequencies, $\overline{\omega}_j(\overline{k})$, we also show in Fig. 1(c) their corresponding long wavelength approximations with frequencies $\overline{\omega}_j^{\rm appr}(\overline{k})$ for $j = 1, 2, 3$. The highest-lying dispersion is approximated with $\overline{\omega}_3^{\rm appr}(\overline{k})$, which is evaluated by making the assumption that an N-layer MLG may be treated as an SLG with an effective conductivity given by $\overline{\sigma}_N(\overline{\omega}) = N\overline{\sigma}(\overline{\omega})$. This assumption yields a dispersion relation with the approximate eigenfrequency $\overline{\omega}_N^{\rm appr}(\overline{k}) = N\sqrt{2\left(-1+\sqrt{1+\frac{\overline{k}^2}{N^2}}\right)}$, shown for $N = 3$ by the dotted line in Fig. 2.31(c). This relation reproduces well the exact dispersion curve $\overline{\omega} = \overline{\omega}_3(\overline{k})$ for sufficiently long wavelengths, but deviations are already observed for $\overline{k} \gtrsim 2$. On the other hand, the two lower-lying dispersion curves that behave as quasi-acoustic modes at long wavelengths, may be approximated to the leading order in $\overline{k}$ by the eigenfrequencies $\overline{\omega}_2^{\rm appr}(\overline{k}) = \overline{k}\sqrt{4\overline{d}/\left(1+4\overline{d}\right)}$ and $\overline{\omega}_1^{\rm appr}(\overline{k}) = \overline{k}\sqrt{4\overline{d}/\left(3+4\overline{d}\right)}$, which are obtained from Eq. (2.15) in the limit $\overline{k} \to 0$. Similarly to $\overline{\omega}_3^{\rm appr}(\overline{k})$, one notices in Fig. 2.31(c) that the lower-lying approximations $\overline{\omega}_{1,2}^{\rm appr}(\overline{k})$ are quite close to the corresponding exact modes $\overline{\omega}_{1,2}(\overline{k})$ for wavenumbers $\overline{k} \lesssim 1$.

For further reference, it is worthwhile commenting on the behavior of the exact dispersion curves with $\overline{\omega}_j(\overline{k})$ in the range of large $\overline{k}$ values, well beyond those shown in Fig. 2.31(c). In Fig. 2.32 we essentially discuss the dispersion relations $\overline{\omega} = \overline{\omega}_j(\overline{k})$ with $j = 1, 2, 3$ for HDPPs in a TLG with the reduced interlayer distance $\overline{d} = 0.1$, which were shown in Fig. 2.31(c) in the range of wavenumbers and frequencies given by $0 < \overline{k} < 3$ and $0 < \overline{\omega} < 3$. In Fig. 2.32 we show those same dispersion relations as blue solid curves over an extended range, $0 < \overline{k} < 40$ and $0 < \overline{\omega} < 9$, and we label them as "Exact" because they were obtained from the exact eigenvalues of the matrix defining the left-hand side in Eq. (2.15). One can see in Fig. 2.32 that, as the wavenumber increases, the dispersion curves start converging at $\overline{k} \sim 15$ and, for still larger wavenumbers, say $\overline{k} \gtrsim 30$, they approach the dispersion relation of a SLG, shown as a solid yellow line.

We also demonstrate in Fig. 2.32 that, for large enough wavenumbers, the converging dispersion curves are reasonably well approximated by their nonretarded (NR) limits, shown by the dotted green lines, which were obtained by setting $q = \sqrt{k^2 - (\omega/c)^2} \to k$ in the matrix on the left-hand side of Eq. (2.15). Finally, to emphasize a dominant role of the interaction between neighboring graphene layers for increasing wavenumbers, we use the red dashed lines in Fig. 2.32 to show the dispersion curves obtained for the TLG with $\overline{d} = 0.1$ in the nearest-neighbor approximation (NNA), discussed later at the end of this section. One notices that the NNA dispersion curves in Fig. 2.32 present an excellent approximation to the exact dispersion curves for $\overline{k} \gtrsim 20$, as well as that the middle NNA dispersion curve, $\overline{\omega} = \overline{\omega}_2(\overline{k})$, coincides with the dispersion curve for SLG.

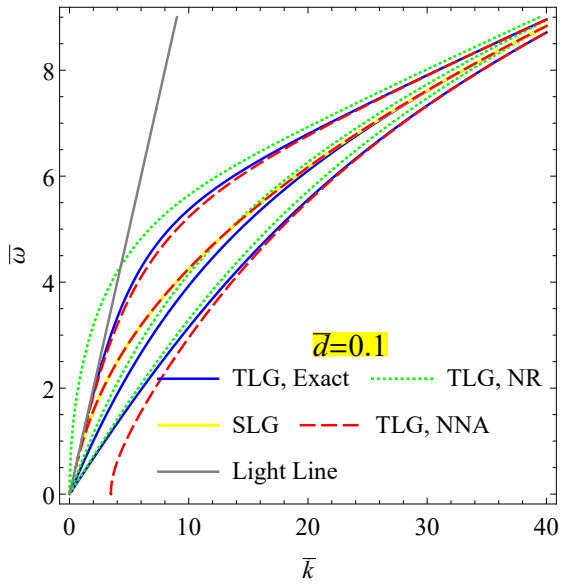

Figure 2.32: Dispersion curves for a three-layer graphene discussed in Fig. 2.31. Results are shown for the exact (solid blue lines), nonretarded (dotted green lines) and the nearest-neighbor-approximation (dashed red lines) solutions of Eq. (2.15), along with the dispersion curve for single-layer graphene (solid yellow line).

In Fig. 2.33, we show a decomposition of the total Ohmic energy loss from Fig. 2.31(a), $\overline{F}_{\rm Ohm}(\overline{k},\overline{\omega}) = \sum_{l=1}^{3} \overline{F}_{{\rm Ohm},l}(\overline{k},\overline{\omega})$, with contributions to the top ($l = 3$, panel a), middle ($l = 2$, panel b), and the bottom ($l = 1$, panel c) graphene layers. In the insets to the panels in Fig. 2.33, we display the cross sections of the corresponding Ohmic energy losses $\overline{F}_{{\rm Ohm},l}(\overline{k},\overline{\omega})$ for $\overline{k} = 0.5$, along with three vertical bars showing the positions of the corresponding HDPP mode frequencies $\overline{\omega}_j(\overline{k})$, evaluated from Fig. 2.31(c) at $\overline{k} = 0.5$ for $j = 1, 2, 3$. It is remarkable that the widths of the peak regions in the spectra $\overline{F}_{{\rm Ohm},l}(\overline{k},\overline{\omega})$ corresponding to the three HDPP dispersions, are differently distributed in different graphene layers. So, for example, in the panel (a) we see that in the top layer ($l = 3$) the widest contribution occurs along the middle dispersion curve $\overline{\omega}_2$, a somewhat narrower contribution occurs along the highest dispersion curve $\overline{\omega}_3$, and the narrowest contribution occurs along the lowest lying dispersion curve $\overline{\omega}_1$. A similar distribution of widths is seen in the panel (c) for the bottom layer ($l = 1$), with two important differences: the contribution in the region above the light line is more abundant than in the top layer for small $\overline{\omega}$ and $\overline{k}$ values and, more interestingly, there exists a *dip* near the position of the dispersion curve $\overline{\omega} = \overline{\omega}_1(k)$, which is clearly discernible on the nearby diffuse background for small $\overline{\omega}$ and $\overline{k}$ values below the light line. A closer inspection of that dip in the inset to the panel (c) shows that the contribution of the lowest lying HDPP mode to Ohmic energy losses in the bottom graphene layer has the characteristics of a Fano resonance [109, 117, 126]. This may be tentatively explained by an assertion that the resonance due to the HDPP mode with $\overline{\omega}_2$ is broad enough and the resonance due to the HDPP mode with $\overline{\omega}_1$ narrow enough, so that destructive interferences between them cause diminishing Ohmic losses at frequencies $\overline{\omega}_1(\overline{k}) \lesssim \overline{\omega} < \overline{\omega}_2(\overline{k})$ in the bottom graphene layer. It should also be noticed in the panel (c) that the strongly asymmetric shape of the Fano resonance near $\overline{\omega} = \overline{\omega}_1(\overline{k})$ in the bottom layer effectively pushes the contribution of the Ohmic loss in that layer towards somewhat lower frequencies than $\overline{\omega}_1$ when compared to the regions below the broadened resonances along the dispersion $\overline{\omega} = \overline{\omega}_1(\overline{k})$ in the middle and top layers. On the other hand, the reason for the lack of a Fano shape in the top graphene layer, as observed in the inset to the panel (a), is not obvious, but may be guessed to be due to insufficient difference between the widths of resonances corresponding to the HDPP modes with $\overline{\omega}_1$ and $\overline{\omega}_2$ in that layer. In any case, those two differences between the Ohmic energy loss distributions in the top and bottom layers signal an asymmetry with respect to the order in which graphene layers are traversed by the external charged particle, pointing to the retardation effects as their common cause.

However, the most striking behavior of the three HDPP modes is observed in the panel (b) of Fig. 2.33 for the middle graphene layer ($l = 2$), where the Ohmic energy loss in the region corresponding to the mode with the middle dispersion curve $\overline{\omega}_2$ is completely missing, whereas the widths of the resonant modes with $\overline{\omega}_1$ and $\overline{\omega}_3$ are similar to the corresponding widths in the top layer in the panel (a). This may be tentatively explained by the nature of charge carrier oscil-

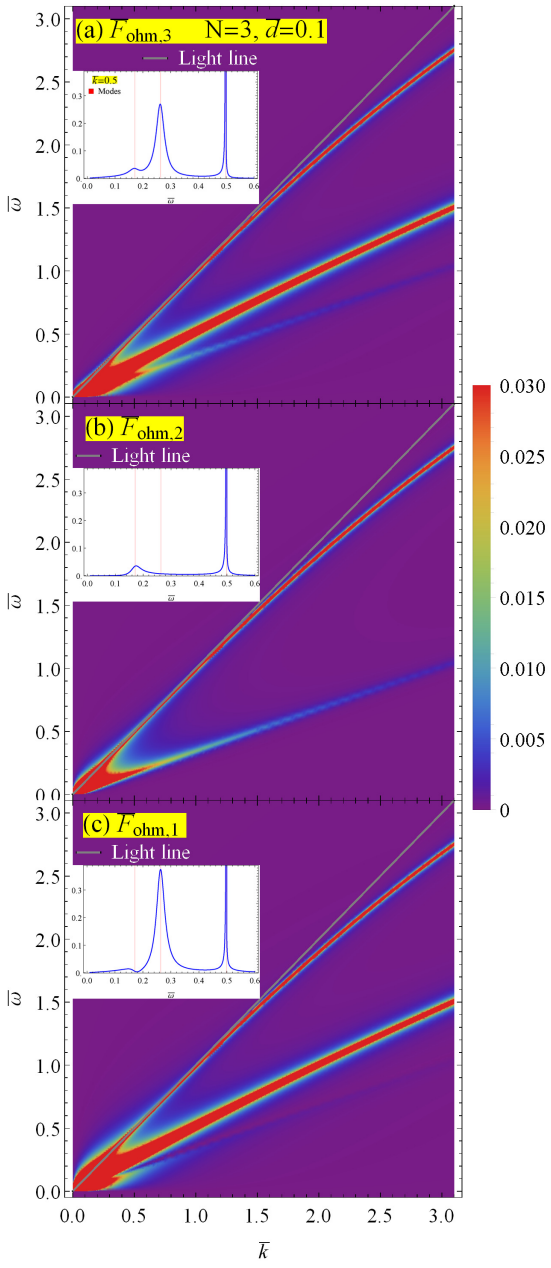

Figure 2.33: A decomposition of the Ohmic energy loss, $\overline{F}_{\mathrm{Ohm},l}(\overline{k},\overline{\omega}) = F_{\mathrm{Ohm},l}(\overline{k},\overline{\omega})/F_c$, is displayed in reduced units with $F_c = 4(Ze)^2/(\pi\omega_c^2 k_c)$, as a function of the reduced wavenumber $\overline{k} = k/k_c$ and the reduced frequency $\overline{\omega} = \omega/\omega_c$, for a three-layer graphene with reduced interlayer distance $\overline{d} = k_c d = 0.1$. Contributions to the top ($l = 3$), middle ($l = 2$), and bottom ($l = 1$) layers are shown in the panels (a), (b) and (c), respectively. The insets display the corresponding cross-sections of $\overline{F}_{\mathrm{Ohm},l}(\overline{k},\overline{\omega})$ for $\overline{k} = 0.5$, with the red vertical bars showing the values of the hybridized Dirac plasmon polariton eigenfrequencies, $\overline{\omega}_j(\overline{k})$ for $j = 1, 2, 3$, evaluated from Fig. 2.31(c) at $\overline{k} = 0.5$.

lations in the three graphene layers, which give rise to the HDPP modes with eigenfrequencies $\overline{\omega}_1$, $\overline{\omega}_2$ and $\overline{\omega}_3$ (see, e.g., Fig. S1(b) in Ref. [106]). Namely, the mode with the highest-lying $\overline{\omega}_3$ is characterized by an in-phase oscillations of charges in all three layers, whereas the mode with the lowest-lying $\overline{\omega}_1$ is characterized by an in-phase oscillations of charges in the outer layers and the out-of-phase oscillations of charges in the middle layer. On the other hand, the mode with the middle eigenfrequency $\overline{\omega}_2$ is characterized by the out-of-phase oscillations of charges in the outer layers, whereas the charges in the middle layer oscillate in phase with charges in either the upper or in the lower graphene layer. Owing to this double-degeneracy of charge configurations at the middle eigenfrequency in a symmetric structure of equally spaced and equally doped graphene layers in a TLG, one may surmise that, on average, there is no charge carrier polarization in the middle layer for the HDPP mode with $\overline{\omega}_2$.

In Fig. 2.34, we show the angular distributions of the spectral density for TR in reduced units, $\overline{\mathcal{S}}(\theta,\overline{\omega}) = \mathcal{S}/S_c$ with $\mathcal{S}_c = (Ze)^2/c$, for a TLG system with (a) $\overline{d} = 0.1$ and (b) $\overline{d} = 1$. One notices in the panel (a) that the angular patterns in the upper and lower half-spaces are largely similar in shape, but slight asymmetry starts appearing for frequencies $\overline{\omega} \gtrsim 1$. On the other hand, one sees in the panel (b) that an increase of the interlayer separation to $\overline{d} = 1$ gives rise to an asymmetry between the angular patterns emitted in the upper and lower half-spaces already for $\overline{\omega} \gtrsim 0.1$, which becomes quite strong with increasing frequency. A similar effect was observed for a DLG in in Subsection 2.3.1, albeit for somewhat larger interlayer separations. One may surmise that, for the MLG systems, which may not be considered optically thin, as is likely the case in Fig. 3(b), there are strong interferences in the TR emission patterns due to retardation effects. These interferences can be ascribed to products of the oscillatory factors $\exp\left[\mp i\kappa\left(z_l - z_{l'}\right)\right]$ and $\exp\left[\mp i\frac{\omega}{v}\left(z_l - z_{l'}\right)\right]$ in Eq. (2.31), which give rise to the observed asymmetry in the radiation energy loss for increasing $\overline{\omega}\overline{d}$ values.

Figure 2.35 shows several integrated probability densities in reduced units, $\overline{P}(\overline{\omega}) = P/P_c$ with $P_c = \frac{4}{\pi}\frac{1}{\varepsilon_F}$, for a TLG system with (a) $\overline{d} = 0.1$ (studied in Fig. 2.31) and (b) $\overline{d} = 1$. In addition to the total Ohmic energy loss and the total radiation energy loss, we show their decompositions into the contributions to different graphene layers, $\overline{P}_{\rm Ohm} = \sum_{l=1}^{3} \overline{P}_{{\rm Ohm},l}$, and contributions to the upper and lower half-spaces, $\overline{P}_{\rm rad} = \overline{P}^{\uparrow}_{\rm rad} + \overline{P}^{\downarrow}_{\rm rad}$, respectively. We also display a result for the total energy loss of the external charged particle evaluated from the definition in Eq. (2.25), showing the conservation of energy in the form $\overline{P}_{\rm ext}(\overline{\omega}) = \overline{P}_{\rm Ohm}(\overline{\omega}) + \overline{P}_{\rm rad}(\overline{\omega})$.

One notices in the panel (a) of Fig. 2.35 that the radiation contributions to the upper and lower half-spaces, $\overline{P}^{\uparrow}_{\rm rad}$ and $\overline{P}^{\downarrow}_{\rm rad}$, are practically identical for $\overline{d} = 0.1$ at all frequencies, which is not surprising given the similarity of the angular patterns in Fig. 2.34(a). On the other hand, the two radiation contributions in the panel (b) of Fig. 2.35 are quite close to each other, with somewhat higher values of the radiation emitted in the upper than in the lower half-space, $\overline{P}^{\uparrow}_{\rm rad} > \overline{P}^{\downarrow}_{\rm rad}$ for

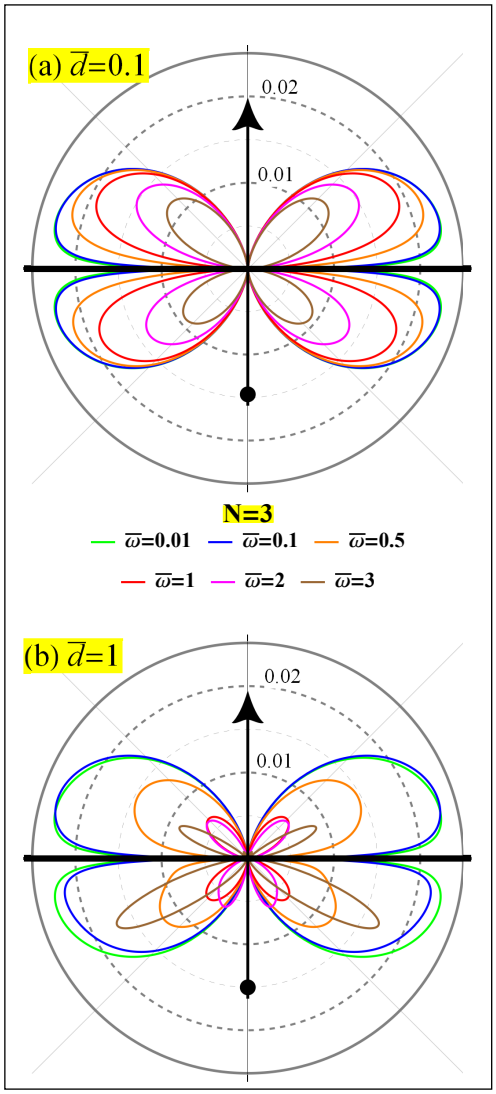

Figure 2.34: Angular distribution of the spectral density for transition radiation, $\overline{\mathcal{S}}(\theta, \overline{\omega}) = \mathcal{S}/S_c$, shown in reduced units with $\mathcal{S}_c = (Ze)^2/c$, for a three-layer graphene with reduced interlayer distances: (a) $\overline{d} = 0.1$ and (b) $\overline{d} = 1$, for several values of the reduced frequency $\overline{\omega}$.

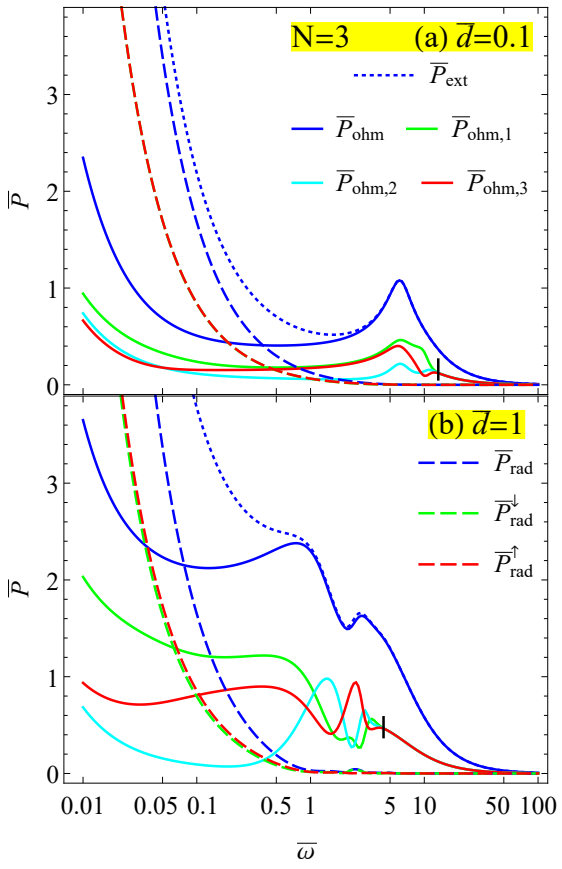

Figure 2.35: Integrated probability density, $\overline{P}(\overline{\omega}) = P(\overline{\omega})/P_c$, shown in reduced units with $P_c = \frac{4}{\pi}\frac{1}{\varepsilon_F}$, for a three-layer graphene with reduced interlayer distances: (a) $\overline{d} = 0.1$ and (b) $\overline{d} = 1$. In addition to the total Ohmic energy loss, $\overline{P}_{\rm Ohm}(\overline{\omega})$ (blue solid lines), and the total radiation energy loss, $\overline{P}_{\rm rad}(\overline{\omega})$ (blue dashed lines), we show their decompositions into different graphene layers, $\overline{P}_{{\rm Ohm},l}(\overline{\omega})$ with $l = 1, 2, 3$ for the bottom, middle and top layers (solid lines), and radiation emitted in the upper/lower half-spaces, $\overline{P}^{\uparrow,\downarrow}_{\rm rad}(\overline{\omega})$ (dashed lines), respectively. Also shown by dotted blue lines is the total energy loss of the external charged particle from Eq. (2.25), confirming the conservation of energy as $\overline{P}_{\rm ext}(\overline{\omega}) = \overline{P}_{\rm Ohm}(\overline{\omega}) + \overline{P}_{\rm rad}(\overline{\omega})$. The black vertical bars at (a) $\overline{\omega} = 13.3$ and (b) $\overline{\omega} = 4.2$ indicate frequencies below which $\overline{P}_{{\rm Ohm},l}(\overline{\omega})$ exhibit large differences.

$\overline{\omega} < 1$. However, it is surprising that, for the case of a TLG with $\overline{d} = 1$, which is not optically thin, the strong asymmetry between the angular patterns observed in Fig. 2.34(b) at frequencies $\overline{\omega} > 1$, does not give rise to any detectable asymmetry between $\overline{P}^{\uparrow}_{\rm rad}$ and $\overline{P}^{\downarrow}_{\rm rad}$ in Fig. 2.35(b) in the same range of frequencies, except for a small "bump" at $\overline{\omega} \approx 2.5$. It should be noted, however, that the radiation energy losses are heavily suppressed for frequencies $\overline{\omega} > 1$ in Fig. 2.35, but they give a dominant contribution to the total energy losses of the external charged particle at frequencies $\overline{\omega} < 0.5$ and $\overline{\omega} < 0.1$ in the panels (a) and (b), respectively. It is remarkable that the radiation energy losses at those frequencies show no significant differences when the interlayer distance changes from $\overline{d} = 0.1$ to $\overline{d} = 1$ in going from the panel (a) to panel (b) in Fig. 2.35. This may be rationalized by asserting that only charge carrier oscillations in the *outer* graphene layers give rise to the emission of electromagnetic energy in the far-field regions, whereas the integration over the angles in Eq. (2.37) causes a massive cancelation in the Poynting vector for radiative components of the electromagnetic fields due to destructive interferences in the regions between graphene layers.

In view of the above discussed similarity between the radiation contributions $\overline{P}^{\uparrow}_{\rm rad}$ and $\overline{P}^{\downarrow}_{\rm rad}$, it is remarkable that in Fig. 2.35 the layer contributions to the total Ohmic energy loss, $\overline{P}_{{\rm Ohm},l}(\overline{\omega})$, show large differences at frequencies $\overline{\omega} < 13.3$ and $\overline{\omega} < 4.2$ in the panels (a) and (b), respectively. We suggest that, in the case of a TLG with the interlayer separation $\overline{d} = 0.1$, differences seen in Fig. 2.35(a) at $\overline{\omega} \lesssim 3$ may be related to different distributions of the weights for the three HDPP modes in the joint distributions $\overline{F}_{{\rm Ohm},l}(\overline{k}, \overline{\omega})$ for each graphene layer, as implied by different widths of those modes in the panels (a-c) of the Fig. 2.33. Namely, the largest difference among those distributions is that $\overline{F}_{{\rm Ohm},2}(\overline{k}, \overline{\omega})$ for the middle graphene layer is missing a contribution from the HDPP mode with the middle dispersion $\overline{\omega}_2$, whereas that mode makes the largest contribution to the Ohmic losses in the bottom and the top graphene layers. Accordingly, one sees in Fig. 2.35(a) that the integrated Ohmic losses in the outer layers, $\overline{P}_{{\rm Ohm},1}(\overline{\omega})$ and $\overline{P}_{{\rm Ohm},3}(\overline{\omega})$, have similar values for $0.5 \lesssim \overline{\omega} \lesssim 3$, which exceed the value of the integrated Ohmic loss in the middle layer, $\overline{P}_{{\rm Ohm},2}(\overline{\omega})$. On the other hand, at frequencies $\overline{\omega} < 0.1$, one observes that $\overline{P}_{{\rm Ohm},2}(\overline{\omega})$ and $\overline{P}_{{\rm Ohm},3}(\overline{\omega})$ take similar values for the middle and top graphene layers, which are mostly determined by the resonant contributions of the HDPP with the lowest lying dispersion, $\overline{\omega}_1$. Those values are seen to be smaller than the value of $\overline{P}_{{\rm Ohm},1}(\overline{\omega})$ at frequencies $\overline{\omega} < 0.1$, which may be tentatively ascribed to increased contribution to the Ohmic energy loss at frequencies lower than $\overline{\omega}_1$ due to the strongly asymmetric Fano resonance near $\overline{\omega} = \overline{\omega}_1(\overline{k})$ for the bottom layer, as displayed in the inset to Fig. 2.33(c).

In the panel (a) of Fig. 2.35, one notices that the integrated Ohmic energy losses $\overline{P}_{{\rm Ohm},l}(\overline{\omega})$ exhibit peculiar and rather different structures in the frequency range $3 \lesssim \overline{\omega} \lesssim 13$. It is interesting that a superposition of those structures gives rise to a well defined and broad peak at $\overline{\omega} \approx 8$ in the total integrated Ohmic energy loss distribution $\overline{P}_{\rm Ohm}(\overline{\omega})$. When the interlayer separation is

increased to $\overline{d} = 1$ in the panel (b), those structures become even more complex and they move to a lower frequency range of $0.5 \lesssim \overline{\omega} \lesssim 5$. In that case, the total integrated Ohmic energy loss distribution exhibits two peaks at $\overline{\omega} \approx 1$ and $\overline{\omega} \approx 3$. This behavior of the layer decomposition and the total Ohmic energy loss distributions for the TLG is surprisingly similar to the behavior of those distributions for a DLG with the same interlayer separations, discussed in Fig. 2.9. We shall demonstrate below that this similarity is not coincidental, but is rather universal for MLG with $N > 2$ in a regime of intermediate optical thickness. Namely, we argue that the DPP hybridization in such MLG is governed mostly by the electromagnetic interaction between the *nearest-neighbor* graphene layers, which should be similar to the hybridization taking place in a DLG. This assertion is further tested in Figures 2.32 and 2.37. In that respect, it is worthwhile mentioning that an analysis of the modal decomposition of the total energy losses in a DLG showed that single- and double-peak structures in $\overline{P}_{\rm Ohm}(\overline{\omega})$ result from an onset of interference in the excitation of the two HDPP modes at frequencies $\overline{\omega} \sim \pi\beta/\overline{d}$ (see Fig. 2.10). We suggest that a similar mechanism may be responsible for the single- and double-peak structures observed in $\overline{P}_{\rm Ohm}(\overline{\omega})$ for the TLG in the panels (a) and (b) of Fig. 2.35.

From the features seen in the distributions in Figs. 2.34 and 2.35, one may conclude that large qualitative differences may arise when the interlayer distance increases from a sufficiently small value for which the MLG may be considered as optically thin, at least in a range of small frequencies, to a large value, $\overline{d} \sim 1$, for which the retardation effects should be strong. Therefore, we next explore the effect of increasing the number of graphene layers and analyze changes in the integrated energy loss spectra as we decrease the interlayer distance further into the regime of optically thin MLG. So, in Fig. 2.36 we show the total Ohmic loss, $\overline{P}^{(N)}_{\rm Ohm}(\overline{\omega})$, and the total radiation loss, $\overline{P}^{(N)}_{\rm rad}(\overline{\omega})$, for $N = 1, 2, 3, 4$ and 5 graphene layers and for $\overline{d} = 0.001, 0.01, 0.1$ and 1. Also shown (by dotted lines) are the results for the integrated Ohmic energy loss in an SLG, $\overline{P}^{\rm SLG}_{\rm Ohm}[\overline{\sigma}_N(\overline{\omega}), \overline{\omega}]$, where the effective conductivity is given by $\overline{\sigma}_N(\overline{\omega}) = N\overline{\sigma}(\overline{\omega})$, with $\overline{\sigma}(\overline{\omega})$ given by the Drude model in Eq. (2.39). Those results are expected to provide a good approximation for $\overline{P}^{(N)}_{\rm Ohm}(\overline{\omega})$ in an optically thin N-layer graphene structure [100, 105, 107].

In order to quantify the criterion for an optically thin MLG regarding the Ohmic loss, we note that the approximation $\sigma_N \approx N\sigma$ follows from Eq. (2.15) when all the exponential factors can be replaced by unity, i.e., when $(N-1)\overline{q}\overline{d} \ll 1$. In order to estimate relevant values of the factor $\overline{q} = \sqrt{\overline{k}^2 - \overline{\omega}^2}$, we may temporarily neglect the role of damping and use the approximate expressions for the HDPP dispersion relations obtained from the approximation $\sigma_N \approx N\sigma$ itself. Thus, for the highest lying mode, using $\overline{\omega} \approx \overline{\omega}^{\rm appr}_N(\overline{k})$ gives a criterion for an optically thin MLG in the form $\overline{\omega} \ll \sqrt{2/\overline{d}}$, independent of N. A rough estimate of the same criterion for lower-lying, quasi-acoustic dispersion relations may be obtained, at least for sufficiently thin MLG, such

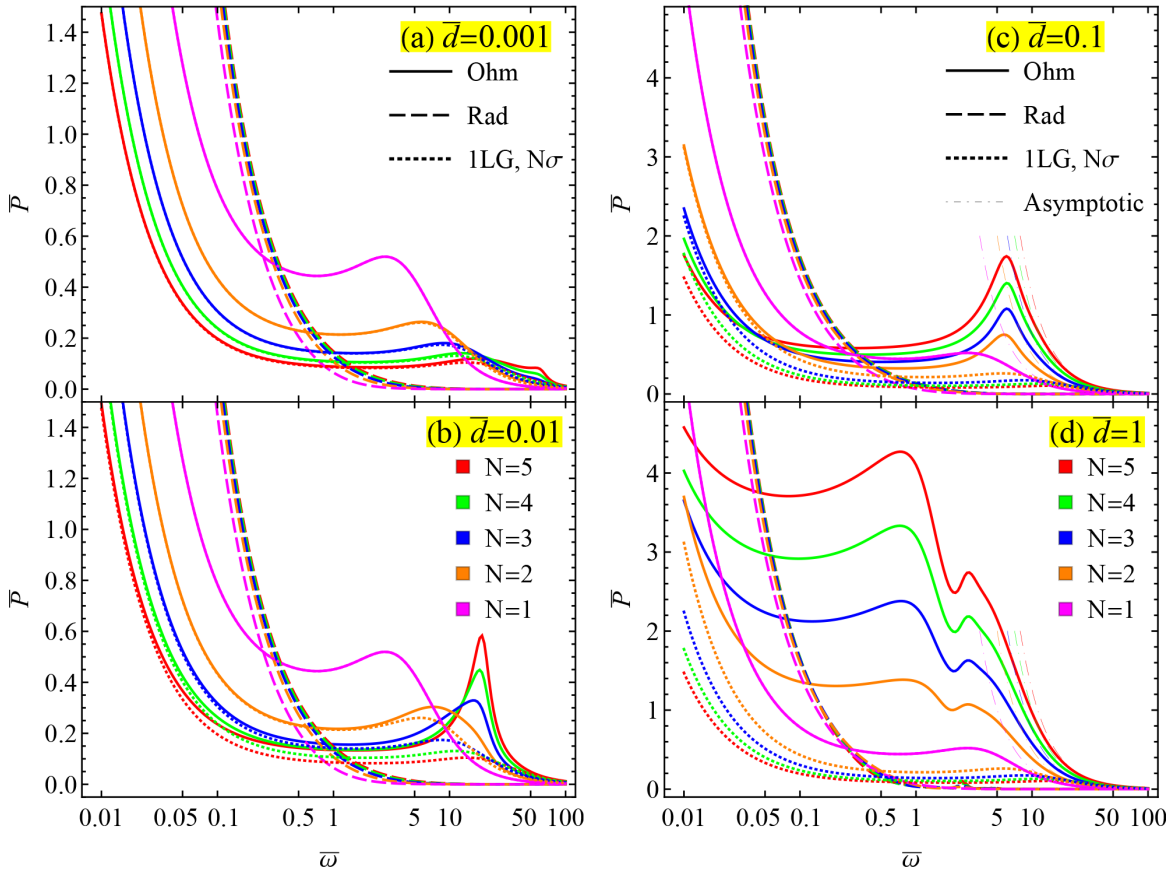

Figure 2.36: The total integrated Ohmic energy loss, $\overline{P}^{(N)}_{\rm Ohm}(\overline{\omega})$ (solid lines), and the total radiation loss, $\overline{P}^{(N)}_{\rm rad}(\overline{\omega})$ (dashed lines), both normalized with $P_c = \frac{4}{\pi}\frac{1}{\varepsilon_F}$, are shown for multilayer structures with $N = 1, 2, 3, 4$ and 5 graphene layers, having several interlayer distances: (a) $\overline{d} = 0.001$, (b) 0.01, (c) 0.1 and (d) 1. Also shown (by dotted lines) is the integrated Ohmic energy loss in a single-layer graphene, $\overline{P}^{\rm SLG}_{\rm Ohm}[\overline{\sigma}_N, \overline{\omega}]$, evaluated with an effective conductivity $\overline{\sigma}_N = N\overline{\sigma}$ for $N = 1, 2, 3, 4$ and 5 with $\overline{\sigma}$ given in Eq. (2.39). The thin dash-dotted lines show the high-frequency asymptotics of the total integrated Ohmic energy loss, $\overline{P}^{(N)}_{\rm Ohm}(\overline{\omega}) \sim 2\pi N/\left(\beta\overline{\omega}\right)^2$, with $\beta = v/c = 0.5$.

that $\overline{d} \ll 1$. With that assumption, an expansion of the exponential factors in Eq. (2.15) to the leading order in $\overline{d}$ gives $\overline{\omega}_j \sim \phi_j \sqrt{\overline{d}}\, \overline{k}$ in the limit of long wavelengths, where ϕ_j is a numerical factor of order one for all $j = 1, 2, \ldots N-1$. Thus, replacing $\overline{k} \sim \overline{\omega}/\sqrt{\overline{d}}$ in $(N-1)\overline{q}\overline{d} \ll 1$ gives a criterion for optically thin MLG in the form $\overline{\omega} \ll 1/\left(N\sqrt{\overline{d}}\right)$. Accordingly, one notices in Fig. 2.36(a) that the distribution $\overline{P}^{\mathrm{SLG}}_{\mathrm{Ohm}}[N\overline{\sigma}(\overline{\omega}), \overline{\omega}]$ provides a very good approximation to $\overline{P}^{(N)}_{\mathrm{Ohm}}(\overline{\omega})$ at frequencies $\overline{\omega} \lesssim 10$ for all N values. This seems to be consistent with the criterion $\overline{\omega} \ll \sqrt{2/\overline{d}}$, showing that the HDPP mode with the highest-lying eigenfrequency likely dominates in the case of the thinnest MLG with $\overline{d} = 0.001$ studied in Fig. 5(a). We remark that the corresponding physical distance of $d = 48$ nm is commensurate with the interlayer distances used in experiments [100, 105]. However, a gradual deterioration of the approximation $\overline{P}^{(N)}_{\mathrm{Ohm}}(\overline{\omega}) \approx \overline{P}^{\mathrm{SLG}}_{\mathrm{Ohm}}[N\overline{\sigma}(\overline{\omega}), \overline{\omega}]$ is observed in the panels (b) and (c) of Fig. 2.36 for frequencies above some critical value, which decreases when both $\overline{d}$ and N increase. This seems to be consistent with the criterion $\overline{\omega} \ll 1/\left(N\sqrt{\overline{d}}\right)$, indicating an increasing role of the $N-1$ quasi-acoustic HDPP modes with increasing interlayer distance, which start affecting the Ohmic energy loss at shorter wavelengths and hence higher frequencies.

A close inspection of the low-frequency dependence of the $\overline{P}^{(N)}_{\mathrm{Ohm}}(\overline{\omega})$ distributions in Figs. 2.36(a,b) shows that the integrated Ohmic energy loss decreases in an inverse proportion to N for frequencies $\overline{\omega} \lesssim \overline{\gamma} = 0.05$ for optically thin MLG. The reason for this behavior is not immediately obvious, but it may be conjectured by recalling that the Ohmic energy loss at low frequencies is dominated by dissipative processes in graphene (see Ref. [42] and Subsection 2.3.1). Namely, the dc resistivity of a SLG may be represented, in reduced units, as $\overline{\rho} = 1/\overline{\sigma}(0) = \pi\overline{\gamma}$, so that the dissipative processes in an optically thin MLG with N graphene layers may be represented by a *parallel* connection of N resistors with the effective resistivity given by $\overline{\rho}_N \approx \overline{\rho}/N = \pi\overline{\gamma}/N$. This argument may be made more quantitative by considering the analytical result for $\overline{P}^{\mathrm{SLG}}_{\mathrm{Ohm}}[N\overline{\sigma}(\overline{\omega}), \overline{\omega}]$ for SLG obtained in Ref. [42], which we have used in this work to calculate the dotted curves in Fig. 5 with $\overline{\sigma}(\overline{\omega})$ given by the Drude model with finite damping rate $\overline{\gamma}$ in Eq. (2.39). Since $\overline{P}^{(N)}_{\mathrm{Ohm}}(\overline{\omega}) \approx \overline{P}^{\mathrm{SLG}}_{\mathrm{Ohm}}[N\overline{\sigma}(\overline{\omega}), \overline{\omega}]$ to a very good approximation at low frequencies in Figs. 2.36(a,b), an analysis of the $\overline{\omega} \to 0$ behavior of $\overline{P}^{\mathrm{SLG}}_{\mathrm{Ohm}}[N\overline{\sigma}(\overline{\omega}), \overline{\omega}]$ shows that

$$\overline{P}^{(N)}_{\mathrm{Ohm}}(\overline{\omega}) \sim \frac{\beta^2}{4N}\frac{\overline{\gamma}}{\overline{\omega}}\left[4\ln\left(\frac{2N}{\beta\overline{\gamma}}\right) + \beta^{-2} - 4 - \ln\left(\beta^{-2} - 1\right)\right], \tag{2.62}$$

to the leading order in $\overline{\gamma}$. This result exposes the predominantly $1/N$ dependence of the integrated Ohmic energy loss at frequencies $\overline{\omega} \lesssim \overline{\gamma} = 0.05$ for optically thin MLG.

Turning our attention to the regime of higher frequencies and larger $\overline{d}$ values, we recall from

Fig. 2.35 that interferences among the HDPP modes give rise to the peak structures in the Ohmic energy loss spectra for $N = 3$ with $\overline{d} = 0.1$ and 1 in a regime that may be considered as intermediate between optically thin and optically thick TLGs. Considering the MLG in Fig. 2.36, peak structures are barely visible at high frequencies for $\overline{d} = 0.001$ in the panel (a), whereas they seem to gradually increase in magnitude with increasing $\overline{d}$ and N values, as seen in the panels (b-d) of that figure. Specifically, single-peak structures appear for $N \geq 2$ in the range $10 \lesssim \overline{\omega} \lesssim 20$ for $\overline{d} = 0.01$ in the panel (b) and at $\overline{\omega} \approx 8$ for $\overline{d} = 0.1$ in the panel (c), whereas a double-peak structure appears at $\overline{\omega} \approx 1$ and $\overline{\omega} \approx 3$ for $\overline{d} = 1$ in the panel (d). While the peak position in the panel (b) increases in the interval $10 \lesssim \overline{\omega} \lesssim 20$ with increasing N values, it is remarkable that the peak structures in the panels (c) and (d) exhibit both the shape *and* position, which are rather independent from the number of layers for $N \geq 2$. This may be qualitatively explained by an argument that, for thicker MLG with $\overline{d} = 0.1$ and $\overline{d} = 1$, the interferences giving rise to the peak structures are mainly governed by the distance between *neighboring* graphene layers, so that the effect of increasing N is merely to increase the magnitude of the peaks. More specifically, it seems that the peaks in the panels (c) and (d) for $N > 2$ are replicas of the peak structure of a DLG, with their magnitudes that scale with the number of layers N. (These notions are further tested later using a nearest-neighbor approximation in solving Eq. (2.15) to generate the curves in Fig. 2.37.)

Such scaling of the total Ohmic energy loss with N at high frequencies may be deduced by considering the limit of an optically thick MLG consisting of N *independent* graphene layers, which formally arises when the exponential factors in Eq. (2.15) may be set to zero, i.e., when $\overline{q}\overline{d} \gg 1$ for sufficiently short wavelengths. Given that in this limit the dispersion relations of all N HDPP modes in an MLG approach the dispersion of a SLG, as shown in Fig. 2.32, one may use the nonretarded form of the SLG dispersion, $\overline{\omega} = \sqrt{2\overline{k}}$, to obtain a criterion for an optically thick MLG as $\overline{\omega} \gg \sqrt{2/\overline{d}}$. Because in that regime we may write $\overline{P}^{(N)}_{\mathrm{Ohm},l}(\overline{\omega}) \approx \overline{P}^{\mathrm{SLG}}_{\mathrm{Ohm}}[\overline{\sigma}(\overline{\omega}), \overline{\omega}]$ for each graphene layer with the conductivity $\overline{\sigma}(\overline{\omega})$ given in Eq. (2.39), the total integrated Ohmic energy loss in an MLG becomes $\overline{P}^{(N)}_{\mathrm{Ohm}}(\overline{\omega}) \approx N\overline{P}^{\mathrm{SLG}}_{\mathrm{Ohm}}[\overline{\sigma}(\overline{\omega}), \overline{\omega}]$ for $\overline{\omega} \gg \sqrt{2/\overline{d}}$. Using the analytical result for $\overline{P}^{\mathrm{SLG}}_{\mathrm{Ohm}}[\overline{\sigma}(\overline{\omega}), \overline{\omega}]$ obtained in Ref. [42] for SLG in the limit of zero damping, we can easily deduce that the asymptotic behavior of the total Ohmic energy loss in an optically thick MLG with $N > 1$ at large frequencies has the form given by $\overline{P}^{(N)}_{\mathrm{Ohm}}(\overline{\omega}) \sim 2\pi N / (\beta\overline{\omega})^2$, which is indicated by the thin dash-dotted curves in Figs. 2.36(c,d).

Finally, it is remarkable to observe in Fig. 2.36 that the total integrated radiation energy loss $\overline{P}^{(N)}_{\mathrm{rad}}(\overline{\omega})$ in an MLG with N layers is largely independent of the interlayer distance and is only weakly increasing with increasing N at sub-THz frequencies. As in Fig. 2.35, this may be explained by the fact that only the charge carrier oscillations in the outer layers give rise

to the radiation emitted in the far-field region, whereas the energy flux due to radiating fields experiences destructive interference in the regions between graphene layers within an MLG.

Nearest-neighbor approximation. The NNA is achieved by retaining only the $l' = l \pm 1$ terms in the summation in Eq. (2.15), which is written for a general MLG. This approximation is justified whenever the distance between the lth graphene layer and its nearest neighbor(s) with $l' = l \pm 1$ is such that the inequality $\exp(-q|z_l - z'_l|) \ll 1$ holds, with $q > 0$ given by its fully retarded form. Applying the NNA to the case of a MLG with $N > 1$ layers having equal conductivities σ and equal interlayer distances d, one can easily obtain approximate eigenvalues, λ_j, of the matrix on the left-hand side in Eq. (2.15) as [127]

$$\lambda_j = 1 + \frac{2\pi i}{\omega} q\,\sigma \left[1 + 2\,\mathrm{e}^{-qd} \cos\left(\frac{j\pi}{N+1}\right)\right], \quad \text{with} \quad j = 1, 2, \ldots, N. \tag{2.63}$$

Then, an approximation to the eigenfrequencies $\omega_j(k)$ is obtained within the NNA by solving the equations $\lambda_j(k,\omega) = 0$ for $j = 1, 2, \ldots, N$. We note that for $N = 2$, Eq. (2.63) gives exact results for the dispersion relations in a DLG with $\cos\left(\frac{j\pi}{3}\right) = \pm 1/2$ for $j = 1, 2$ (Eq. (2.48) with $\sigma_1 = \sigma_2 = \sigma$), whereas for increasing N values, the boundedness of the $\cos\left(\frac{j\pi}{N+1}\right)$ factor in that equation indicates the emergence of a well-defined plasmon band in the (k, ω) plane [33].

In order to further demonstrate the utility of the NNA, we show in Fig. 2.37 the total integrated Ohmic energy loss, $P_{\mathrm{Ohm}}(\omega)$, in MLG with $N = 2, 3, 4$ and 5 layers for two reduced interlayer distances, $\overline{d} = 0.1$ and $\overline{d} = 1$, corresponding to the cases discussed in Figs. 2.36(c) and (d). Besides the results obtained by using the exact solution of Eq. (2.15), which are shown in Fig. 2.37 by solid lines that reproduce the solid lines from Figs. 2.36(c) and (d), we also use dashed lines in Fig. 2.37 to show the results for $P_{\mathrm{Ohm}}(\omega)$ obtained by using the solution of Eq. (2.15) with the matrix on the left-hand side of that equation expressed in the NNA. One sees in Fig. 2.37 that the NNA curves agree very well with the exact curves for $\overline{\omega} \gtrsim 5$ and $\overline{\omega} \gtrsim 1$ at the interlayer distances $\overline{d} = 0.1$ and $\overline{d} = 1$, shown in the panels (a) and (b), respectively. Moreover, the shapes of the peak structures seen in those frequency ranges appear remarkably independent of the number of graphene layers N, which may be related to the emergence of a plasmonic band with well-defined boundaries for increasing N values [33].

These observations confirm our assertion that the peak structures seen in $P_{\mathrm{Ohm}}(\omega)$ for MLG with $N > 2$ in the panels (c) and (d) of Fig. 2.36 appear as replicas of the peak structure for a DLG because of the prevalence of hybridization between the plasmon modes in *neighboring* layers for increasing interlayer distances and/or increasing frequencies.

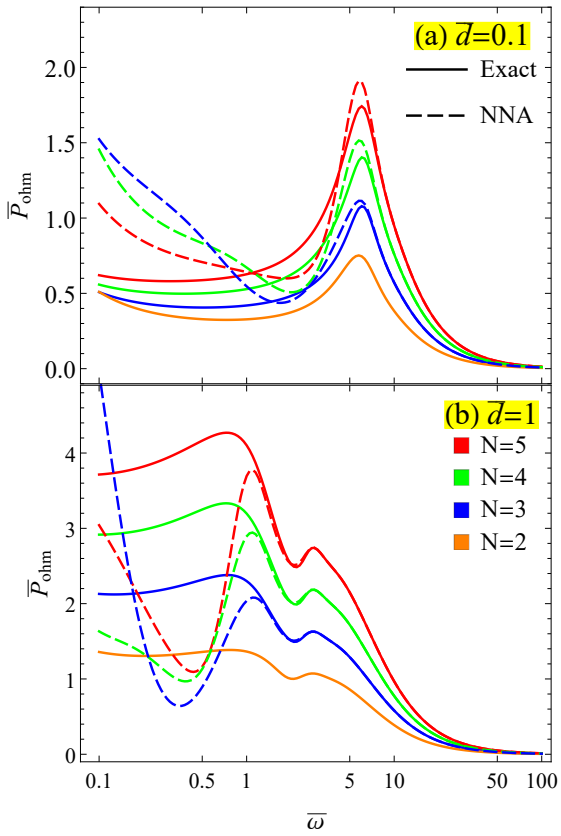

Figure 2.37: The total integrated Ohmic energy loss density, normalized as $\overline{P}_{\rm Ohm} = P_{\rm Ohm}/P_c$, corresponding to the cases discussed in Figs. 2.36(c) and (d), but shown here over different ranges on the axes. Results are shown for the exact (solid lines) and the nearest-neighbor-approximation (dashed lines) solutions of Eq. (2.15).

2.4 Concluding remarks

In this chapter, we have presented a fully relativistic treatment of energy losses and transition radiation from multilayer graphene (MLG) with N layers traversed by an electron at a speed typical for scanning transmission electron microscope (STEM). Our model uses standard definitions, which demonstrate that probability density of the total energy loss of an external charged particle is given by a sum of the probability densities for Ohmic losses in graphene layers and the energy emitted in the far-field region as transition radiation (TR). In particular, Ohmic losses are dominated by excitations of the hybridized Dirac plasmon polariton (HDPP) modes at frequencies located outside the light cone, and are accompanied by release of the Joule heat in the presence of finite damping rates in graphene, taking place at frequencies located both outside and inside the light cone. Adopting the Drude model for the conductivity of graphene we have concentrated on a terahertz (THz) range of frequencies and analyzed , first, the case of two graphene layers (DLG), $N = 2$, and, then, the case of MLG with $N > 2$.

Our main interest in the study of the DLG structure was to reveal the effects of interlayer distance d and the difference in doping densities of charge carriers in those layers, n_1 and n_2, as the two parameters that are most relevant for the design of graphene-based nano-photonic and nano-plasmonic devices. For this structure, strong hybridization takes place between the DPPs in individual graphene layers, giving rise to a low-frequency, quasi-acoustic mode designated as bonding mode, and a high-frequency, quasi-optical mode designated as antibonding mode. As a result, Ohmic losses are dominated by excitations of the bonding and antibonding modes for $0 < \omega < ck$, and subsequent Joule heat due to finite damping rates in graphene for $\omega > 0$.

We have seen that the effects of retardation are quantitatively relevant for frequencies $\lesssim 10$ THz for typical doping densities of graphene. Moreover, the total energy loss of the external particle is completely determined by the Ohmic losses for frequencies $\gtrsim 1$ THz, whereas radiation losses are comparable to the Ohmic losses around ~ 1 THz, and they become dominant in a sub-THz range of frequencies.

Our calculations also aimed at analyzing interferences due to retardation effects, which may give rise to observable asymmetries in: directional decomposition of the radiation emitted in the upper and lower half-spaces, layer-wise decomposition of the Ohmic losses in graphene, and modal decomposition of the excitation probability density for hybridized plasmon polariton modes.

We have found that differences between the angular distributions of radiation spectra emitted in the upper and lower half-spaces show strong asymmetry with respect to the direction of motion of the external charged particle for frequencies satisfying $\omega \gtrsim c/d$, where c is the speed of light in vacuum. This effect of retardation was observed when the graphene layers have equal doping

densities, and was found to be greatly magnified when there is a difference in doping densities, such that the ratio of the Fermi wavenumbers in graphene layers, $\rho = k_{F,1}/k_{F,2} = \sqrt{|n_1|/|n_2|}$, falls in an interval $0.1 \lesssim \rho \lesssim 10$. This asymmetry in the radiation spectra is reduced when $\omega \lesssim c/d$ or when the ratio ρ falls outside the indicated interval. On the other hand, when the radiated spectra are integrated over all angles, both their asymmetry and their dependence on the interlayer distance and the ratio ρ are diminished.

We have further discovered a surprising asymmetry in Ohmic energy losses at frequencies $\omega \lesssim k_F v_F v_B/c$ (i.e., sub-THz frequencies for typical doping densities), such that a graphene layer with given doping density absorbs more Ohmic energy when it is first traversed by the external charged particle than when it is traversed last. While this is true for both the case of graphene layers with equal doping densities and the case of layers with different doping densities for a distance $d \sim c^2/(v_B v_F k_F)$ (≈ 73 μm for typical doping densities), a reduction of the interlayer distance diminishes such asymmetry in Ohmic losses.

At higher frequencies (typically supra-THz), excitations of the hybridized Dirac plasmon polariton modes play a decisive role in the Ohmic energy losses and, accordingly, in the total energy losses of the external charged particle. We have found that, if two graphene layers have equal doping densities, then there is onset of strong oscillations in the modal decomposition at a frequency $\omega \sim \pi v/d$ (where v is the speed of the external particle), giving rise to observable interference features in the Ohmic energy spectra. If the graphene layers have sufficiently different doping densities, then oscillations subside in the modal decomposition. In that case it was found that the graphene layer with smaller doping density predominantly absorbs Ohmic energy by excitation of the bonding mode, whereas the layer with higher doping density absorbs Ohmic energy by excitation of the antibonding mode. In general, Ohmic losses at supra-THz frequencies were found to be strongly dependent on both d and ρ in a nontrivial manner, mostly owing to the sensitivity of the bonding mode to variations in values of those two parameters.

After performing the modal decomposition, we have analyzed the average number of hybridized plasmons excited by a charged particle traversing a DLG. We considered different doping densities in each layer in the nondissipative limit ($\gamma_l \to 0^+$) to obtain the probability density of exciting the HDPP modes and the average number of excited bonding and antibonding modes, $\nu_{\mp}$. We showed that the interlayer distance d, the asymmetry parameter ρ and the incident particle velocity v are the relevant quantities that determine the production of the HDDP modes. In particular, the cusp-like structure around $\rho = 1$ revealed an extreme sensitivity of the system to small variations of the doping densities in two graphene layers that are nominally doped with equal charge carrier densities. This observation along with the intricate interplay between the speed v and the inter-graphene distance should be taken into account in future devices design.

Besides the effects of varying interlayer distance and doping densities of graphene layers,

we have also investigated the effects of varying damping rates in graphene layers and varying speed of the external electron. As in the case of SLG [42], we have found a strong increase in Ohmic losses in DLG at sub-THz frequencies with increasing damping rate(s). In particular, when graphene layers are characterized with different damping rates, $\gamma_1 \neq \gamma_2$, there arises a surprisingly large asymmetry in the layer-wise decomposition of Ohmic losses with respect to the direction of motion of the external charged particle, even in the case of graphene layers with nominally equal doping densities. On the other hand, radiative losses were found to be rather independent of the damping rate when $\gamma \lesssim 0.1$ THz, but strongly suppressed when the damping rate increases above $\gamma \sim 1$ THz, while still exhibiting directional asymmetry in the angular spectra at frequencies $\omega \gtrsim c/d$.

As for the speed v of the external electron, we have found a strong increase in the magnitude of radiation losses with increasing v, as expected. While the overall shapes of the angular spectra of emitted radiation change with increasing v in a manner similar to that observed for SLG [42], the directional asymmetry in the spectra from a DLG is observed over a broad range of the electron speeds for large interlayer distances. On the other hand, Ohmic losses also exhibit a strong increase in magnitude with increasing v at frequencies $\omega \lesssim 1$ THz, whereas this effect is reversed at frequencies $\omega \gtrsim 1$ THz.

As for the study of the Ohmic and radiation energy losses in an MLG with $N > 2$ layers traversed by a fast charged particle under normal incidence, we assumed equal interlayer distances d and equal doping densities n of the constituent graphene layers, where we have explored the limits of both optically thin MLG and optically thick MLG in terms of plasmon hybridization among the constituent graphene layers in the THz range of frequency ω. By adopting the Drude model for the optical conductivity of each graphene layer, $\sigma(\omega)$, we found that an optically thin/thick MLG is roughly defined by values of the Ohmic energy loss $\hbar\omega$ being much smaller/larger than the parameter $\sim e\sqrt{\varepsilon_F/d}$, where ε_F is the Fermi energy in individual graphene layers.

Performing a layer-wise decomposition of the Ohmic energy loss in a three-layer graphene (TLG) structure, $N = 3$, we have found that the hybridized plasmon mode with the middle eigenfrequency is not excited in the middle graphene layer, which was explained by a double-degeneracy of the corresponding charge oscillation patterns in that layer. This observation may be of technological interest, as the excitation of such mode in the middle layer appears to be efficiently prevented by the presence of the outer graphene layers in a TLG, thereby providing a symmetry protected plasmonic channel.

On the other hand, we have observed important differences between the distributions of the Ohmic energy losses in the outer graphene layers in a TLG, as well as between the angular distributions of the TR emitted in the half-spaces on either side of the TLG. Such differences indicate asymmetry of those processes with respect to the order in which graphene layers are traversed by

the external charged particle, pointing to the retardation effects as the likely cause of the asymmetry. As a possible manifestation of those effects in a TLG, we have found that the Ohmic energy loss distribution in the graphene layer, which is first traversed by the external charged particle, exhibits a Fano resonance near the lowest-lying hybridized plasmon eigenfrequency, whereas such resonance is not observed in the graphene layer that is traversed last.

Whereas the observed asymmetry in the angular distributions of the TR should be detectable by using parabolic mirrors in a STEM setting, we have found that the integrated distribution of the radiative energy loss is rather independent of both the interlayer distance and the number of graphene layers in an MLG. This is explained by the fact that only charge carrier oscillations in the outer layers in an MLG give rise to the radiation emitted in the far-field region, whereas the energy flux due to radiating fields experiences cancelation due to destructive interference in the interior regions of the MLG.

We have further observed that prominent peak structures develop in the integrated Ohmic energy loss distributions at the supra-THz frequencies due to interferences between hybridized plasmon modes in MLG systems with $N \geq 2$. Those peaks were found to be very similar in shape and position to the peak structures in a DLG ($N = 2$), but with their magnitudes that scale with the number of graphene layers for $N > 2$. This is explained by asserting that, in an MLG that is intermediate between the optically thin and optically thick systems, plasmon hybridization is governed mostly by the electromagnetic interaction between the nearest-neighbor graphene layers.

For an optically thin MLG with N layers, we have confirmed that representing its structure as a single-layer with the effective conductivity $N\sigma$ provides a very good approximation to the distribution of the integrated Ohmic energy loss at low frequencies. Moreover, the magnitude of that distribution was found to decrease in an inverse proportion to N at low frequencies, which was explained by recalling that graphene's response at such frequencies is dominated by dissipative processes. Given that the plasmon damping is generally unwanted process in graphene-based nano-photonic and nano-plasmonic devices, whereas the damping rate is largely unknown parameter in modeling of such devices, it is therefore remarkable that the effects of damping may be efficiently suppressed, at least at sub-THz frequencies, by using optically thin MLG with increasing number of graphene layers [51, 115].

We remark that the above conclusions are deduced for a system represented by a stack of graphene layers suspended in free space. In most experimental setups, there is a substrate, which would probably affect the observed asymmetry with respect to the traversal order of graphene layers by the incident charged particle. Moreover, a possible presence of dielectric spacers between graphene layers would affect the hybridization between their plasmon modes, not only via screening provided by their dielectric constant(s), but also by additional hybridization of

graphene plasmons with phonon modes in those layers [115]. On the other hand, the presence of a substrate and dielectric spacers would also strongly affect the radiation spectra due to Cherenkov radiation in those materials at sufficiently large particle speeds, as well as TR arising when this particle traverses a boundary between materials with different dielectric constants.

Chapter 3

Energy Loss Rate in Isotropic 2D Materials due to Fast Charged Particle Moving in Parallel Trajectory

In this chapter, we present a fully relativistic formulation for the energy loss rate of a charged particle moving parallel to a sheet containing two-dimensional electron gas, allowing that its in-plane polarization may be described by different longitudinal and transverse conductivities. We apply our formulation to the case of a doped graphene layer in the terahertz range of frequencies, where excitation of the Dirac plasmon polariton (DPP) in graphene plays a major role. By using the Drude model with zero damping we evaluate the energy loss rate due to excitation of the DPP, and show that the retardation effects are important when the incident particle speed and its distance from graphene both increase. Interestingly, the retarded energy loss rate obtained in this manner may be both larger and smaller than its nonretarded counterpart for different combinations of the particle speed and distance.

3.1 Introduction

In recent years there has been an increase of interest in using electron beams to generate radiation from graphene in the terahertz (THz) range of frequencies using different electron trajectories, including aloof scattering [25, 50]. It has been shown that, when the incident charged particle moves parallel to graphene, its velocity may be used as additional tuning parameter, besides the chemical potential in graphene, for creating radiation at various frequencies [25, 50]. Being

interested in the THz frequencies, those authors adopted a model for dynamic polarization of doped graphene based on the Drude model [25, 50, 52], which was also found to be reliable in many other applications of graphene in the area of Nanoplasmonics [3, 119].

In Refs. [128, 129], the authors have studied stopping power and image force on charged particles moving parallel to graphene using a nonrelativistic approach to elucidate the role of Dirac plasmon in doped graphene. More recently, the authors in [42] have developed a fully relativistic treatment of the energy loss and induced transition radiation from graphene traversed by a fast charged particle under normal incidence applied to a single-layer graphene, and also we have developed the formulation to multiple graphene layers in the previous chapter.

In this chapter we adapt the relativistic treatment to the case of a charged particle moving parallel to a single layer of doped graphene. When the particle moves with constant speed in the absence of other polarizable media, no radiation is generated from graphene, whereas its energy loss to the electron excitations in graphene occurs at a constant rate, which is related to the usual stopping power for a parallel incidence trajectory [128, 129]. The study of relativistic effects in stopping power of charged particles has a long history, mostly focusing on solid targets (see, e.g., Ref. [130] and references therein) and their surfaces [131, 132], whereas relatively less is known for strictly 2D targets. In that respect, we note that our formulation of the energy loss rate for incident particle is given in terms of the 2D conductivity of the target and hence it may be applied to any 2D material, not just graphene.

The main novelty regarding our description of graphene in comparison with Ref. [42] and Chapter 2 is that, in the case of parallel trajectory of the incident particle, graphene may exhibit differences between its longitudinal and transverse polarizations. Accordingly, our formulation of the problem in this work is more general, allowing for a tensorial in-plane conductivity of graphene. However, since we are primarily interested in the processes occurring in graphene at the THz to mid-infrared (MIR) range of frequencies, it is safe to take the long wavelength limit of the graphene's conductivity [43]. In that limit, the longitudinal and transverse conductivities become equal, and are well described by a sum of the Drude model describing the intraband electron transitions and a term, which describes interband transitions between graphene's π electron bands [133, 134, 135]. Moreover, focusing on the role of Dirac plasmon in doped graphene at the THz frequencies, it turns out that using just the Drude term for graphene conductivity suffices [3, 25, 50, 52, 119].

While it was shown in the previous chapter that the damping factor in the Drude model exerts rather strong effects on energy losses of the perpendicularly incident charged particle due to the excitations of charge carriers in graphene [42], taking the limit of zero damping can provide an insight into the efficiency of exciting the collective mode in graphene known as the Dirac plasmon polariton (DPP), see subsection 2.2.4. Accordingly, taking the limit of zero damping

in this work will enable us to evaluate the energy loss rate due to the excitation of the long-lived DPP in doped graphene as a function of the incident particle speed and its distance from graphene.

After outlining a general theoretical formulation in the *Theory* section 3.2, we present and discuss several results for the energy loss rate based on the Drude model with zero damping in the *Results and disscusion* section 3.3, which are followed by our *concluding remarks* in Section 3.4.

3.2 Theory

We consider an infinitely large conducting layer of zero thickness, placed in vacuum, which occupies the $z = 0$ plane of a three-dimensional Cartesian system with coordinates $\mathbf{R} = \{x, y, z\}$, and assume that a point charge Ze moves with constant velocity $\mathbf{v}$ parallel to that layer at a fixed distance b . Since both the external charge and the induced charge in the layer are moving uniformly, no electromagnetic radiation is expected in the absence of dielectric environment. We assume that the conducting layer is isotropic in the direction of the in-plane coordinates $\mathbf{r} = \{x, y\}$, but the polarization of its electron gas may depend on the direction of propagation relative to the in-plane wavevectors $\mathbf{k} = \{k_x, k_y\}$. This property is generally captured by a tensorial in-plane conductivity of the layer that depends on $k = \sqrt{k_x^2 + k_y^2}$ and frequency ω, but may exhibit distinct longitudinal and transverse components, $\sigma_l(k, \omega)$ and $\sigma_t(k, \omega)$, which describe different responses of the electron gas in the directions of the unit vectors $\hat{\mathbf{k}}$ and $\hat{\boldsymbol{\tau}} = \hat{\mathbf{z}} \times \hat{\mathbf{k}}$, respectively. Accordingly, we shall also define the longitudinal and transverse components of the external particle's velocity via $\mathbf{v} = \hat{\mathbf{k}} v_l + \hat{\boldsymbol{\tau}} v_t$.

3.2.1 Self-consistent solution for the induced electromagnetic fields

As in Ref. [42] and the previous chapter, we use the Hertz vector $\mathbf{\Pi}(\mathbf{R}, t)$ [120] and perform Fourier transforms with respect to the in-plane coordinates and time, according to

$$\mathbf{\Pi}(\mathbf{k}, z, \omega) = \iint d^2\mathbf{r}\, \mathrm{e}^{-i\mathbf{k}\cdot\mathbf{r}} \int_{-\infty}^{\infty} dt\, \mathrm{e}^{i\omega t}\, \mathbf{\Pi}(\mathbf{R}, t), \tag{3.1}$$

which enables us to express the corresponding electric field as

$$\begin{aligned} \mathbf{E}(\mathbf{k}, z, \omega) &= \frac{\omega^2}{c^2}\left[\mathbf{\Pi}_\parallel(\mathbf{k}, z, \omega) + \hat{\mathbf{z}}\Pi_z(\mathbf{k}, z, \omega)\right] \\ &\quad + \left(i\mathbf{k} + \hat{\mathbf{z}}\frac{\partial}{\partial z}\right)\left[i\mathbf{k}\cdot\mathbf{\Pi}_\parallel(\mathbf{k}, z, \omega) + \frac{\partial}{\partial z}\Pi_z(\mathbf{k}, z, \omega)\right], \end{aligned} \tag{3.2}$$

where $\mathbf{\Pi}_{\parallel}(\mathbf{k}, z, \omega)$ and $\Pi_z(\mathbf{k}, z, \omega)$ are components of the Hertz vector parallel and perpendicular to the conducting layer, and c is the speed of light in vacuum. The advantage of using the Hertz vector is that it may be expressed in terms of the source charge current, $\mathbf{J}(\mathbf{k}, z, \omega)$, by means of a free-space, retarded Green's function, $G_{\Pi 0}(k, z, \omega)$, for a nonhomogeneous Helmholtz equation in scalar form (see Appendix. A) as

$$\mathbf{\Pi}(\mathbf{k}, z, \omega) = \int_{-\infty}^{\infty} dz'\, G_{\Pi 0}(k, z-z', \omega)\, \mathbf{J}(\mathbf{k}, z', \omega), \tag{3.3}$$

where

$$G_{\Pi 0}(k, z, \omega) = \frac{2\pi i}{\omega \alpha(k, \omega)} \mathrm{e}^{-|z|\alpha(k,\omega)} \tag{3.4}$$

with

$$\alpha(k, \omega) = \sqrt{k^2 - \left(\frac{\omega}{c}\right)^2}, \tag{3.5}$$

for $|\omega| < ck$.

Note that the current density of the moving external charge may be written as

$$\mathbf{J}_{\mathrm{ext}}(\mathbf{R}, t) = \mathbf{v} \rho_{\mathrm{ext}}^{\mathrm{CM}}(\mathbf{r} - \mathbf{v}t, z), \tag{3.6}$$

where $\rho_{\mathrm{ext}}^{\mathrm{CM}}(\mathbf{r}, z) = Ze\delta(\mathbf{r})\delta(z - b)$ is the density of a point charge in its center-of-mass (CM) frame of reference. Performing the Fourier transform, we obtain

$$\mathbf{J}_{\mathrm{ext}}(\mathbf{k}, z, \omega) = 2\pi Ze\mathbf{v}\delta(\omega - \mathbf{k}\cdot\mathbf{v})\delta(z - b), \tag{3.7}$$

which gives the corresponding Hertz vector from Eq. (3.3) in the form

$$\mathbf{\Pi}_{\mathrm{ext}}(\mathbf{k}, z, \omega) = G_{\Pi 0}(k, z - b, \omega)\, 2\pi Ze\mathbf{v}\delta(\omega - \mathbf{k}\cdot\mathbf{v}). \tag{3.8}$$

Clearly, the Dirac's delta function in Eq. (3.8) only selects frequencies $\omega = \mathbf{k}\cdot\mathbf{v} = kv_l$, corresponding to a resonance condition for exciting the polarization modes in the conducting layer, which lie outside the light cone, $|\omega| < ck$. While using Eq. (3.8) in Eq. (3.2) gives an electric field due to the external charge that has all three non-zero Cartesian components, we only require its components parallel to the conducting layer, which may be conveniently decomposed into the longitudinal and transverse parts via $\mathbf{E}_{\mathrm{ext}}^{\parallel} = \hat{\mathbf{k}} E_{\mathrm{ext},l} + \hat{\boldsymbol{\tau}} E_{\mathrm{ext},t}$, where

$$E_{\mathrm{ext},l}(\mathbf{k}, z, \omega) = \left(\frac{\omega^2}{c^2} - k^2\right) G_{\Pi 0}(k, z - b, \omega)\, 2\pi Zev_l\delta(\omega - \mathbf{k}\cdot\mathbf{v}), \tag{3.9}$$

$$E_{\mathrm{ext},t}(\mathbf{k}, z, \omega) = \frac{\omega^2}{c^2} G_{\Pi 0}(k, z - b, \omega)\, 2\pi Zev_t\delta(\omega - \mathbf{k}\cdot\mathbf{v}). \tag{3.10}$$

On the other hand, the induced charge carrier current density in the conducting layer may be written as

$$\mathbf{J}_{\rm ind}(\mathbf{k},z,\omega) = \delta(z)\,\mathbf{j}(\mathbf{k},\omega), \tag{3.11}$$

where the in-plane current density may be expressed in terms of a generalized Ohm's law as $\mathbf{j}(\mathbf{k},\omega) = \overleftrightarrow{\sigma}(k,\omega)\cdot\mathbf{E}^{\parallel}(\mathbf{k},0,\omega)$, with $\overleftrightarrow{\sigma} = \sigma_l\,\hat{\mathbf{k}}\hat{\mathbf{k}} + \sigma_t\,\hat{\boldsymbol{\tau}}\hat{\boldsymbol{\tau}}$ being a conductivity tensor in diagonal form and $\mathbf{E}^{\parallel}(\mathbf{k},0,\omega)$ the in-plane (tangential) component of the total electric field evaluated at the plane $z = 0$. Using Eq. (3.11) in Eq. (3.3) gives the Hertz vector due to the induced currents in the form

$$\mathbf{\Pi}_{\rm ind}(\mathbf{k},z,\omega) = G_{\Pi 0}(k,z,\omega)\,\overleftrightarrow{\sigma}(k,\omega)\;\cdot\;\mathbf{E}_{\parallel}(\mathbf{k},0,\omega), \tag{3.12}$$

which when used in Eq. (3.2) yields all three Cartesian components of the corresponding electric field. However, we only require components of the induced electric field that are parallel to the conducing layer, which are again decomposed into the longitudinal and transverse parts via $\mathbf{E}^{\parallel}_{\rm ind} = \hat{\mathbf{k}}E_{{\rm ind},l} + \hat{\boldsymbol{\tau}}E_{{\rm ind},t}$, where

$$E_{{\rm ind},l}(\mathbf{k},z,\omega) = \left(\frac{\omega^2}{c^2} - k^2\right) G_{\Pi 0}(k,z,\omega)\,\sigma_l(k,\omega)E_l(\mathbf{k},0,\omega) \tag{3.13}$$

$$E_{{\rm ind},t}(\mathbf{k},z,\omega) = \frac{\omega^2}{c^2}\,G_{\Pi 0}(k,z,\omega)\,\sigma_t(k,\omega)E_t(\mathbf{k},0,\omega). \tag{3.14}$$

In order to obtain a self-consistent set of equations for the longitudinal and transverse components of the total in-plane electric filed, $E_{lt}(\mathbf{k},0,\omega) = E_{{\rm ext},lt}(\mathbf{k},0,\omega) + E_{{\rm ind},lt}(\mathbf{k},0,\omega)$, we set $z = 0$ in Eqs. (3.9), (3.9), (3.13), and (3.14), whence adding Eqs. (3.9) and (3.13) and solving the resulting equation gives

$$E_l(\mathbf{k},0,\omega) = \frac{\left(\frac{\omega^2}{c^2} - k^2\right) G_{\Pi 0}(k,b,\omega)}{1 - \left(\frac{\omega^2}{c^2} - k^2\right) G_{\Pi 0}(k,0,\omega)\sigma_l(k,\omega)}\,2\pi Zev_l\delta(\omega - \mathbf{k}\cdot\mathbf{v}), \tag{3.15}$$

whereas adding Eqs. (3.9) and (3.14) and solving the resulting equation gives

$$E_t(\mathbf{k},0,\omega) = \frac{\frac{\omega^2}{c^2}\,G_{\Pi 0}(k,b,\omega)}{1 - \frac{\omega^2}{c^2}\,G_{\Pi 0}(k,0,\omega)\sigma_t(k,\omega)}\,2\pi Zev_t\delta(\omega - \mathbf{k}\cdot\mathbf{v}). \tag{3.16}$$

Using the results obtained in Eqs. (3.15) and (3.16) in the right hand sides of Eqs. (3.13) and (3.14) gives final expressions for the longitudinal and transverse components of the induced electric fields at arbitrary position z, respectively.

Notice that the thus obtained expressions for $E_{\mathrm{ind},lt}(\mathbf{k},z,\omega)$ contain a delta function $\delta(\omega-\mathbf{k}\cdot\mathbf{v})$, which is "inherited" from the external current density in Eq. (3.7). Thus, performing the inverse Fourier transform shows that the induced electric field is stationary in the moving frame of reference attached to the external particle, so that the spatiotemporal dependence of its parallel component may be written as $\mathbf{E}_{\mathrm{ind}\parallel}(\mathbf{R},t)=\mathbf{E}^{\mathrm{CM}}_{\mathrm{ind}\parallel}(\mathbf{r}-\mathbf{v}t,z)$. Here, the induced electric field parallel to the conducting layer is defined in the CM frame via its 2D spatial Fourier transform as

$$\begin{aligned}\mathbf{E}^{\mathrm{CM}}_{\mathrm{ind}\parallel}(\mathbf{k},z) = &-2\pi i Ze\,\mathrm{e}^{-(|z|+|b|)\alpha(k,kv_l)}\\ &\times\left\{\hat{\mathbf{k}}\frac{\alpha(k,kv_l)}{k}\left[\frac{1}{\epsilon_l(k,kv_l)}-1\right]-\hat{\boldsymbol{\tau}}\frac{v_lv_t}{c^2}\frac{k}{\alpha(k,kv_l)}\left[\frac{1}{\epsilon_t(k,kv_l)}-1\right]\right\},\end{aligned}\tag{3.17}$$

where we have taken into account that $\omega=\mathbf{k}\cdot\mathbf{v}=kv_l$, and we defined the longitudinal and transverse dielectric functions of the conducting layer by

$$\epsilon_l(k,\omega) = 1+2\pi i\frac{\alpha(k,\omega)}{\omega}\sigma_l(k,\omega),\tag{3.18}$$

$$\epsilon_t(k,\omega) = 1-2\pi i\frac{\omega}{c^2\alpha(k,\omega)}\sigma_t(k,\omega),\tag{3.19}$$

respectively.

3.2.2 Energy loss rate

One may further refer to Eq. (3.6) and write the rate of energy dissipation in the conducting layer as

$$\begin{aligned}\frac{dW}{dt} &= -\iiint d^3\mathbf{R}\,\mathbf{J}_{\mathrm{ext}}(\mathbf{R},t)\cdot\mathbf{E}_{\mathrm{ind}}(\mathbf{R},t)\\ &= -\iint d^2\mathbf{r}\int dz\,\rho^{\mathrm{CM}}_{\mathrm{ext}}(\mathbf{r}-\mathbf{v}t,z)\,\mathbf{v}\cdot\mathbf{E}^{\mathrm{CM}}_{\mathrm{ind}\parallel}(\mathbf{r}-\mathbf{v}t,z)\\ &= -\iint d^2\mathbf{r}\int dz\,\rho^{\mathrm{CM}}_{\mathrm{ext}}(\mathbf{r},z)\,\mathbf{v}\cdot\mathbf{E}^{\mathrm{CM}}_{\mathrm{ind}\parallel}(\mathbf{r},z)\\ &= -Ze\iint\frac{d^2\mathbf{k}}{(2\pi)^2}\,\mathbf{v}\cdot\mathbf{E}^{\mathrm{CM}}_{\mathrm{ind}\parallel}(\mathbf{k},b).\end{aligned}\tag{3.20}$$

Using Eq. (3.17) in the last line of Eq. (3.20) and performing the angular integration over the direction of $\mathbf{k}$ with respect to $\mathbf{v}$, one may invoke parity properties of the functions $\sigma_{l,t}(k,\omega)$ to

express the energy loss rate in a more familiar form involving integration over the frequency and the in-plane wavenumber [128],

$$\frac{dW}{dt} = \frac{2}{\pi}(Ze)^2 \int_0^\infty \frac{dk}{k} \int_0^{kv} d\omega\, \omega\, \mathrm{e}^{-2|b|\alpha(k,\omega)} \times \left\{ \frac{\alpha(k,\omega)}{\sqrt{k^2v^2-\omega^2}} \Im\left[\frac{-1}{\epsilon_l(k,\omega)}\right] + \frac{\sqrt{k^2v^2-\omega^2}}{c^2\alpha(k,\omega)} \Im\left[\frac{1}{\epsilon_t(k,\omega)}\right] \right\}. \quad (3.21)$$

This result represents a modification of the formula (5.30) of Ref. [130], derived for the stopping power in the bulk of a solid, to the case of a charged particle moving parallel to a 2D target. From the expression in Eq. (3.21), it is obvious that any resonant modes in the conducting layer are given by the zeros of the 2D dielectric functions $\epsilon_{l,t}(k,\omega)$ in the (ω,k) plane. Those modes may be excited by the externally moving charged particle if their dispersion relations (in the limit of vanishing damping) traverse the boundary of the region $0 < \omega \leq kv$. Clearly, the two terms within the curly brackets in Eq. (3.21) represent contributions to the energy loss of the external charged particle resulting from the longitudinal and transverse polarizations of the electron gas in the conducting layer.

In the nonretarded limit, one lets $c \to \infty$ and hence $\alpha(k,\omega) \to k$ in Eq. (3.21), so that only the longitudinal contribution survives, giving the familiar expression for the energy loss rate [128, 136, 137, 138]

$$\left.\frac{dW}{dt}\right|_{\mathrm{nr}} = \frac{2}{\pi}(Ze)^2 \int_0^\infty dk \int_0^{kv} d\omega\, \frac{\omega}{\sqrt{k^2v^2-\omega^2}} \mathrm{e}^{-2|b|k} \Im\left[\frac{-1}{\epsilon_{\mathrm{nr}}(k,\omega)}\right], \quad (3.22)$$

with the usual definition of dielectric function for a 2D electron gas in the nonretarded limit,

$$\epsilon_{\mathrm{nr}}(k,\omega) = 1 + 2\pi i \frac{k}{\omega}\sigma_l(k,\omega). \quad (3.23)$$

3.2.3 Conductivity model

While the formalism developed in the previous subsection can be directly applied to any isotropic 2D material with tensorial in-plane conductivity, we limit our focus on doped graphene, where low-energy electron excitations within and between its π electron bands give rise to the Dirac plasmon, with an appealing property of tunability by changing the doping density of charge carriers in graphene, n, by using external gates [70]. Calculations of the conductivity of graphene

using the Dirac cone approximation for its π electron bands [134, 135], as well as the *ab initio* calculations based on all graphene bands [43], show that the longitudinal and transverse conductivities, $\sigma_{l,t}(\mathbf{k},\omega)$, exhibit rather different behaviors when the dependence on the wavevector $\mathbf{k}$ is included in those functions. On the other hand, applications of the DPP in Nanophotonics involve rather low frequencies, ranging from THz to MIR [70], so that it is safe to consider conductivities in the optical limit by letting $k \to 0$, in which case one finds that $\sigma_l(0,\omega) = \sigma_t(0,\omega) = \sigma(\omega)$ [133, 134, 135].

The dispersion relation for the DPP is readily deduced from zeros of the longitudinal dielectric function, $\epsilon_l(k,\omega) = 0$, by using a simple Drude model for conductivity in Eq. (3.18). This model describes *intraband* electron excitations in doped graphene in the optical limit, and is given at zero temperature by

$$\sigma_{\text{intra}}(\omega) = i\frac{v_B}{\pi}\frac{\omega_F}{\omega + i\gamma}, \tag{3.24}$$

where the parameters in the Drude model are the same as those of introduced in the previous chapter valid for the frequency range of $kv_F \ll \omega \ll \omega_F$.

On the other hand, a collective mode due to transverse polarization of graphene has proven to be more elusive. Its existence was predicted theoretically by including *interband* electron transitions between the π electron bands in the Dirac cone approximation, which may be described in the optical limit by a contribution to the conductivity, given at zero temperature and with zero damping by [133]

$$\sigma_{\text{inter}}(\omega) = \frac{v_B}{4}\left[\Theta(\omega - 2\omega_F) + \frac{i}{\pi}\ln\left|\frac{\omega - 2\omega_F}{\omega + 2\omega_F}\right|\right], \tag{3.25}$$

with Θ being the Heaviside unit step function. Combining the Drude and the interband contributions, Eqs. (3.24) and (3.25), gives a conductivity model $\sigma(\omega) = \sigma_{\text{intra}}(\omega) + \sigma_{\text{inter}}(\omega)$, which relaxes the requirement $\omega \ll \omega_F$. Using this model in Eq. (3.19) gives a condition for the transverse plasmon polariton (TPP) from zeros of the transverse dielectric function, $\epsilon_t(k,\omega) = 0$. It was found that the dispersion of such a collective mode is pinned at the light line, $\omega = ck$, and would only be observable in a narrow range of frequencies close to $2\omega_F$ [133]. Since excitation of such a mode by an external charge moving parallel to graphene would require that the resonance condition is satisfied, $\omega = kv$, it appears that only ultrarelativistic particles with $v \to c$ would be capable of exciting the TPP in doped graphene placed in vacuum. While this indicates that the so-called relativistic density effect (see Section 5.6.4 in Ref. [130]) is possibly much weaker in graphene than in a solid target, a further detailed analysis of the TPP contribution in Eq. (3.21) is warranted, but is left for the next chapter.

Therefore, we shall only study here energy loss of the external charged particle due to excitation of the DPP in doped graphene in the optical limit. Limiting our consideration to frequencies $\omega \ll \omega_F$ and taking the limit of zero damping, $\gamma \to 0^+$, in Eq. (3.24), one can show that the contribution of the transverse polarization in Eq. (3.21) vanishes, whereas the contribution of the longitudinal polarization may be well described by using just the Drude conductivity, Eq. (3.24), in Eq. (3.18), provided that the external charged particle is sufficiently fast.

To facilitate the computations, it is useful to introduce the reduced wavenumber and reduced frequency, $\overline{k} = k/k_c$ and $\overline{\omega} = \omega/\omega_c$, respectively, where $k_c = v_B v_F k_F/c^2$ and $\omega_c = ck_c = v_B v_F k_F/c$ [42]. We note that, using $|n| = 10^{13}$ cm^{-2} as typical doping density of graphene, the characteristic wavenumber attains the value $k_c \approx 1.36 \times 10^{-5}$ nm^{-1}, whereas the corresponding characteristic frequency yields $\hbar\omega_c \approx 2.69$ meV or $\nu_c = \omega_c/(2\pi) \approx 0.65$ THz. Using the reduced quantities, the conditions validating the Drude model may be written as $\frac{v_F}{c}\overline{k} \ll \overline{\omega} \ll \frac{c}{v_B}$.

3.3 Results and discussion

By taking the limit of zero damping in Eq. (3.24), one can further show that the loss function $\Im\left[-1/\epsilon_l(k,\omega)\right]$ in Eq. (3.21) yields a Dirac's delta function that is peaked at the dispersion curve of the DPP, given in the reduced form by $\overline{\omega} = \sqrt{2\left(-1+\sqrt{1+\overline{k}^2}\right)}$. Note that, in the nonretarded limit, this dispersion is reduced to $\overline{\omega} = \sqrt{2\overline{k}}$. Moreover, the resonance condition for exciting the DPP by a particle moving with the reduced speed $\beta = v/c$ may be written as $\overline{\omega} = \beta\overline{k}$, which crosses the DPP dispersion curve in a fully retarded limit at the reduced wavenumber $\overline{k}_r = \frac{2}{\beta}\sqrt{\beta^{-2}-1}$. It may be then shown that the pair of values $\overline{k}_r$ and $\overline{\omega}_r = \beta\overline{k}_r$ may be chosen so that the conditions validating the Drude model, are fulfilled when the speed of the external charged particle is $v \gg v_B$, or $\beta \gtrsim 0.1$.

In Fig. 3.1 we show both the retarded and nonretarded dispersion relations in the reduced units. One notices significant differences, where the retarded dispersion is placed below the light line for all wavenumbers, whereas the nonretarded dispersion lies above the light line for $0 < \overline{k} < 2$. Similarly, considering the resonance line for a particle with $v = 0.5\,c$, one sees that its intersections with the retarded and nonretarded dispersions occur at $\overline{k} \approx 7$ and $\overline{k} \approx 8$, respectively.

Next, taking advantage of the Dirac's delta function that results from the loss function $\Im\left[-1/\epsilon_l(k,\omega)\right]$ in Eq. (3.21), and introducing the auxiliary variable $y = (vk/\omega)^2 \equiv \left(\beta\overline{k}/\overline{\omega}\right)^2$, one can write the

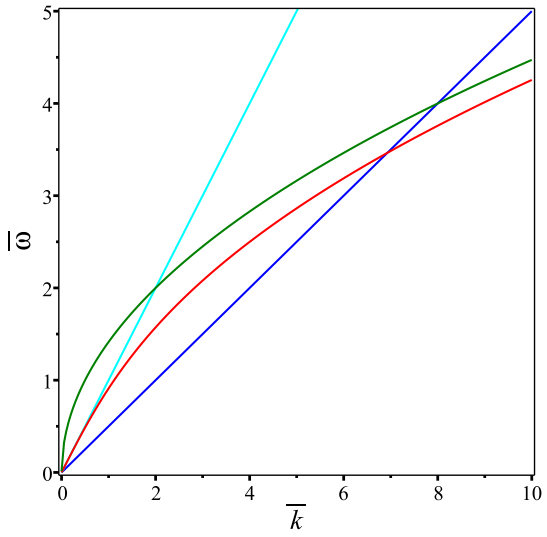

Figure 3.1: Dispersion relations in reduced variables $\overline{\omega} = \omega/\omega_c$ and $\overline{k} = k/k_c$. Red: Dirac plasmon polariton (including retardation), $\overline{\omega} = \sqrt{2\left(-1+\sqrt{1+\overline{k}^2}\right)}$. Green: Dirac plasmon (nonretarded limit), $\overline{\omega} = \sqrt{2\overline{k}}$. Blue: resonance line, $\overline{\omega} = \beta\overline{k}$, for external charge with the reduced speed $\beta = v/c = 0.5$. Cyan: light line, $\overline{\omega} = \overline{k}$.

final expression for the energy loss rate to the DPP excitation as

$$\frac{dW}{dt} = \frac{R}{\beta^3}\int_1^\infty dy\,\frac{(y-\beta^2)^{3/2}}{y\sqrt{y-1}}\,\exp\left[-4\frac{\bar{b}}{\beta^2}\left(y-\beta^2\right)\right], \tag{3.26}$$

where $R = (2Zek_c)^2c \approx 3.2\times10^8$ eV/sec $\approx 5.1\times10^{-11}$ W, and $\bar{b} = |b|k_c$ is the reduced distance. Notice that the value $\bar{b}=1$ corresponds to a rather large physical distance of $|b| \approx 73.5$ μm.

To obtain the nonretarded result for energy loss, one needs to transform the expression that appears twice in the parentheses in Eq. (3.26) according to $(y-\beta^2)\to y$ giving

$$\left.\frac{dW}{dt}\right|_{\rm nr} = \widetilde{R}\int_1^\infty dy\,\sqrt{\frac{y}{y-1}}\,\exp\left(-4\tilde{b}y\right) \tag{3.27}$$

$$= \frac{\widetilde{R}}{2}\,{\rm e}^{-2\tilde{b}}\left[K_0(2\tilde{b})+K_1(2\tilde{b})\right], \tag{3.28}$$

where $\widetilde{R}\equiv R/\beta^3 = (2Zek_Fv_Fv_B)^2/v^3$ and $\tilde{b}\equiv\bar{b}/\beta^2 = |b|k_Fv_Fv_B/v^2$, whereas K_0 and K_1 are modified Bessel functions of the second kind.

Using the expressions in Eqs. (3.26) and (3.27), we evaluate the corresponding energy loss rates and show them in Fig. 3.2 as a function of the reduced distance $\bar{b}$ (for several reduced speeds β) and in Fig. 3.3 as a function of the reduced speed (for several reduced distances). One notices in Fig. 3.2 that the retardation effects increase with increasing distance and increasing speed, as expected. It is somewhat surprising that, at larger speeds, the retarded energy loss tends to exceed the nonretarded loss at large distances, but this trend is reversed for intermediate and shorter distances.

Given the strong decrease of the energy loss rate with distance, we have multiplied each curve in Fig. 3.3 by a suitable factor, so that all the retarded curves in that figure have the same maximum value, with a position that depends on the reduced speed. One notices that the positions of these maxima increase with the reduced distance, as expected. Moreover, as the distance increases, one also notices increasing differences between the retarded and nonretarded energy loss rates, such that the nonretarded energy losses are larger than the retarded losses at sufficiently large speeds, whereas this trend is reversed at lower speeds.

Both Figs. 3.2 and 3.3 exhibit an interesting dependence of the ratio of the retarded to the nonretarded energy loss rates as a function of the reduced particle speed in a range $0.2 \lesssim \beta < 1$

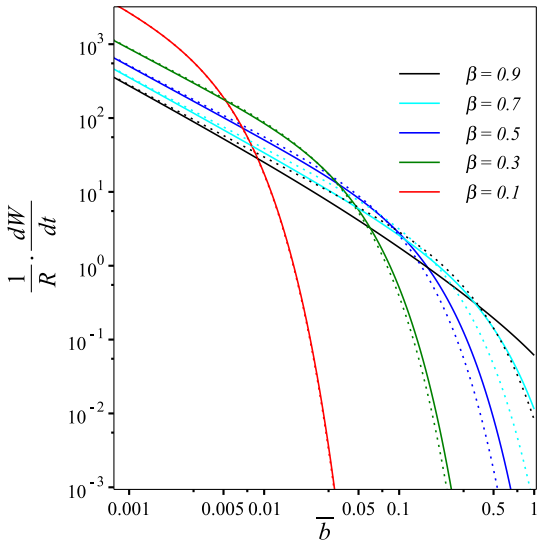

Figure 3.2: Solid lines show the retarded, and the dotted lines show the nonretarded energy loss rate $\frac{dW}{dt}$ divided by the factor R as a function of the reduced distance $\overline{b} = |b|k_c$ of external charged particle with $Z = 1$ that moves parallel to doped graphene at the reduced speed $\beta = v/c$, which takes values $\beta = 0.1$ (red curves), $\beta = 0.3$ (green curves), $\beta = 0.5$ (blue curves), $\beta = 0.7$ (cyan curves) and $\beta = 0.9$ (black curves).

and the reduced distance in a range $0.01 \lesssim \overline{b} \lesssim 1$. This behavior may be qualitatively analyzed by applying the Mean-Value Theorem to the factor $(y-\beta^2)^{3/2}$ in the integral in Eq. (3.26), giving

$$\frac{dW}{dt} = \mathrm{e}^{4\overline{b}} \left(1 - \frac{\beta^2}{y_*}\right)^{3/2} \left.\frac{dW}{dt}\right|_{\rm nr}, \tag{3.29}$$

where $y_* \gtrsim 1$. This expression shows that the ratio of the retarded to the nonretarded energy loss rates may take values < 1 for increasing β and decreasing $\overline{b}$, and > 1 for increasing $\overline{b}$ and decreasing β. However, from both Figs. 3.2 and 3.3, one observes that at distances shorter than about $\overline{b} = 10^{-3}$, i.e., for $|b| \lesssim 73.5$ nm, there are practically no differences between the retarded and nonretarded energy loss rates in the full range of the incident particle speeds.

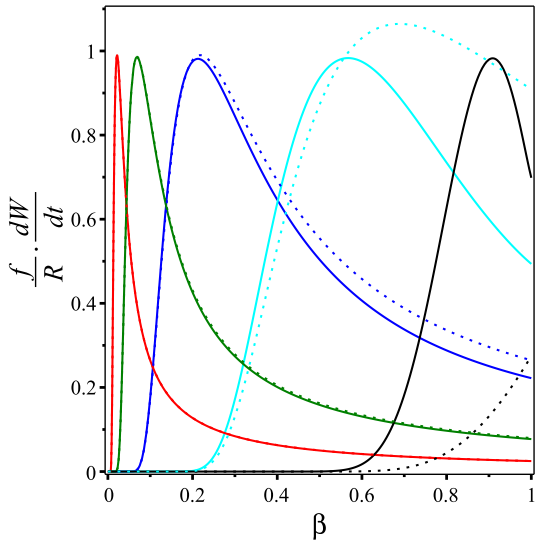

Figure 3.3: Solid lines show the retarded, and the dotted lines show the nonretarded energy loss rate $\frac{dW}{dt}$ multiplied by the factor $\frac{f}{R}$ as a function of the reduced speed $\beta = v/c$ of external charged particle with $Z = 1$ that moves parallel to doped graphene at the reduced distance $\overline{b} = |b|k_c$, which takes values $\overline{b} = 10^{-4}$ (red curves with $f = 10^{-5}$), $\overline{b} = 10^{-3}$ (green curves with $f = 3.15 \times 10^{-4}$), $\overline{b} = 10^{-2}$ (blue curves with $f = 10^{-2}$), $\overline{b} = 10^{-1}$ (cyan curves with $f = 0.34$) and $\overline{b} = 1$ (black curves with $f = 16$).

It may be worthwhile mentioning that, by attaching a semiclassical interpretation to the expressions for the energy loss rate given in Eqs. (3.21) and (3.22), one can calculate the corresponding inverse inelastic lifetimes of the external charged particle, Γ and $\Gamma_{\rm nr}$, respectively. This is achieved by simply replacing the factor ω in the integrands in those equations with a factor

$1/\hbar$ [137]. Furthermore, by taking the limit of zero damping in the loss function $\Im\left[-1/\epsilon_l(k,\omega)\right]$, the thus obtained expressions for Γ and $\Gamma_{\rm nr}$ yield the rates of excitation of the DPP in doped graphene by the external charged particle in a fully retarded and nonretarded regimes, respectively. It is interesting that, following the same procedure as that used in deriving Eqs. (3.26) and (3.27), both those rates can be evaluated in terms of elementary functions as

$$\Gamma = \frac{Q}{\beta}\,\mathrm{e}^{4\bar{b}}\left[\frac{1}{\sqrt{\bar{b}}}\mathrm{e}^{-4\frac{\bar{b}}{\beta^2}} - 2\sqrt{\pi}\beta\,\mathrm{erfc}\left(\frac{2}{\beta}\sqrt{\bar{b}}\right)\right], \tag{3.30}$$

where $Q = \sqrt{\pi}\omega_F\left(\frac{v_B}{c}\right)^2 \approx 53$ GHz, and erfc is the complementary error function, and

$$\Gamma_{\rm nr} = \frac{\widetilde{Q}}{\sqrt{\tilde{b}}}\,\mathrm{e}^{-4\tilde{b}}, \tag{3.31}$$

where $\widetilde{Q} = Q/\beta^2$ and $\tilde{b} = \bar{b}/\beta^2$. A simple analysis of Eqs. (3.30) and (3.31) shows that the ratio of the retarded and nonretarded excitation rates for the DPP, $\Gamma/\Gamma_{\rm nr}$, exhibits a similar dependence on the reduced particle speed β and the reduced distance $\bar{b}$ as the ratio of the energy loss rates, discussed above.

3.4 Concluding remarks

We have presented a fully relativistic formulation for the energy loss rate of a charged particle moving parallel to a sheet containing two-dimensional electron gas, and applied it to a single doped graphene layer. While our formulation of the problem allows for different longitudinal and transverse in-plane conductivities of graphene, limiting our attention to the terahertz range of frequencies allowed us to work in the optical limit, where those conductivities are well approximated by a Drude model. Taking this model in the limit of zero damping allowed us to evaluate the energy loss rates due to excitation of the Dirac plasmon polariton in doped graphene by a charged particle that moves at speeds in excess of about one tenth of the speed of light.

We have observed that the retardation effects are important when the incident particle speed and its distance from graphene both increase, as expected. However, there are some interesting, nonmonotonous relations between the values of the retarded and nonretarded energy loss rates. Namely, for a given particle speed, the retarded loss rate is greater than the nonretarded rate at large distances, but this trend is reversed at shorter distances, whereas for a given distance, the nonretarded loss rate is greater than the retarded rate at high speeds, but this trend is reversed at lower speeds. On the other hand, using the parameters relevant for the Dirac plasmon in a

typically doped graphene layer, we have found no significant retardation effects for distances of the charged particle trajectory up to ~ 100 nm. Given that in most experiments using aloof scattering of electrons the distance of closest approach does not reach so large values, we may conclude that nonrelativistic treatment would be valid for studying Dirac plasmons in graphene.

Chapter 4

Energy Loss and Transition Radiation in Isotropic 2D Materials Traversed by Fast Charged Particle under Oblique Incidence

In this chapter, we perform fully relativistic calculations of the energy loss channels for a charged particle traversing a single layer of graphene under oblique incidence in a setting pertinent to a scanning transmission electron microscope (STEM), where we distinguish between the energy deposited in graphene in the form of electronic excitations (Ohmic loss) and the energy emitted in the far-field in the form of transition radiation (TR). Our formulation of the problem uses a definition of two in-plane, dielectric functions of graphene, which describe the longitudinal and transverse excitation processes that contribute separately to those two energy loss channels. Using several models for the electric conductivity of graphene as the input in those dielectric functions enables us to discuss the effects of oblique incidence on several processes in a broad range of frequencies, from the terahertz (THz) to the ultraviolet (UV). In particular, at the THz frequencies, we demonstrate that the nonlocal effect in the graphene's conductivity is not important in the retarded regime, and we show that the longitudinal and transverse contributions to the emitted TR spectra exhibit strongly anisotropic angular patterns that are readily distinguishable in a cathodoluminescence measurement in a STEM. Moreover, we explore the possibility of exciting the so-called transverse mode in the optical response of graphene at the mid-infrared (MIR) range of frequencies by means of a fast charged particle under oblique incidence. Finally, we demonstrate that, besides the usual high-energy peaks in the longitudinal contribution to the Ohmic energy loss in the MIR to the UV frequency range, there may arise strongly directional features in the in-plane distribution of the transverse contribution to the Ohmic energy loss for an oblique trajectory, which could be possibly observed via momentum- and angle-resolved electron

energy loss spectroscopy of graphene in STEM.

4.1 Introduction

In Chapter 2 we have developed a fully relativistic description of the energy losses suffered by an energetic electron perpendicularly traversing a single layer of graphene (SLG), as well as a multilayered graphene stack (MLG). An extension of this work also considered the stopping of electrons traveling on aloof trajectories, parallel to a graphene layer in Chapter 3. Our formulation gave analytical expressions for the probability density of energy loss. We have shown that the total energy lost by the electron comes from an Ohmic contribution, due to electronic excitations, and a radiative term due to transition radiation (TR), generated by the passage of the electron through the interface. The radiative term is purely relativistic and is absent in the parallel trajectory case. For a perpendicular trajectory, only longitudinal fields are relevant since the transverse terms are canceled out due to symmetries of the considered configuration; hence, it is sufficient to consider a scalar in-plane conductivity to describe the response function of graphene. For a parallel trajectory, on the other hand, it was found necessary to include transverse polarization in the response of graphene by using a tensorial formulation for its conductivity.

In the present chapter, we extend our formalism to an arbitrary oblique trajectory, and accordingly we consider a tensorial conductivity with different components along the longitudinal and the transverse directions with respect to the in-plane wave vector k. The formulation is made for a general conductivity tensor, which allows us to apply different models to describe the energy losses of the external charged particle in both the low-energy range (therhertz (THz) to mid-inferared (MIR)) and in the ultraviolet (UV) domain. We find that both the longitudinal and transverse excitation mechanisms operate in the case of a general oblique trajectory, which are conveniently described by introducing two novel in-plane dielectric functions for the response of graphene layer. In each frequency range, we assess contributions to the external particle energy loss coming from both the radiative and non-radiative (Ohmic) channels, and for each one of them we distinguish between the longitudinal and transverse contributions. By exploring the parameter space, specifically, the charged particle speed and its incidence angle, we are able to analyze the ranges of importance for relativistic effects, which govern both the radiative energy loss and the transverse component of the Ohmic energy loss.

The chapter is structured as follows: in the *Theory* section 4.2 we describe the theoretical formulation used to obtain the probability densities of energy loss, in terms of the induced electromagnetic (EM) fields and the conductivity tensor, giving a detailed description of different models used for the conductivity. Next section, *Results and Discussion* 4.3, is devoted to present and analyze the obtained results. Finally, in Section 4.4 we give some *concluding remarks*.

4.2 Theory

We consider a structure with monolayer graphene of large area placed in the xy-plane ($z = 0$) in a three-dimensional (3D) Cartesian coordinate system with coordinates $\mathbf{R} = \{\mathbf{r}, z\}$, where $\mathbf{r} = \{x, y\}$. Graphene is traversed by an external point-like particle with charge Ze, moving with constant velocity $\mathbf{v}$ at an arbitrary angle θ_0 with respect to the z axis. We assume that the structure is placed in vacuum in order to be able to neglect any other sources of radiation or dissipation, apart from those pertaining to graphene. While the assumption of a free-standing graphene layer is realistic in the context of EELS experiments in STEM [35], we note that the existence of a dielectric substrate with the relative dielectric constant $\epsilon_d > 1$ on one side of graphene, could possibly give rise to Cherenkov radiation for the incident particle speeds exceeding the threshold $c/\sqrt{\epsilon_d} > 1$, as well as to the transition radiation that normally arises when a charged particle traverses an interface between materials with different dielectrics constants [63]. Those two sources of radiation would be absent when graphene is surrounded by a homogeneous, nonmagnetic material with the dielectric constant ϵ_d and for the particle speeds below the threshold for Cherenkov radiation, but details of the dispersion relation for the collective modes in graphene would be modified near the THz frequencies by widening of the light cone in such material [139]. At the same time, the magnitude of the incident charged particle electromagnetic (EM) fields would be reduced by a factor of $1/\epsilon_d$, giving rise to an overall reduction of its interaction with the charge carriers in graphene. Moreover, the existence of dynamic modes in the surrounding material(s), which could be encoded via a frequency-dependent dielectric function $\epsilon_d(\omega)$, such as in the case of a polar substrate or nearby metallic gate(s) [140], could give rise to a strong hybridization of their modes with those in graphene [115]. However, studying the above effects of dielectric substrate(s) is beyond the scope of the present work (see the proposed future research in Chapter 6).

Considering the geometry of the problem, we find it convenient to introduce a dyadic Green's function (DGF), which may be derived from the electric Hertz vector [120]. This vector can be easily obtained by solving a nonhomogeneous Helmholtz vector equation with an electric current density as the source term by means of a free-space, retarded, scalar Green's function [42], as outlined in Appendix A.

4.2.1 Self-consistent solution for the induced electromagnetic fields

Assuming translational invariance inside the graphene sheet, we may perform a 2D spatial Fourier transform ($\mathbf{r} \to \mathbf{k}$), as well as a Fourier transform with respect to time ($t \to \omega$). Thus, defining

the electric field as

$$\mathbf{E}(\mathbf{R},t)=\iint\frac{d^2\mathbf{k}}{(2\pi)^2}\mathrm{e}^{i\mathbf{k}\cdot\mathbf{r}}\int_{-\infty}^{\infty}\frac{d\omega}{2\pi}\,\mathrm{e}^{-i\omega t}\mathbf{E}(\mathbf{k},z,\omega),\tag{4.1}$$

we may express it in the Fourier space in terms of the corresponding current density $\mathbf{J}$ as

$$\mathbf{E}(\mathbf{k},z,\omega)=\int_{-\infty}^{+\infty}dz'\,\overleftrightarrow{G}_{E0}(\mathbf{k},z-z',\omega)\cdot\mathbf{J}(\mathbf{k},z',\omega),\tag{4.2}$$

where $\overleftrightarrow{G}_{E0}(\mathbf{k},z-z',\omega)$ is the electric DGF (EDGF) for free space. Although the above relation can be always expressed in Cartesian coordinates, we take advantage of the fact that graphene is isotropic in the $z=0$ plane and express all quantities in terms of their longitudinal and transverse (LT) in-plane components. With $\hat{\mathbf{z}}$ being a unit vector in the direction of the z-axis, and $\hat{\mathbf{k}}$, the unit vector in the direction of the in-plane wavevector $\mathbf{k}$. that describes longitudinal components, we define the unit vector $\hat{\boldsymbol{\tau}}=\hat{\mathbf{z}}\times\hat{\mathbf{k}}$, which describes transverse in-plane components, see Fig. 4.1. Thus, adopting the triad $\left(\hat{\mathbf{k}},\hat{\boldsymbol{\tau}},\hat{\mathbf{z}}\right)$, the EDGF may be written in tensorial form as

$$\overleftrightarrow{G}_{E0}(\mathbf{k},z,\omega)=\frac{i}{\omega}\frac{2\pi}{q}\left\{-q^2\hat{\mathbf{k}}\hat{\mathbf{k}}+k_0^2\,\hat{\boldsymbol{\tau}}\hat{\boldsymbol{\tau}}-ikq\,\mathrm{sign}(z)\,\left(\hat{\mathbf{z}}\hat{\mathbf{k}}+\hat{\mathbf{k}}\hat{\mathbf{z}}\right)+\left[k^2-2q\delta(z)\right]\,\hat{\mathbf{z}}\hat{\mathbf{z}}\right\}\mathrm{e}^{-q|z|},\tag{4.3}$$

where $k_0=\omega/c$ and

$$q(k,\omega)=\begin{cases}-i\frac{\omega}{c}\sqrt{1-\left(\frac{ck}{\omega}\right)^2}\equiv-i\kappa(k,\omega), & |\omega|>ck\\ \frac{|\omega|}{c}\sqrt{\left(\frac{ck}{\omega}\right)^2-1}\equiv\alpha(k,\omega), & |\omega|<ck.\end{cases}\tag{4.4}$$

In the above equation, $\alpha\equiv\sqrt{k^2-k_0^2}$ describes the inverse of the localization length for collective excitation modes of charge carriers in graphene that occur in the range of the (k,ω) plane lying outside the light cone.

Defining the volume charge density associated with the external charged particle as $\rho_{\mathrm{ext}}(\mathbf{R},t)=Ze\,\delta(\mathbf{R}-\mathbf{v}t)$, we obtain the Fourier transform of the corresponding current density as

$$\mathbf{J}_{\mathrm{ext}}(\mathbf{k},z,\omega)=\frac{Ze}{v_z}\,\mathbf{v}\,\mathrm{e}^{iQz},\tag{4.5}$$

where $Q=\Omega/v_z$ with $\Omega=\omega-\mathbf{k}\cdot\mathbf{v}_{\parallel}$, whereas $\mathbf{v}_{\parallel}$ and $v_z=\hat{\mathbf{z}}\cdot\mathbf{v}=v\cos\theta_0$, with $v=\|\mathbf{v}\|$, are the parallel and perpendicular components of its velocity $\mathbf{v}$ with respect to the plane of graphene. Given that graphene exhibits in-plane isotropy, it is natural to express the wavevector $\mathbf{k}$ using

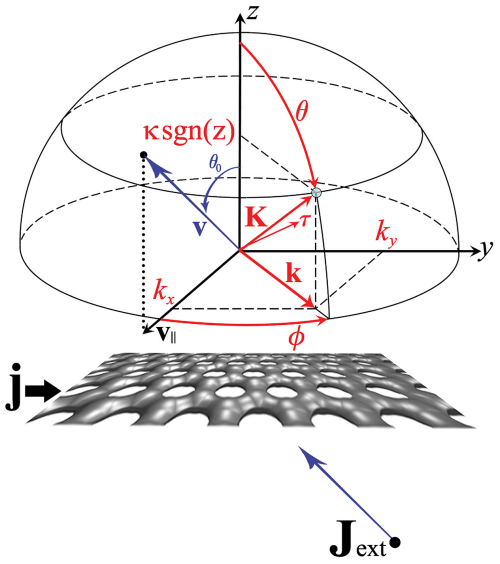

Figure 4.1: Geometry of the problem consisting of a 2D graphene sheet placed in vacuum and traversed by a fast charged particle under oblique incidence.

the plane polar coordinates, $\mathbf{k} = \{k, \phi\}$, where $k = \|\mathbf{k}\|$ and ϕ is the angle with respect to the direction of $\mathbf{v}_\parallel$, so that $\hat{\mathbf{k}} \cdot \mathbf{v}_\parallel = v_\parallel \cos\phi$ and $\hat{\boldsymbol{\tau}} \cdot \mathbf{v}_\parallel = -v_\parallel \sin\phi$, where $v_\parallel = \|\mathbf{v}_\parallel\| = v \sin\theta_0$. In order to obtain the electric field produced by the external particle, we insert Eqs. (4.5) and (4.3) into Eq. (4.2), giving

$$\mathbf{E}_{\text{ext}}(\mathbf{k}, z, \omega) = \frac{i}{\omega} A(k, \omega) \left[-q^2 \hat{\mathbf{k}}\hat{\mathbf{k}} + k_0^2 \hat{\boldsymbol{\tau}}\hat{\boldsymbol{\tau}} - kQ \left(\hat{\mathbf{k}}\hat{\mathbf{z}} + \hat{\mathbf{z}}\hat{\mathbf{k}} \right) + \left(k_0^2 - Q^2 \right) \hat{\mathbf{z}}\hat{\mathbf{z}} \right] \cdot \mathbf{J}_{\text{ext}}(\mathbf{k}, z, \omega), \tag{4.6}$$

where

$$A(k, \omega) = \frac{4\pi}{q^2 + Q^2}. \tag{4.7}$$

As a consequence of the dynamic polarization of charge carriers in graphene due to the moving external charge, the induced in-plane charge current in graphene may be expressed via the 2D Ohm's low, $\mathbf{j}(\mathbf{k}, \omega) = \overleftrightarrow{\sigma}(k, \omega) \cdot \mathbf{E}_\parallel(\mathbf{k}, 0, \omega)$, where $\mathbf{E}_\parallel(\mathbf{k}, 0, \omega)$ is the component of the total electric field parallel to graphene, evaluated at $z = 0$, simply the in-plane electric field. Here, $\overleftrightarrow{\sigma}(k, \omega)$ is the 2D conductivity tensor of graphene,

$$\overleftrightarrow{\sigma}(k, \omega) = \sigma_l(k, \omega)\, \hat{\mathbf{k}}\hat{\mathbf{k}} + \sigma_t(k, \omega)\, \hat{\boldsymbol{\tau}}\hat{\boldsymbol{\tau}}, \tag{4.8}$$

where any non-local effects are expressed via its dependence on $k = \|\mathbf{k}\|$ owing to the isotropy of graphene. Invoking the zero thickness approximation for graphene, the induced current in the structure may be written as

$$\begin{aligned} \mathbf{J}_{\text{ind}}(\mathbf{k}, z, \omega) &= \delta(z)\, \mathbf{j}(\mathbf{k}, \omega) \\ &= \delta(z)\, \overleftrightarrow{\sigma}(k, \omega) \cdot \mathbf{E}_{\parallel}(\mathbf{k}, 0, \omega). \end{aligned} \tag{4.9}$$

We may easily obtain the induced electric field by inserting Eqs. (4.3) and (4.9) back into Eq. (4.2) as

$$\mathbf{E}_{\text{ind}}(\mathbf{k}, z, \omega) = \overleftrightarrow{G}_{E0}(\mathbf{k}, z, \omega) \cdot \overleftrightarrow{\sigma}(k, \omega) \cdot \mathbf{E}_{\parallel}(\mathbf{k}, 0, \omega). \tag{4.10}$$

Thus, in order to determine induced electric field throughout the structure, we require a self-consistent procedure to find the in-plane total electric field, $\mathbf{E}_{\parallel}(\mathbf{k}, 0, \omega)$. This may be achieved by taking the in-plane components of Eqs. (4.5) and (4.9), followed by setting $z = 0$, and using them to express $\mathbf{E}_{\parallel}(\mathbf{k}, 0, \omega) = \mathbf{E}_{\text{ext}\parallel}(\mathbf{k}, 0, \omega) + \mathbf{E}_{\text{ind}\parallel}(\mathbf{k}, 0, \omega)$. As a result, we obtain a 2D "constitutive relation" in graphene,

$$\overleftrightarrow{\epsilon}(\mathbf{k}, \omega) \cdot \mathbf{E}_{\parallel}(\mathbf{k}, 0, \omega) = \mathbf{E}_{\text{ext}\parallel}(\mathbf{k}, 0, \omega), \tag{4.11}$$

where $\mathbf{E}_{\text{ext}\parallel}(\mathbf{k}, 0, \omega)$ is the component of the external electric field parallel to graphene, evaluated at $z = 0$. In the above equation, we have introduced a 2D dielectric tensor of graphene as

$$\overleftrightarrow{\epsilon}(k, \omega) = \epsilon_l(k, \omega)\, \hat{\mathbf{k}}\hat{\mathbf{k}} + \epsilon_t(k, \omega)\, \hat{\boldsymbol{\tau}}\hat{\boldsymbol{\tau}}, \tag{4.12}$$

where the longitudinal and transverse dielectric functions of graphene are defined as

$$\epsilon_l(k, \omega) = 1 + 2\pi i \frac{q(k, \omega)}{\omega} \sigma_l(k, \omega), \tag{4.13}$$

$$\epsilon_t(k, \omega) = 1 - 2\pi i \frac{\omega}{c^2 q(k, \omega)} \sigma_t(k, \omega), \tag{4.14}$$

respectively.

It is clear from Eqs. (4.11) and (4.12) that the longitudinal and transverse responses of graphene are decoupled. By evaluating the in-plane external electric field $\mathbf{E}_{\text{ext}\parallel}(\mathbf{k}, 0, \omega)$ from Eq. (4.6), one can easily solve Eq. (4.11) for the in-plane total electric field, which we write as $\mathbf{E}_{\parallel}(\mathbf{k}, 0, \omega) = E_{0l}\, \hat{\mathbf{k}} + E_{0t}\, \hat{\boldsymbol{\tau}}$, and obtain its longitudinal and transverse components as

$$E_{0l} = \frac{\mathcal{A}}{\epsilon_l} \left(1 - \frac{\omega}{c^2 k} \hat{\mathbf{k}} \cdot \mathbf{v}_{\parallel}\right), \tag{4.15}$$

$$E_{0t} = -\frac{\mathcal{A}}{\epsilon_t} \frac{\omega}{c^2 k} \hat{\boldsymbol{\tau}} \cdot \mathbf{v}_{\parallel}, \tag{4.16}$$

respectively. Here, $\mathcal{A} = -ik\frac{Ze}{v_z}A$ is the amplitude of the longitudinal component of the in-plane external electric field in the case of normal incidence, $\mathbf{v}_\parallel = \mathbf{0}$. It is obvious from Eq. (4.16) that the transverse component of the total in-plane electric field can only be exited in graphene in the case of oblique incidence, i.e., when $\mathbf{v}_\parallel \neq \mathbf{0}$.

Finally, having obtained $\mathbf{E}_\parallel(\mathbf{k}, 0, \omega) = E_{0l}\hat{\mathbf{k}} + E_{0t}\hat{\boldsymbol{\tau}}$, we can use Eq. (4.10) to express the induced electric filed throughout the structure as

$$\mathbf{E}_{\text{ind}}(\mathbf{k}, z, \omega) = 2\pi \mathrm{e}^{-q|z|}\left[\left(\frac{-iq}{\omega}\sigma_l E_{0l}\right)\hat{\mathbf{k}} + \left(\frac{i\omega}{c^2 q}\sigma_t E_{0t}\right)\hat{\boldsymbol{\tau}} + \left(\frac{k}{\omega}\,\text{sign}(z)\,\sigma_l E_{0l}\right)\hat{\mathbf{z}}\right]. \quad (4.17)$$

Moreover, one can obtain the induced magnetic field by the help of Eq. (4.17) along with Maxwell's equations as

$$\begin{aligned}\mathbf{H}_{\text{ind}}(\mathbf{k}, z, \omega) &= \frac{1}{ik_0}\left(i\mathbf{k} + \hat{\mathbf{z}}\frac{\partial}{\partial z}\right) \times \mathbf{E}_{\text{ind}}(\mathbf{k}, z, \omega) \\ &= \frac{2\pi}{c}\mathrm{e}^{-q|z|}\left[(\sigma_t E_{0t})\ \text{sign}(z)\,\hat{\mathbf{k}} - (\sigma_l E_{0l})\ \text{sign}(z)\,\hat{\boldsymbol{\tau}} + i\frac{k}{q}(\sigma_t E_{0t})\,\hat{\mathbf{z}}\right].\end{aligned} \quad (4.18)$$

4.2.2 Definitions of probability densities

As shown in Ref. [42] and the previous chapters, relativistic treatment of the interaction of an external charged particle with 2D materials in vacuum implies that the total energy lost by that particle may go into two contributions: (1) the Ohmic loss due to the electronic excitations and subsequent damping processes in those materials, and (2) the energy emitted in the far-field region in the form of TR. Accordingly, for each contribution, we may define the corresponding joint probability density as a function of the energy loss, $\hbar\omega \geq 0$, and the momentum transfer, $\hbar\mathbf{k}$, of the external particle. For the total energy loss of the external charged particle, we obtain

$$\begin{aligned}F_{\text{ext}}(\mathbf{k}, \omega) &= -\frac{1}{4\pi^3\omega}\Re\left\{\int_{-\infty}^{+\infty} dz\,\mathbf{J}_{\text{ext}}(\mathbf{k}, z, \omega)\cdot\mathbf{E}^*_{\text{ind}}(\mathbf{k}, z, \omega)\right\} \\ &= \frac{|\mathcal{A}|^2}{4\pi^3\omega}\left[\left(1 - \frac{\omega}{c^2 k}\hat{\mathbf{k}}\cdot\mathbf{v}_\parallel\right)^2\Re\left\{\frac{\sigma_l}{\epsilon_l}\right\} + \left(\frac{\omega}{c^2 k}\hat{\boldsymbol{\tau}}\cdot\mathbf{v}_\parallel\right)^2\Re\left\{\frac{\sigma_t}{\epsilon_t}\right\}\right],\end{aligned} \quad (4.19)$$

with ϵ_l and ϵ_t given in Eqs. (4.13) and (4.14), respectively. The joint density for the Ohmic loss is obtained as

$$\begin{aligned}F_{\text{ohm}}(\mathbf{k}, \omega) &= \frac{1}{4\pi^3\omega}\Re\left\{\int_{-\infty}^{+\infty} dz\,\mathbf{J}_{\text{ind}}(\mathbf{k}, z, \omega)\cdot\mathbf{E}^*(\mathbf{k}, z, \omega)\right\} \\ &= \frac{1}{4\pi^3\omega}\left[|E_{0l}|^2\,\Re\{\sigma_l\} + |E_{0t}|^2\,\Re\{\sigma_t\}\right],\end{aligned} \quad (4.20)$$

with E_{0l} and E_{0t} given in Eqs. (4.15) and (4.16), respectively.

The joint density for the radiative energy loss in the upper/lower half-space is obtained from the complex Poynting vector for $\omega > ck$ as

$$F_{\rm rad}^{\uparrow\downarrow}(\mathbf{k},\omega) = \frac{1}{4\pi^3\omega}\lim_{z\to\pm\infty}\Re\left\{\pm\hat{\mathbf{z}}\cdot\mathbf{S}(\mathbf{k},z,\omega)\right\}, \tag{4.21}$$

where the complex Poynting vector is defined via

$$\begin{aligned}\mathbf{S}(\mathbf{k},z,\omega) &= \frac{c}{4\pi}\,\mathbf{E}_{\rm ind}(\mathbf{k},z,\omega)\times\mathbf{H}^{*}_{\rm ind}(\mathbf{k},z,\omega)\\ &= \frac{\pi}{\omega}\left(|\sigma_l|^2\,|E_{0l}|^2 + \frac{\omega^2}{c^2\kappa^2}\,|\sigma_t|^2\,|E_{0t}|^2\right)\mathbf{K},\end{aligned} \tag{4.22}$$

with $\mathbf{K} = \mathbf{k} + \kappa\,\mathrm{sign}(z)\,\hat{\mathbf{z}}$ being the 3D wavevector with the magnitude of $\|\mathbf{K}\| = \omega/c$, which represents the direction of the Poynting vector, i.e., the direction of the transfer of EM energy into the far-field region. One may, also, obtain the total radiative energy loss, $F_{\rm rad}(\mathbf{k},\omega) = F_{\rm rad}^{\uparrow}(\mathbf{k},\omega) + F_{\rm rad}^{\downarrow}(\mathbf{k},\omega)$, as

$$F_{\rm rad}(\mathbf{k},\omega) = \frac{\kappa}{2\pi^2\omega^2}\left[|\sigma_l|^2\,|E_{0l}|^2 + \left(\frac{\omega}{c\kappa}\right)^2|\sigma_t|^2\,|E_{0t}|^2\right], \tag{4.23}$$

with E_{0l} and E_{0t} given in Eqs. (4.15) and (4.16), respectively. Furthermore, for radiation emitted at a frequency ω in a direction with the angle θ with respect to $\hat{\mathbf{z}}$ and with polar angle ϕ with respect to $\mathbf{v}_{\parallel}$, one can replace $k = \frac{\omega}{c}\sin\theta$ in the expression for $F_{\rm rad}(\mathbf{k},\omega) = F_{\rm rad}(k,\phi,\omega)$ in Eq. (4.23), and hence obtain the spectral angular distribution of the radiative energy loss as

$$\mathcal{S}(\theta,\phi,\omega) = \frac{\omega^3}{c^2}\,|\cos\theta|\,F_{\rm rad}\left(\frac{\omega}{c}\sin\theta,\phi,\omega\right). \tag{4.24}$$

It should be mentioned that the longitudinal contribution in Eq. (4.23) is a result of the term $E_{{\rm ind},l}H^{*}_{{\rm ind},t}$ in the complex Poynting vector, so that the radiated wave is transverse magnetic (TM) polarized, whereas the transverse contribution in Eq. (4.23) is a result of the term $E_{{\rm ind},t}H^{*}_{{\rm ind},l}$ in the complex Poynting vector, so that the radiated wave is transverse electric (TE) polarized with respect to the direction of propagation $\hat{\mathbf{K}}$ in the far-field region.

One should notice that in all of the above expressions for the joint energy loss densities, Eqs. (4.19), (4.20), and (4.23), the first terms in square brackets represent the contributions of the longitudinal response of graphene, while the second terms in square brackets represent the contributions of the transverse response of graphene. Moreover, it can be easily verified that the conservation of energy is explicitly upheld via the relation $F_{\rm ext}(\mathbf{k},\omega) = F_{\rm ohm}(\mathbf{k},\omega) + F_{\rm rad}(\mathbf{k},\omega)$.

While the radiative losses are restricted to frequencies above the light line, $\omega > ck$, both the total energy loss of the external particle and the Ohmic energy loss occur at all frequencies, $\omega > 0$. In a range below the light line, $\omega < ck$, we can denote the energy loss by $F^{<}_{\mathrm{ext}}(\mathbf{k},\omega) = F^{<}_{\mathrm{ohm}}(\mathbf{k},\omega)$, which may be written in a more familiar form in terms of the longitudinal and transverse loss functions of graphene, $\Im\{-1/\epsilon_l\}$ and $\Im\{1/\epsilon_t\}$, as

$$F^{<}_{\mathrm{ohm}}(\mathbf{k},\omega) = \frac{2}{\pi^2}\left(\frac{Ze}{v_z}\right)^2 \frac{1}{\left(\alpha^2+Q^2\right)^2\alpha}\left[\left(k-k_0\beta_\parallel\cos\phi\right)^2\Im\left\{\frac{-1}{\epsilon_l}\right\}+\alpha^2\beta_\parallel^2\sin^2\phi\,\Im\left\{\frac{1}{\epsilon_t}\right\}\right], \tag{4.25}$$

where we have defined the reduced parallel speed as $\beta_\parallel = v_\parallel/c$. In the non-retarded limit, one should set $\beta_\parallel \to 0$ and change $\alpha \to k$ in Eq. (4.25), confirming that transverse response of graphene only arises in a fully retarded regime.

It is further of interest to study the role of collective modes pertaining to the charge carrier excitations in graphene. Those modes can be formally identified in domains of the (k,ω) plane where: (a) the interband electron transitions may be neglected, (b) Landau damping due to the continuum of electron-hole excitations is absent, and (c) dissipative processes due to electron scattering on impurities, phonons or atomic-scale defects in graphene are sufficiently small. Under such conditions, one may set $\Re\{\sigma_l\} \to 0^+$ and $\Re\{\sigma_t\} \to 0^+$, so that the loss functions $\Im\{-1/\epsilon_l\}$ and $\Im\{1/\epsilon_t\}$ in Eq. (4.25) become proportional to Dirac delta functions peaked along the dispersion relations for longitudinal and transverse modes in graphene, $\omega = \omega_l(k)$ and $\omega = \omega_t(k)$, respectively. The corresponding eigenfrequencies, $\omega_l(k)$ and $\omega_t(k)$, may be obtained under such conditions by solving the equations $\Re\left\{\epsilon_l(k,\omega)\right\} = 0$ and $\Re\left\{\epsilon_t(k,\omega)\right\} = 0$, where

$$\Re\left\{\epsilon_l(k,\omega)\right\} = 1 - 2\pi\,\frac{\alpha(k,\omega)}{\omega}\Im\left\{\sigma_l(k,\omega)\right\}, \tag{4.26}$$

$$\Re\left\{\epsilon_t(k,\omega)\right\} = 1 + 2\pi\,\frac{\omega}{c^2\alpha(k,\omega)}\Im\left\{\sigma_t(k,\omega)\right\}, \tag{4.27}$$

showing that the longitudinal and transverse modes in graphene can only exist at frequencies below the light line, such that $\Im\left\{\sigma_l(k,\omega)\right\} > 0$ and $\Im\left\{\sigma_t(k,\omega)\right\} < 0$, respectively.

Finally, an integrated probability density can be expressed as the integration of the joint probability densities over the whole wavevector range via

$$\begin{aligned} P_\Lambda(\omega) &= \frac{1}{\hbar^2}\iint d^2\mathbf{k}\,F_\Lambda(\mathbf{k},\omega) \\ &= \frac{1}{\hbar^2}\int_0^{2\pi} d\phi\int_0^{\infty} dk\,k\,F_\Lambda(k,\phi,\omega), \end{aligned} \tag{4.28}$$

where $\Lambda = \mathrm{ext},\mathrm{ohm},\mathrm{rad}$. As one would expect, the energy conservation maintains that $P_{\mathrm{ext}}(\omega) = P_{\mathrm{ohm}}(\omega) + P_{\mathrm{rad}}(\omega)$ for all $\omega > 0$.

4.2.3 Models of conductivity

For the optical response of graphene in the THz-MIR range of frequencies, it suffices to take into account low-energy excitations involving its π electron bands described within the Dirac cone approximation. We consider in this work three models of conductivity of doped graphene in this range of frequencies: (a) Drude model for intraband excitations, suitable at THz frequencies, (b) optical conductivity of graphene combining the intra– and inter–band excitations, suitable at the THz to MIR frequencies, and (c) a model due to Lovat *et al.* [141], which includes the intraband electron-hole continuum of excitations, and is suitable at THz frequencies and finite wavenumbers k. While the Drude model and the optical conductivity are given in a strict long wavelength limit, $k \to 0$, the Lovat's model introduces non-local effects into the Drude model.

We note that the longitudinal and transverse conductivities of graphene, $\sigma_l(k,\omega)$ and $\sigma_t(k,\omega)$, are generally different quantities when the wavenumber k is finite, as in the case of Lovat's model, but in the long wavelength limit, they both become equal to a frequency dependent conductivity of graphene, $\sigma_l(0,\omega) = \sigma_t(0,\omega) = \sigma(\omega)$, which may be modeled either by the Drude conductivity or by the optical conductivity of graphene.

We will also consider a higher frequency range, corresponding to the energy losses of $\omega \gtrsim 1$ eV, which is usually probed in the low-energy EEL spectrum obtained with a (S)TEM [35, 37, 38, 39]. In this case, we employ a two-fluid hydrodynamic model (HD) suitable for describing high-energy interband electron transitions in intrinsic (undoped) graphene in the optical regime, which we amend by a Dirac correction to account for the lower energy interval [40].

Drude model conductivity

It has been shown that the intraband excitations in doped graphene are well represented by a Drude-type model of conductivity, [119, 142] which is given at finite temperature T by

$$\sigma_{\text{intra}}(\omega) = \frac{i}{4\pi}\frac{v_F^2 k_{TF}}{\omega + i\gamma}, \tag{4.29}$$

where $k_{TF} = 8e^2 \frac{k_B T}{(\hbar v_F)^2} \ln\left[2\cosh\left(\frac{\mu}{2k_B T}\right)\right]$ is the Thomas-Fermi wavenumber, with μ being the chemical potential of graphene and $v_F \approx c/300$ its Fermi speed. In the zero temperature limit, one obtains $\mu \to \mathcal{E}_F = \hbar v_F k_F$ and hence $k_{TF} \to 4\frac{v_B}{v_F}k_F$, where $\mathcal{E}_F$ is the Fermi energy of graphene and $k_F = \sqrt{\pi |n|}$ its Fermi wavenumber for charge carrier density n, whereas $v_B \equiv \frac{e^2}{\hbar} \approx c/137$ is the Bohr speed. In Eq. (4.29), γ is the damping rate due to electron scattering processes, which is largely unknown parameter that depends on the purity of graphene.

It is convenient to adopt nondimensionalized variables $\overline{k} = \frac{k}{k_c}$ and $\overline{\omega} = \frac{\omega}{\omega_c}$, where $k_c = \frac{1}{4}k_{TF}\left(\frac{v_F}{c}\right)^2$ and $\omega_c = ck_c$. We note that, for typical doping densities of graphene, the relevant unit of frequency is $\nu_c = \frac{2\pi}{\omega_c} \sim 1$ THz. Thus, the Drude conductivity is given in reduced form by $\overline{\sigma}_{\text{intra}} \equiv \frac{\sigma_{\text{intra}}}{c} = \frac{i}{\pi}\frac{1}{\overline{\omega}+i\overline{\gamma}}$, where $\overline{\gamma} = \frac{\gamma}{\omega_c}$ is the reduced damping rate. In an idealized case when $\overline{\gamma} \to 0$, upon using the Drude conductivity in Eqs. (4.26) and (4.27), one obtains a longitudinal mode pertaining to the so-called Dirac plasmon polariton (DPP), whereas no transverse modes exist because $\Im\{\overline{\sigma}_{\text{intra}}\} > 0$. A dispersion relation for the DPP mode obtained from the Drude model may be then expressed in a simple form using the reduced variables as $\overline{\alpha} = \frac{1}{2}\overline{\omega}^2$, where $\overline{\alpha} \equiv \frac{\alpha}{k_c} = \sqrt{\overline{k}^2 - \overline{\omega}^2}$.

The range of validity of the Drude model in Eq. (4.29) is given by a double inequality $kv_F \ll \omega \ll \omega_F$, where $\omega_F = \mathcal{E}_F/\hbar$ is the frequency associated with the Fermi energy in graphene [91]. In the reduced units, these inequalities amount to $\frac{v_F}{c}\overline{k} \ll \overline{\omega} \ll \varphi$, where $\varphi \equiv \frac{c}{v_B} \approx 137$ is the inverse of the fine structure constant.

Non-local model conductivity

Effects due to finite wavenumber k can be introduced into the conductivity of graphene at sufficiently low frequencies, such that $\omega \ll \omega_F$, by using the model developed by Lovat *et al.* [141]. Their model essentially generalizes the Drude conductivity by introducing the effects of intraband electron-hole continuum in the domain $0 < \omega < kv_F$ of the (k, ω) plane, thereby relaxing the lower frequency constraint of the Drude model, $kv_F \ll \omega$. Those authors obtained the longitudinal and transverse conductivities of graphene, which may be expressed in the reduced units used in our work as

$$\overline{\sigma}_l(\overline{k}, \overline{\omega}) = 2\frac{\overline{\sigma}_{\text{intra}}}{1+\chi}\frac{1}{\chi - i\frac{\overline{\gamma}}{\overline{\omega}}(1-\chi)}, \tag{4.30}$$

$$\overline{\sigma}_t(\overline{k}, \overline{\omega}) = 2\frac{\overline{\sigma}_{\text{intra}}}{1+\chi}, \tag{4.31}$$

respectively. Here, $\overline{\sigma}_{\text{intra}}(\overline{\omega})$ is the Drude conductivity given in Eq. (4.29) and the auxiliary factor $\chi(\overline{k}, \overline{\omega})$ is defined as

$$\chi = \sqrt{1 - \left(\frac{v_F}{c}\right)^2\left(\frac{\overline{k}}{\overline{\omega}+i\overline{\gamma}}\right)^2}. \tag{4.32}$$

While the longitudinal and transverse conductivities attain different values in the model due to Lovat *et al.*, the smallness of the factor $\left(\frac{v_F}{c}\right)^2 \approx 10^{-5}$ indicates that nonlocal effects are only observable at frequencies $\overline{\omega} \ll \overline{k}$, which lie deeply in the non-retarded regime, and hence they are

expected to be suppressed in the transverse response of graphene in comparison to its longitudinal response. Therefore, to the order of $\left(\frac{v_F}{c}\right)^2 \approx 10^{-5}$, the longitudinal and transverse conductivities become equal, and are given by the Drude model, $\overline{\sigma}_l = \overline{\sigma}_t = \overline{\sigma}_{\text{intra}}(\overline{\omega})$.

On the other hand, taking the limit $\overline{\gamma} \to 0$ for frequencies outside the continuum of intraband single-electron excitations, $\overline{\omega} > \overline{k}\,\frac{v_F}{c}$, one can ensure that the real parts of both $\overline{\sigma}_l$ and $\overline{\sigma}_t$ vanish, while their imaginary parts are found to be both positive. Therefore, by using Eqs. (4.30) and (4.31) in Eqs. (4.26) and (4.27), respectively, it follows that only a longitudinal mode exists with a dispersion relation, which is very close to that of a DPP mode from the Drude conductivity model.

Optical model conductivity

The upper frequency constraint of the Drude model, $\omega \ll \omega_F$, may be relaxed by adding to it the low-energy interband contribution, which is sometimes called Dirac conductivity. This contribution is given at zero temperature by [55, 142]

$$\sigma_{\text{inter}}(\omega) = i\frac{v_B}{4\pi}\ln\left(\frac{2\omega_F - \omega - i\gamma}{2\omega_F + \omega + i\gamma}\right). \tag{4.33}$$

It was shown by *ab initio* calculations [115] that, in the strict long wavelength limit, the conductivity of graphene at frequencies up to about $2\omega_F$ is well represented by the sum of the intra– and inter–band contributions given in Eqs. (4.29) and (4.33), $\sigma_{\text{opt}}(\omega) = \sigma_{\text{intra}}(\omega) + \sigma_{\text{inter}}(\omega)$, respectively. We shall call such model optical conductivity and apply it to the range of frequencies up to MIR, corresponding to an energy loss of the incident particle of about 1 eV.

Switching to reduced variables, we note that in the zero damping limit, $\overline{\gamma} \to 0$, the reduced interband conductivity becomes [55]

$$\overline{\sigma}_{\text{inter}} = \frac{1}{4\varphi}\left[\Theta(\overline{\omega} - 2\varphi) + \frac{i}{\pi}\ln\left|\frac{\overline{\omega} - 2\varphi}{\overline{\omega} + 2\varphi}\right|\right], \tag{4.34}$$

where Θ is the unit step function. One observes that $\Re\{\overline{\sigma}_{\text{inter}}\} \approx 0$ and $\Im\{\overline{\sigma}_{\text{inter}}\} < 0$ for frequencies $\overline{\omega} < 2\varphi \approx 274$, thus opening the possibility for excitation of a transverse mode in that interval. Indeed, by taking $\overline{\gamma} \to 0$ in that same frequency interval for the optical conductivity, we ensure that its real part vanishes, $\Re\{\overline{\sigma}_{\text{opt}}(\overline{\omega})\} \to 0$, while its imaginary part, $\Im\{\overline{\sigma}_{\text{opt}}(\overline{\omega})\}$, changes its sign at a critical frequency $\overline{\omega}_* \approx 1.667\,\varphi \approx 228$. Therefore, using the optical conductivity $\overline{\sigma}_{\text{opt}}(\overline{\omega})$ in Eqs. (4.26) and (4.27), one finds that a longitudinal mode can be excited at frequencies $0 < \overline{\omega} < \overline{\omega}_*$ and a transverse mode can be excited in the interval $\overline{\omega}_* < \overline{\omega} < 2\varphi$. We note that this interval covers a range around 1 eV, using the physical units. The corresponding

dispersion relations of those modes are given in reduced units as $\overline{\alpha} = \overline{\alpha}_l(\overline{\omega})$ and $\overline{\alpha} = \overline{\alpha}_t(\overline{\omega})$, where

$$\overline{\alpha}_l(\overline{\omega}) = \frac{\overline{\omega}^2}{2}\left[1+\frac{\overline{\omega}}{4\varphi}\ln\left(\frac{2\varphi-\overline{\omega}}{2\varphi+\overline{\omega}}\right)\right]^{-1}, \quad 0<\overline{\omega}<\overline{\omega}_*, \tag{4.35}$$

$$\overline{\alpha}_t(\overline{\omega}) = -2\left[1+\frac{\overline{\omega}}{4\varphi}\ln\left(\frac{2\varphi-\overline{\omega}}{2\varphi+\overline{\omega}}\right)\right], \quad \overline{\omega}_*<\overline{\omega}<2\varphi. \tag{4.36}$$

Therefore, in the case of optical conductivity, we can use Eq. (4.25) to obtain a modal decomposition in the regime when $\Re\{\overline{\sigma}(\overline{\omega})\} \to 0$, where the loss functions for the longitudinal and transverse responses of graphene are to be replaced by the Dirac delta functions, according to

$$\Im\left\{\frac{-1}{\epsilon_l}\right\} \to \pi\overline{\alpha}_l(\overline{\omega})\,\delta(\overline{\alpha}-\overline{\alpha}_l(\overline{\omega}))\,, \quad \text{for} \quad 0<\overline{\omega}<\overline{\omega}_*, \tag{4.37}$$

$$\Im\left\{\frac{1}{\epsilon_t}\right\} \to \pi\overline{\alpha}_t(\overline{\omega})\,\delta(\overline{\alpha}-\overline{\alpha}_t(\overline{\omega}))\,, \quad \text{for} \quad \overline{\omega}_*<\overline{\omega}<2\varphi, \tag{4.38}$$

respectively.

We note that the transverse mode in doped graphene was predicted by Mikhailov and Ziegler [133], and was studied in some detail by Stauber [101], but its confirmation has eluded experimentalists so far. Therefore, we use the optical model of conductivity to explore here the possibility to excite the transverse mode in graphene via electron beam under oblique incidence.

It is interesting to mention that, if a small gap Δ is opened between graphene's valence and conduction π electron bands, then the optical conductivity for an undoped graphene would be given by an expression similar to that given in Eq. (4.33) for interband transitions, but with the frequency ω_F replaced by $\Delta/(2\hbar)$ [101]. When a graphene layer that exhibits a finite gap Δ is also doped with its Fermi level shifted into the conduction or the valence band, then its optical conductivity would consist of both interband term governed by Δ, and an intraband term of the Drude form in Eq. (4.29), governed by the doping density of gapped graphene.

Extended hydrodynamic model conductivity

The optical response of graphene in the range of high frequencies, from MIR to UW, corresponding to the energy losses in an interval $1-30$ eV, is characterized by the high-energy $\pi \to \pi^*$ and $\sigma \to \sigma^*$ interband transitions [34, 43]. The energy loss function shows conspicuous features at about 4 eV and 14 eV [33, 143], which are usually labeled as the π and $\sigma+\pi$ "plasmon" peaks,

and their dispersion can be assessed through standard $k-$resolved EELS experiments. [37] In that range of energies, a two-fluid hydrodynamic (HD) model was found to be a good description for the polarization function χ_0, obtained as the sum of the contributions from π and σ electrons, $\chi_0 = \chi_\pi + \chi_\sigma$, with

$$\chi_\nu(q,\omega) = \frac{n_\nu^0 q^2/m_\nu^*}{s_\nu^2 q^2 + \omega_{\nu r}^2 - \omega(\omega + i\gamma_\nu)}, \tag{4.39}$$

where n_ν^0, m_ν^*, $\omega_{\nu r}$, $s_{\nu r}$, and γ_ν are the equilibrium surface number density of electrons, effective electron mass, restoring frequency, acoustic speed, and the damping rate in the νth fluid (where $\nu = \pi, \sigma$), respectively. In the optical limit, the conductivity of graphene is obtained as the sum of two Drude-Lorentz-like terms,

$$\begin{aligned} \sigma_{HD}(\omega) &= -ie^2\omega \lim_{q\to 0} \frac{\chi_0(q,\omega)}{q^2} \\ &= -ie^2\omega \left[\frac{n_\pi^0/m_\pi^*}{\omega_{\pi r}^2 - \omega(\omega + i\gamma_\pi)} + \frac{n_\sigma^0/m_\sigma^*}{\omega_{\sigma r}^2 - \omega(\omega + i\gamma_\sigma)} \right]. \end{aligned} \tag{4.40}$$

While this model provided a good fit of the dominant π and $\sigma + \pi$ peak structures in the spectra of graphene at energy losses $\gtrsim 3$ eV [33, 35], there are indications in the more recent experimental data that the Dirac physics of low-energy excitations in graphene could play important role at energy losses $\lesssim 2$ eV [30, 38, 39, 40]. The inadequacy of the model in Eq. (4.40) at such energies is readily indicated by the fact that $\sigma_{HD}(0) = 0$, whereas the conductivity of undoped graphene should approach the value of $v_B/4$ when $\omega \to 0$, i.e., the so-called universal optical conductivity of graphene [144]. In order to include the low-energy range, Djordjević *et al.* [40] extended the hydrodynamic model by adding a Dirac term $\sigma_D(\omega)$ describing the $\pi \to \pi^*$ interband electron transitions that occur near the K points in the Brillouin zone of graphene. The structure of the extended HD (eHD) model and its various parameters are determined through the application of the Kramers--Kronig relations and the f-sum rule, which maintains the conservation of the number of electrons participating in various excitation processes [40]. This yields the conductivity of undoped graphene in the form

$$\begin{aligned} \sigma_{eHD}(\omega) &= e^2 \left\{ \frac{1}{4\hbar} \frac{\omega_*^4}{\omega_*^4 + \omega^4} + i\frac{\omega}{m_e} \left[\frac{\omega_*^2 + \omega^2}{\omega_*^4 + \omega^4} \frac{\omega_* m_e \sqrt{2}}{8\hbar} \right.\right. \\ &\quad \left.\left. - \left(1 - \frac{\omega_* m_e \sqrt{2}}{8\hbar n_{at}} \right) \frac{n_\pi^0}{\omega_{\pi r}^2 - \omega(\omega + i\gamma_\pi)} - \frac{n_\sigma^0}{\omega_{\sigma r}^2 - \omega(\omega + i\gamma_\sigma)} \right] \right\}. \end{aligned} \tag{4.41}$$

It should be noted that the addition of the Dirac term introduces a parameter ω_* in Eq. (4.41), so that the universal conductivity of graphene is approached when $\omega \ll \omega_*$, giving $\sigma_{eHD}(0) = v_B/4$.

The parameter ω_* may be qualitatively interpreted as a cut-off frequency that separates the low-energy $\pi \to \pi^*$ electron transitions near the K points in the Brillouin zone of undoped graphene, which give rise to the universal conductivity when $\omega \to 0$, from the high-energy $\pi \to \pi^*$ electron transitions near the M points, which give rise to the π plasmon peak near $\omega_{\pi r}$ [40].

We adopt the above model with the following values for the parameters: $n_\pi^0 = n_{at} = 38$ nm^{-2}, $n_\sigma^0 = 114$ nm^{-2}, $\omega_{\pi r} = 4.19$ eV, $\omega_{\sigma r} = 14.15$ eV, $\gamma_\pi = 2.04$ eV, $\gamma_\sigma = 2.178$ eV, and $\omega_* = 3.54$ eV. These values ensure that the model reproduces satisfactorily several sets of experimental data for EELS on single-layered graphene [40], and agrees well with *ab initio* calculations of graphene's optical conductivity in a broad range of frequencies [115].

4.3 Results and discussion

In this section, we present calculations corresponding to the energy loss spectra of the electrons impinging on graphene under oblique incidence, using the conductivity models described in the previous section for diverse frequency regimes. One should note that, while the results of calculations using the eHD conductivity model for the high-frequency range are presented in the physical units, it is convenient to nondimensionalize the relevant variables in the other three models for low frequencies, covering the THz to MIR range, as described in the previous section.

There are several parameters that influence the low-energy loss spectra; two of them are associated with the external charged particle, i.e., the direction of its motion relative to graphene (quantified by θ_0) and its speed (quantified by β), and two of them are associated with the graphene sheet, i.e., the damping of its charge carriers' excitations (quantified by the rate γ) and the collective excitations of its charge carriers, or plasmon polariton modes described by the corresponding dispersion relations in the (k, ω) plane. In the low-frequency regime, we shall keep the normalized damping ratio fixed at a relatively low value of $\overline{\gamma} = 0.05$, unless we turn to a discussion of the role of the dispersion relations, which are obtained from the zeros of the dielectric functions in Eqs. (4.13) and (4.14) in the limit of vanishing damping. We have chosen a relatively small value of $\overline{\gamma} = 0.05$ in order to emphasize resonant features in the spectra due to the excitation of plasmon polariton modes at low energy losses. However, it should be stressed that we have found in the previous chapters that increasing values of $\overline{\gamma}$ exert rather strong influence on both the Ohmic and radiation energy losses, especially at the sub-THz frequencies, as in Ref. [42].

Throughout this section, we shall present and compare the decomposition of all energy loss channels into their longitudinal and transverse components in order to emphasize the importance of the oblique trajectories of the external particle for generating EM fields with different polar-

izations by the two types of the excitation mechanisms of charge carriers in graphene, which are descried by the dielectric functions in Eqs. (4.13) and (4.14).

4.3.1 Energy losses at the THz frequencies

The dynamic response of graphene in the THz range of frequencies is expected to be well described by the Lovat's model, as well as by the Drude model as its local limit. By comparing the results from those two models, we can directly assess the effects of nonlocality in the energy loss densities at those frequencies.

Figure 4.2 shows the normalized integrated energy loss density of the external charged particle, $\overline{P}_{\rm ext} = P_{\rm ext}/P_c$ with $P_c = 4/(\pi\mathcal{E}_F)$ where $\mathcal{E}_F$ is the Fermi energy of graphene, for two angles of incidence: $\theta_0 = 0$ in panel (a) and $\theta_0 = 60^\circ$ in panel (b), and for several external particle speeds β. We also show in each panel two separate contributions to the function $\overline{P}_{\rm ext}(\overline{\omega})$ coming from the longitudinal (dashed curves) and transverse (dotted curves) dielectric functions, see Eq. (4.19) with Eq. (4.28).

Under the normal incidence ($\theta_0 = 0$), shown in panel (a), there only exists a longitudinal contribution to the energy loss density $\overline{P}_{\rm ext}(\overline{\omega})$. The effect of nonlocality only becomes visible in the frequency range $0.1 \lesssim \overline{\omega} \lesssim 100$ for the very low speed of $\beta = 0.01$, i.e., in the nonretarded regime. For the low frequency range, $\overline{\omega} \lesssim 0.1$, the function $\overline{P}_{\rm ext}(\overline{\omega})$ exhibits a $\propto \overline{\omega}^{-1}$ dependence and increases in magnitude with the increasing speed of the charged particle. This is consistent with the findings of the prvious work [42] and Chapter 2, where it was shown that both the Ohmic energy loss (for finite damping rate) and the radiative energy loss exhibit the characteristic $\propto \overline{\omega}^{-1}$ dependence when $\overline{\omega} \to 0^+$, with their respective magnitudes increasing with β. Specifically, for the Ohmic energy loss, this can be seen from Eq. (2.62) in Chapter 2, whereas for the radiative energy loss, one can obtain from Eq. (48) in Ref. [42] that, in the limit $\overline{\omega} \to 0^+$ and for zero damping, the normalized integrated radiation energy loss density scales as $\overline{P}_{\rm rad}(\overline{\omega}) \sim \frac{2}{3}\frac{\beta^2}{\overline{\omega}}$ to within an accuracy of 10% for the normal incidence at the speeds $\beta \lesssim 0.5$.

On the other hand, a peak is observed in panel (a) of Fig. 4.2 at frequencies $\overline{\omega} \gtrsim 1$, where the Ohmic energy loss plays a dominant role (see Fig. 3 in Ref. [42]). That peak results from an interplay of the longitudinal Dirac plasmon polariton (LDPP) mode in graphene and the amplitude $|\mathcal{A}|^2$, see Eq. (4.19). The position of this LDPP-induced peak is seen in panel (a) to shift towards higher frequencies as the particle speed decreases. To understand such behavior of the peak in the energy loss spectra under the normal incidence, it suffices to consider the limit of zero damping, and refer to Eq. (47) in Ref. [42], which yields a peak in the integrated Ohmic energy loss density that is positioned at $\overline{\omega}_{\rm peak} = 2\sqrt{\beta^{-2} - 2}$. This shows that the peak frequency decreases with increasing speed, and the peak disappears for the speeds $\beta > 1/\sqrt{2}$.

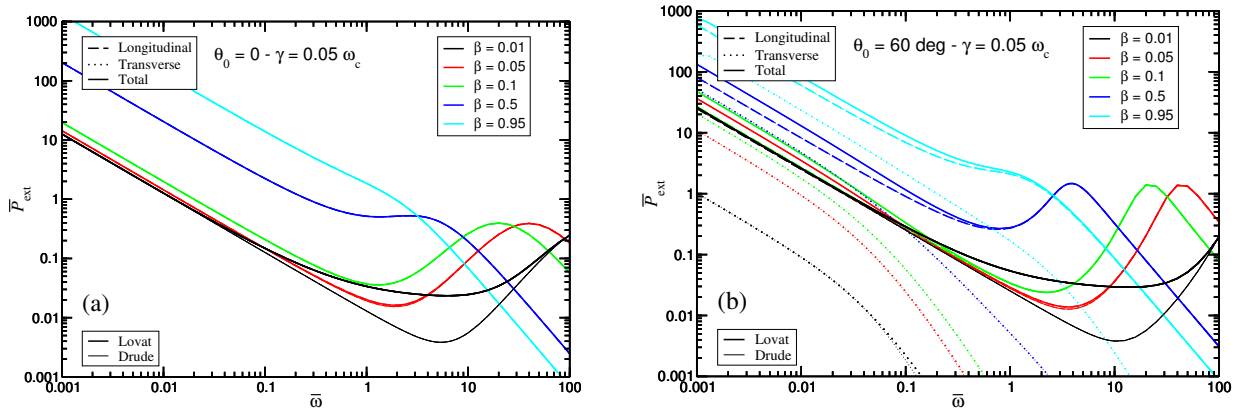

Figure 4.2: Normalized integrated energy loss density of the external charged particle, $\overline{P}_{\rm ext} = P_{\rm ext}/P_c$ with $P_c = 4/(\pi\mathcal{E}_F)$ where $\mathcal{E}_F$ is the Fermi energy of graphene, for two angles of incidence: (a) $\theta_0 = 0$ and (b) $\theta_0 = 60°$, and for several external particle speeds β, versus the reduced frequency $\overline{\omega} = \omega/\omega_c$. Also, shown are, in each panel, two separate contributions of longitudinal (dashed curves) and transverse (dotted curves) dielectric functions to the external loss. Nonlocal effects of the graphene's conductivity model on the loss spectra is depicted by the comparison of the Lovat's (thick lines) and Drude (thin lines) models. The reduced damping rate is fixed at $\overline{\gamma} = \gamma/\omega_c = 0.05$.

When the charged particle's trajectory becomes oblique to the plane of graphene, the transverse part begins to contribute to the energy loss density $\overline{P}_{\rm ext}(\overline{\omega})$, which is shown in panel (b) of Fig. 4.2 with the same speeds as in panel (a), but for the angle of incidence of $\theta_0 = 60^\circ$. It is observed that the transverse part mostly contributes to the energy loss in the low frequency range. Even though the transverse contribution remains generally smaller than the longitudinal contribution, their magnitudes can become comparable, e.g., for the speed $\beta \sim 0.1$ at frequencies $\overline{\omega} \lesssim 0.01$, as seen in panel (b). Furthermore, the effect of the nonlocality, which is exposed by comparing the Lovat's and Drude models for both the longitudinal and transverse contributions, appears to be similar to what was observed in panel (a). Namely, the nonlocal effect is only visible for sufficiently low speeds, i.e., in the nonretarded regime and, while it affects the longitudinal contribution in the same range of frequencies as in the case of the normal incidence, the nonlocal effect is practically ignorable for the transverse contribution, as indicated by the dotted black lines in panel (b). It is further noticed that both the transverse and the longitudinal contributions exhibit the same characteristic $\propto \overline{\omega}^{-1}$ dependence at the lowest frequencies, which is accompanied by an increase in magnitude with increasing particle speed, similar to the behavior observed in panel (a). On the other hand, while the longitudinal contribution exhibits a LDPP-induced peak at frequencies $\overline{\omega} \gtrsim 1$ in panel (b), with a similar peak position as in panel (a), the transverse contribution is heavily suppressed at such frequencies.

As was noticed above, the nonlocal effects only matter at low speeds, i.e., in the nonretarded regime. In order to investigate this regime in some detail, we study in Fig. 4.3 the normalized integrated densities for both the Ohmic energy loss, $\overline{P}_{\rm ohm} = P_{\rm ohm}/P_c$, in panel (a), and the radiative energy loss, $\overline{P}_{\rm rad} = P_{\rm rad}/P_c$, in panel (b), for the charged particle speed of $\beta = 0.01$ and for several angles of incidence. In this figure, one can further clarify the differences between the Lovat's and Drude models, as well as elucidate the relative weights of the longitudinal and transverse contributions to the Ohmic and radiative integrated densities in a nonretarded limit. As expected for this low speed, the effect of nonlocality is apparent at frequencies $\overline{\omega} \gtrsim 0.1$, but only for the Ohmic energy loss, as shown in panel (a). At the same time, panel (b) confirms that there is no effect of the nonlocality in the radiative energy loss, neither in the longitudinal nor in the transverse contributions, which is expected since the radiation loss is a purely relativistic phenomenon.

Regarding the magnitude of various contributions to the energy loss in Fig. 4.3, one notices that the radiative loss channels are significantly smaller than the corresponding Ohmic loss channels, as expected at such low speed. Moreover, the nonretarded regime is also responsible for the transverse contributions to both the Ohmic and the radiative energy losses being much smaller than the corresponding longitudinal contributions. Comparing panels (a) and (b) in that figure at frequencies $\overline{\omega} \lesssim 1$, one further notices that the longitudinal contribution to the Ohmic energy loss increases, while the same contribution to the radiation energy loss decreases with

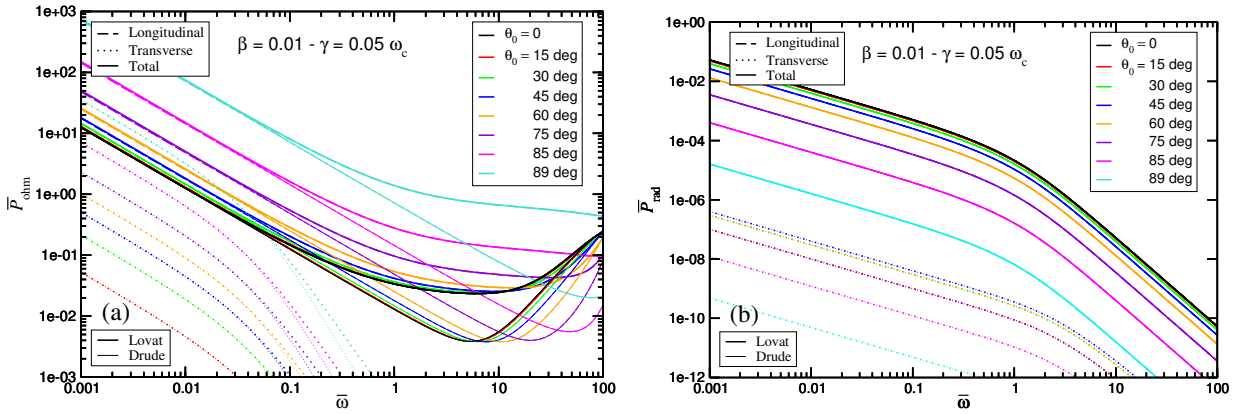

Figure 4.3: Normalized integrated probability densities for (a) Ohmic energy loss, $\overline{P}_{\rm ohm}(\overline{\omega}) = P_{\rm ohm}/P_c$, and (b) radiative energy loss, $\overline{P}_{\rm rad}(\overline{\omega}) = P_{\rm rad}/P_c$, for the charged particle speed of $\beta = 0.01$ (the nonretarded case) and for several angles of incidence. The differences between the Lovat's (thick lines) and Drude (thin lines) models, as well as the relative weights of the longitudinal (dashed lines) and transverse (dotted lines) contributions to the Ohmic and radiative integrated densities in a nonretarded limit are also shown. The reduced damping rate is fixed at $\overline{\gamma} = 0.05$.

increasing angle of incidence θ_0. The latter observation is consistent with the observations in Fig. 4.2, implying that it is the normal component of the external particle speed, $\beta\cos\theta_0$, that likely governs the magnitude of the longitudinal contribution to the radiative energy loss channels. Namely, given that the radiation is most effectively produced by accelerating the charge carriers in graphene, a reduction in the perpendicular component of the speed would bring down the "abruptness" of graphene's interaction with the external charged particle and hence reduce the production of TR. Clearly, for a strictly parallel trajectory, there can be no radiation (Chapter 3). For a more quantitative assessment, one may invoke the analysis of Fig. 4.2(a) based on Eq. (48) in Ref. [42], and hence surmise that the longitudinal contribution to the radiative energy loss scales as $\propto (\beta\cos\theta_0)^2$.

Regarding the dependence of the transverse contributions to the Ohmic and radiative energy losses on the incident angle, similar conclusions can be drawn as for the longitudinal contributions, with a peculiar "anomaly" seen in panel (b), where the transverse contribution to the radiative energy loss exhibits an apparently symmetric maximum about the incident angle $\theta_0 = \pi/4$. This can be explained in the following way. By looking at the transverse part of Eq. (4.23), with the transverse component of the in-plane tangential electric field given in Eq. (4.16), which contains the factor $\hat{\boldsymbol{\tau}} \cdot \mathbf{v}_{\parallel}$. Therefore, the magnitude of the transverse contribution to the radiative energy loss is proportional to $\sin^2\theta_0$, so it vanishes as the incident particle approaches graphene

under a grazing angle of incidence, i.e., on a near-parallel trajectory. On the other hand, one notices in panel (b) that there exist equal spacings between any pair of the curves representing the transverse or longitudinal contributions to the radiative energy loss at low frequencies, $\overline{\omega} \lesssim 1$, for incident angles $\theta_0 \geq \pi/4$. This indicates that the transverse contribution likely scales the same way as the longitudinal contribution to the radiative energy loss in terms of the normal component of the external particle speed, that is, $\propto \cos^2\theta_0$. Thus, one may surmise that the transverse contribution to the radiative energy loss is proportional to $\sin^2(2\theta_0)$ for the incident speeds $\beta \lesssim 0.5$, and it therefore should exhibit a symmetric maximum about $\theta_0 = \pi/4$.

As we have discussed so far, the effect of nonlocality on the energy loss spectra becomes salient for nonretarded speeds. However, relative contribution of the transverse part with respect to the longitudinal part in the energy loss is expected to increase with increasing speed of the external particle, i.e., by going into the regime where the retardation effects dominate. To explore that regime, we show in Fig. 4.4 a decomposition into the longitudinal and transverse contributions to the energy loss spectra in a manner similar to that employed in Fig. 4.3, but for a significantly higher incident speed of $\beta = 0.5$. In this regime, the Ohmic and radiative energy losses attain comparable magnitudes, at least at the frequencies $\overline{\omega} \lesssim 1$ and at the angles of incidence that are not too oblique. Thus, in addition to showing the Ohmic energy loss in panel (a) and the radiative energy loss in panel (b), we also show the total energy loss of the external particle in panel (c) of in Fig. 4.4, all for various angles of incidence. As expected, no differences are observed between the Drude and Lovat's models in any of the shown spectra, confirming that the nonlocal effects are negligible at such high speed.

The dependencies on the angle of incidence for all contributions shown in panels (a) and (b) of Fig. 4.4 at low frequencies, are analogous to the trends observed in Fig. 4.3. As in Fig. 4.3(a), one notices in Fig. 4.4(a) that the longitudinal contribution to the Ohmic loss at low frequencies increases with the increasing angle of incidence. This may be tentatively explained by the increasing time that the incident particle spends interacting with the near fields induced by the graphene's charge carriers, which scales as $\propto \sec\theta_0$. However, it is remarkable that, for incident angles $\theta_0 > 60°$, the longitudinal contribution to the Ohmic energy loss at low frequencies in Fig. 4.4(a) has a comparable magnitude as the same contribution in Fig. 4.3(a), which is quite surprising given the large difference in the incident speed β between the two figures and the trend observed in Fig. 4.2.

One can observe in panel (a) of Fig. 4.4 that, while both contributions to the Ohmic loss increase in magnitude with increasing angle of incidence, the longitudinal contribution dominates at higher frequencies, where it exhibits an LDPP-induced peak, whereas the transverse contribution may become dominant at lower frequencies, say $\overline{\omega} \lesssim 0.1$, for sufficiently oblique trajectories, say $\theta_0 \gtrsim 60°$. The latter observation may be rationalized by recalling that the transverse contribution is mostly a result of retardation effects, which are enhanced at lower frequencies

and for larger parallel components of the incident speed. At the same time, one observes in panel (b) of Fig. 4.4 that the total radiative energy loss decreases with increasing angle of incidence, with a similar rationale as that provided in the case studied in Fig. 4.3. Moreover, for all directions of incidence, the transverse contribution to the radiative energy loss is seen to be negligible compared to the longitudinal contribution, while still exhibiting a symmetric maximum at the incident angle $\theta_0 = \pi/4$, as discussed in Fig. 4.3(b).

The LDPP-induced peak in the longitudinal contribution to the Ohmic energy loss density is observed in panels (a) and (c) of Fig. 4.4 at a frequency that is significantly lower than the peak in panel (a) of Fig. 4.3, which is consistent with the trend observed Fig. 4.2 for increasing total speed β. It is important to notice that this peak grows larger in magnitude for trajectories closer to the parallel direction. This may be also rationalized by noticing that, the more time the incident particle spends interacting with the near fields induced by the graphene's charge carriers, the more of its energy will go to the excitation of the LDPP mode in graphene.

It is worthwhile exploring the evolution of the position and the shape of the LDPP-induced peak as the incident angle θ_0 of the charged particle increases towards parallel trajectory. To that effect, we consider the overlap of the resonance condition for exciting the LDPP mode with a dispersion relation [42] $\overline{\omega} = \overline{\omega}_{\rm LDPP}(\overline{k})$, where $\overline{\omega}_{\rm LDPP}(\overline{k}) = \sqrt{2\left(-1+\sqrt{1+\overline{k}^2}\right)}$ [42], and the so-called kinematic condition, $\omega = \mathbf{k}\cdot\mathbf{v}_\parallel$, which maximizes the amplitude A of the excitation mechanism, given in Eq. (4.7) (see Chapter 3). One notices that the latter condition covers the region $0 \leq \overline{\omega} \leq \overline{k}\beta_\parallel$ in the $(\overline{k},\overline{\omega})$ plane, with an upper boundary that increases with increasing incident angle. In the limit of a (near-) parallel trajectory, we may refer to the longitudinal contribution in Eq. (3.21) of Chapter 3, to further observe that the Ohmic energy loss *rate*, $\mathcal{R} = \frac{dW}{dt}$, is maximized when $\omega = kv_\parallel$, or $\overline{\omega} = \overline{k}\beta_\parallel$. Hence, using the crossing of the LDPP dispersion relation with the upper boundary of the kinematic region in the $(\overline{k},\overline{\omega})$ plane, we obtain an equation $\overline{\omega}_{\rm LDPP}(\overline{k}) = \overline{k}\beta_\parallel$, which is readily solved for $\overline{k}$ to yield a reduced frequency $\overline{\omega}_\parallel = 2\sqrt{\beta_\parallel^{-2}-1} = 2\sqrt{\beta^{-2}\mathrm{cosec}^2\theta_0 - 1}$, corresponding to a maximal rate of excitation of the LDPP mode for a given incident trajectory. This frequency is found to closely match the positions of the cusp-like peaks observed in Fig. 4.4(a) in the solid curves describing the longitudinal contribution to the Ohmic energy loss for sufficiently large angles of incidence.

Moreover, one can estimate the total energy, W, lost to the excitation of the LDPP mode for a near-parallel trajectory by invoking the result for the energy loss rate $\mathcal{R}(b)$ for the case of a parallel trajectory with the external particle moving at a fixed distance b from graphene, which is given by the first term in Eq. (3.21) of Chapter 3. Using the adiabatic approximation [145], one may then write $W = \frac{1}{v_z}\int_{-\infty}^{\infty} db\,\mathcal{R}(b) \equiv \hbar^2\int_0^\infty d\omega\,\omega P_\parallel(\omega)$, which, in the limit of zero damping, readily yields an estimate for the longitudinal contribution to the Ohmic energy loss density for

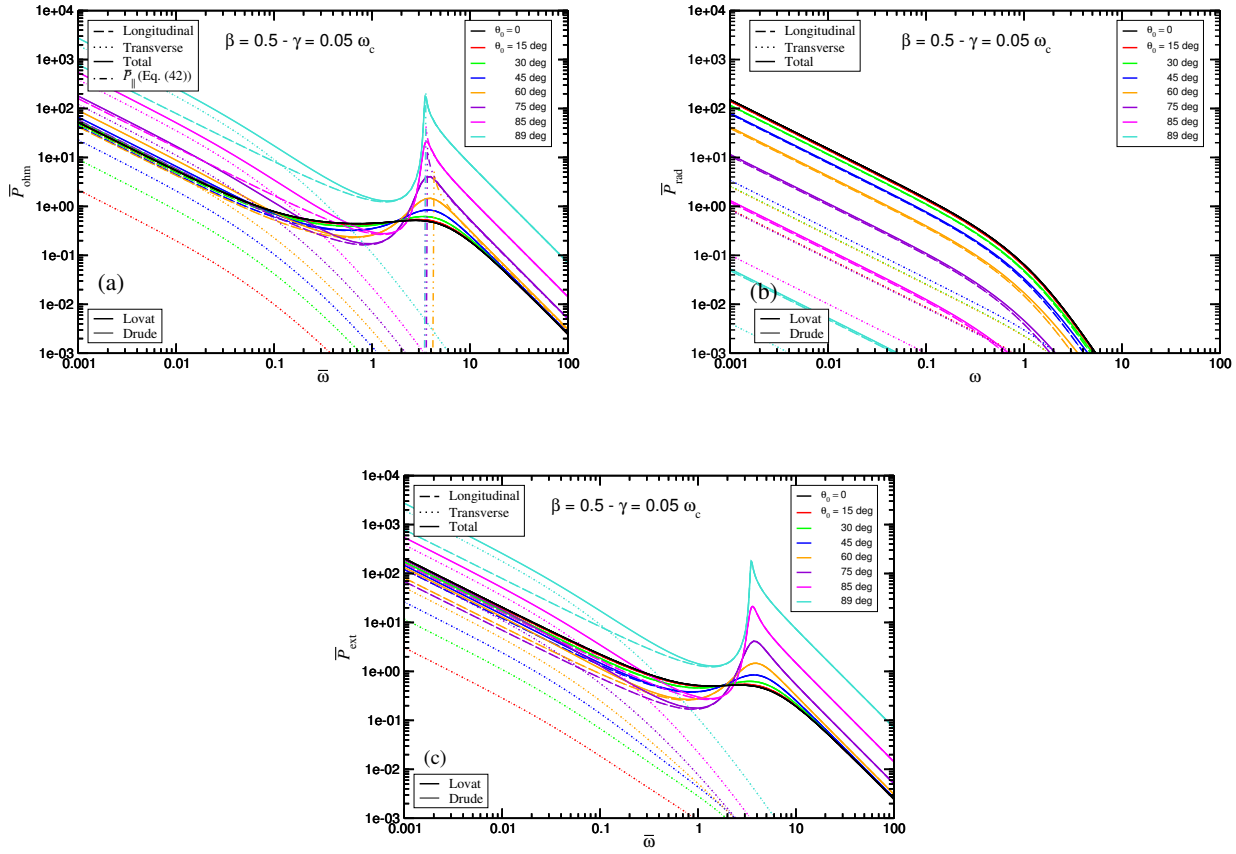

Figure 4.4: Normalized integrated probability densities for (a) Ohmic energy loss, $\overline{P}_{\rm ohm}(\overline{\omega})$, (b) radiative energy loss, $\overline{P}_{\rm rad}(\overline{\omega})$, and (c) external energy loss, $\overline{P}_{\rm ext}(\overline{\omega}) = \overline{P}_{\rm ohm}(\overline{\omega}) + \overline{P}_{\rm rad}(\overline{\omega})$, for the charged particle speed of $\beta = 0.5$ and for several angles of incidence. The differences between the Lovat's (thick lines) and Drude (thin lines) models, as well as the decomposition of the longitudinal (dashed lines) and transverse (dotted lines) contributions to those integrated densities are shown. Also included are, in panel (a), calculations for the Ohmic energy loss density at high frequencies using the approximation for $\overline{P}_{||}$ given in Eq. (4.42), for $\theta_0 \gtrsim 60°$ (dash-double dotted curves). The reduced damping rate is fixed at $\overline{\gamma} = 0.05$.

a sufficiently grazing angle of incidence,

$$\overline{P}_{\parallel} \approx \frac{2\pi}{\beta^2 \sin(2\theta_0)} \frac{\overline{\omega}}{\overline{\omega}^2 + 4} \frac{\Theta(\overline{\omega} - \overline{\omega}_{\parallel})}{\sqrt{\overline{\omega}^2 - \overline{\omega}_{\parallel}^2}}. \tag{4.42}$$

We note that the result in Eq. (4.42) closely reproduces solid curves in Fig. 4.4(a) for frequencies $\overline{\omega} > \overline{\omega}_{\parallel}$ and for the incident angles $\theta_0 \gtrsim 60^\circ$.

4.3.2 Angular distribution of the emitted THz radiation

Since the transverse contribution to the radiative energy loss densities in panels (b) of the Figs. 4.3 and 4.4 was always found to have much smaller magnitude than the longitudinal contribution, it is instructive to further compare those two contributions in the angular distribution of TR at several typical frequencies. In Fig. 4.5, we show the angular distribution of the spectral density for TR in reduced units, $\overline{\mathcal{S}}(\theta, \phi, \overline{\omega}) = \mathcal{S}/\mathcal{S}_c$ with $\mathcal{S}_c = (Ze)^2/c$ for the external particle with the speed $\beta = 0.5$ and the angle of incidence of $\theta_0 = 60^\circ$, and for three different frequencies, $\overline{\omega} = 0.5$, 1 and 5. In the left, middle and right columns, we show the longitudinal contribution, transverse contribution and the total angular radiative spectra, respectively. As expected, the radiation patterns are always symmetric with respect to the plane of graphene, as well as with respect to the xz-plane, i.e., the plane of incidence of the external charged particle. By the comparison of the left and middle columns, it is seen that, generally, the longitudinal contribution is larger in magnitude when compared to the transverse contribution, but the difference is not as large as implied by the curves in Fig. 4.4(a). As a matter of fact, by increasing the frequency, the transverse contribution in Fig. 4.5 becomes even comparable to the longitudinal contribution when viewed in different directions, although both contributions decrease in overall magnitude as the frequency increases.

Another important point to note is that the longitudinal contribution mostly radiates in directions far from the z axis or, more precisely, in directions close to the plane of graphene, $\theta \approx \pi/2$, covering a broad range of the polar angle ϕ values with a peak in the (projected) direction of motion of the external particle. At the same time, the transverse contribution mostly radiates in directions close to the z-axis, i.e., perpendicular to graphene with θ close to 0 or π, whereas the range of values covered by the polar angle ϕ becomes broader with increasing frequency $\overline{\omega}$, showing a pronounced minimum in the (projected) direction of motion of the external particle, $\phi = 0$. Thus, the longitudinal and the transverse contributions to TR exhibit somewhat complementary angular patterns, both with respect to the plane of graphene and the plane of incidence of the external charged particle.

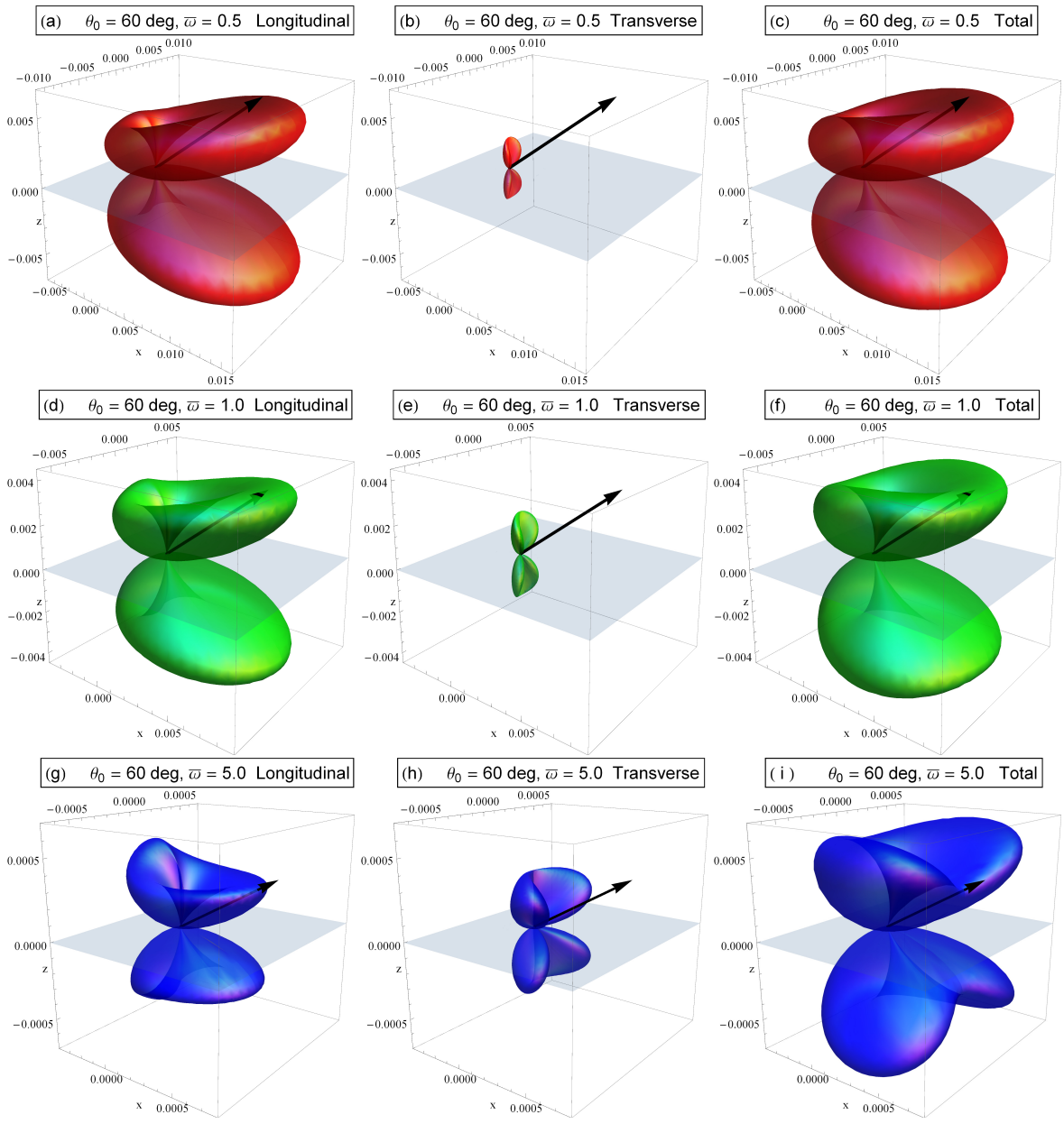

Figure 4.5: Angular distribution of the spectral density for TR in reduced units, $\overline{\mathcal{S}}(\theta, \phi, \overline{\omega}) = \mathcal{S}/\mathcal{S}_c$ with $\mathcal{S}_c = (Ze)^2/c$ for the external particle with the speed $\beta = 0.5$ and the angle of incidence of $\theta_0 = 60°$, and for three different frequencies, $\overline{\omega} = 0.5$, 1 and 5. In the left, middle and right columns, we show the longitudinal contribution, transverse contribution and the total angular radiative spectra, respectively. The reduced damping rate is fixed at $\overline{\gamma} = 0.05$ and the Lovat's model has been used for the conductivity tensor.

In order to further expose the anisotropy of the radiation patterns, we show in Fig. 4.6 the cross sections of the angular distribution of the spectral density for TR in the plane of incidence, $\overline{\mathcal{S}}(\theta, \phi = 0, \overline{\omega})$, for an external particle with the speed $\beta = 0.5$ and three angles of incidence, $\theta_0 = 15°$ in panel (a), $\theta_0 = 45°$ in panel (b), and $\theta_0 = 85°$ in panel (c), for several frequencies. These panels represent the total angular distribution, which is identical to the longitudinal contribution, because the factor $\sin^2\phi$ renders the transverse contribution identically zero in the plane of incidence, see Eqs. (4.16), (4.23) and (4.24). One can see in Fig. 4.6 that the overall magnitude of the TR patterns decreases with increasing frequency and with increasing angle of incidence θ_0. In general, all the TR patterns are skewed towards the plane of graphene, and they become more asymmetric with respect to the z-axis as the incident trajectory becomes more oblique. Interestingly, while the main lobes of the TR patterns occur between the direction of motion of the external particle and graphene, i.e., in a range of emission angles $\theta_0 < \theta < \pi/2$ for the incident angles $\theta_0 = 15°$ and $\theta_0 = 45°$, when the angle of incidence is very close to graphene, $\theta_0 = 85°$, the lobes of the maximum TR occur at the emission angles above the direction of motion, $\theta > \theta_0$, although quite close to it. With such peculiar features, it would be quite feasible to perform the CL type of measurements of the emitted radiation in STEM [53], which would be able to not only detect the anisotropy in the angular patterns of the emitted radiation from graphene, but also resolve the polarization of the emitted waves coming from the longitudinal and transverse contributions as the TM and TE polarizations, respectively.

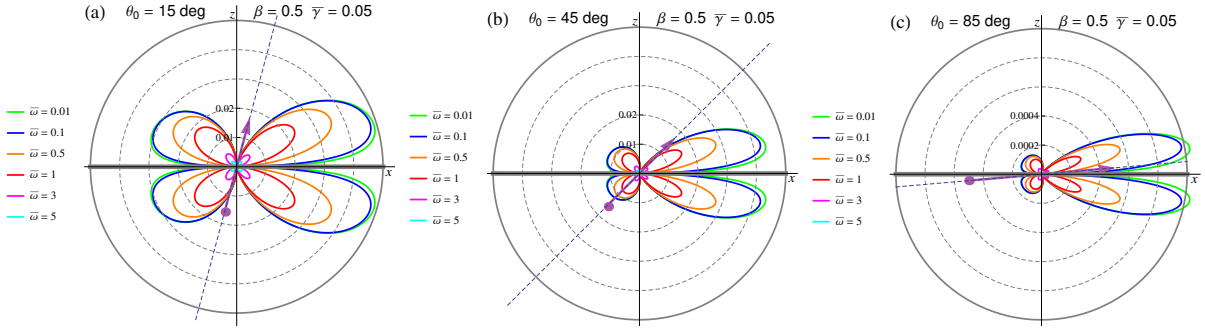

Figure 4.6: The cross section of the angular distribution of the spectral density for TR in the plane of incidence, $\overline{\mathcal{S}}(\theta, \phi = 0, \overline{\omega})$, for an external particle with the speed $\beta = 0.5$ and three angles of incidence, (a) $\theta_0 = 15°$, (b) $\theta_0 = 45°$, and (c) $\theta_0 = 85°$, for several frequencies. These panels represent the total angular distribution, which is identical to the longitudinal contribution. The spectra are calculated employing Lovat's conductivity model for graphene where the reduced damping rate is fixed at $\overline{\gamma} = 0.05$.

On the other hand, the interaction of externally moving charged particles with 2D materials plays an important role in the prospective design of a stable, highly tunable source of THz ra-

diation. In this regard, there have been several recent proposals to use the EM radiation from graphene induced by a fast electron beam, moving either parallel [25, 50] or normal to graphene [52]. In all of those proposals, both the doping density in graphene and the speed of the external particle were suggested as possible tuning parameters for such radiation sources, while the issue of the polarizability of the radiated EM waves was not explicitly addressed. We have seen that the direction of the trajectory of motion of the external particle relative to a 2D material may also be used as a suitable tuning parameter for such sources of radiation, which could possibly help select different polarizations of the radiated EM waves.

4.3.3 A search for the transverse mode

While all the above results were obtained using the Drude and the Lovat's models of graphene's conductivity, which cover the frequencies $\overline{\omega} \lesssim 100$, we next investigate the possibility to excite the transverse mode by adopting the optical model of graphene's conductivity, which supports both the LDPP mode due to the intraband electronic excitations at low frequencies and the transverse mode due to the interband electronic transitions involving the range of frequencies $228 < \overline{\omega} < 274$, as discussed in the previous section. Figure 4.7 depicts the integrated probability density for the Ohmic energy loss, $P_{\rm ohm}$, of a graphene sheet described by the optical conductivity model, along with its decomposition into the longitudinal and transverse contributions, for a charged particle at the speed $\beta = 0.5$. While in panel (a) we show the results for different angles of incidence, in panel (b) we explore the effects of varying the damping rate $\overline{\gamma}$.

One observes in Fig. 4.7(a) that the Ohmic energy loss increases in magnitude as the external particle's trajectory becomes more inclined towards graphene, as noted above. Particularly, the LDPP-induced peak at $\overline{\omega} > 1$ in the longitudinal contribution becomes more pronounced with increasing θ_0, whereas at low frequencies, both the longitudinal and transverse contributions to the Ohmic energy loss echo the behavior observed in Fig. 4.4(a) at $\overline{\omega} < 1$. As was discussed in our previous work [42] and also Chapter 2, the very low frequency range, $\overline{\omega} \lesssim 1$, is where the effect of damping rate is rather strong, and the middle frequency range, $1 \lesssim \overline{\omega} \lesssim 100$, is where the excitation of the LDPP mode is dominant, whereas the MIR frequency range of $228 \leq \overline{\omega} \leq 274$, shown in the insets in Fig. 4.7, is where the excitation of the transverse mode should take place. In the inset of panel (a), we see negligibly small energy loss densities for both the longitudinal and transverse contributions, which do increase with the increasing angle of incidence. However, the transverse contribution is always smaller than the longitudinal contribution, which exhibits a high-frequency tail, with a dip that extends over the frequency range $228 < \overline{\omega} < 274$, owing to the finite value of damping rate, $\overline{\gamma} = 0.05$, used in panel (a).

In order to demonstrate a regime where only the transverse contribution would survive, we

explore the effects of varying the damping ratio in panel (b) of Fig. 4.7 with a special role played by the idealized case of zero damping, $\overline{\gamma} = 0$. Namely, in that case the only mechanism for energy loss of the external charged particle involves Ohmic losses due to excitation of the collective modes in graphene (see Chapter 2). Specifically, by using Eq. (4.25) in (4.28) to evaluate the Ohmic energy loss density by means of Eqs. (4.37) and (4.38), we expect that the LDPP mode will give a nonzero longitudinal contribution in the range of frequencies $0 < \overline{\omega} < 228$, and a nonzero transverse contribution in the range of frequencies $228 < \overline{\omega} < 274$, respectively.

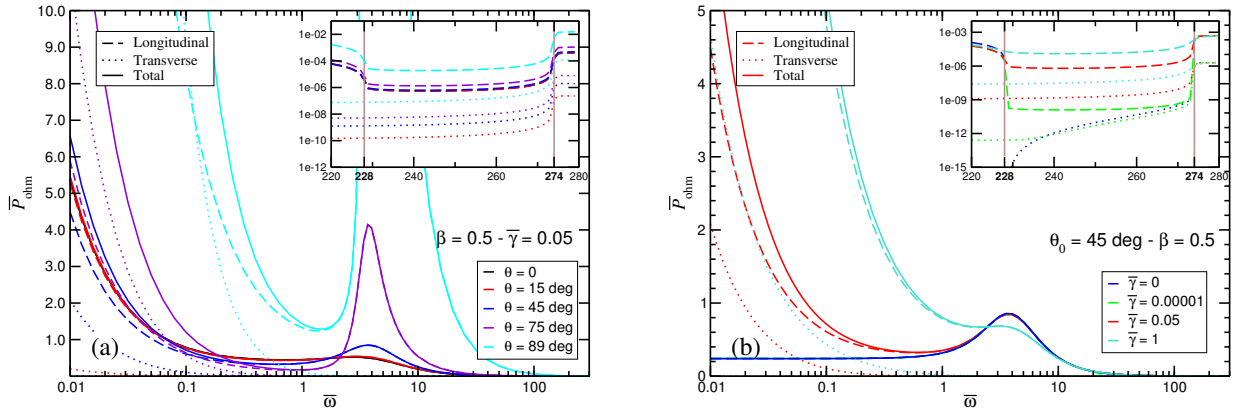

Figure 4.7: Integrated probability density for the Ohmic energy loss, $P_{\rm ohm}$, of a graphene sheet described by the optical conductivity model, along with its decomposition into the longitudinal (dashed lines) and transverse (dotted lines) contributions, for a charged particle at the speed $\beta = 0.5$. Panel (a) represents the results for different angles of incidence with fixed $\overline{\gamma} = 0.05$ and panel (b) shows the investigation of the effects of varying the damping rate $\overline{\gamma}$ which includes the probability density for the excitations of the LDPP and TDPP modes. The inset of each panel depicts a closer focus at the range of $228 \lesssim \overline{\omega} \lesssim 274$ where the excitation of the transverse mode occurs.

While both the longitudinal and transverse contributions to the Ohmic energy loss in panel (b) show great variability with increasing $\overline{\gamma}$ at low frequencies, $\overline{\omega} \lesssim 1$, the situation in the inset to panel (b) is not much changed compared to the inset to panel (a), except in the case $\overline{\gamma} = 0$. Namely, one observes in the inset to Fig. 4.7(b) that, for $\overline{\gamma} = 0$, the tail of the density for the longitudinal contribution (blue dashed line) terminates at the frequency $\overline{\omega} = 228$, whereas the density of the transverse contribution (blue dotted line) shows an onset on that frequency, and it continues increasing with the frequency going up to $\overline{\omega} = 274$, where this contribution terminates. Hence, this shows that the transverse mode may indeed be excited by an external charged particle under oblique incidence upon graphene, although its signature in the energy loss density would

not be in the form of a well-defined peak, as in the case of the LDPP mode. Rather, the transverse mode in a graphene with negligible damping of its charge carriers would show as a cusp in the Ohmic energy density at a frequency $\overline{\omega} \leq 274$, with a hopelessly low probability.

It should be finally mentioned that the effects of finite temperature make the transverse mode unstable, as shown in Ref. [146].

4.3.4 EELS of graphene at high frequencies

While most experiments using EELS of graphene in STEM [35, 38, 39], as well as the theoretical models of those experiments [33, 34, 38, 40], considered fast electrons under normal incidence upon graphene, there has been recent work that also studied oblique incidence in a momentum-resolved measurement of the dispersion properties of the π and $\sigma + \pi$ "plasmon" peaks in the energy loss spectra [37]. With the advent of the novel monochromatic techniques in STEM [30], it became possible to probe electron energy losses well below 1 eV, thereby accessing the range of the low-energy interband $\pi \rightarrow \pi^*$ electronic transitions in intrinsic (undoped) graphene in the Dirac cone approximation. Therefore, we use the eHD model of graphene's conductivity to assess the relative roles of the longitudinal and transverse contributions to both the Ohmic and radiative energy loss spectra of electrons traversing the graphene layer under oblique incidence in a STEM setting.

In panel (a) of Fig. 4.8 we show the integrated probability density of the energy loss, $P_{\rm ext}(\omega)$, as a function of the energy ω (we set here $\hbar = 1$), lost by an incident electron with the speed $\beta = 0.5$ for a broad range of incident angles, whereas in the inset to that figure we show the corresponding energy loss due to the emitted TR, $P_{\rm rad}(\omega)$. One notices that the magnitude of the radiation energy loss is very much smaller than $P_{\rm ext}(\omega)$, so that practically $P_{\rm ext}(\omega) \approx P_{\rm ohm}(\omega)$. One may confirm from Fig. 4.8(a) that, while the Ohmic energy loss density increases in magnitude with increasing angle of incidence, in a proportion that scales with $\sec\theta_0$ for angles $\theta_0 \gtrsim 60°$, the opposite trend is seen for the radiative energy loss density in the inset to that figure, which decreases with the increasing θ_0. Those trends are consistent with observations made in Figs. 4.3 and 4.4 at the THz range of frequencies. Namely, the increase in the Ohmic energy loss scales with increased time the external particle spends interacting with the near-fields induced by the excitation of graphene's charge carriers, whereas the decrease in the radiative energy loss is governed by a decrease in the perpendicular component of the external particle speed, $\beta\cos\theta_0$, which reduces the "abruptness" of the graphene interaction with the external particle. On the other hand, one notices a small red shift in the main peaks in $P_{\rm rad}(\omega)$ in comparison to the peak positions in $P_{\rm ext}(\omega)$, but it is interesting that the positions and the shapes of the peaks in each of those densities are rather insensitive to variations of the incident angle. We note that the strong

increase observed in both $P_{\rm ext}$ and $P_{\rm rad}$ as $\omega \to 0$ is a signature of the Dirac-term contribution to the eHD conductivity, coming from the low-energy interband $\pi \to \pi^*$ electronic transitions in undoped graphene. Such feature in the experimental EELS data of graphene may have been observed in recent measurements [30, 39].

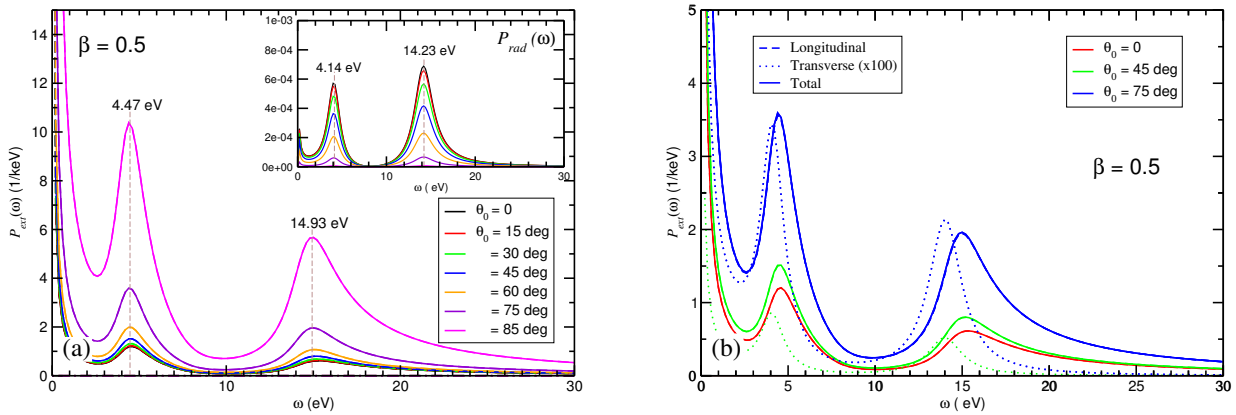

Figure 4.8: (a) integrated probability density of the external energy loss, $P_{\rm ext}(\omega)$, as a function of the energy ω (with $\hbar = 1$) lost by an incident electron with the speed $\beta = 0.5$ for a broad range of incident angles. Shown in the inset of panel (a) is the corresponding energy loss due to the emitted TR, $P_{\rm rad}(\omega)$. Since the magnitude of the radiation energy loss is very much smaller than $P_{\rm ext}(\omega)$, practically $P_{\rm ext}(\omega) \approx P_{\rm ohm}(\omega)$. (b) integrated probability density of the energy loss of the external particle, $P_{\rm ext}$ (solid lines), as well as the longitudinal (dashed lines) and transverse (dotted lines) contributions to that density for several incident angles. For both panels the eHD conductivity model for graphene, with the parameters fixed at $n_\pi^0 = 38$ nm^{-2}, $n_\sigma^0 = 115$ nm^{-2}, $\omega_{\pi r} = 4.19$ eV, $\omega_{\sigma r} = 14.15$ eV, $\gamma_\pi = 2.04$ eV, $\gamma_\sigma = 2.178$ eV, and $\omega_* = 3.54$ eV, is used.

In panel (b) of Fig. 4.8 we show the integrated probability density of the energy loss of the external particle, $P_{\rm ext}$, as well as the longitudinal and transverse contributions to that density for several incident angles. One notices that, while the transverse contribution is absent for the normal incidence, its density for oblique incidence resembles that of the longitudinal contribution, except for a small red shift in the main peak positions and a significantly smaller magnitude. While the data for $P_{\rm ext}(\omega)$ in Fig. 4.8(b) practically refer to the Ohmic energy loss, we show in Fig. 4.9 a decomposition of both the Ohmic (panel a) and the radiative (panel b) energy losses into their respective longitudinal and transverse contributions for the incident angle $\theta_0 = 45°$. What is remarkable to observe in Fig. 4.9(b) is that the transverse and longitudinal contributions to the radiative energy loss have similar magnitudes, which is not the case for such contributions to the Ohmic energy loss shown in Figs. 4.8(b) and 4.9(a). Moreover, unlike the red shifts observed among the peak positions in the longitudinal and transverse contributions to the Ohmic

energy loss in Figs. 4.8(b) and 4.9(a), one sees in Fig. 4.9(b) that the longitudinal and transverse contributions to the radiative energy loss exhibit main peaks at approximately equal energies.

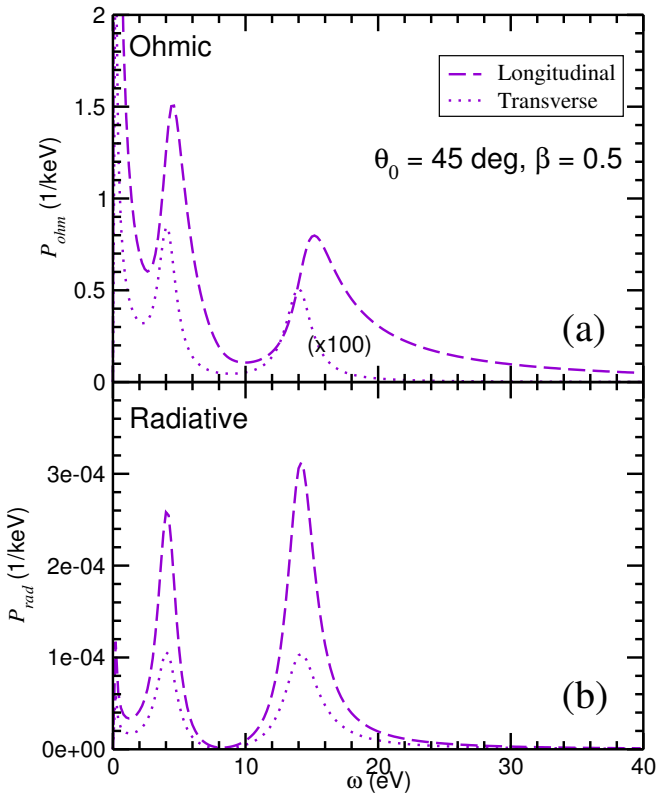

Figure 4.9: A decomposition of (a) the Ohmic and (b) the radiative energy losses into their respective longitudinal (dashed lines) and transverse (dotted lines) contributions for the incident angle $\theta_0 = 45°$. For both panels the eHD conductivity model for graphene, with the parameters fixed at $n_\pi^0 = 38$ nm^{-2}, $n_\sigma^0 = 115$ nm^{-2}, $\omega_{\pi r} = 4.19$ eV, $\omega_{\sigma r} = 14.15$ eV, $\gamma_\pi = 2.04$ eV, $\gamma_\sigma = 2.178$ eV, and $\omega_* = 3.54$ eV, is used.

Finally, in Fig. 4.10, we show the joint probability densities for the longitudinal (left column) and transverse (middle column) contributions to the Ohmic energy loss, along with their sum, $F_{\rm ohm}(k, \phi, \omega)$ (right column), which practically represents the total energy loss density of the external charged particle, given the smallness of the radiative energy loss. Results show the dependence on the wavenumber k and the energy loss ω, in the direction of $\phi = \pi/4$ with respect to the x-axis, i.e., the (projected) direction of motion for an external particle having the speed $\beta = 0.5$ and taking three angles of incidence relative to the z-axis: $\theta_0 = 0$ (top row), $\theta_0 = 45°$ (middle row) and $\theta_0 = 75°$ (bottom row). One notices that, for $\theta_0 = 45°$, there is only

a moderate increase in the longitudinal contribution compared to the normal incidence, $\theta_0 = 0$, accompanied by a small transverse contribution near $k = 0$ and $\omega = 0$. By increasing the angle of incidence to $\theta_0 = 75^\circ$, there is a substantial increase in the longitudinal contribution for intermediate wavenumbers, $k \sim k_{\rm max}$, at the energies intermediate between the two main peaks corresponding to the π and $\sigma + \pi$ "plasmons", as well as an increase in that contribution for large wavenumbers, $k \gtrsim 2k_{\rm max}$, at the energy close to that of the $\sigma + \pi$ "plasmon".

We note that the color coding in Fig. 4.10 is adopted so that all the probability density values exceeding the relatively small value of 1 Å^2/eV are shown in red, as indicated in the color bars. This is done so that sub-dominant resonant features can be observable in that figure, in addition to the dominant peaks.

What is interesting to observe in the middle panel of the bottom row in Fig. 4.10, is that the transverse contribution exhibits a well defined mode-like intensity for the incident angle $\theta_0 = 75^\circ$, which extends between $\omega = 0$ and the energy of the π "plasmon", with a peculiar linear dispersion with k, lying well below the light line. Noting that the magnitude of the joint probability densities is shown in Fig. 4.10 with equal scaling factors, this observation is even more remarkable, given that the transverse contribution plays negligible role in the integrated Ohmic energy loss in Figs. 4.8(b) and 4.9(a). Like in the case of the angular distribution of the radiation energy loss in the far-field region at the THz frequencies in Fig. 4.5, one may assert from Fig. 4.10 that the momentum- and angle-resolved density of the Ohmic energy loss in graphene at the MIR to UV frequencies also exhibits strong anisotropy and complementarity in its longitudinal and transverse contributions. This points to the potentially interesting effects of the in-plane anisotropy in the excitation of the high-energy interband electronic transitions in graphene by a fast electron under oblique incidence, which could be possibly observed in STEM via EELS by using a detector with narrow slit to collect the transmitted electrons, and by rotating the slit with respect to the incident plane in order to probe angles ϕ that would expose the transverse contribution to the Ohmic energy loss.

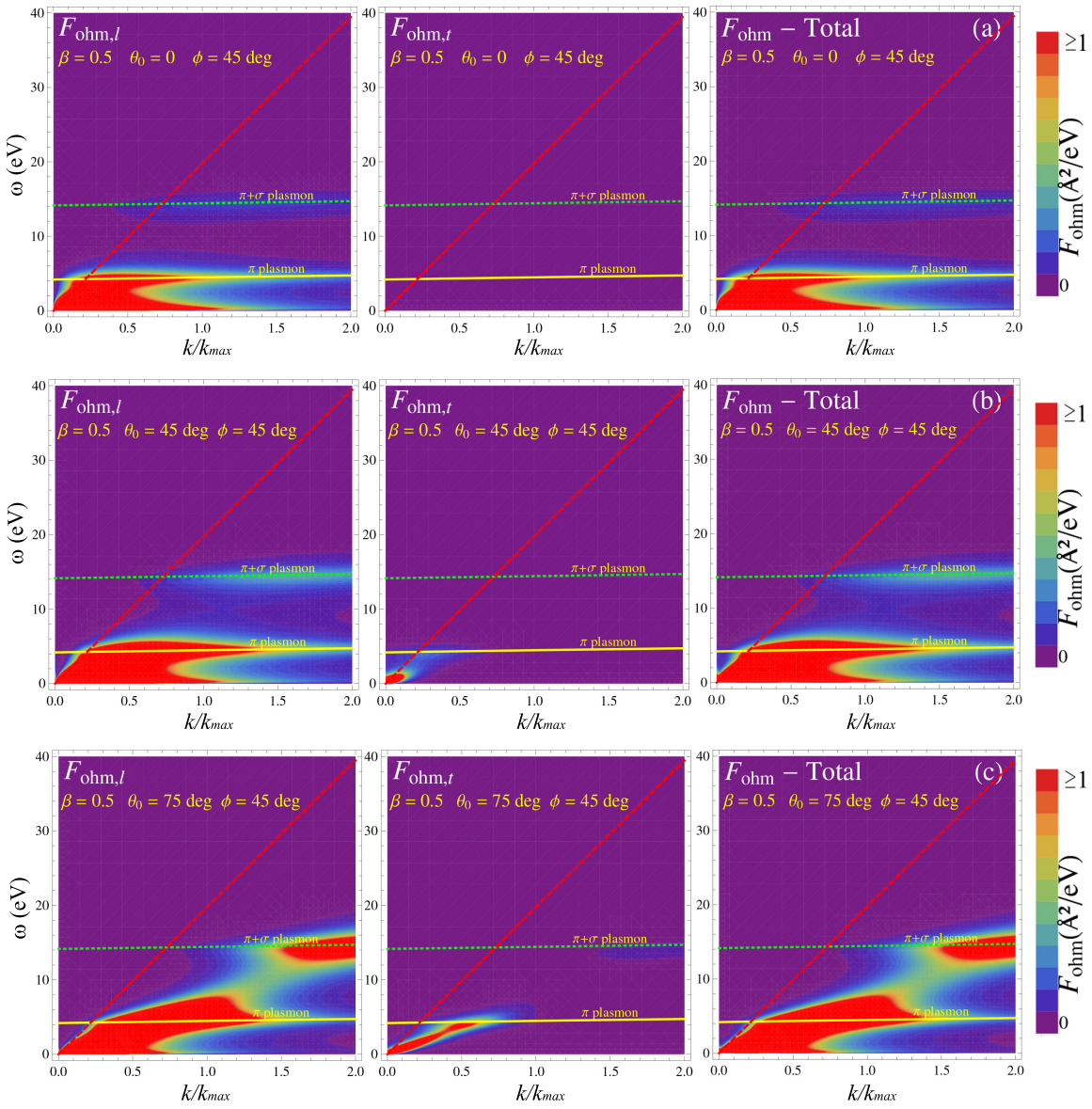

Figure 4.10: Joint probability densities for the longitudinal (left column) and transverse (middle column) contributions to the Ohmic energy loss, along with their sum, $F_{\mathrm{ohm}}(k, \phi, \omega)$ (right column), which practically represents the total energy loss density of the external charged particle, given the smallness of the radiative energy loss. Results are shown as functions of the wavenumber k and the energy loss ω, in the direction of $\phi = \pi/4$ with respect to the x-axis, i.e., the (projected) direction of motion for an external particle having the speed $\beta = 0.5$ and for three angles of incidence relative to the z-axis: $\theta_0 = 0$ (top row), $\theta_0 = 45°$ (middle row) and $\theta_0 = 75°$ (bottom row). For all panels the eHD conductivity model for graphene, with the parameters fixed at $n_\pi^0 = 38$ nm^{-2}, $n_\sigma^0 = 115$ nm^{-2}, $\omega_{\pi r} = 4.19$ eV, $\omega_{\sigma r} = 14.15$ eV, $\gamma_\pi = 2.04$ eV, $\gamma_\sigma = 2.178$ eV, and $\omega_* = 3.54$ eV, is used. Also shown are the nonrelativistic dispersion relations of the π (solid yellow line) and $\pi + \sigma$ (dotted green line) plasmons for single-layer graphene [33], and the light line by the dashed red line. Here, $k_{\mathrm{max}} = 0.1$ nm^{-1}.

4.4 Concluding remarks

We have studied, in this chapter, the interaction of an external charged particle with single-layer graphene in broad ranges of the relative particle speed $\beta = v/c$ and the incidence angle θ_0 with respect to an axis normal to the plane of graphene. We have evaluated and compared decompositions of the Ohmic and radiative energy losses of the external particle into their longitudinal and transverse components in order to emphasize the importance of the oblique incidence for generating electromagnetic (EM) fields with different polarizations by two types of the excitation processes of charge carriers in graphene. Those processes were described by defining two in-plane dielectric functions, which incorporate suitable models of graphene's longitudinal and transverse electrical conductivity. Our observations are given below.

In the terahertz (THz) frequency range, we have used the standard Drude model for conductivity describing the low-energy intraband excitations of Dirac's electrons in graphene, as well as the model due to Lovat *et al.*, which introduces nonlocal effects in the conductivity of graphene at those frequencies. While the Drude model is suitable for describing the longitudinal Dirac plasmon polariton (LDPP) mode in the supra-THz frequency range, it also reveals the effects of retardation, which are most prominent at the sub-THz frequencies. By comparing the results from the Lovat's and Drude models, we have assessed the effects of the nonlocality in the integrated energy loss densities at the THz frequencies. We have found that this effect is only pronounced around the THz frequency for the Ohmic energy loss at very low speeds of the incident particle, i.e., in the nonretarded regime. In that regime, the radiative energy loss is heavily suppressed and it exhibits no effect of the nonlocality, which is expected, since the radiative loss is a purely relativistic phenomenon.

On the other hand, in the retarded regime, i.e., for high incident speeds, the Ohmic and the radiative energy losses can attain comparable magnitudes at the sub-THz frequencies and at the angles of incidence that are not too oblique. Moreover, in this regime, both the longitudinal and transverse contributions to the integrated Ohmic energy loss density increase with increasing angle of incidence. This is true for a full range of frequencies, from the THz to the UV, and it may be tentatively explained by the increasing time that the incident particle spends interacting with the near fields induced by the graphene's charge carriers, which scales as $\propto \sec\theta_0$. The longitudinal contribution to the Ohmic energy loss dominates at the supra-THz frequencies, where it exhibits a pronounced peak related to the LDPP, whereas the transverse contribution is heavily suppressed at such frequencies. On the other hand, at the sub-THz frequencies, the transverse contribution to the Ohmic energy loss may even surpass the longitudinal contribution for high enough speeds and sufficiently oblique trajectories of the charged particle. This may be rationalized by recalling that the transverse contribution is mostly a result of retardation effects, which are enhanced at lower frequencies and for larger parallel components of the incident speed.

The longitudinal contribution to the integrated radiation energy loss density decreases with increasing angle of incidence in a manner that seems to be governed by a decrease in the normal component of the external particle speed, $\beta \cos\theta_0$. This is true for a full range of frequencies, from the THz to the ultraviolet (UV), and it may be explained by recalling that the radiation is most effectively produced by accelerating the charge carriers in graphene, so that a reduction in the normal component of the speed would bring down the "abruptness" of graphene's interaction with the external charged particle, and hence it would reduce the production of the transition radiation (TR) from graphene. The transverse contribution to the integrated radiation energy loss density exhibits a symmetric maximum at the incident angle $\theta_0 = \pi/4$, and is found to be much smaller than the longitudinal contribution to the integrated radiation energy loss in the full range of frequencies, for all incident speeds and all angles of incidence.

However, this relation between these two contributions to the radiation energy losses is different when considering the angle-resolved spectra of the emitted TR. Namely, both the longitudinal and the transverse contributions to the TR exhibit rather anisotropic angular distributions, with somewhat complementary patterns of the emitted EM field intensity. Specifically, while the longitudinal contribution mostly radiates in broad patterns skewed towards the plane of graphene, the transverse contribution radiates preferably in a direction perpendicular to graphene, but away from the plane of incidence of the external particle. Interestingly, unlike the case of the integrated radiative energy loss density, peaks in the radiation lobes in the angular distribution that result from the longitudinal and transverse contributions may attain comparable magnitudes when viewed in different directions. Therefore, we propose that a cathodoluminescence type of measurements of the emitted radiation in scanning transmission electron microscope (STEM) could be used to explore this anisotropy in the angular patterns of the emitted radiation from graphene, where detection of the polarization of the emitted EM waves as the transverse magnetic (TM) or transverse electric (TE) may be used to identify contributions coming from the longitudinal or transverse excitation processes in graphene, respectively.

By adding a contribution due to the low-energy interband electron excitations in graphene to the Drude model, we have used an optical conductivity model that is valid up to the mid-infrared (MIR) range of frequencies in order to explore the possibility of exciting a transverse collective mode in doped graphene by means of a fast electron under oblique incidence. We have indeed found an evidence that such excitation would be identifiable in the transverse contribution to the integrated Ohmic energy loss in an ideal case of doped graphene with zero damping, but with an impractically low probability. This confirms that, despite the fact that the Joule energy dissipation rate in the transverse dielectric function could be substantial in the sub-THz range, the energy confined in the near field of graphene due to excitation of the transverse mode is negligible in comparison with that of the longitudinal mode, as shown in Ref. [147].

Finally, we have used an extended hydrodynamic model of graphene's conductivity in the

MIR to UV frequency range to study electron energy loss spectroscopy (EELS) for electrons traversing the graphene layer under oblique incidence in a STEM setting. We have found that the integrated radiation energy loss density is much smaller than the integrated Ohmic energy loss density, and that they both exhibit main peak features with the positions and shapes that are insensitive to the variation in the incident angle. Moreover, while the transverse contribution is much smaller than the longitudinal contribution in the integrated Ohmic energy loss, the longitudinal and transverse contributions in the integrated radiative energy loss have comparable magnitudes but, even when added together, they constitute a negligible fraction of the total integrated energy loss of the external charged particle. As for the dependence on the angle of incidence, observations in the MIR to UV range are analogous to those at the THz frequencies: the overall magnitude of the integrated Ohmic energy loss density increases and the integrated radiative energy loss density decreases with increasing angle of incidence.

Considering the momentum k and the angle ϕ dependence of a joint probability density for the Ohmic energy loss in graphene, we have observed an increase in the longitudinal contribution in different regions of the (k, ϕ) plane with increasing angle of incidence θ_0 of the external charge particle. For a sufficiently oblique incident trajectory, we have also observed a well-defined, mode-like feature in the transverse contribution to the Ohmic energy loss, exhibiting a linear energy dispersion in the direction $\phi = \pi/4$ with respect to the incident plane of the charged particle. We therefore propose an experiment in STEM using a narrow slit detector to collect obliquely incident electrons upon graphene, which can be rotated with respect to the plane of incidence on order to search for such directional modes as a signature of the transverse excitation processes in graphene at the MIR to the UV range of frequencies.

Chapter 5

Energy Loss and Transition Radiation in Anisotropic 2D Materials Traversed by Fast Charged Particles under Oblique Incidence

In this chapter, we present fully relativistic expressions for the energy loss channels for a charged particle traversing a single layer of anisotropic material surrounded by a homogeneous lossless dielectric under oblique incidence in a setting pertinent to a scanning transmission electron microscope (STEM), and we perform calculations for the case of a free-standing phosphorene in vacuum. As in previous chapters, we distinguish between the energy deposited in phosphorene in the form of electronic excitations (Ohmic loss) and the energy emitted in the far-field in the form of transition radiation (TR). Our formulation of the problem uses a definition of an in-plane, dielectric tensor with Cartesian component functions along the principal axes of phosphorene, which describe the anisotropic excitation processes that contribute to those energy loss channels. Using a phenomenological model for the electric conductivity of phosphorene as the input in those dielectric functions, enables us to discuss the effects of oblique incidence on several processes in a broad range of frequencies, from the terahertz to the mid-infrared. In particular, at low frequencies, known as purely anisotropic regime, we demonstrate that the plasmon dispersion surface forms an ellipsoid affected strongly by retardation. Also, we show that the energy loss contribution to the emitted TR spectra exhibits strongly anisotropic angular patterns that are readily distinguishable in a cathodoluminescence measurement in a STEM. It is observed that the angular patterns of TR are markedly different from those of an isotropic sheet even in the case of normal incidence. As for the higher frequency range, called hyperbolic regime, we demonstrate

that the plasmon dispersion surface forms a hyperbloid not affected by retardation. We also show eccentric radiation angular spectra in hyperbolic regime.

Moreover, for both regimes, we explore the possibility of exciting the directional elliptic and hyperbolic plasmons by an external charged particle. It is observed that, using an extremely oblique incidence of charged particle, the directionality of plasmon excitation may be tuned by the azimuthal angle, as well as by the speed of charged particle, which is of great technological and experimental importance.

5.1 Introduction

Efforts towards understanding the electromagnetic (EM) properties of anisotropic two-dimensional (2D) materials, such as the anisotropy of the in-plane optical conductivity, the on-off current ratio, high mobility of charge carriers, and tunability of the band gap, have already begun to deliver interesting results for phosphorene [148, 149, 150]. The *ab initio* calculations of electron energy loss spectroscopy (EELS) for phosphorene were performed in Ref. [151] in order to understand the plasmonic and excitonic peaks in the loss spectra, as well as their dispersion relations in the nonretarded regime. The tunability of a multilayer black phosphorus (BP) and its dependence on the layer thickness, doping density and the applied light polarization were investigated in Ref. [152], yielding an anisotropic diagonal conductivity tensor. In conjunction with those results, it was also shown that the in-plane static screening by phosphorene is isotropic, in contrast to the anisotropy of its collective mode excitations [153]. A phenomenological local conductivity model for doped phosphorene was proposed in Ref. [125] to probe the light-matter interaction as a function of the charge carrier concentration, with an emphasis on the hyperbolic plasmon dispersion in the EM response of phosphorene. It is worth to mention that such topologically-induced behavior of collective modes in anisotropic 2D materials, like elliptic and hyperbolic plasmon dispersions, has opened the possibility to utilize those materials in diverse nanophotonics applications. Researchers have also made progress in exploring the effect of nonlocality on the conductivity, loss spectra, and the plasmonic behavior of phosphorene in Refs. [154, 155]. Moreover, Margulis *et al.* developed a two-band analytical model for optical conductivity of both pristine [156] and doped [157] phosphorene placed on a substrate. In addition, the tunability of plasmon excitation in phosphrene nano-ribbons was studied in Ref. [158], exhibiting variations of the absorption spectra versus several parameters, such as the spatial dimension and the doping density.

In this chapter, we present a formulation of the interaction of fast charged particles with a general anisotropic monolayer placed in a lossless surrounding dielectric, taking relativistic effects into account. In this regard, we analyze the energy loss channels of the external charged

particles, and evaluate the corresponding loss probability densities, in order to understand the EM spectral behavior of the anisotropic sheet. As in the previous chapters on graphene [42, 57, 59], we show that the total energy loss of the an incident charged particle consists of the energy deposited in the sheet in the form of electronic excitations (Ohmic losses), which include excitation of its 2D plasmon modes, and the energy emitted in the far-field region in the form of TR. In particular, we assume an obliquely incident particle, enabling us to explore the effects of the anisotropy of the sheet on the efficiency of the plasmon excitations and the angular anisotropy of the emitted TR spectra as a function of the incident particle's direction relative to the principal directions of the sheet. Accordingly, in addition to the incident particle energy, its angle of incidence is established as an important quantity that may be considered as a significant tuning parameter for the EM response of the anisotropic sheet.

The chapter is organized as follows. In the *Theory* section 5.2, we present a derivation of the EM fields and we define probability densities of various energy loss channels for a general anisotropic layer in a lossless homogeneous medium, followed by applications to the case of a monolayer phosphorene by using an appropriate 2D conductivity tensor model. The *Results and Discussion* section 5.3 is divided in two parts, dedicated to a low-frequency range and a high-frequency range, elucidating the regimes of the elliptic and hyperbolic dispersion relations for phosphorene plasmons, respectively. Our findings are summarized in the *Concluding remarks* section 5.4.

5.2 Theory

The structure under consideration consists of a 2D material, or a conducting sheet that represents an atomic monolayer with large area, placed in the xy-plane ($z = 0$) of a three-dimensional (3D) Cartesian coordinate system with coordinates $\mathbf{R} = \{\mathbf{r}, z\}$, where $\mathbf{r} = \{x, y\}$, as depicted in Fig. 5.1. We assume that the external particle is represented by an electric point charge Ze, which moves with constant velocity of $\mathbf{v}$ on a straight-line trajectory and traverses the sheet under oblique incidence, defined by the (azimuthal) angle θ_0 with respect to the z-axis and the (polar) angle ϕ_0 with respect to the x-axis. We further assume that the entire structure is placed in a lossless dielectric medium with the relative permittivity $\epsilon_d > 0$. Assuming that the surrounding dielectric is homogeneous enables us to neglect the effect of the dielectric discontinuities on TR, and we only consider values of the incident particle speed, $v = \|\mathbf{v}\|$, smaller than the threshold for Cherenkov radiation in that dielectric, $v < c/\sqrt{\epsilon_d}$.

In order to evaluate the EM fields, it is convenient to introduce dyadic Green's function (DGF) of the first kind [121], which may be directly derived from the electric Hertz vector potential $\mathbf{\Pi}(\mathbf{R}, t)$ [120]. This vector, in turn, may be easily obtained for the proposed geometry of the

problem by solving a nonhomogeneous Helmholtz vector equation by means of a retarded scalar GF, with the external charged particle represented by an electric current density as the source term in that equation [42]. The procedure of calculating DGF is outlined in A.

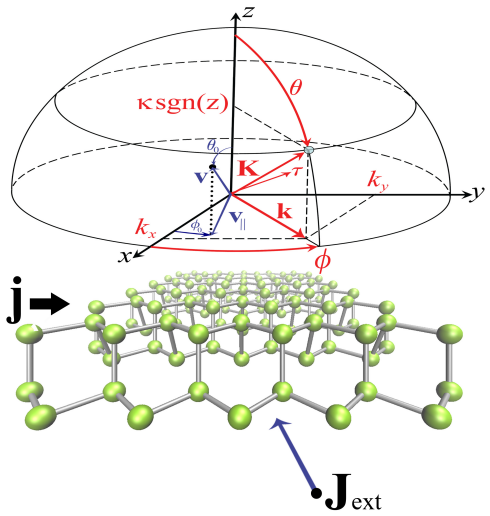

Figure 5.1: Schematic geometry of the structure for probing the single-layer anisotropic specimen by an electron under oblique incidence in a STEM.

5.2.1 Self-consistent solution for the induced electromagnetic fields

Assuming translational invariance inside the sheet, we may perform a 2D spatial Fourier transform ($\mathbf{r} = \{x, y\} \rightarrow \mathbf{k} = \{k_x, k_y\}$), as well as a Fourier transform with respect to time ($t \rightarrow \omega$) with the time dependence $\mathrm{e}^{-i\omega t}$, enabling us to express the electric field $\mathbf{E}$ arising due to the current density $\mathbf{J}$ as

$$\mathbf{E}(\mathbf{k}, z, \omega) = \int_{-\infty}^{+\infty} dz' \overleftrightarrow{G}_{E0}(\mathbf{k}, z - z', \omega) \cdot \mathbf{J}(\mathbf{k}, z', \omega), \tag{5.1}$$

where $\overleftrightarrow{G}_{E0}(\mathbf{k}, z - z', \omega)$ is the electric DGF (EDGF) for a homogeneous medium, with the subscript implying the zero kind EDGF [121]. While the above relation and the corresponding vectors may be expressed in any arbitrary coordinate system, Cartesian coordinates suitably encompass most of our needs for an anisotropic monolayer placed in a homogeneous medium. In

that respect, the EDGF may be written in the Cartesian coordinate system as

$$\overleftrightarrow{G}_{E0}(\mathbf{k},z,\omega) = \overleftrightarrow{G}^{||}_{E0}(\mathbf{k},z,\omega) + \frac{2\pi i}{\omega q \epsilon_d}\left\{-ik_x q\,\mathrm{sign}(z)\,(\hat{\mathbf{x}}\hat{\mathbf{z}}+\hat{\mathbf{z}}\hat{\mathbf{x}}) - ik_y q\,\mathrm{sign}(z)\,(\hat{\mathbf{y}}\hat{\mathbf{z}}+\hat{\mathbf{z}}\hat{\mathbf{y}}) + \left[k^2 - 2q\delta(z)\right]\hat{\mathbf{z}}\hat{\mathbf{z}}\right\}\mathrm{e}^{-q|z|}, \tag{5.2}$$

where, for future convenience, we define that part of the EDGF, which only involves components parallel to the conducting sheet by

$$\overleftrightarrow{G}^{||}_{E0}(\mathbf{k},z,\omega) = \frac{2\pi i}{\omega q \epsilon_d}\left[\left(k_d^2 - k_x^2\right)\hat{\mathbf{x}}\hat{\mathbf{x}} - k_x k_y\,(\hat{\mathbf{x}}\hat{\mathbf{y}}+\hat{\mathbf{y}}\hat{\mathbf{x}}) + \left(k_d^2 - k_y^2\right)\hat{\mathbf{y}}\hat{\mathbf{y}}\right]\mathrm{e}^{-q|z|}. \tag{5.3}$$

Here, $k_d = \frac{\omega}{c}\sqrt{\epsilon_d}$ is the magnitude of a 3D wavevector, or the wavenumber of the EM radiation propagating at the frequency ω through the surrounding dielectric, whereas the field dependence on the z coordinate is governed by

$$q(k,\omega) = \begin{cases} -i\frac{\omega}{c}\sqrt{\epsilon_d - \left(\frac{ck}{\omega}\right)^2} \equiv -i\kappa(k,\omega), & |\omega| > ck/\sqrt{\epsilon_d} \\ \frac{|\omega|}{c}\sqrt{\left(\frac{ck}{\omega}\right)^2 - \epsilon_d} \equiv \alpha(k,\omega), & |\omega| < ck/\sqrt{\epsilon_d}, \end{cases} \tag{5.4}$$

where $k = \|\mathbf{k}\| = \sqrt{k_x^2 + k_y^2}$. In the above equation, $\alpha \equiv \sqrt{k^2 - k_d^2} > 0$ describes an inverse of the localization length for collective excitation modes of charge carriers in the conducting sheet that occur in the range of the $(\mathbf{k},\omega)$ space lying outside the light cone, $|\omega| < ck/\sqrt{\epsilon_d}$. Unlike α, which is a characteristics of evanescent waves, the wavenumber $\kappa \equiv \mathrm{sign}(\omega)\sqrt{k_d^2 - k^2}$ characterizes the propagation of traveling waves in directions perpendicular to the sheet, in the range of the $(\mathbf{k},\omega)$ space lying inside the light cone, $|\omega| > ck/\sqrt{\epsilon_d}$.

We further define the volume density of the external charged particle as $\rho_{\mathrm{ext}}(\mathbf{R},t) = Ze\,\delta(\mathbf{R} - \mathbf{v}t)$, with its velocity given in the Cartesian coordinates by $\mathbf{v} = \{\mathbf{v}_{||}, v_z\}$, where the parallel and perpendicular components of the velocity with respect to the plane of the conducting sheet are given by $\mathbf{v}_{||} \equiv \{v_x, v_y\} = \{v\sin\theta_0\cos\phi_0, v\sin\theta_0\sin\phi_0\}$ and $v_z = v\cos\theta_0$, respectively (see Fig. 5.1). This enables us to write the Fourier transform of the associated current density as

$$\mathbf{J}_{\mathrm{ext}}(\mathbf{k},z,\omega) = \frac{Ze}{v_z}\,\mathbf{v}\,\mathrm{e}^{iQz}, \tag{5.5}$$

where $Q = \Omega/v_z$ with $\Omega = \omega - \mathbf{k}\cdot\mathbf{v}_{||}$. This current density, primarily, produces an electric field in the homogeneous medium, $\mathbf{E}_{\mathrm{ext}}(\mathbf{k},z,\omega)$, which can be obtained by inserting Eq. (5.5) and Eq. (5.2) into Eq. (5.1). Resulting from the structure of the EDGF, the external electric field

may also be decomposed into Cartesian components parallel and perpendicular to the conducting sheet as $\mathbf{E}_{\text{ext}}(\mathbf{k},z,\omega) = \mathbf{E}_{\text{ext}||}(\mathbf{k},z,\omega) + E_{\text{ext},z}(\mathbf{k},z,\omega)\hat{\mathbf{z}}$. The parallel component of that field may be conveniently written as $\mathbf{E}_{\text{ext}||}(\mathbf{k},z,\omega) = \mathcal{A}\left(\widetilde{E}_{\text{ext},x}\hat{\mathbf{x}} + \widetilde{E}_{\text{ext},y}\hat{\mathbf{y}}\right)\mathrm{e}^{iQz}$, where the amplitude defined by $\mathcal{A} = -ik\frac{Ze}{v_z\epsilon_d}\frac{4\pi}{q^2+Q^2}$ plays an important role in the subsequent definitions of the energy loss densities, whereas the dimensionless, in-plane ($z = 0$) values of the x and y components of that field are given by

$$\begin{aligned}\widetilde{E}_{\text{ext},x} &= \frac{1}{k\omega}\left(k_d^2 v_x - k_x\omega\right), \\ \widetilde{E}_{\text{ext},y} &= \frac{1}{k\omega}\left(k_d^2 v_y - k_y\omega\right).\end{aligned} \tag{5.6}$$

The dynamic polarization of charge carriers in the atomic monolayer by the external charged particle gives rise to the induced 2D current density in that layer, $\mathbf{j}(\mathbf{k},\omega)$. To capture the anisotropic nature of the atomic monolayer, the induced in-plane current may be expressed via the 2D Ohm's low for a conducting sheet, $\mathbf{j}(\mathbf{k},\omega) = \overleftrightarrow{\sigma}(\mathbf{k},\omega)\cdot\mathbf{E}_{||}(\mathbf{k},0,\omega)$, where $\mathbf{E}_{||}(\mathbf{k},0,\omega)$ is the component of the total electric field parallel to the sheet, evaluated at $z = 0$, which we simply call the in-plane total electric field. Here, $\overleftrightarrow{\sigma}(\mathbf{k},\omega)$ is the 2D conductivity tensor describing the dynamic response of an anisotropic conducting sheet. It should be mentioned that, in the most general case, each component of this tensor may be dependent on both the direction and the magnitude of the in-plane wavevector, $\mathbf{k}$, as well as on the operating frequency, ω. Components of the conductivity tensor expose distinct properties of different types of 2D materials. For instance, in the case of Weyl semimetals [159], superconductors [160], or gapped Dirac systems [161], the chirality of the electronic bands plays an important role, so that macroscopically one has $\sigma_{xy} = -\sigma_{yx}$ for the off-diagonal components of the conductivity tensor represented in the Cartesian coordinates. Fundamentally, the effects of chirality, which are in close connection with the Berry phase and the quantum Hall effect alter the Bloch bands, and may ultimately be considered as the origin of the chiral (edge) plasmons [161, 162, 163].

With the above specifications, we are in the position to define the induced 3D current density as $\mathbf{J}_{\text{ind}}(\mathbf{k},z,\omega) = \delta(z)\,\mathbf{j}(\mathbf{k},\omega)$, where $\delta(z)$ is the Dirac's delta function peaked at the conducting sheet. Inserting $\mathbf{J}_{\text{ind}}(\mathbf{k},z,\omega)$, along with Eq. (5.2), into Eq. (5.1), readily gives the induced electric field as

$$\mathbf{E}_{\text{ind}}(\mathbf{k},z,\omega) = \overleftrightarrow{G}_{E0}(\mathbf{k},z,\omega)\cdot\overleftrightarrow{\sigma}(\mathbf{k},\omega)\cdot\mathbf{E}_{||}(\mathbf{k},0,\omega). \tag{5.7}$$

Thus, in order to determine the induced electric field throughout the structure, we require a self-consistent procedure to find the in-plane total electric field, $\mathbf{E}_{||}(\mathbf{k},0,\omega)$. This may be achieved by setting $z = 0$ in Eq. (5.7) to deduce an expression for the in-plane induced electric field,

$\mathbf{E}_{\mathrm{ind}||}(\mathbf{k},0,\omega)$, so that the in-plane total electric field may be written as $\mathbf{E}_{||}(\mathbf{k},0,\omega) = \mathbf{E}_{\mathrm{ext}||}(\mathbf{k},0,\omega) + \mathbf{E}_{\mathrm{ind}||}(\mathbf{k},0,\omega)$ and inserted back in the right-hand side of Eq. (5.7). This gives a "constitutive relation" for the conducting sheet, which involves the in-plane total electric field and the in-plane external electric field, $\mathbf{E}_{\mathrm{ext}||}(\mathbf{k},0,\omega)$, as

$$\overleftrightarrow{\epsilon}(\mathbf{k},\omega)\cdot\mathbf{E}_{||}(\mathbf{k},0,\omega) = \mathbf{E}_{\mathrm{ext}||}(\mathbf{k},0,\omega), \tag{5.8}$$

where we have introduced an effective 2D dielectric tensor, $\overleftrightarrow{\epsilon}(\mathbf{k},\omega)$, as a key parameter to be used in the following discussion. This tensor is defined in terms of the EDGF and the 2D conductivity tensor as

$$\overleftrightarrow{\epsilon}(\mathbf{k},\omega) = \overleftrightarrow{I}_{||} - \overleftrightarrow{G}^{||}_{E0}(\mathbf{k},0,\omega)\cdot\overleftrightarrow{\sigma}(\mathbf{k},\omega), \tag{5.9}$$

where $\overleftrightarrow{G}^{||}_{E0}(\mathbf{k},0,\omega)$ is the EDGF with parallel components, given in Eq. (5.3) and evaluated in the plane of the conducting sheet ($z=0$), whereas $\overleftrightarrow{I}_{||}$ is the in-plane identity tensor. We emphasize that the constitutive relation in Eq. (5.8) involves only the in-plane values of the parallel electric field components and it provides a self-consistent expression for the total in-plane electric field by a straightforward inversion of the effective 2D dielectric tensor in Eq. (5.9), $\mathbf{E}_{||}(\mathbf{k},0,\omega) = \overleftrightarrow{\epsilon}^{-1}(\mathbf{k},\omega)\cdot\mathbf{E}_{\mathrm{ext}||}(\mathbf{k},0,\omega)$. Hence, the determinant of the 2D dielectric tensor, $\Delta = \det\{\overleftrightarrow{\epsilon}\}$, is a key quantity that is used to extract the dispersion relation for plasmon modes in the conducting sheet by solving the equation $\Delta = 0$ in the $(\mathbf{k},\omega)$ plane. Solving Eq. (5.8) will give us the in-plane values of the total parallel electric field on the anisotropic sheet, which we write as $\mathbf{E}_{||}(\mathbf{k},0,\omega) \equiv \mathcal{A}\left(\widetilde{E}_{0x}\hat{\mathbf{x}} + \widetilde{E}_{0y}\hat{\mathbf{y}}\right)$, with $\widetilde{E}_{0x}$ and $\widetilde{E}_{0y}$ being the dimensionless field components.

Finally, having obtained $\mathbf{E}_{||}(\mathbf{k},0,\omega)$, one can finalize the calculation of the full induced electric field $\mathbf{E}_{\mathrm{ind}}(\mathbf{k},z,\omega)$ by means of Eq. (5.7) and, consequently, find the full induced magnetic field by the help of the Faraday-Maxwell's equation, $\mathbf{H}_{\mathrm{ind}}(\mathbf{k},z,\omega) = \frac{1}{ik_d}\nabla\times\mathbf{E}_{\mathrm{ind}}(\mathbf{k},z,\omega)$.

5.2.2 Energy loss probability densities

From the classical point of view, a swift charged particle with constant velocity $\mathbf{v}$ undergoes energy loss due to the force exerted by the induced electric field $\mathbf{E}_{\mathrm{ind}}$. Accordingly, this picture invokes a physical definition of the total energy loss of the external charged particle, $W_{\mathrm{ext}} = -\int dt \int d^3\mathbf{R}\,\mathbf{J}_{\mathrm{ext}}\cdot\mathbf{E}_{\mathrm{ind}}$. As mentioned above, we only focus here on the energy loss of the external particle due to the induced field of the anisotropic sheet since the lossless surrounding dielectric cannot produce induced field. We also neglect Cherenkov radiation by assuming $v < c/\sqrt{\epsilon_d}$.

As shown in Ref. [42] and the previous chapters, relativistic treatment of the interaction of an external charged particle with 2D materials in a homogeneous medium implies that the total energy lost by that particle is decomposed into two contributions only: (i) the Ohmic energy loss, $W_{\rm Ohm}$, due to electronic excitations, which include any collective modes in those materials and their subsequent damping, and (ii) the radiative energy, $W_{\rm rad}$, emitted in the far-field region in the form of TR. One should note that the energy balance of the system endorses that $W_{\rm ext} = W_{\rm Ohm} + W_{\rm rad}$. Accordingly, for each contribution, we may define the corresponding joint probability density, $F(\mathbf{k},\omega)$, as a function of the energy loss of the external particle, $\hbar\omega \geq 0$, and its momentum transfer to the 2D materials, $\hbar\mathbf{k}$, as well as the integrated probability density, $P(\omega)$, as a function of the energy loss of the external particle. Invoking the parity properties of the Fourier transformed quantities, we may express the energy loss for each of those channels via the following integrals

$$W_{\rm L} \equiv \iint d^2\mathbf{k} \int_0^{+\infty} d\omega\, \omega\, F_{\rm L}(\mathbf{k},\omega) \equiv \hbar^2 \int_0^{\infty} d\omega\, \omega\, P_{\rm L}(\omega), \tag{5.10}$$

where L = ext, Ohm, rad.

Considering the Physical definition of each contribution and following the formalism presented in Ref. [42], we first obtain for the total energy loss of the external charged particle due to the work done by the induced field on that particle,

$$F_{\rm ext}\left(\mathbf{k},\omega\right) = \frac{1}{4\pi^3\omega} \Re\left\{ \mathbf{E}^H_{\rm ext}(\mathbf{k},0,\omega) \cdot \overleftrightarrow{\sigma}(\mathbf{k},\omega) \cdot \overleftrightarrow{\epsilon}^{-1}(\mathbf{k},\omega) \cdot \mathbf{E}_{\rm ext}(\mathbf{k},0,\omega) \right\}, \tag{5.11}$$

where the superscript H indicates the Hermitian conjugate of a tensor. Recalling Eq. (5.4), one notices that the total energy loss density of the external particle $F_{\rm ext}$ may be decomposed into two contributions, $F^{>}_{\rm ext}$ and $F^{<}_{\rm ext}$, coming from different regions of the $(\mathbf{k},\omega)$ space, both inside the light cone and outside the light cone, respectively.

On the other hand, as a result of the work done by the total electric field acting on the induced current density in the conducting sheet, $W_{\rm Ohm} = \int dt \int d^3\mathbf{R}\, \mathbf{J}_{\rm ind} \cdot \mathbf{E}$, one may evaluate the joint density for the Ohmic energy loss as

$$F_{\rm Ohm}\left(\mathbf{k},\omega\right) = \frac{1}{4\pi^3\omega} \Re\left\{ \mathbf{E}^H_{\rm ext}(\mathbf{k},0,\omega) \cdot \left(\overleftrightarrow{\epsilon}^{-1}\right)^H \cdot \overleftrightarrow{\sigma} \cdot \overleftrightarrow{\epsilon}^{-1} \cdot \mathbf{E}_{\rm ext}(\mathbf{k},0,\omega) \right\}. \tag{5.12}$$

We note that the Ohmic energy loss density $F_{\rm Ohm}$ may also be decomposed into two contributions, $F^{>}_{\rm Ohm}$ and $F^{<}_{\rm Ohm}$, coming from the regions inside and outside the light cone, respectively. Finally, the joint density for the radiative energy loss in both the upper and lower half-spaces relative to the conducting sheet is obtained from the Poynting vector in the region inside the light

cone as

$$F_{\rm rad}(\mathbf{k},\omega)=\frac{-1}{4\pi^3\omega}\left\{\mathbf{E}^H_{\rm ext}(\mathbf{k},0,\omega)\cdot\left(\overleftrightarrow{\epsilon}^{-1}\right)^H\cdot\overleftrightarrow{\sigma}^H\cdot\overleftrightarrow{G}^{||}_{E0}(\mathbf{k},0,\omega)\cdot\overleftrightarrow{\sigma}\cdot\overleftrightarrow{\epsilon}^{-1}\cdot\mathbf{E}_{\rm ext}(\mathbf{k},0,\omega)\right\}. \tag{5.13}$$

To simplify the notation in Eqs. (5.12) and (5.13), we have dropped the variables $(\mathbf{k},\omega)$ in the tensors $\overleftrightarrow{\sigma}$ and $\overleftrightarrow{\epsilon}$, but we kept them in the electric field components. Referring to Eqs. (5.3) and (5.4), one should note that inside the light cone and for a lossless surrounding dielectric, $\overleftrightarrow{G}^{||}_{E0}(\mathbf{k},0,\omega)$ appearing in Eq. (5.13) is a purely real-valued symmetric tensor.

The conservation of energy at the level of the joint densities may be shown to be fulfilled in the form $F_{\rm ext}(\mathbf{k},\omega)=F_{\rm Ohm}(\mathbf{k},\omega)+F_{\rm rad}(\mathbf{k},\omega)$, valid over the entire $(\mathbf{k},\omega)$ space. Accordingly, the decomposition of various energy loss densities with respect to different regions in that plane necessitates that $F^{<}_{\rm ext}=F^{<}_{\rm Ohm}$ outside the light cone, and $F^{>}_{\rm ext}=F^{>}_{\rm Ohm}+F_{\rm rad}$ inside the light cone. The first equality confirms that the evanescent waves remain localized in the near-field region and are associated with the excitation of plasmon modes and their subsequent decay due to damping processes, giving rise to the Joule heat in the conducting sheet. On the other hand, the second equality shows that the Ohmic energy losses may play a role inside the light cone in the presence of damping processes, while the radiating far-field contribution of the traveling waves gives rise to the energy loss due to the emitted TR.

In order to better understand and visualize the wavefront pattern of the traveling waves in the far-field region due to TR, the total joint probability density for the radiation energy loss, $F_{\rm rad}(\mathbf{k},\omega)$, may be related to the spectral angular distribution of the radiation, $\mathcal{S}(\theta,\phi,\omega)$, where θ is the angle of the emitted radiation with respect to the z-axis and ϕ is the angle the emitted radiation with respect to the x axis, via the relation

$$W_{\rm rad}\equiv\iint d^2\hat{\Omega}\int_0^\infty d\omega\,\mathcal{S}(\theta,\phi,\omega). \tag{5.14}$$

In the above equation, we used spherical coordinates to express $\mathbf{k}=\{k_x,k_y\}=\frac{\omega}{c}\sin\theta\,\{\cos\phi,\sin\phi\}$ and defined the differential solid angle by $d^2\hat{\Omega}=\sin\theta\,d\theta\,d\phi$, with $0\le\theta\le\pi$ and $0\le\phi<2\pi$.

Finally, the integrated probability density can be expressed as the integration of the joint probability densities over the whole wavevector range via

$$P_{\rm L}(\omega)=\frac{1}{\hbar^2}\iint d^2\mathbf{k}\,F_{\rm L}(\mathbf{k},\omega), \tag{5.15}$$

where $\mathrm{L}=\mathrm{ext},\mathrm{Ohm},\mathrm{rad}$. With this definition of the integrated probability density, one may also relate the radiation integrated probability density to the spectral angular distribution via an

integration over whole range of solid angles as

$$P_{\mathrm{rad}}(\omega) = \frac{1}{\hbar^2\omega} \iint d^2\hat{\Omega}\, \mathcal{S}(\theta, \phi, \omega). \tag{5.16}$$

We finally note that the conservation of energy is also maintained at the level of the integrated probability densities is the form $P_{\mathrm{ext}}(\omega) = P_{\mathrm{Ohm}}(\omega) + P_{\mathrm{rad}}(\omega)$.

We emphasize that the expressions derived in this subsection for the energy loss densities hold for the general case of any 2D material surrounded by a homogeneous lossless dielectric. Those expressions may be generalized to multilayer structures, with the dynamic response of each layer described by a suitable conductivity tensor.

5.2.3 Phosphorene as an highly anisotropic 2D material

Within the family of 2D materials, a single layer of BP, or phosphorene, is a direct band-gap semiconductor, which has a puckered hexagonal atomic structure with two nonequivalent in-plane crystal directions known as armchair (AC) and zigzag (ZZ). As a result of its peculiar atomic lattice, phosphorene has a highly anisotropic band structure giving rise to a tensorial optical conductivity model [125, 151, 156, 157]. In the local limit ($k \to 0$), when the components of the optical conductivity tensor in Cartesian coordinates only depend on frequency, one can diagonalize the in-plane conductivity tensor as

$$\overleftrightarrow{\sigma}(\omega) = \sigma_x(\omega)\, \hat{\mathbf{x}}\hat{\mathbf{x}} + \sigma_y(\omega)\, \hat{\mathbf{y}}\hat{\mathbf{y}}. \tag{5.17}$$

Practically, this allows us to set our coordinate system according to the crystal's lattice principal axes. Accordingly, for the case of phosphorene, we assume that our x-axis is set in the AC direction and the y-axis is set in the ZZ direction of the phosphorene atomic lattice.

Having adopted the conductivity tensor of the form given in Eq. (5.17), the 2D dielectric tensor in Eq. (5.9) also takes a simpler form. Thus, one may further streamline the definitions of the energy loss probability densities from Eqs. (5.11), (5.12), and (5.13) into

$$F_{\mathrm{ext}}\left(\mathbf{k}, \omega\right) = \frac{|\mathcal{A}|^2}{4\pi^3\omega} \left[\widetilde{E}_{\mathrm{ext},x} \Re\left\{\sigma_x\, \widetilde{E}_{0x}\right\} + \widetilde{E}_{\mathrm{ext},y} \Re\left\{\sigma_y\, \widetilde{E}_{0y}\right\}\right], \tag{5.18}$$

$$F_{\mathrm{Ohm}}\left(\mathbf{k}, \omega\right) = \frac{|\mathcal{A}|^2}{4\pi^3\omega} \left[\left|\widetilde{E}_{0x}\right|^2 \Re\left\{\sigma_x\right\} + \left|\widetilde{E}_{0y}\right|^2 \Re\left\{\sigma_y\right\}\right], \tag{5.19}$$

and

$$F_{\rm rad}(\mathbf{k},\omega)=\frac{|\mathcal{A}|^2}{4\pi^3\omega}\frac{2\pi}{\omega\kappa\epsilon_d}\left[\left(k_d^2-k_x^2\right)\left|\sigma_x\,\widetilde{E}_{0x}\right|^2+\left(k_d^2-k_y^2\right)\left|\sigma_y\,\widetilde{E}_{0y}\right|^2-2k_xk_y\Re\left\{\sigma_x\,\widetilde{E}_{0x}\,\sigma_y^*\,\widetilde{E}_{0y}^*\right\}\right], \tag{5.20}$$

respectively, where the dimensionless components of the in-plane total electric field are given by

$$\begin{aligned}\widetilde{E}_{0x}&=\frac{1}{\Delta}\left\{\widetilde{E}_{{\rm ext},x}-\frac{2\pi i}{qkc^2}\,\sigma_y\left[\left(k_d^2-k_y^2\right)v_x+k_x\left(k_yv_y-\omega\right)\right]\right\},\\ \widetilde{E}_{0y}&=\frac{1}{\Delta}\left\{\widetilde{E}_{{\rm ext},y}-\frac{2\pi i}{qkc^2}\,\sigma_x\left[\left(k_d^2-k_x^2\right)v_y+k_y\left(k_xv_x-\omega\right)\right]\right\}.\end{aligned} \tag{5.21}$$

with $\widetilde{E}_{{\rm ext},x}$ and $\widetilde{E}_{{\rm ext},y}$ given in Eq. (5.6).

Surface plasmon polaritons supported by phosphorene may be investigated with the help of a dispersion relation using $\Delta=\det\{\overleftrightarrow{\epsilon}\}$, which is for a diagonal conductivity tensor given by

$$\Delta=1+\frac{2\pi i}{\omega q\epsilon_d}\left[\left(k_x^2-k_d^2\right)\sigma_x(\omega)+\left(k_y^2-k_d^2\right)\sigma_y(\omega)\right]+\frac{4\pi^2}{\epsilon_dc^2}\sigma_x(\omega)\sigma_y(\omega). \tag{5.22}$$

By setting $\Delta=0$ and taking the limit of vanishing damping, $\Re\{\sigma_x\}=\Re\{\sigma_y\}\to 0^+$, one obtains the dispersion relation of the plasmon polariton modes in the (k_x,k_y,ω) space in the form

$$\frac{k_x^2-k_d^2}{\Im\{\sigma_y(\omega)\}}+\frac{k_y^2-k_d^2}{\Im\{\sigma_x(\omega)\}}=2\alpha\omega\left(\frac{\epsilon_d}{4\pi\Im\{\sigma_x(\omega)\}\,\Im\{\sigma_y(\omega)\}}-\frac{\pi}{c^2}\right), \tag{5.23}$$

where we introduced $\alpha=\sqrt{k_x^2+k_y^2-k_d^2}$ from Eq. (5.4), while noting that all the solutions of the above equation occur outside or on the light cone, $k_x^2+k_y^2-k_d^2\geq 0$. Equation (5.23) is written in a form exposing the fact that, depending on the form of $\Im\{\sigma_{x,y}(\omega)\}$ and the range of operating frequency, the iso-frequency curves of the dispersion relation may have different topology in the (k_x,k_y) plane, such as circular, elliptic, or hyperbolic, which we shall discuss in detail in the subsequent section. It should be noted that, in the limit of vanishing damping, there would be no Ohmic energy losses in the region inside the light cone, i.e., $F^{>}_{\rm Ohm}(\mathbf{k},\omega)=0$, whereas the function $F^{<}_{\rm Ohm}(\mathbf{k},\omega)$ would contain delta functions peaked along the dispersion relation from Eq. (5.23), so that practically all the energy losses of the external particle in the region outside the light cone would be going to the excitation of the plasmon polariton modes with infinite lifetime.

Topology of plasmon dispersion and the conductivity model

The dispersion relation of phosphorene's plasmon modes given in Eq. (5.23) represents a surface that is quadratic in $\mathbf{k} = (k_x, k_y)$, residing in the $(\mathbf{k}, \omega)$ space with $\omega \in \mathbb{R}^+$ and $\mathbf{k} \in \mathbb{R}^2$. Depending on the sign of the functions $\Im\{\sigma_x(\omega)\}$ and $\Im\{\sigma_y(\omega)\}$, that surface may be described by an ellipsoid or hyperboloid. If $\Im\{\sigma_x(\omega)\}$ and $\Im\{\sigma_y(\omega)\}$ have the same/opposite signs then the dispersion surface is ellipsoid/hyperboloid. Accordingly, the level (isofrequency) curves illustrate ellipses (or circles) implying the excitation of elliptic (circular) plasmon mode and hyperbolas implying the excitation of the hyperbolic plasmon mode.

Taking the nonretarded limit in Eq. (5.23) (which might be useful for the hyperbolic plasmon mode), we have

$$\frac{k_x^2}{\Im\{\sigma_y(\omega)\}} + \frac{k_y^2}{\Im\{\sigma_x(\omega)\}} = 2k\omega \left(\frac{\epsilon_d}{4\pi \Im\{\sigma_x(\omega)\}\, \Im\{\sigma_y(\omega)\}} \right). \tag{5.24}$$

For the isotropic case, $\Im\{\sigma_x(\omega)\} = \Im\{\sigma_y(\omega)\} = \Im\{\sigma_{\text{iso}}(\omega)\}$, the above equation reduces to $\frac{\omega}{\Im\{\sigma_{\text{iso}}(\omega)\}} = \frac{2\pi k}{\epsilon_d}$, which results in the familiar dispersion relation $\omega \propto \sqrt{k}$ when $\sigma_{\text{iso}}(\omega)$ is given by a simple Drude model, as in the case of graphene at terahertz (THz) frequencies.

In the case of intrinsic (or undoped) phosphorene, the $\sigma_j(\omega)$ conductivity components (with $j = x, y$) are characterized by a step-like onset of *interband* electronic transitions for frequencies $\omega > \omega_g$, where ω_g is related to the band gap energy of phosphorene, which lies in the visible frequency range. As a consequence, in the interval of frequencies $0 < \omega < \omega_g$, the real parts of the conductivity are negligibly small, $\Re\{\sigma_j(\omega)\} \to 0^+$, while the imaginary parts are negative, $\Im\{\sigma_j(\omega)\} < 0$. When phosphorene is doped with charge carriers by applying, e.g., an external gate potential, there also arise contributions of the *intraband* electronic transitions to the conductivities $\sigma_j(\omega)$, which dominate at the THz frequencies and are well described by a Drude-type model. While the Drude weights generally take different values for different directions $j = x, y$ due to the anisotropy of phosphorene, it is noteworthy that this model generally gives positive imaginary parts of the conductivity, $\Im\{\sigma_j(\omega)\} > 0$. Since the total conductivity in each direction is given by the sum of the respective interband and intraband contributions, it is obvious that $\Im\{\sigma_x\}$ and $\Im\{\sigma_y\}$ in doped phosphorene can change their signs at different frequencies, which can be tuned within the THz to the infrared (IR) range by changing its doping density, i.e., by varying the external gate potential.

Therefore, one can identify two distinct regimes in the electromagnetic response of *doped* phosphorene. If the frequency is sufficiently low, the conductivities $\sigma_j(\omega)$ are predominantly of the Drude type, with both $\Im\{\sigma_x(\omega)\} > 0$ and $\Im\{\sigma_y(\omega)\} > 0$, giving rise to an elliptic iso-frequency dispersion curve in the (k_x, k_y) plane, according to Eq. (5.23). This regime is

labeled by Nemilentsau *et al*. as purely anisotropic [125]. If the frequency is sufficiently high, but still lower than the gap value ω_g augmented by the Pauli blocking [157], the contribution from the interband electron transitions may become dominant, and the imaginary part of the total conductivity component $\sigma_j(\omega)$ may become negative at some IR frequency. Because of the crystal asymmetry, $\Im\{\sigma_x\}$ and $\Im\{\sigma_y\}$ can in principle change their signs at different frequencies. Therefore, there may exist a range of frequencies where $\Im\{\sigma_x(\omega)\}\Im\{\sigma_y(\omega)\} < 0$, giving rise to a hyperbolic iso-frequency dispersion curve in the (k_x, k_y) plane, according to Eq. (5.23). Then, it can be said that phosphorene operates in a hyperbolic regime [125].

While the above discussion of the optical conductivity is of a general character, Nemilentsau *et al*. provided a minimal model for the optical conductivity of doped phosphorene, which captures all of the mentioned features, and is given by [125]

$$\sigma_j(\omega) = \frac{ie^2}{\omega + i\gamma}\frac{n}{m_j} + s_j\left[\Theta(\omega - \omega_j) + \frac{i}{\pi}\ln\left|\frac{\omega - \omega_j}{\omega + \omega_j}\right|\right], \tag{5.25}$$

for $j = x, y$. Here, n is the doping density, γ is the damping rate, and m_j is the effective electron or hole mass, arising in the Drude term that describes the intraband contributions. On the other hand, the interband contributions to the conductivity in Eq. (5.25) are weighted by the parameter s_j, with the real part given by the Heaviside function $\Theta(\omega - \omega_j)$ at a gap-related frequency ω_j and the corresponding imaginary part ensuring that the Kramers-Kronig relations are satisfied. The specific values for the parameters, proposed in Ref. [125] are: $m_x = 0.2\, m_0$, $m_y = m_0$ (with m_0 being the free electron mass), $\omega_x = 1$ eV, $\omega_y = 0.35$ eV, and $s_x = 1.7\, s_0$, $s_y = 3.7\, s_0$, where $s_0 = v_B/4$ with $v_B = e^2/\hbar \approx c/137$ being the Bohr speed.

In order to normalize the conductivity of doped phosphorene in the THz frequency range, where this material operates in a purely anisotropic regime [125], we define a characteristic wave number as $k_c = \frac{\pi n e^2}{2c^2}\left(\frac{1}{m_x} + \frac{1}{m_y}\right)$ and a characteristic angular frequency as $\omega_c = ck_c$. Then, the reduced wave number and the reduced frequency are defined as $\overline{k} = k/k_c$ and $\overline{\omega} = \omega/\omega_c$, respectively. Using the effective electron masses from Ref. [125] one can show that the value of $\omega_c = 4.14$ meV, corresponding to the frequency of $\nu_c = \omega_c/(2\pi) = 1$ THz, can be achieved by the doping density of $|n| \approx 7.9 \times 10^{13}$ cm^{-2}. Thus, in the regime where $\overline{\omega} \sim 1$, one has $\omega \ll \min(\omega_x, \omega_y)$, so that the interband contributions in Eq. (5.25) may be neglected, leaving only the Drude terms, which give the reduced conductivities, $\overline{\sigma}_j = \sigma_j/c$, as

$$\overline{\sigma}_{x,y}(\overline{\omega}) = \frac{i}{\pi}\frac{2}{1 + \rho^{\mp 1}}\frac{1}{\overline{\omega} + i\overline{\gamma}}. \tag{5.26}$$

Here, $\overline{\gamma} = \gamma/\omega_c$ and the parameter $\rho = m_y/m_x = 5$ introduces anisotropy due to the difference in the effective electron masses [125]. Note that, with the above normalization of the Drude

conductivity, we have lumped the only tunable parameter of the model, the doping density n of phosphorene, into the variables $\overline{k}$ and $\overline{\omega}$, while keeping the light cone in the form $\overline{\omega} = \overline{k}$. It should be mentioned that, for the typical doping density of $n = 7.9 \times 10^{13}$ cm^{-2}, the onset of interband transitions occurs when $\overline{\omega} > 84.6$, corresponding to $\omega > \omega_y = 0.35$ eV.

In order to obtain the normalized conductivity components of phosphorene up to the IR frequencies by using Eq. (5.25) [125], we introduce a new characteristic angular frequency, $\omega_r = \omega_x \omega_y / (\omega_x + \omega_y) \approx 0.26$ eV, corresponding to $\nu_r = \omega_r/(2\pi) \approx 62.8$ THz. By choosing then the characteristic wavenumber as $k_r = \omega_r/c$, we define the new reduced frequency as $\overline{\omega} = \omega/\omega_r$ and the new reduced wavenumber as $\overline{k} = k/k_r$, so that the light cone relation retains the same form, $\overline{\omega} = \overline{k}$, as in the low-frequency normalization. Using the new reduced variables, the jth component of the normalized tensor conductivity of phosphorene, $\overline{\sigma} \equiv \overline{\sigma}_j = \sigma_j/c$ (for $j = x, y$), which includes both the intraband and interband contributions, is given by

$$\overline{\sigma}_j(\overline{\omega}) = \frac{v_B}{c}\left(\frac{i}{\overline{\omega} + i\overline{\gamma}}\frac{\overline{n}}{\overline{m}_j} + \frac{1}{4}\overline{s}_j\left[\Theta(\overline{\omega} - \overline{\omega}_j) + \frac{i}{\pi}\ln\left|\frac{\overline{\omega} - \overline{\omega}_j}{\overline{\omega} + \overline{\omega}_j}\right|\right]\right), \tag{5.27}$$

where $\overline{\gamma} = \gamma/\omega_r$ and the doping density is defined in the reduced form by $\overline{n} = n/n_r$, with $n_r = \omega_r m_0/\hbar \approx 3.4 \times 10^{14}$ cm^{-2}. The other fixed parameters of the model in Eq. (5.27) are obtained from Ref. [125] as: $\overline{m}_x = 0.2$, $\overline{m}_y = 1$, $\overline{s}_x = 1.7$, $\overline{s}_y = 3.7$, $\overline{\omega}_x \approx 3.86$ and $\overline{\omega}_y \approx 1.35$. We note that, with the above normalization, limiting our considerations to the range of the reduced frequency in the interval $0 < \overline{\omega} < 1$ will ensure that the contributions of the step-like interband jumps in $\Re\{\overline{\sigma}_j\}$ vanish for both for $j = x, y$ in the full range of frequencies from THz to mid-IR, which includes the hyperbolic regime of phosphorene's optical response.

Directionality of the plasmon excitation by the incident charged particle

From the above discussion of anisotropic plasmon dispersions in phosphorene, it appears that the interaction of those modes with a charged particle under oblique incidence may be strongly affected by the direction of its parallel velocity component, $\mathbf{v}_\parallel$. In this section, we propose a method to explore that directionality.

From the discussion of the average number of excited plasmons in Chapter 2, one can resort to the regime of vanishing damping rates, $\Re\{\overline{\sigma}_j\} \to 0^+$ for $j = x, y$, and consider the probability density of Ohmic energy loss in phosphorene, $F_{\mathrm{Ohm}}(\mathbf{k}, \omega)$, which is then dominated by delta-function-like factors located at the dispersion surfaces of the plasmon modes, residing outside the light cone. In order to expose the directional dependence of the excitation of those modes,

we define an auxiliary function,

$$\Gamma(\mathbf{k}) = \frac{1}{\hbar}\int_0^\infty d\omega\, F_{\mathrm{Ohm}}\left(\mathbf{k},\omega\right), \tag{5.28}$$

which gives the probability density for exciting modes with 2D wavenumber $\mathbf{k} = (k_x, k_y) = (k\cos\phi, k\sin\phi)$, regardless of their frequency. Then, the total number of the excited modes may be written as

$$\nu_{\mathrm{tot}} = \iint d^2\mathbf{k}\,\Gamma(\mathbf{k}) = \int_{-\pi}^{\pi} d\phi\,\nu(\phi), \tag{5.29}$$

which helps us define the probability density for exciting modes that propagate in the direction defined by the angle ϕ, regardless of the magnitude of their in-plane wavevector (the in-plane wavenumber), as follows

$$\nu(\phi) = \int_0^\infty dk\,k\,\Gamma(k,\phi). \tag{5.30}$$

Furthermore, one may conclude from the discussion in Chapters 3 and 4 that directional effects in the plasmon excitation by the incident particle are best exposed by considering the limit of an extremely oblique incidence, or the near-parallel incidence of the charged particle, where $\theta_0 \to \frac{\pi}{2}$, i.e., $\beta_z \ll \beta_\parallel$. Then, one can show that the squared amplitude in Eq. (5.19) may be replaced according to

$$|\mathcal{A}|^2 \to 16\pi^3\frac{(Ze)^2k^2}{v_z\alpha^3}\,\delta\big(\omega - \mathbf{k}\cdot\mathbf{v}_\parallel\big), \tag{5.31}$$

where the delta function expresses the kinematic resonance condition, $\omega = \mathbf{k}\cdot\mathbf{v}_\parallel$, which automatically places the relevant regions of the $(\mathbf{k},\omega)$ space outside the light cone, hence justifying the choice $q = \alpha$.

Thus, the joint probability density for the Ohmic energy loss may be written approximately as

$$F_{\mathrm{Ohm}}\left(\mathbf{k},\omega\right) = \frac{4(Ze)^2k^2}{v_z\omega\alpha^3}\,\delta\big(\omega - \mathbf{k}\cdot\mathbf{v}_\parallel\big)\left[\left|\widetilde{E}_{0x}\right|^2\Re\left\{\sigma_x\right\} + \left|\widetilde{E}_{0y}\right|^2\Re\left\{\sigma_y\right\}\right], \tag{5.32}$$

or in the reduced form, $\overline{F}_{\mathrm{Ohm}} = F_{\mathrm{Ohm}}/F_c$ with $F_c = \frac{4(Ze)^2}{\pi\omega_c^2 k_c}$, where

$$\overline{F}_{\mathrm{Ohm}}\left(\overline{k}_x,\overline{k}_y,\overline{\omega}\right) = \pi\frac{1}{\beta_z}\frac{\overline{k}^2}{\overline{\omega}\,\overline{\alpha}^3}\,\delta\big(\overline{\omega} - \overline{k}_x\beta_x - \overline{k}_y\beta_y\big)\left[\left|\widetilde{E}_{0x}\right|^2\Re\left\{\overline{\sigma}_x\right\} + \left|\widetilde{E}_{0y}\right|^2\Re\left\{\overline{\sigma}_y\right\}\right]. \tag{5.33}$$

Then, the function in Eq. (5.28) can be evaluated in the limit of an extremely oblique incidence as

$$\Gamma(\mathbf{k}) = \Gamma_c \frac{1}{\beta_z} \frac{\overline{k}^2}{\overline{\omega}\,\overline{\alpha}^3} \left[\left| \widetilde{E}_{0x} \right|^2 \Re\left\{ \overline{\sigma}_x \right\} + \left| \widetilde{E}_{0y} \right|^2 \Re\left\{ \overline{\sigma}_y \right\} \right] \Theta(\overline{\omega}) \Big|_{\overline{\omega}=\overline{k}_x\beta_x+\overline{k}_y\beta_y}, \tag{5.34}$$

where we took advantage of the delta function in Eq. (5.32) and accordingly indicated that substitution $\overline{\omega} = \overline{k}_x\beta_x + \overline{k}_y\beta_y$ is to be made in all the occurrences of frequency, subject to the constraint $\overline{k}_x\beta_x + \overline{k}_y\beta_y > 0$, as enforced by the Heaviside function $\Theta(\overline{\omega})$, which follows from our consideration of positive values of the Ohmic energy loss in Eq. (5.28). We have also introduced a normalizing factor in that equation, defined by $\Gamma_c = \frac{4v_B}{ck_c^2}$.

Finally, the expression in Eq. (5.34) may be used in Eq. (5.30) upon substitution $\overline{k}_x = \overline{k}\cos\phi$ and $\overline{k}_y = \overline{k}\sin\phi$, subject to the constraint on the angles of plasmon propagation, ϕ, relative to the angle of the charged particle incidence, ϕ_0, given by $\cos(\phi - \phi_0) > 0$, or $|\phi - \phi_0| < \frac{\pi}{2}$, which follows from the Heaviside function Θ in that expression.

5.3 Results and discussion

While the formalism developed in the preceding section can be directly applied to any anisotropic 2D material described by a tensorial conductivity placed in a lossless dielectric surrounding, we assume here that a free-standing phosphorene layer is placed in vacuum, so that $\epsilon_d = 1$, and hence $k_d = k_0 = \frac{\omega}{c}$. In the following, we shall discuss our results separately in the regimes of low and high frequencies, characterizing the purely isotropic and the hyperbolic responses of doped phosphorene, respectively. As stated before, since the former regime operates in the THz range of frequencies, while the later regime operates in the mid-IR range, we shall adopt different normalizations of the relevant variables. Hence, one should carefully note that the range of frequency and wavenumber is very different due to different normalization factors.

5.3.1 Low frequency spectroscopy for purely anisotropic regime

Figure 5.2 shows level curves $\overline{\omega}(\overline{k}_x, \overline{k}_y) = \text{constant}$ in the $(\overline{k}_x, \overline{k}_y)$ plane, describing plasmon dispersion in the purely anisotropic regime based on the conductivity model in Eq. (5.26) with $\overline{\gamma} = 0$, for some typical values of the reduced frequencies: (a) $\overline{\omega} = 0.5$, (b) $\overline{\omega} = 1$, and (c) $\overline{\omega} = 5$. In each panel of the figure, the green solid lines represent the retarded plasmon dispersions from Eq. (5.23), the red dashed lines represent the nonretarded dispersions from Eq. (5.24), whereas

the gray circles identify the light cone, $\overline{\omega} = \overline{k}$, for the same set of frequencies. One notices that part of the nonretarded dispersion curve is inside the light cone and the effect of retardation is to push the dispersion curves outside the light cone. As discussed before, the topology of the dispersion for this range of frequencies is elliptic. As we move toward higher frequencies, due to weaker retardation effects, the retarded and nonretarded dispersion curves tend to coincide and lie out side the light cone. Also, the topology of dispersion tends to change to hyperbolic geometry at higher frequencies.

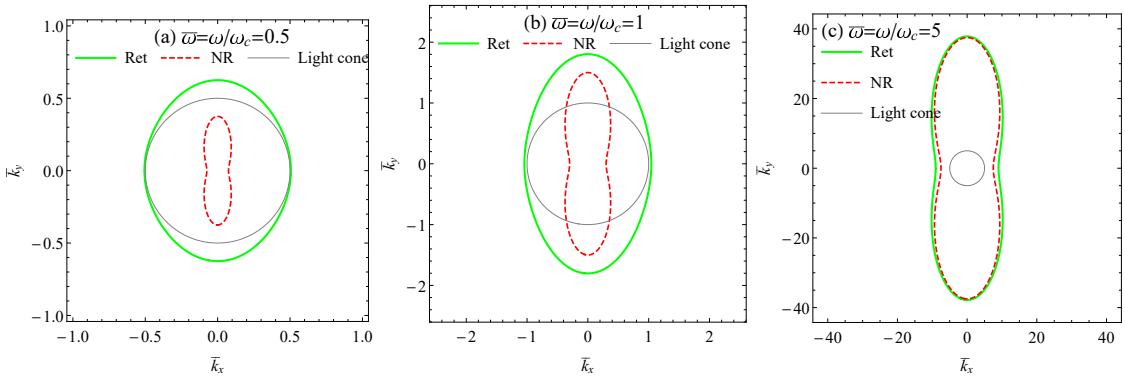

Figure 5.2: Dispersion level curves based on purely anisotropic conductivity model, shown using reduced units, $\overline{\omega}(\overline{k}_x, \overline{k}_y) = \text{const}$, for three frequencies: (a) $\overline{\omega} = 0.5$, (b) $\overline{\omega} = 1$, and (c) $\overline{\omega} = 5$. The retarded regime is shown with green solid curves, nonretarded regime with red dashed curves, while the gray circles show the light cones.

One notices in Fig. 5.2 that the retarded dispersion curves are tangential to the light circle when the component of wavevector in the ZZ direction of the phosphorene's crystal is vanishing, i.e., $\overline{k}_y = 0$. As the wavenumber in the ZZ direction increases, the dispersion curves fall off of the light circle. Hence, one can conclude that the retardation effects are magnified in the AC direction compared to the ZZ direction. This is because the reactive part of the conductivity component in the AC direction has larger magnitude compared to that of the ZZ direction, i.e., $\Im\{\sigma_x\} \geq \Im\{\sigma_y\}$, as a result of the atomic arrangement of the crystaline structure of phosphorene.

In Fig. 5.3(a), we show the 3D version of the retarded plasmon dispersion by the green surface, along with a red plane describing the kinematic resonance condition, $\overline{\omega} = \overline{k}_x\beta_x + \overline{k}_y\beta_y$, for a highly oblique incidence of the external charged particle with the speed $\beta = 0.5$ and angles $\theta_0 = 75°$, $\phi_0 = 0$, while the light cone is shown as a narrow blue cone.

In the panels (b) and (d) of Fig. 5.3, we show the intensity landscape of the Ohmic energy loss density, $\overline{F}_{\text{Ohm}}\left(\overline{k}_x, \overline{k}_y, \overline{\omega}\right)$ evaluated for $\overline{\omega} = 1$ and $\overline{\omega} = 2$, respectively, whereas in the panels (c) and (e) of Fig. 5.3, we show the intensity landscape of the radiative energy loss density,

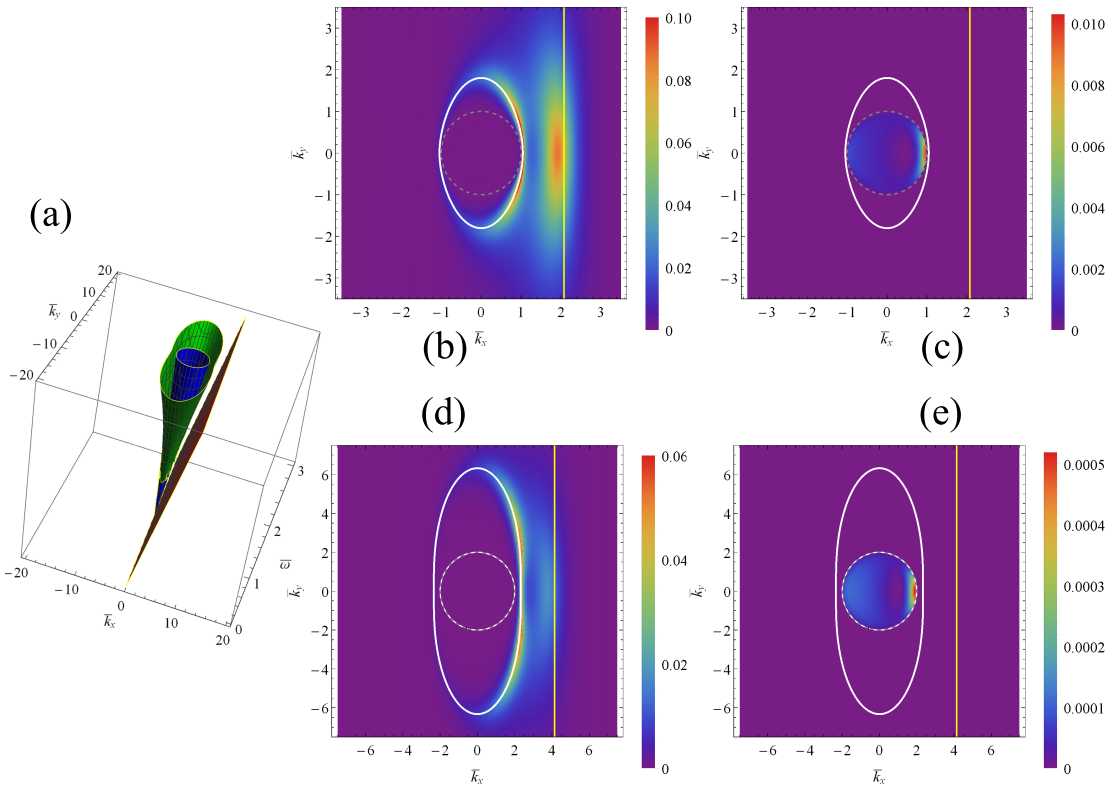

Figure 5.3: (a) Three-dimensional dispersion relation (obtained with $\overline{\gamma} = 0$) is shown by the green surface, accompanied by the plane for kinematic resonance condition with $\theta_0 = 75°$, $\phi_0 = 0$ and $\beta = 0.5$, shown in red, and the blue cone representing the light cone, all in purely anisotropic regime. The Ohmic energy loss density, $\overline{F}_{\rm Ohm}(\overline{k}_x, \overline{k}_y, \overline{\omega})$ (obtained with $\overline{\gamma} = 0.24$), is shown for two frequencies: (b) $\overline{\omega} = 1$ and (d) $\overline{\omega} = 2$. The radiative energy loss density, $\overline{F}_{\rm rad}(\overline{k}_x, \overline{k}_y, \overline{\omega})$ (obtained with $\overline{\gamma} = 0.24$), is shown for two frequencies: (c) $\overline{\omega} = 1$ and (e) $\overline{\omega} = 2$. Also shown are the corresponding level curves for the dispersion surfaces (white curves, obtained with $\overline{\gamma} = 0$), the kinematic resonance (yellow lines), and the light cone (grey dashed circles).

$\overline{F}_{\rm rad}\left(\overline{k}_x, \overline{k}_y, \overline{\omega}\right)$, also evaluated for $\overline{\omega} = 1$ and $\overline{\omega} = 2$, respectively. Furthermore, displayed are yellow straight lines, showing cross sections of the kinematic resonance plane $\overline{k}_x\beta_x + \overline{k}_y\beta_y = \overline{\omega}$ with the frequencies $\overline{\omega} = 1$ (panels b and c) and $\overline{\omega} = 2$ (panels d and e), which match frequencies used for the energy loss densities. In the panels (b)-(e), we also show level curves of the plasmon dispersion relations (using white solid lines), which are obtained from Eq. (5.23) for the same set of frequencies, $\overline{\omega} = 1$ (panels b and c) and $\overline{\omega} = 2$ (panels d and e), whereas the cross sections of the light cone with the corresponding frequencies are shown by the dashed grey circles.

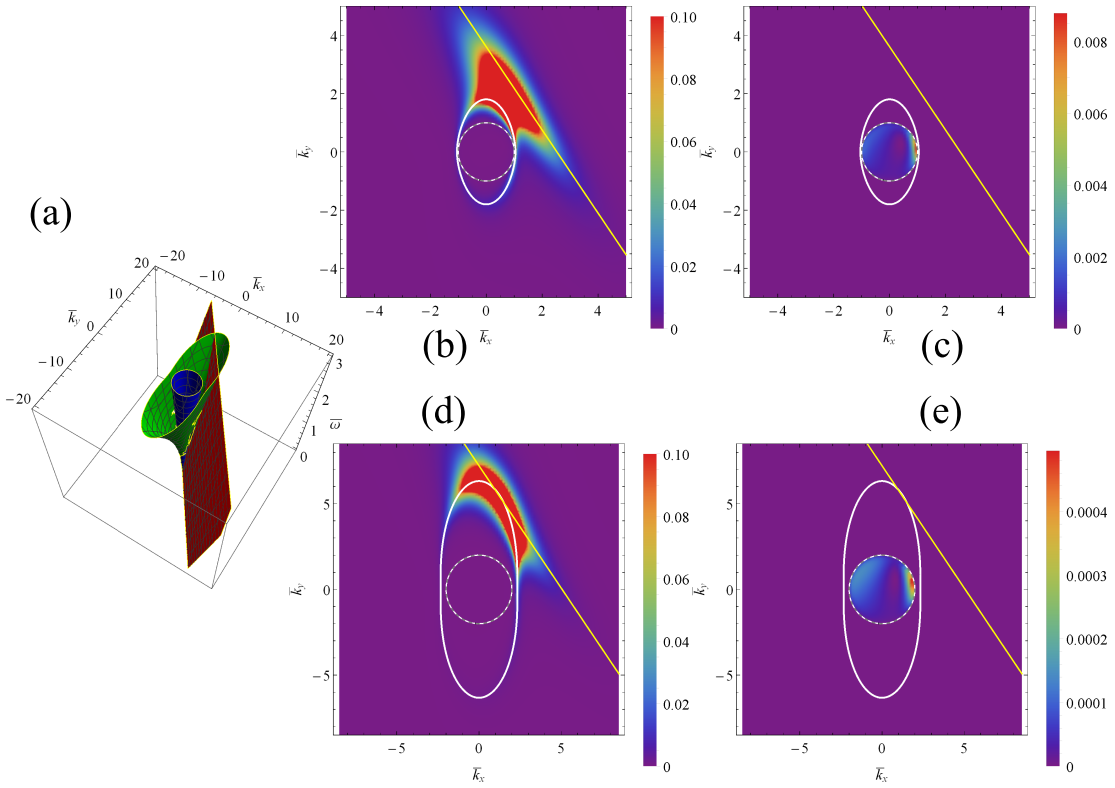

Figure 5.4: The same as Fig. 5.3, but with $\phi_0 = 35°$.

In Figs. 5.4, 5.5 and 5.6, we show the same set of data as in Fig. 5.3, obtained using the same set of parameters, while we only change in those three figures the azimuthal angle of incidence of the charged particle relative to the x-axis, so that $\phi_0 = 35°$, $\phi_0 = 55°$ and $\phi_0 = 90°$, respectively.

One can see in the panels (b) and (d) in all of the Figs. 5.3, 5.4, 5.5 and 5.6 that the intensity landscapes of the function $\overline{F}_{\rm Ohm}\left(\overline{k}_x, \overline{k}_y, \overline{\omega}\right)$ for frequencies $\overline{\omega} = 1$ and 2 are peaked along the corresponding dispersion level curves, as expected owing to the prevalence of the plasmon excitation channel in the Ohmic energy losses, but the distribution of that intensity is strongly

skewed toward the line that indicates the corresponding kinematic resonance condition. While the kinematic resonance line in Fig. 5.3 is parallel to the $\overline{k}_y$-axis (because $\phi_0 = 0$) and is relatively distant from the dispersion level curves, which are elongated along that same axis, increasing the direction angle ϕ_0 of the incident charged particle can bring the kinematic resonance line into close proximity of the plasmon dispersion curves, as shown in Figs. 5.4, 5.5(b) and 5.6(b), and can even cause that line to intersect dispersion curves at certain points $(\overline{k}_x^*, \overline{k}_y^*)$, as shown in Figs. 5.5(d) and 5.6(d).

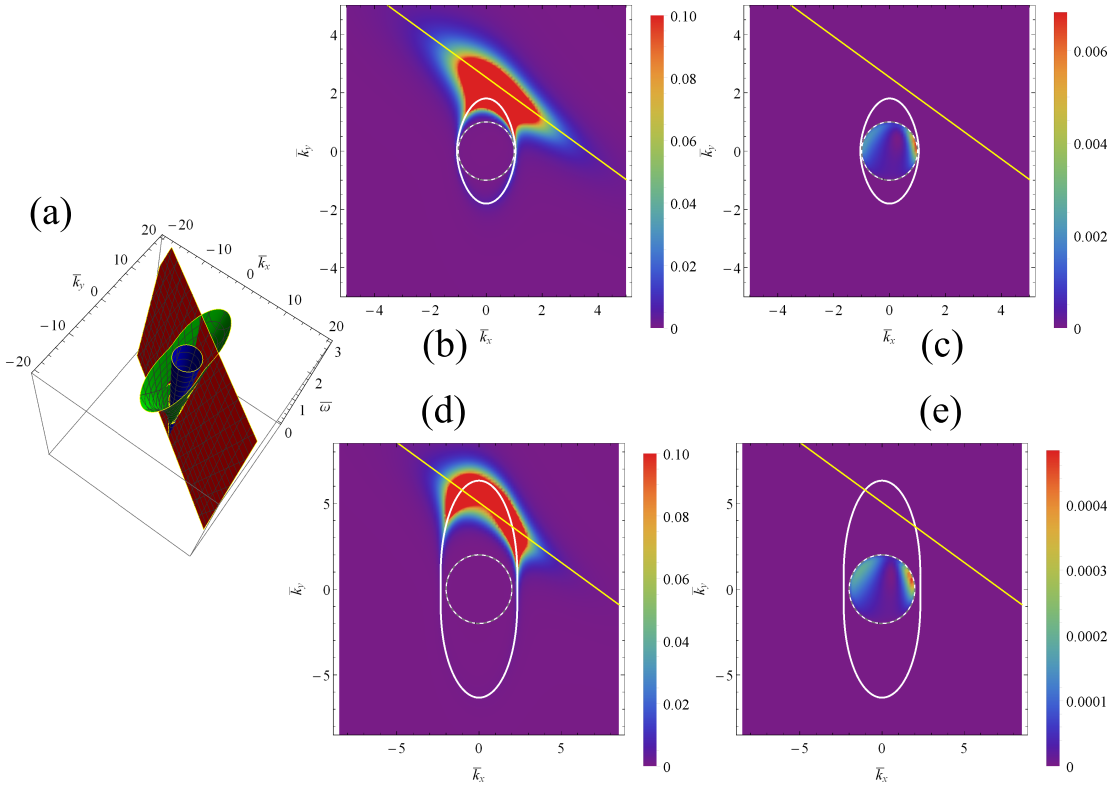

Figure 5.5: The same as Fig. 5.3, but with $\phi_0 = 55°$.

In the cases where the kinematic resonance line is close to becoming tangent to the dispersion curves, one expects that directions of the plasmon emission across the plane of phosphorene will be broadly distributed about the direction of motion of the incident particle owing to a close match of the direction of the group velocity of the plasmon dispersion, $\frac{\partial \omega}{\partial \mathbf{k}}$, with the direction of the parallel velocity component of the particle, $\mathbf{v}_{\|}$. In the cases when the intersection points $(\overline{k}_x^*, \overline{k}_y^*)$ of the kinematic resonance line with the dispersion curves are well-localized, as in Figs. 5.5(d) and 5.6(d), one expects that strongly directional plasmon emission will take place

in the directions defined by the angle $\phi = \arctan\left(\overline{k}_y^*/\overline{k}_x^*\right)$ for each intersection point.

Referring to Fig. 5.2, one may assert that the above conditions for the directionality of plasmon emission may be quite different if the nonretarded form of the plasmon dispersion is used, given in Eq. (5.24). Of course, the directionality conditions for plasmon emission change with changing the values of $\overline{\omega}$, as indicated in the panels (a) of Figs. 5.3, 5.4, 5.5 and 5.6. Therefore, it is desirable to consider those conditions by integrating over all frequencies and all wavenumber magnitudes $\overline{k} = \sqrt{\overline{k}_x^2 + \overline{k}_y^2}$.

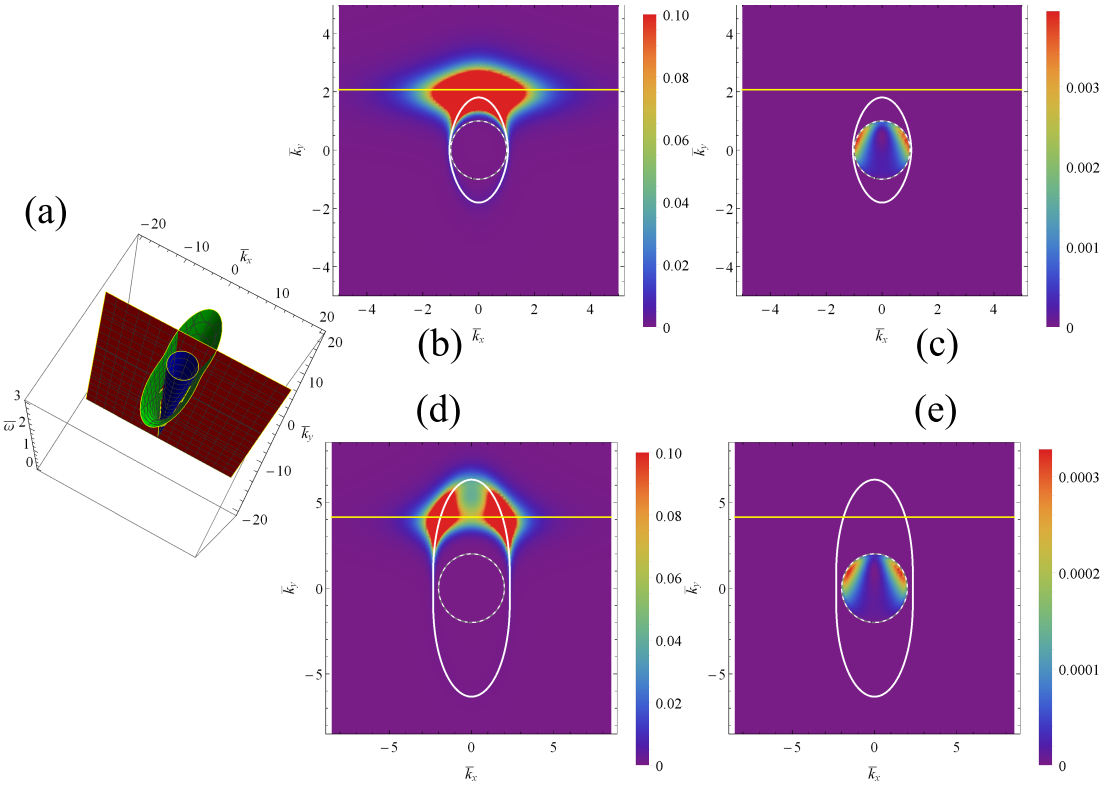

Figure 5.6: The same as Fig. 5.3, but with $\phi_0 = 90°$.

In Fig. 5.7, we show the total number of plasmons, $\nu(\phi)$, excited in phosphorene in the purely anisotropic regime as a function of their angle of propagation ϕ, regardless of their frequency, $\overline{\omega}$, and regardless of the magnitude of their wavevector, $\overline{k}$, as defined in Eq. (5.30). Because se present here only preliminary calculations of the directionality of the plasmon excitation due to the changing direction of the incident particle, we simplify our computations of $\nu(\phi)$ by using the approximation of extremely oblique incidence, giving Eq. (5.34), where relativistic effects

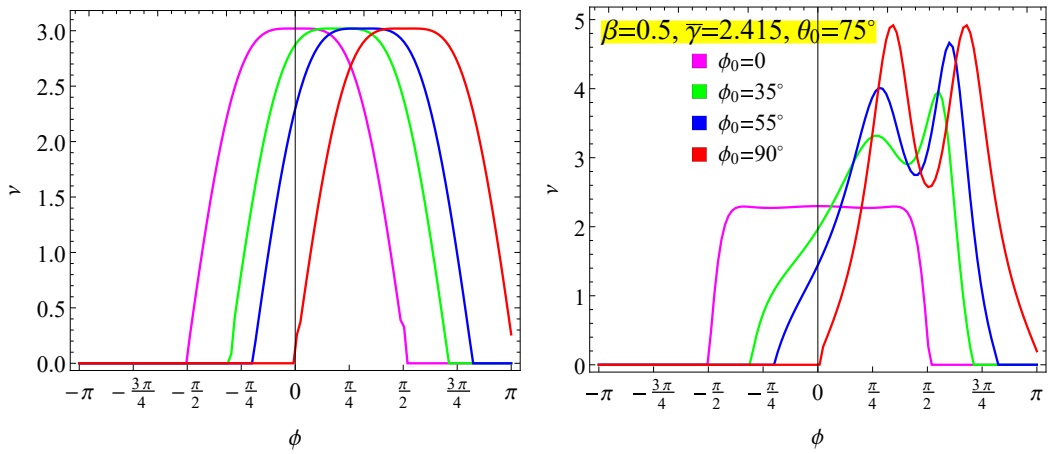

Figure 5.7: Average number of the excited plasmons as a function of their propagation angle ϕ in the purely anisotropic regime, obtained from Eq. (5.30) with Eq. (5.34) for two different scenarios: (a) a fictitious isotropic case, obtained by setting $\rho = 1$ in the conductivity model in Eq. (5.26) with $\overline{\gamma} = 0.24$, and (b) the anisotropic case, obtained Eq. (5.26) with $\rho = 5$ and $\overline{\gamma} = 0.24$. The incident charged particle speed is $\beta = 0.5$ and the polar angle is $\theta_0 = 75°$, whereas the pink, green, blue and red curves represent different azimuthal incidence angles: $\phi_0 = 0$, $35°$, $55°$ and $90°$, respectively.

are fully retained, while the conductivity model in Eq. (5.26) is used with small, but finite $\overline{\gamma}$. We consider in Fig. 5.7 a charged particle moving at the speed $\beta = 0.5$, with a rather oblique angle of incidence $\theta_0 = 75°$ upon the phosphorene plane, which justifies the use of Eq. (5.34), whereas the azimuthal incidence angles of $\phi_0 = 0$, $35°$, $55°$ and $90°$ are chosen to match those used in Figs. 5.3, 5.4, 5.5 and 5.6, respectively.

We first consider in Fig. 5.7(a) an artificially designed isotropic conductivity model, obtained by setting the asymmetry factor $\rho = 1$ in the model in Eq. (5.26). Such model is akin to the Drude model for low-frequency conductivity in doped graphene, studied in previous chapters. In that case, the dispersion level curves would be given by concentric circles in the $(\overline{k}_x, \overline{k}_y)$ plane, so that no variations are expected in $\nu(\phi)$ with changing the incidence angle ϕ_0 of the charged particle. Indeed, one observes in Fig. 5.7(a) that $\nu(\phi)$ is given by a broad, structureless distribution in the interval $|\phi - \phi_0| < \frac{\pi}{2}$.

On the other hand, in Fig. 5.7(b), we use the fully anisotropic conductivity model of phosphorene at low frequencies with $\rho = 5$ in Eq. (5.26), as implied by the parametrization due to Nemilentsau *et al.* [125]. In the case of the incident angle $\phi_0 = 0$, which was also discussed in

Fig. 5.3, one notices a rather broad and flat distribution of $\nu(\phi)$ for angles $|\phi| < \frac{\pi}{2}$, which echoes the fact that the plasmon dispersion curves in Fig. 5.3 are elongated in the direction parallel to the kinematic resonance line. Namely, in that figure, one may assert that the group velocity of the plasmon dispersion is almost parallel to the incident velocity of the charged particle $\mathbf{v}_{\parallel}$ over a broad range of the wavenumbers $\overline{k}_y$, giving a rather flat angular distribution of plasmon emission directions.

As the incidence angle ϕ_0 increases in Fig. 5.7(b), one notices that a well developed, double-peak structure arises in $\nu(\phi)$ in the interval of plasmon emission angles $|\phi - \phi_0| < \frac{\pi}{2}$. Those peaks are generally asymmetric, except in the case of $\phi_0 = 90^\circ$, discussed in Fig. 5.6. A separation between two peaks in the plasmon emission directions was predicted to occur at a higher frequency of $\overline{\omega} = 2$, used in Figs. 5.5(d) and 5.6(d) for the incidence angles $\phi_0 = 55^\circ$ and $\phi_0 = 90^\circ$, respectively, but not necessarily at a lower frequency or lower incidence angle. In that respect, it is a remarkable that one may conclude from Fig. 5.7(b) that integration over all plasmon frequencies gives rise to well-separated peaks even the incidence angle of $\phi_0 = 35^\circ$, and quite possibly for still smaller angles $\phi_0 \neq 0$.

Moreover, the peak positions in Fig. 5.7(b) seem to be dependent of the incidence angle ϕ_0, while one may assert that the angular separation between the peaks could be controlled by changing the total speed of the incident particle and/or its angle of incidence θ_0 upon the surface of graphene. Since the existence of the well-defined peaks in the distribution of the excited plasmons $\nu(\phi)$ Fig. 5.7(b) implies preferred directions of the plasmon propagation in the plane of phosphorene, one may conclude from the above analysis that it is indeed the anisotropy in the retarded plasmon dispersion of phosphorene that gives rise to the directionality effects in plasmon emission, which can be controlled by changing the direction of motion and the energy of the incident charged particle.

Finally, we consider the effects of anisotropy of phosphorene on the radiative energy loss. One observes in Figs. 5.3, 5.4, 5.5 and 5.6 that the intensity landscapes of the function $\overline{F}_{\mathrm{rad}}\left(\overline{k}_x, \overline{k}_y, \overline{\omega}\right)$, which were computed with $\overline{\omega} = 1$ and 2 in the panels (c) and (e) of those figures, respectively, are strictly localized inside the circles generated by the light cone at those two frequencies. On the other hand, the distribution of the intensity of radiation inside those circles is anisotropic and is strongly affected by the direction angle ϕ_0 of the incident charged particle in a rather unexpected manner. This is best illustrated by considering the cases of the incident angles $\phi_0 = 0$ and $\phi_0 = 90^\circ$ in Figs. 5.3 and 5.6, respectively. Namely, in the panels (c) and (e) of Fig. 5.3, one sees a peak in the radiation intensity in the region of the light circle nearest to the line corresponding to the kinematic resonance condition with $\phi_0 = 0$. On the other hand, in the panels (c) and (e) of Fig. 5.6 one sees a splitting of the intensity into two peaks, both leaning towards the kinematic resonance line with $\phi_0 = 90^\circ$, with a local dip in the region of the light circle nearest to that line. In principle, such dynamically induced anisotropies in the radiation distribution could be

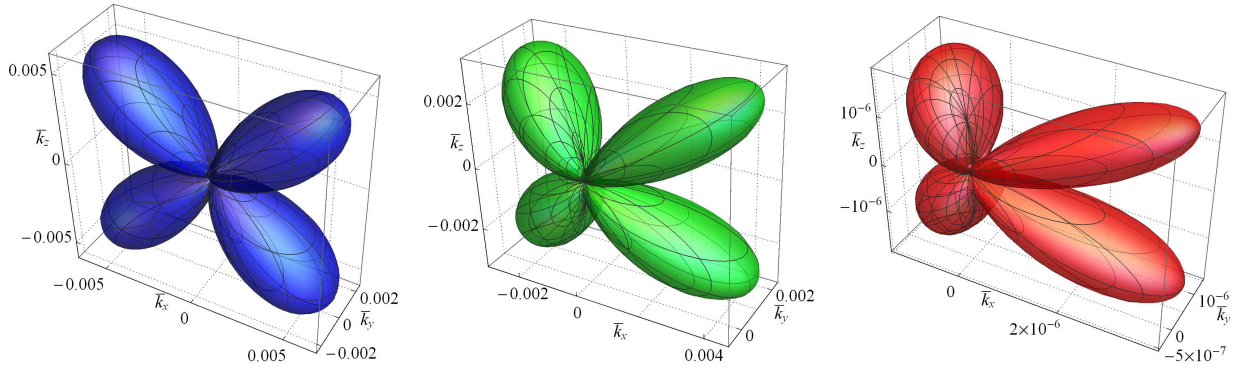

(a) (b) (c)

Figure 5.8: Angular distribution of the spectral density for TR emitted from phosphorene in the purely anisotropic regime, shown in reduced units as $\overline{\mathcal{S}}(\theta, \phi, \overline{\omega}) = \mathcal{S}/\mathcal{S}_c$, where $\mathcal{S}_c = (Ze)^2/c$ with $\overline{\omega} = 0.1$ and $\overline{\gamma} = 2.415$, for charged particle moving at the speed $\beta = 0.5$ and three combinations of the incidence angles: (a) $\theta_0 = 0$ and $\phi_0 = 0$, (b) $\theta_0 = \frac{\pi}{4}$ and $\phi_0 = \frac{\pi}{3}$, and (c) $\theta_0 \approx \frac{\pi}{2}$ (corresponding to a near-glancing incidence) and $\phi_0 = \frac{\pi}{6}$.

observed in the angle-resolved measurements in STEM.

In Fig. 5.8 we show the angular spectra of the emitted TR, $\overline{\mathcal{S}}(\theta, \phi, \overline{\omega})$, where $\overline{\mathcal{S}} = \mathcal{S}/\mathcal{S}_c$ with $\mathcal{S}_c = (Ze)^2/c$. Results are obtained for charged particle moving at the speed $\beta = 0.5$, for several selected combinations of its incident angles θ_0 and ϕ_0. Note that, in the figure, the emission angles of the TR are introduced via $\overline{k}_x = \overline{\omega}\sin\theta\cos\phi$, $\overline{k}_y = \overline{\omega}\sin\theta\sin\phi$, and $\overline{k}_z = \overline{\omega}\cos\theta$ using fixed frequency of $\overline{\omega} = 0.1$. In the case of normal incidence with $\theta_0 = 0$, shown in Fig. 5.8(a), one can immediately observe rather strong effects of anisotropic conductivity of phosphorene. Namely, the well-known "butterfly" spectra of TR in isotropic 2D materials, such as graphene, are axially symmetric about the surface normal to the target, in sharp contrast to the spectrum seen Fig. 5.8(a), which is localized in the direction of emission angles around $\phi = 0$, generating four symmetric lobes. Increasing the angle of incidence to $\theta_0 = \frac{\pi}{4}$ in Fig. 5.8(b) does not change much in the TR spectrum, whereas the near-grazing incidence with $\theta_0 \approx \frac{\pi}{2}$ ($\theta_0 = 89°$) in Fig. 5.8(c) opens the possibility to generate additional asymmetry in the spectra, which is controlled by changing the incidence angle ϕ_0.

5.3.2 High frequency spectroscopy for hyperbolic regime

As discussed in the previous section of this chapter, in the regime of higher frequencies, up to IR, the plasmon dispersion level curves may exhibit hyperbolic shapes. It should be stressed

here that, in this regime, the plasmon dispersion surface departs significantly away from the light cone and extends into a range of large in-plane wavenumbers. Therefore, in practice, one may safely use the nonretarded expression for plasmon dispersion, given in Eq. (5.24), which was not the case in the regime of low frequencies, characterized by elliptic dispersion curves, seen in Fig. 5.2. We note that, while calculations in the present subsection were performed with the retarded dispersion relation from Eq. (5.23), practically no change in the displayed results would occur if the nonretarded limit of Eq. (5.24) were used.

Figure 5.9 depicts the plasmon dispersion level curves in the reduced units pertinent to the hyperbolic regime, $\overline{\omega}(\overline{k}_x, \overline{k}_y) = \text{constant}$, for four different reduced frequencies: $\overline{\omega} = 0.4$ (green curve), $\overline{\omega} = 0.7$ (blue curve), $\overline{\omega} = 1$ (red curve), and $\overline{\omega} = 1.3$ (pink curve), obtained from Eq. (5.23) using the conductivity model from Eq. (5.27) with $\overline{\gamma} = 0$. We see that the low-frequency green curve is still not quite in the hyperbolic regime, but as the frequency increases, the dispersion curves evolve into hyperbolas with ever larger foci (larger linear eccentricity) and with less steep asymptotes. It should be stressed that a fully linear dependence is achieved in those asymptotes only at rather large wavenumbers, $|\overline{k}_x| \gtrsim 100$ and $|\overline{k}_y| \gtrsim 100$ in Fig. 5.9. At the same time, it should be remarked that circles related to the light cone, $\overline{k}_x^2 + \overline{k}_y^2 = \overline{\omega}^2$, would be barely visible in the ranges of axes used in that figure.

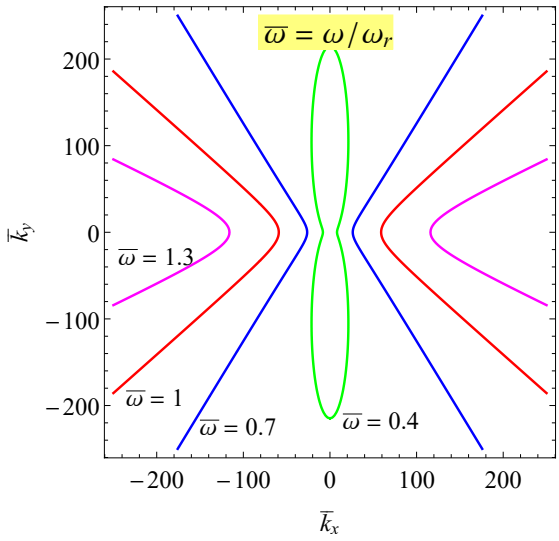

Figure 5.9: Dispersion level curves in hyperbolic regime are shown using reduced units, $\overline{\omega}(\overline{k}_x, \overline{k}_y) = \text{const}$, for four different reduced frequencies: $\overline{\omega} = 0.4$ (green curve), $\overline{\omega} = 0.7$ (blue curve), $\overline{\omega} = 1$ (red curve), and $\overline{\omega} = 1.3$ (pink curve), where $\overline{\gamma} = 0$. Note that the green line with $\overline{\omega} = 0.4$ is still not in hyperbolic range.

Guided by the analysis of the low-frequency regime in the preceding subsection, preferred directions of the plasmon excitation may be expected when the direction of the group velocity of the plasmon dispersion, $\frac{\partial\omega}{\partial\mathbf{k}}$, is closely matched with the direction of the parallel velocity component of the particle, $\mathbf{v}_{\parallel}$. In other words, it should be feasible to select the slope in the straight lines from the kinematic resonance condition, $\overline{\omega} = \overline{k}_x\beta_x + \overline{k}_y\beta_y$, to match the slope of any given pair of asymptotes in the dispersion level curves shown in Fig. 5.9 . However, because of the need for large wavenumbers to achieve a significant overlap of the dispersion level curves and the line $\overline{\omega} = \overline{k}_x\beta_x + \overline{k}_y\beta_y$ at frequencies $\overline{\omega} \sim 1$ used in that figure, one concludes that the parallel velocity components of the incident charged particle must be rather small, on the order of $\beta_x \sim 0.01$ and $\beta_y \sim 0.01$.

In Fig. 5.10, we show the intensity landscape of the Ohmic energy loss density, $\overline{F}_{\rm Ohm}(\overline{k}_x, \overline{k}_y, \overline{\omega})$, evaluated for three frequencies in the range $\overline{\omega} < 1$ using the conductivity model in Eq. (5.27) with doping density of $n = 3 \times 10^{13}$ cm^{-2}. Also displayed in Fig. 5.10 are yellow straight lines, showing cross sections of the kinematic resonance plane $\overline{k}_x\beta_x + \overline{k}_y\beta_y = \overline{\omega}$ with the same set frequencies for the incident particle speeds of $\beta = 0.2, 0.5, 0.035$ and incidence angle of $(\theta_0, \phi_0) = (75°, 0), (45°, 45°), (75°, 55°)$ with respect to the phosphorene plane, for panels (a), (b) and (c), respectively. We also show level curves of the plasmon dispersion relations (using white solid lines), which are obtained from Eq. (5.23) for the same set of frequencies and setting $\overline{\gamma} = 0$, whereas the cross sections of the light cone with the corresponding frequencies are shown by the barely visible dashed grey circles.

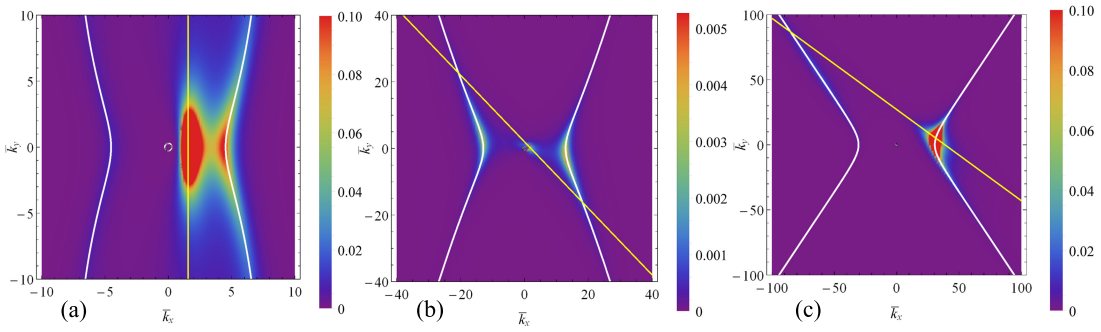

Figure 5.10: The Ohmic energy loss density, $\overline{F}_{\rm Ohm}(\overline{k}_x, \overline{k}_y, \overline{\omega})$, in the hyperbolic regime (obtained using the model in Eq. (5.27) with $\overline{\gamma} = 0.04$), is shown for: (a) $\overline{\omega} = 0.3$, $\beta = 0.2$, $\theta_0 = 75°$, $\phi_0 = 0$ (b) $\overline{\omega} = 0.5$, $\beta = 0.5$, $\theta_0 = 45°$, $\phi_0 = 45°$ and (c) $\overline{\omega} = 0.75$, $\beta = 0.035$, $\theta_0 = 75°$, $\phi_0 = 55°$. Also shown, for the same set of parameters, are the corresponding dispersion level curves (white lines, obtained from Eq. (5.23) with $\overline{\gamma} = 0$), as well as the kinematic resonance condition (yellow lines), $\overline{k}_x\beta_x + \overline{k}_y\beta_y = \overline{\omega}$. The level curves of the light cone (shown as grey dashed circles) are barely visible in the centers of the plots.

As in the preceding subsection, one can see in Fig. 5.10 that the intensity landscape of the function $\overline{F}_{\mathrm{Ohm}}\left(\overline{k}_x, \overline{k}_y, \overline{\omega}\right)$ is generally peaked along the corresponding dispersion level curves, as expected owing to the prevalence of the plasmon excitation channel in the Ohmic energy losses, but the distribution of that intensity seems to be skewed toward the line that indicates the corresponding kinematic resonance condition. In the panel (a) for $\theta_0 = 75^\circ$ and $\phi_0 = 0$ with $\overline{\omega} = 0.3$ and $\beta = 0.2$, where the kinematic resonance line is running between and parallel to the two branches of "not yet hyperbolas," one can expect strong excitation of the anisotropic plasmon (which may be considered as quasi-hyperbolic plasmon as the shape of partly illuminated dispersion curve suggests) in a broad range of directions $|\phi| < \pi/2$, originating from the branch closer to the kinematic resonance line. In the panel (b) for $\theta_0 = 45^\circ$ (where the kinematic resonance is weaker compared to that of panels (a) and (c)) and $\phi_0 = 45^\circ$ with $\overline{\omega} = 0.5$ and $\beta = 0.5$, there does not appear any particularly pronounced local enhancement in the intensity of the Ohmic energy loss which implies the poor excitation of hyperbolic plasmon for that particular angle of incidence and relativistic speed, whereas in the panel (c) for $\theta_0 = 75^\circ$ and $\phi_0 = 55^\circ$ with $\overline{\omega} = 0.75$ and $\beta = 0.035$, one notices a strong local enhancement of the intensity near the crossing point of the kinematic resonance line with the right branch of corresponding hyperbolic dispersion curve. This localization of the intensity of the Ohmic energy loss density indicates that a hyperbolic plasmon may be launched with a narrow angular distribution.

While the cases discussed in Fig. 5.10 were selected somewhat haphazardly, they nevertheless demonstrate the possibility to launch hyperbolic plasmons with narrowly distributed angles of propagation across the plane of phosphorene, which can be controlled by the velocity and the angles of incidence of the charged particle. Given the large size of the parameter space in this problem, a more detailed investigation is warranted. In particular, it would be desirable to evaluate the integrated average number of the excited plasmons $\nu(\phi)$, as in the previous subsection, but computations proved to be rather challenging in the hyperbolic regime so far, so they are left to be completed in near future.

Finally, we consider the effects of anisotropy of phosphorene on the radiative energy loss in the hyperbolic regime. While it was found that low speeds are desirable for the incident charged particle to be able to launch directionally-resolved hyperbolic plasmons, as discussed in Fig. 5.10, at such low speeds one expects significantly reduced radiative energy loss. Therefore, in order to explore any signatures of phosphorene's anisotropy in the angular spectra of the TR, we again consider Fig. 5.11 a fast charged particle, moving at $\beta = 0.5$.

The conductivity of phosphorene is modeled by Eq. (5.27) with doping density of $n = 3 \times 10^{13}$ cm^{-2} and $\overline{\gamma} = 0.03857$, and the angular spectra of TR are evaluated in Fig. 5.11 at frequency $\overline{\omega} = 0.5$ for three combinations of the incidence angles. When compared to the spectra shown in Fig. 5.8 for the low-frequency case, one notices large differences. The spectra in Fig. 5.11 show more asymmetry for the oblique incidence in the hyperbolic regime (panels b and c), and

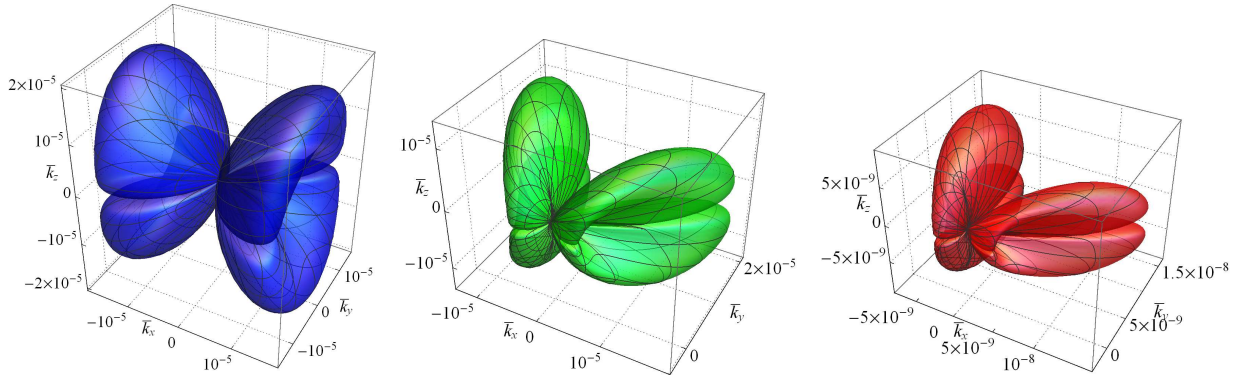

(a) (b) (c)

Figure 5.11: Angular distribution of the spectral density for TR emitted from phosphorene in the hyperbolic regime (obtained using the model in Eq. (5.27) with $\overline{\gamma} \approx 0.04$), shown in reduced units as $\overline{\mathcal{S}}(\theta, \phi, \overline{\omega}) = \mathcal{S}/\mathcal{S}_c$, where $\mathcal{S}_c = (Ze)^2/c$ with $\overline{\omega} = 0.5$ and $n = 3 \times 10^{13}$ cm^{-2}, for charged particle moving at the speed $\beta = 0.5$ and three combinations of the incidence angles: (a) $\theta_0 = 0$ and $\phi_0 = 0$, (b) $\theta_0 = \frac{\pi}{4}$ and $\phi_0 = \frac{\pi}{4}$, and (c) $\theta_0 \approx \frac{\pi}{2}$ (corresponding to a near-glancing incidence) and $\phi_0 = \frac{\pi}{6}$.

even for the normal incidence (panel a), there is a very atypical distribution of the TR intensity. One sees in Fig. 5.11 that the angular distribution of TR is heavily skewed towards the plane of phosphorene. At the same time, it exhibits a much broader distribution over $\bar{k}_y$ values than in Fig. 5.8, whereas the TR in the $\bar{k}_x = 0$ direction is sharply depleted, similar to Fig. 5.8. As the angle of incidence becomes oblique, one notices in Fig. 5.11 that the TR angular distribution is strongly skewed in the direction of motion of the incident particle. All these remarkable angular patterns of the TR from phosphorene in the IR frequency range should be readily detectable in STEM experiments.

5.4 Conclusions

We have developed a theory to study the interaction of an external charged particle with a general anisotropic two-dimensional (2D) material and applied it to a single-layer phosphorene in the retarded and nonretarded relative particle speed $\beta = v/c$ and the incidence angles (θ_0, ϕ_0) with respect to the normal to the plane and the armchair (AC) principal axis of phosphorene, respectively. We have evaluated and expressed the Ohmic and radiative energy losses of the external particle with respect to their dependency on the Cartesian components of the wavevector in

order to emphasize the role of anisotropic excitation processes of charge carriers in phosphorene under the oblique incidence. Those processes were described by defining an in-plane dielectric tensor with Cartesian component functions, which incorporate suitable models of phosphorene's anisotropic electrical conductivity. We use a phonomenological model proposed in Ref. [125] where a diagonal conductivity tensor is given in terms of the principal crystal axes of phosphorene (here, they are equal to the in-plane Cartesian coordinates). We have also focused on the directionality of plasmon excitation by a very obliquely incident charged particle.

Doped phosphorene responds to electromagnetic fields in two distinct manners. In a low-frequency range it shows purely anisotropic response, in which a Drude-type model is involved to describe intraband excitations of electrons, and in a high-frequency regime it shows hyperbolic behavior, where the contribution from interband transitions may become dominant, so that the signs of the imaginary parts of the conductivity components become different. For both regimes, the Ohmic intensity landscapes are peaked along the corresponding dispersion level curves, owing to the prevalence of the plasmon excitation channel, but the distribution of that intensity is strongly skewed toward the line that indicates the corresponding kinematic resonance condition. In general, we expect that in the cases where the kinematic resonance line is close to becoming tangent to the dispersion curves, the directions of the plasmon emission across the plane of phosphorene will be broadly distributed about the direction of motion of the incident particle owing to a close match of the direction of the group velocity of the plasmon dispersion, with the direction of the parallel velocity component of the particle. In the cases when the intersection points of the kinematic resonance line with the dispersion curves are well-localized, strongly directional plasmon emission will take place in particular directions depending on the coordinates of the intersection points in the wavevector plane.

In the terahertz frequency range, i.e., purely anisotropic regime, the dispersion surface forms an ellipsoid, where the effect of retardation is to push the dispersion surfaces outside the light cone. As we move toward higher frequencies, due to weaker retardation effects, the retarded and nonretarded dispersion level curves tend to coincide, lie out side the light circle, and also, change to hyperbolic geometry at higher frequencies. At the same time, we can see that the retardation effects are magnified in the AC direction compared to the zigzag direction.

In the case of the incident angle $\phi_0 = 0$, the average number of plasmon $\nu(\phi)$ forms a rather broad and flat distribution versus ϕ for angles $|\phi| < \frac{\pi}{2}$, which echoes the fact that the plasmon dispersion curves are elongated in the direction parallel to the kinematic resonance line. As the incidence angle ϕ_0 increases, a well developed, double-peak structure arises in $\nu(\phi)$ in the interval of plasmon emission angles $|\phi - \phi_0| < \frac{\pi}{2}$. Those peaks are generally asymmetric, except in the case of $\phi_0 = 90^\circ$. Moreover, the peak positions seem to be dependent of the incidence angle ϕ_0, while one may assert that the angular separation between the peaks could be controlled by changing the total speed of the incident particle and/or its angle of incidence θ_0 upon the

surface of graphene. Since the existence of the well-defined peaks in the distribution of the excited plasmons $\nu(\phi)$ implies preferred directions of the plasmon propagation in the plane of phosphorene, one may conclude from the performed analysis that it is indeed the anisotropy in the retarded plasmon dispersion of phosphorene that gives rise to the directionality effects in plasmon emission, which can be controlled by changing the direction of motion and the energy of the incident charged particle.

As for the radiative loss in purely anisotropic regime, the distribution of the intensity of radiation inside the light level circles is anisotropic in the wavevector plane and is strongly affected by the direction angle ϕ_0 of the incident charged particle in a rather unexpected manner. While there exists a peak in the radiation intensity in the region of the light circle nearest to the line corresponding to the kinematic resonance condition with $\phi_0 = 0$, one sees a splitting of the intensity into two peaks, both leaning towards the kinematic resonance line with $\phi_0 = 90^\circ$, with a local dip in the region of the light circle nearest to that line. In addition to the joint radiative loss spectra, rather strong effects of anisotropic conductivity of phosphorene are observed in the angular distributions of transition radiation (TR). Namely, the well-known "butterfly" spectra of TR in isotropic 2D materials, such as graphene, are axially symmetric about the surface normal to the target, in sharp contrast to the spectra of phosphorene, which are localized in the direction of emission angles around $\phi = 0$, generating four symmetric lobes. Increasing the angle of incidence to $\theta_0 = \frac{\pi}{4}$ does not change much in the TR spectrum, whereas the near-grazing incidence opens the possibility to generate additional asymmetry in the spectra, which is controlled by changing the incidence angle ϕ_0. In principle, such dynamically induced anisotropies in the radiation distribution could be observed in the angle-resolved measurements in scanning transmission electron microscope (STEM).

On the other hand, in a high-frequency range up to infrared (IR), i.e., hyperbolic regime, the plasmon dispersion surface departs significantly away from the light cone and extends into a range of large in-plane wavenumbers suggesting that is safe to apply nonretarded expression for plasmon dispersion. In such a range, the dispersion surface forms hyperbloids, where as the frequency increases, the dispersion level curves evolve into hyperbolas with ever larger foci (larger linear eccentricity) and with less steep asymptotes.

The Ohmic intensity landscape, in the case where the kinematic resonance line is running between and parallel to the two branches of hyperbolas, demonstrates strong excitation of the hyperbolic plasmon in a broad range of directions $|\phi| < \pi/2$, originating from the branch closer to the kinematic resonance line. By increasing the incidence angle ϕ_0, we notice a strong local enhancement of the intensity near the crossing point of the kinematic resonance line with the right branch of corresponding hyperbolic dispersion curve implying that a hyperbolic plasmon may be launched with a narrow angular distribution across the plane of phosphorene. This feature can be controlled by the velocity and the angles of incidence of the charged particle.

We have, also, investigated the angular spectra of TR at a typical frequency $\overline{\omega} = 0.1$ for three combinations of the incidence angles. In comparison to those of low-frequency range, the spectra in hyperbolic regime show more asymmetry, which should be readily detectable in STEM experiments.

Chapter 6

Summary, Conclusion, and Future Perspective

6.1 Summary and conclusion

The study of the interaction of relativistic charged particles with matter in nanoscale is very crucial since it is at the core of many problems in Mathematical Physics, Electromagnetic (EM) Theory, Condensed Matter Physics, Nanoscience and Technology, Electrical Engineering, Material Science, etc. In particular, interactions of graphene and other two-dimensional (2D) materials with externally moving charged particles have been studied in recent years in the context of electron energy loss spectroscopy (EELS), which has become a very popular experimental technique for exploring the plasmon excitations in graphene over a broad range of energies [32, 35, 38]. On the other hand, the technological need for a stable and tunable source of terahertz (THz) radiation has prompted several recent studies of the electromagnetic radiation from graphene, induced by its interaction with a fast electron beam [25, 50, 52]. In this thesis, we have proposed a theoretical framework to analyze the interaction of externally moving charged particles with 2D materials in the context of classical and relativistic electrodynamics.

In this regard, we have developed a fully relativistic treatment of the energy loss of a fast charged particle traversing a multilayer of isotropic conducting sheets with scalar conductivities (applied to multilayer graphene, MLG) under normal incidence (chapter 2), the stopping power of a charged particle moving parallel to an isotropic 2D material (applied to single-layer graphene, SLG) (chapter 3), energy loss of a fast charged particle traversing a monolayer of isotropic sheet (applied to SLG) under oblique incidence (chapter 4), as well as energy loss of a fast charged particle traversing a single layer of anisotropic material (applied to phosphorene)

under oblique incidence (chapter 5). In order to emphasize the role of electron excitations in 2D materials, as well as to elucidate the transition radiation (TR) from the 2D materials, we have assumed that the monolayers are placed in air (or vacuum) and neglected the recoil of the incident charged particle.

The formalism rendered in the thesis to develop the theoretical framework is as follows: (1) we have employed macroscopic EM theory based on Maxwell's equations. We have obtained self-consistent solutions of Maxwell's equations for the electric and magnetic fields by treating each layer as an infinitely large and infinitesimally thin, planar conductive sheet, for which a 2D Ohm's law may be invoked to express the in-plane induced charge current in terms of the tangential component of the total electric field by using a scalar or 2D conductivity tensor of the sheets. To this end, we have solved inhomogeneous vector wave equation for which we used the retarded scalar/dyadic Green's function approach depending on the geometry of the problem and the treatment of the boundary conditions. (2) Because we have dealt with 2D material boundary conditions, we have adopted a dielectric function approach in order to define a 2D in-plane dielectric response for the structure in the tangential directions across the 2D material. After finalizing the self-consistent solutions for the EM fields, (3) we have calculated the different contributions to the energy loss of the external charged particle, based on the Physical definition of EM work. Last but not least, (4) using the semiclassical approach of stochastic interpretation of the energy transfer, we have identified the probability density for each contribution to the energy loss of the external charged particle. Ultimately, we have analyzed the results and drawn conclusion for the potential applications in nanophotonics and nanoplasmonics.

6.1.1 Main contributions of the thesis

The research presented in this thesis was initiated by Miskovic *et al.* in Ref. [42] where they analyzed the EELS and TR of a charged particle traversing SLG under normal incidence over a wide range of frequency from terahertz (THz) to ultraviolet (UV). Accordingly, they adopted three different models of graphene's conductivity: Drude Model (intraband electron transitions in doped graphene) suitable for THz range, optical (Drude + Dirac) model suitable for THz to mid-infrared (MIR) range, and Drude-Lorentz (or hydrodynamic) model (interband electron transitions in undoped graphene) for MIR to UV range also known as optical range. A list of Miskovic *et al.* [42] main contributions is as follows:

- THz frequency range:
  - Effects of retardation on the dispersion of DPP and loss spectra
  - Comparable Ohmic and radiative contributions

  - Strong effects of damping rate on each contribution of loss spectra
  - Features of Ohmic loss spectrum:
    * Localized peak of Dirac plasmon polariton (DPP), located outside the light cone
    * Strong relativistic effects (by comparing retarded with nonretarded contributions)
    * Effective excitation of DPP with ~ 100 keV electrons in doped graphene
  - Features of radiative loss spectrum:
    * Broadly distributed and only extended within the light cone
    * Axially symmetric and skewed angular distribution of TR towards the plane of graphene (with the decrease in damping rate)
    * Efficient source of sub-THz radiation with a broad energy spectrum and characteristically skewed angular distribution

- Optical frequency range:
  - Suppression of radiative energy loss compared to the Ohmic loss
  - Displacement of the characteristic π and $\pi+\sigma$ peaks in the spectra towards the lower k values as the speed of charged particle increases, falling inside the light cone at relativistic electron energies
  - Relativistic effects give rise to $\sim 10\%$ increase in the characteristic peak heights in integrated energy loss density, which is dominated by the Ohmic loss
  - π and $\pi+\sigma$ peaks in the integrated TR loss density (red shifted in comparison to those of Ohmic loss)

In the first part of this thesis, a continuation of the work from Ref. [42] was performed to generalize the results for double-layer graphene (DLG) and MLG structures where we embarked to investigate the effect of retardation in the THz range. Hence, we only employed a suitable Drude model (intraband transitions), where for the DLG structure we considered both cases of equal and different conductivities, while for the case of MLG with $N > 2$, we considered equal interlayer distances and equal conductivities. Our main interest in the analysis of DLG was to analyze the interference as a result of retardation and the effects due to different choices of (1) inter-graphene distance d and (2) graphene layers' doping densities n_1 and n_2. A list of the main contributions of the results given in chapter 2 is given below, where the particularly intriguing ones are marked in red.

- Symmetric DLG ($n_1 = n_2$):

- Strong hybridization of DPPs $\begin{cases} \text{low-frequency, quasi-acoustic mode (bonding mode)} \\ \text{high-frequency, quasioptical mode (antibonding mode)} \end{cases}$
- Features of Ohmic loss:
  - Dominated by excitations of the bonding and antibonding modes outside the light cone
  - Release of the Joule heat due to finite damping rates, both outside and inside the light cone
  - Comparison of retarded with nonretarded distributions shows strong relativistic effects for $\lesssim 10$ THz for typical doping of graphene
- Features of radiative losses:
  - TR vs. Ohmic loss: comparable at ~ 1 THz, dominance of TR at sub-THz frequencies
  - Pronounced independence of angle-integrated TR energy loss distribution from inter-graphene distance d
- Interference due to retardation gives rise to asymmetry with respect to the direction of motion of the incident charged particle, including:
  - Asymmetry in directional decomposition of angle-resolved spectra of radiation emitted in the upper and lower half-spaces
  - Asymmetry in layer-wise decomposition of the Ohmic loss
  - Asymmetry in modal decomposition of the excitation probability density for hybridized Dirac plasmon polaritons (HDPPs)
  - Any asymmetry increases with the increase of the inter-graphene distance d

- Asymmetric DLG ($n_1 \neq n_2$):
  - Increasing the deviation of the asymmetry ratio $\rho = n_1/n_2$ from the symmetric case ($\rho = 1$) enhance retardation effects, which amplify asymmetries
  - Integration of the TR density over all angles implies reduction of: directional asymmetry, d-dependence, and ρ-dependence
  - The dependency of the average numbers of bonding and antibonding plasmons on the asymmetry ratio ρ shows cusp-like behavior near $\rho = 1$

For the case of MLG, the main contributions are:

- TLG ($N = 3$)
  - Absence of middle eigenfrequency HDPP mode in the middle layer (symmetry-protected plasmonic channel)
  - Even stronger asymmetries with respect to the direction of motion of charged particle
  - Fano resonance is observed near the lowest-lying HDPP eigenfrequency in the Ohmic loss distribution in the first traversed layer by the external particle, but is not observed in the last traversed layer
- MLG ($N > 2$)
  - Peaks and valley structures, which are observed in the integrated Ohmic energy loss distributions at supra-THz frequencies due to interference between HDPP modes, are reminiscent of the DLG features
  - Applicability of the concepts of optically thin and optically thick structures for the integrated Ohmic energy loss distributions
  - Applicability of the approximation representing an optically thin MLG (N layers) by SLG with the effective conductivity $N\sigma$
  - Pronounced independence of the angle-integrated TR energy loss distribution from the inter-graphene distance and the number of layers

We have also investigated the energy loss rate of a charged particle moving with speed v parallel to SLG at the distance b (impact parameter) in chapter 3. In this chapter we used the suitable Drude model. The main contributions of this chapter are:

- Calculations of the Ohmic energy loss rate at THz range (there is no radiation)
- The theory incorporates longitudinal and transverse in-plane conductivities
- Limit of zero damping implies excitation of the DPP in doped graphene by aloof electrons
- Increase in the importance of the retardation effects by increasing the particle's speed and the impact parameter
- Comparison of the retarded with nonretarded energy loss rates: interesting, nonmonotonous trends

  - v = constant: the retarded loss rate > nonretarded rate at large distances, reversed trend at shorter distances
  - b = constant: nonretarded loss rate > the retarded rate at high speeds, reversed trend at lower speeds

Next, we considered the third structure where a charged particle traverses SLG under oblique incidence. In chapter 4, we employed four different models for graphene's conductivity: Drude model for THz range (intraband transitions), Lovat's (nonlocal) model [141] for THz range (intraband transitions), Optical model for THz to MIR range (intraband and interband transitions), and Drude-Lorentz (hydrodynamic) model [40] for MIR to UV range (interband transitions). The major contributions of Chapter 4 are as follows:

- Ohmic and radiative contributions to energy loss are clearly decomposed into longitudinal and transverse components
- The angle of incidence as an additional tuning parameter for efficiently exciting plasmons or TR
- THz range:
  - Insignificance of nonlocal effect in the retarded regime
  - Strongly anisotropic angular patterns for longitudinal and transverse contributions to the emitted TR spectra
  - Distinction between the polarizations of traveling waves into the far-field
- MIR range:
  - Excitation of transverse mode is possible under suitable conditions, but with extremely low probability
- High energy (MIR to UV) range:
  - Strong directional features may arise in the in-plane distribution of the transverse contribution to the Ohmic loss

Finally, we investigated the energy loss channels of a charged particle traversing a monolayer of phosphorene under oblique incidence. In this case we employed a phonomenological (Drude + Dirac) model for the anisotropic conductivity of phosphorene proposed in [125].

- Elliptic topology of plasmon dispersion for purely anisotropic regime ($\sim$THz)
- Hyperbolic topology of plasmon dispersion for hyperbolic regime ($\sim$MIR)
- The new exotic behavior of collective modes may affect the energy loss spectra of the incident particle and the directional patterns of the emitted TR
- Directional and tunable surface plasmon polariton excitation can be achieved and controlled by changing the incident particle trajectory parameters

6.2 Prospective of future

The results presented in this thesis were calculated in the case of free-standing 2D materials in vacuum in order to investigate the fundamental optical properties of such materials. It is of great interest to integrate 2D materials with dielectric(s), and hence analyze the effects of the presence of the dielectric(s) and the resulting discontinuities at the boundary conditions on the energy loss and TR. More importantly, one can investigate and calculate the energy loss probability density due to presence of Cherenkov radiation. This can fall under a new research topic of:

- The effect of Cherenkov radiation in the EELS of 2D materials.

More interestingly, the topic may be generalized to consider polar substrates giving the topic of:

- Hybridization of phonons and plasmons in EELS.

In both of those topics the mathematical formulation requires the identification of dyadic Green's function for inhomogenouos layered media [121].

In general, in this thesis the relativistic treatment of energy transfer in the interaction of fast charged particles with 2D materials was considered. The proposed framework may be solidly extended to calculate the relativistic linear momentum transfer and reciprocating relativistic force between charged particles and 2D materials. The generalization of such work may be identified under the topic of:

- Fully relativistic treatment of 4-momentum transfer in the interaction of fast charged particles with 2D materials.

One of our main limitations in this thesis is that for all the considered 2D materials with zero thickness, we introduced a 2D in-plane conductivity model. Recently, researchers showed a great deal of interest in the accomodation of the out-of-plane polarizability of 2D materials in their analysis [164, 165, 166, 167, 168]. For us, it is of great interest to propose the full mathematical formulation for the electromagnetics of the zero-thickness conducting sheets with the out-of-plane polarizability component in order to efficiently satisfy the EM boundary conditions, continuity equation, and Ohm's law. This project may fall into the subject of:

- 2D materials with out-of-plane polarizability: electrodynamics and EELS.

In our future research, we may also plan to augment the analytical models by including concepts from Differential Geometry to analyze more complex structures. This subject of interest may be introduced as:

- The effect of geometry of 2D materials on EELS, plasmon excitation and radiation.

Ultimately, as the last suggestion, it is of great importance to include the effects of quantum optical excitations in 2D materials traversed by fast charged particles [169]. Such an effort involves concepts from Quantum Field Theory and Quantum Electrodynamics to tackle more fundamental aspects of our research pertaining to Condensed Matter Physics and Relativistic Electrodynamics. This may also fall into the topic of:

- Quantum Field Theory description of EELS of 2D materials by fast charged particles.

References

[1] K. S. Novoselov, A. K. Geim, S. V. Morozov, D. Jiang, Y. Zhang, S. V. Dubonos, I. V. Grigorieva, and A. A. Firsov. Electric field effect in atomically thin carbon films. *Science*, 306(5696):666–669, 2004.

[2] Ruben Mas-Balleste, Cristina Gomez-Navarro, Julio Gomez-Herrero, and Felix Zamora. 2d materials: to graphene and beyond. *Nanoscale*, 3:20–30, 2011.

[3] Fengnian Xia, Han Wang, Di Xiao, Madan Dubey, and Ashwin Ramasubramaniam. Two-dimensional material nanophotonics. *Nat. Photonics*, 8:899, nov 2014.

[4] D. N. Basov, M. M. Fogler, and F. J. García de Abajo. Polaritons in van der waals materials. *Science*, 354(6309), 2016.

[5] Tony Low, Andrey Chaves, Joshua D Caldwell, Anshuman Kumar, Nicholas X Fang, Phaedon Avouris, Tony F Heinz, Francisco Guinea, Luis Martin-Moreno, and Frank Koppens. Polaritons in layered two-dimensional materials. *Nat. Mater.*, 16:182, nov 2016.

[6] Vinod K. Sangwan and Mark C. Hersam. Electronic transport in two-dimensional materials. *Annual Review of Physical Chemistry*, 69(1):299–325, 2018. PMID: 29463170.

[7] B. Radisavljevic, A. Radenovic, J. Brivio, V. Giacometti, and A. Kis. Single-layer MoS_2 transistors. *Nat. Nanotechnol.*, 6(3):147–150, jan 2011.

[8] Q. Wang, K. Kalantar-Zadeh, K. Andras, J. Coleman, and M. Strano. Electronics and optoelectronics of two-dimensional transition metal dichalcogenides. *Nat. Nanotechnol.*, 193:699–712, nov 2012.

[9] Alessandro Molle, Joshua Goldberger, Michel Houssa, Yong Xu, Shou Cheng Zhang, and Deji Akinwande. Buckled two-dimensional Xene sheets. *Nat. Mater.*, 16(2):163–169, jan 2017.

[10] Han Liu, Adam T. Neal, Zhen Zhu, Zhe Luo, Xianfan Xu, David Tománek, and Peide D. Ye. Phosphorene: An unexplored 2d semiconductor with a high hole mobility. *ACS Nano*, 8(4):4033–4041, 2014. PMID: 24655084.

[11] Likai Li, Yijun Yu, Guo Jun Ye, Qingqin Ge, Xuedong Ou, Hua Wu, Donglai Feng, Xian Hui Chen, and Yuanbo Zhang. Black phosphorus field-effect transistors. *Nat. Nanotechnol.*, 9:372, mar 2014.

[12] Steven P. Koenig, Rostislav A. Doganov, Hennrik Schmidt, A. H. Castro Neto, and Barbaros Özyilmaz. Electric field effect in ultrathin black phosphorus. *Applied Physics Letters*, 104(10):103106, 2014.

[13] H. Liu, A. T. Neal, M. Si, Y. Du, and P. D. Ye. The effect of dielectric capping on few-layer phosphorene transistors: Tuning the schottky barrier heights. *IEEE Electron Device Letters*, 35(7):795–797, July 2014.

[14] Meysam Akhtar, George Anderson, Rong Zhao, Adel Alruqi, Joanna E Mroczkowska, Gamini Sumanasekera, and Jacek B Jasinski. Recent advances in synthesis, properties, and applications of phosphorene. *npj 2D Mater. Appl.*, 1(1):5, 2017.

[15] C. J. Powell and J. B. Swan. Origin of the characteristic electron energy losses in aluminum. *Phys. Rev.*, 115:869–875, Aug 1959.

[16] R. H. Ritchie. Plasma losses by fast electrons in thin films. *Phys. Rev.*, 106:874–881, Jun 1957.

[17] R F Egerton. Electron energy-loss spectroscopy in the tem. *Reports on Progress in Physics*, 72(1):016502, 2009.

[18] F J García de Abajo. Optical excitations in electron microscopy. *Reviews of Modern Physics*, 82(1):209–275, February 2010.

[19] W. Zhou, J. Lee, J. Nanda, S. T. Pantelides, S. J. Pennycook, and J.-C. Idrobo. Atomically localized plasmon enhancement in monolayer graphene. *Nature Nanotechnology*, 7:161–165, Mar 2012.

[20] Toon Coenen, Benjamin J.M. Brenny, Ernst Jan Vesseur, and Albert Polman. Cathodoluminescence microscopy: Optical imaging and spectroscopy with deep-subwavelength resolution. *MRS Bulletin*, 40(4):359–365, 2015.

[21] Michael Stöger-Pollach, Lukáš Kachtík, Bernhard Miesenberger, and Philipp Retzl. Transition radiation in EELS and cathodoluminescence. *Ultramicroscopy*, 173:31–35, February 2017.

[22] Tetsuyuki Ochiai. Efficiency and angular distribution of graphene-plasmon excitation by electron beam. *Journal of the Physical Society of Japan*, 83(5):054705, 2014.

[23] B.G. Mendis, A. Howkins, D. Stowe, J.D. Major, and K. Durose. The role of transition radiation in cathodoluminescence imaging and spectroscopy of thin-foils. *Ultramicroscopy*, 167:31 – 42, 2016.

[24] Liang Jie Wong, Ido Kaminer, Ognjen Ilic, John D Joannopoulos, and Marin Soljačić. Towards graphene plasmon-based free-electron infrared to X-ray sources. *Nature Photonics*, 10:46, nov 2015.

[25] Tianrong Zhan, Dezhuan Han, Xinhua Hu, Xiaohan Liu, Siu-Tat Chui, and Jian Zi. Tunable terahertz radiation from graphene induced by moving electrons. *Phys. Rev. B*, 89:245434, Jun 2014.

[26] Tao Zhao, Sen Gong, Min Hu, Renbin Zhong, Diwei Liu, Xiaoxing Chen, Ping Zhang, Xinran Wang, Chao Zhang, Peiheng Wu, and Shenggang Liu. Coherent and Tunable Terahertz Radiation from Graphene Surface Plasmon Polarirons Excited by Cyclotron Electron Beam. *Scientific Reports*, 5:16059, nov 2015.

[27] Shenggang Liu, Min Hu, Renbin Zhong, Xiaoxing Chen, Ping Zhang, Sen Gong, and Tao Zhao. Electron beam excitation of surface plasmon polaritons and transformation into electromagnetic radiation. *International Journal of Terahertz Science and Technology*, 8(2):69–84, 2015.

[28] Mathieu Kociak and Odile Stephan. Mapping plasmons at the nanometer scale in an electron microscope. *Chem. Soc. Rev.*, 43:3865–3883, 2014.

[29] D. Rossouw, M. Couillard, J. Vickery, E. Kumacheva, and G. A. Botton. Multipolar plasmonic resonances in silver nanowire antennas imaged with a subnanometer electron probe. *Nano Letters*, 11(4):1499–1504, 2011. PMID: 21446717.

[30] Juan C. Idrobo and Wu Zhou. A short story of imaging and spectroscopy of two-dimensional materials by scanning transmission electron microscopy. *Ultramicroscopy*, 180:156 – 162, 2017. Ondrej Krivanek: A research life in EELS and aberration corrected STEM.

[31] Jamie H Warner, Yung-Chang Lin, Kuang He, Masanori Koshino, and Kazu Suenaga. Atomic level spatial variations of energy states along graphene edges. *Nano letters*, 14(11):6155—6159, November 2014.

[32] Antonio Politano and Gennaro Chiarello. Plasmon modes in graphene: status and prospect. *Nanoscale*, 6:10927–10940, 2014.

[33] V. Borka Jovanovic, I. Radovic, D. Borka, and Z. L. Miskovic. High-energy plasmon spectroscopy of freestanding multilayer graphene. *Phys. Rev. B*, 84:155416, Oct 2011.

[34] V. Despoja, D. Novko, K. Dekanić, M. Šunjić, and L. Marušić. Two-dimensional and π plasmon spectra in pristine and doped graphene. *Phys. Rev. B*, 87:075447, Feb 2013.

[35] T. Eberlein, U. Bangert, R. R. Nair, R. Jones, M. Gass, A. L. Bleloch, K. S. Novoselov, A. Geim, and P. R. Briddon. Plasmon spectroscopy of free-standing graphene films. *Phys. Rev. B*, 77:233406, Jun 2008.

[36] Mhairi H Gass, Ursel Bangert, Andrew L Bleloch, Peng Wang, Rahul R Nair, and A K Geim. Free-standing graphene at atomic resolution. *Nat. Nanotechnol.*, 3:676, sep 2008.

[37] S. C. Liou, C.-S. Shie, C. H. Chen, R. Breitwieser, W. W. Pai, G. Y. Guo, and M.-W. Chu. π-plasmon dispersion in free-standing graphene by momentum-resolved electron energy-loss spectroscopy. *Phys. Rev. B*, 91:045418, Jan 2015.

[38] Florence J. Nelson, Juan-Carlos Idrobo, John D. Fite, Zoran L. Miskovic, Stephen J. Pennycook, Sokrates T. Pantelides, Ji Ung Lee, and Alain C. Diebold. Electronic excitations in graphene in the 1–50 ev range: The π and $\sigma + \pi$ peaks are not plasmons. *Nano Letters*, 14(7):3827–3831, 2014. PMID: 24884760.

[39] P. Wachsmuth, R. Hambach, M. K. Kinyanjui, M. Guzzo, G. Benner, and U. Kaiser. High-energy collective electronic excitations in free-standing single-layer graphene. *Phys. Rev. B*, 88:075433, Aug 2013.

[40] Tijana Djordjevic, Ivan Radovic, Vito Despoja, Keenan Lyon, D Borka, and Zoran L. Miskovic. Analytical modeling of electron energy loss spectroscopy of graphene: Ab initio study versus extended hydrodynamic model. *Ultramicroscopy*, 184:134–142, 09 2017.

[41] K. Lyon, D. J. Mowbray, and Z. L. Miskovic. Modelling relativistic effects in momentum-resolved electron energy loss spectroscopy of graphene. *Radiation Effects and Defects in Solids*, 173(1-2):8–21, 2018.

[42] Zoran L Miskovic, Silvina Segui, Juana L Gervasoni, and Néstor R Arista. Energy losses and transition radiation produced by the interaction of charged particles with a graphene sheet. *Physical Review B*, 94(12):125414, September 2016.

[43] Dino Novko, Marijan Sunjic, and Vito Despoja. Optical absorption and conductivity in quasi-two-dimensional crystals from first principles: Application to graphene. *Phys. Rev. B*, 93(12):125413, March 2016.

[44] Ido Kaminer, Yaniv Tenenbaum Katan, Hrvoje Buljan, Yichen Shen, Ognjen Ilic, Josué J López, Liang Jie Wong, John D Joannopoulos, and Marin Soljačić. Efficient plasmonic emission by the quantum Čerenkov effect from hot carriers in graphene. *Nature Communications*, 7:ncomms11880, jun 2016.

[45] Xiao Lin, Sajan Easo, Yichen Shen, Hongsheng Chen, Baile Zhang, John D Joannopoulos, Marin Soljačić, and Ido Kaminer. Controlling Cherenkov angles with resonance transition radiation. *Nature Physics*, 14(8):816–821, 2018.

[46] Xiao Lin, Ido Kaminer, Xihang Shi, Fei Gao, Zhaoju Yang, Zhen Gao, Hrvoje Buljan, John D. Joannopoulos, Marin Soljačić, Hongsheng Chen, and Baile Zhang. Splashing transients of 2d plasmons launched by swift electrons. *Science Advances*, 3(1), 2017.

[47] Xihang Shi, Xiao Lin, Fei Gao, Hongyi Xu, Zhaoju Yang, and Baile Zhang. Caustic graphene plasmons with kelvin angle. *Phys. Rev. B*, 92:081404, Aug 2015.

[48] Xihang Shi, Xiao Lin, Ido Kaminer, Fei Gao, Zhaoju Yang, John D Joannopoulos, Marin Soljačić, and Baile Zhang. Superlight inverse Doppler effect. *Nature Physics*, 14(10):1001–1005, 2018.

[49] Yi Yang, Aviram Massuda, Charles Roques-Carmes, Steven E Kooi, Thomas Christensen, Steven G Johnson, John D Joannopoulos, Owen D Miller, Ido Kaminer, and Marin Soljačić. Maximal spontaneous photon emission and energy loss from free electrons. *Nat. Phys.*, 14(9):894–899, 2018.

[50] Shenggang Liu, Chao Zhang, Min Hu, Xiaoxing Chen, Ping Zhang, Sen Gong, Tao Zhao, and Renbin Zhong. Coherent and tunable terahertz radiation from graphene surface plasmon polaritons excited by an electron beam. *Applied Physics Letters*, 104(20):201104, 2014.

[51] Tao Zhao, Min Hu, Renbin Zhong, Sen Gong, Chao Zhang, and Shenggang Liu. Cherenkov terahertz radiation from graphene surface plasmon polaritons excited by an electron beam. *Applied Physics Letters*, 110(23):231102, 2017.

[52] Kai-Chun Zhang, Xiao-Xing Chen, Chang-Jian Sheng, Kelvin J. A. Ooi, Lay Kee Ang, and Xue-Song Yuan. Transition radiation from graphene plasmons by a bunch beam in the terahertz regime. *Opt. Express*, 25(17):20477–20485, Aug 2017.

[53] Ernst Jan R. Vesseur, Javier Aizpurua, Toon Coenen, Alejandro Reyes-Coronado, Philip E. Batson, and Albert Polman. Plasmonic excitation and manipulation with an electron beam. *MRS Bulletin*, 37(8):752–760, 2012.

[54] Adam Brandstetter-Kunc, Guillaume Weick, Charles A. Downing, Dietmar Weinmann, and Rodolfo A. Jalabert. Nonradiative limitations to plasmon propagation in chains of metallic nanoparticles. *Phys. Rev. B*, 94:205432, Nov 2016.

[55] B Wunsch, T Stauber, F Sols, and F Guinea. Dynamical polarization of graphene at finite doping. *New Journal of Physics*, 8(12):318–318, dec 2006.

[56] E. H. Hwang and S. Das Sarma. Dielectric function, screening, and plasmons in two-dimensional graphene. *Phys. Rev. B*, 75:205418, May 2007.

[57] Kamran Akbari, Zoran L. Miskovic, Silvina Segui, Juana L. Gervasoni, and Nestor R. Arista. Energy losses and transition radiation in multilayer graphene traversed by a fast charged particle. *ACS Photonics*, 4(8):1980–1992, 2017.

[58] Kamran Akbari, Silvina Segui, Juana L. Gervasoni, Zoran L. Miskovic, and Nestor R. Arista. Production of plasmons in two layers of graphene with different doping densities traversed by swift electrons. *Applied Surface Science*, 446:191 – 195, 2018. 12th International Conference on Surfaces, Coatings and Nanostructured Materials - NANOSMAT 2017.

[59] Kamran Akbari, Zoran L Miskovic, Silvina Segui, Juana L Gervasoni, and Nestor R Arista. Excitation of hybridized dirac plasmon polaritons and transition radiation in multilayer graphene traversed by a fast charged particle. *Nanotechnology*, 29(22):225201, 2018.

[60] Zoran L. Miskovic, Kamran Akbari, Silvina Segui, Juana L. Gervasoni, and Nestor R. Arista. Relativistic effects in the energy loss of a fast charged particle moving parallel to a two-dimensional electron gas. *Nuclear Instruments and Methods in Physics Research Section B: Beam Interactions with Materials and Atoms*, 422:18 – 23, 2018.

[61] Kamran Akbari, Silvina Segui, Zoran L. Mišković, Juana L. Gervasoni, and Néstor R. Arista. Energy losses and transition radiation in graphene traversed by a fast charged particle under oblique incidence. *Phys. Rev. B*, 98:195410, Nov 2018.

[62] K. Akbari. Excitation of hyperbolic plasmons and transition radiation in phosphorene by a swift electron. In *2018 18th International Symposium on Antenna Technology and Applied Electromagnetics (ANTEM)*, pages 1–2, Aug 2018.

[63] John David Jackson. *Classical electrodynamics*. Wiley, New York, 3rd ed. edition, 1999.

[64] F Bonaccorso, Z Sun, T Hasan, and A C Ferrari. Graphene photonics and optoelectronics. *Nature Photonics*, 4:611, aug 2010.

[65] A N Grigorenko, M Polini, and K S Novoselov. Graphene plasmonics. *Nature Photonics*, 6:749, nov 2012.

[66] F Javier García de Abajo. Graphene Plasmonics: Challenges and Opportunities. *ACS Photonics*, 1(3):135–152, mar 2014.

[67] Mahmood Aliofkhazraei, Nasar Ali, William I Milne, Cengiz S Ozkan, Stanislaw Mitura, and Juana L Gervasoni. *Graphene Science Handbook, Six-Volume Set*. Crc Press, 2016.

[68] Achim Woessner, Mark B Lundeberg, Yuanda Gao, Alessandro Principi, Pablo Alonso-González, Matteo Carrega, Kenji Watanabe, Takashi Taniguchi, Giovanni Vignale, Marco Polini, James Hone, Rainer Hillenbrand, and Frank H L Koppens. Highly confined low-loss plasmons in graphene-boron nitride heterostructures. *Nature Materials*, 14:421, dec 2014.

[69] Jianing Chen, Michela Badioli, Pablo Alonso-González, Sukosin Thongrattanasiri, Florian Huth, Johann Osmond, Marko Spasenović, Alba Centeno, Amaia Pesquera, Philippe Godignon, Amaia Zurutuza Elorza, Nicolas Camara, F Javier García de Abajo, Rainer Hillenbrand, and Frank H L Koppens. Optical nano-imaging of gate-tunable graphene plasmons. *Nature*, 487:77, jun 2012.

[70] Z Fei, A S Rodin, G O Andreev, W Bao, A S McLeod, M Wagner, L M Zhang, Z Zhao, M Thiemens, G Dominguez, M M Fogler, A H Castro Neto, C N Lau, F Keilmann, and D N Basov. Gate-tuning of graphene plasmons revealed by infrared nano-imaging. *Nature*, 487:82, jun 2012.

[71] A. H. Castro Neto, F. Guinea, N. M. R. Peres, K. S. Novoselov, and A. K. Geim. The electronic properties of graphene. *Rev. Mod. Phys.*, 81:109–162, Jan 2009.

[72] Qiaoliang Bao and Kian Ping Loh. Graphene Photonics, Plasmonics, and Broadband Optoelectronic Devices. *ACS Nano*, 6(5):3677–3694, 2012.

[73] Emre O Polat, Hasan Burkay Uzlu, Osman Balci, Nurbek Kakenov, Evgeniya Kovalska, and Coskun Kocabas. Graphene-Enabled Optoelectronics on Paper. *ACS Photonics*, 3(6):964–971, 2016.

[74] T J Echtermeyer, L Britnell, P K Jasnos, A Lombardo, R V Gorbachev, A N Grigorenko, A K Geim, A C Ferrari, and K S Novoselov. Strong plasmonic enhancement of photovoltage in graphene. *Nature Communications*, 2:458, aug 2011.

[75] Xiaochang Miao, Sefaattin Tongay, Maureen K Petterson, Kara Berke, Andrew G Rinzler, Bill R Appleton, and Arthur F Hebard. High Efficiency Graphene Solar Cells by Chemical Doping. *Nano Letters*, 12(6):2745–2750, jun 2012.

[76] L. Wu, H. S. Chu, W. S. Koh, and E. P. Li. Highly sensitive graphene biosensors based on surface plasmon resonance. *Opt. Express*, 18(14):14395–14400, Jul 2010.

[77] Leiming Wu, Jun Guo, Hailin Xu, Xiaoyu Dai, and Yuanjiang Xiang. Ultrasensitive biosensors based on long-range surface plasmon polariton and dielectric waveguide modes. *Photon. Res.*, 4(6):262–266, Dec 2016.

[78] Omer Salihoglu, Sinan Balci, and Coskun Kocabas. Plasmon-polaritons on graphene-metal surface and their use in biosensors. *Applied Physics Letters*, 100(21):213110, may 2012.

[79] Eden Morales-Narvaez, Luis Baptista-Pires, Alejandro Zamora-Gálvez, and Arben Merkoçi. Graphene-based biosensors: Going simple. *Advanced Materials*, 29(7):1604905, 2017.

[80] Mingshan Zhu, Penglei Chen, and Minghua Liu. Graphene Oxide Enwrapped Ag/AgX (X = Br, Cl) Nanocomposite as a Highly Efficient Visible-Light Plasmonic Photocatalyst. *ACS Nano*, 5(6):4529–4536, jun 2011.

[81] Ming-Kai Chuang, Shih-Wei Lin, Fang-Chung Chen, Chih-Wei Chu, and Chain-Shu Hsu. Gold nanoparticle-decorated graphene oxides for plasmonic-enhanced polymer photovoltaic devices. *Nanoscale*, 6:1573–1579, 2014.

[82] Tony Low and Phaedon Avouris. Graphene Plasmonics for Terahertz to Mid-Infrared Applications. *ACS Nano*, 8(2):1086–1101, feb 2014.

[83] Dimitrios Bitounis, Hanene Ali-Boucetta, Byung Hee Hong, Dal-Hee Min, and Kostas Kostarelos. Prospects and challenges of graphene in biomedical applications. *Advanced Materials*, 25(16):2258–2268, 2013.

[84] Hongshi Ma, Chuan Jiang, Dong Zhai, Yongxiang Luo, Yu Chen, Fang Lv, Zhengfang Yi, Yuan Deng, Jinwu Wang, Jiang Chang, and Chengtie Wu. A bifunctional biomaterial with photothermal effect for tumor therapy and bone regeneration. *Advanced Functional Materials*, 26(8):1197–1208, 2016.

[85] Sheneve Z Butler, Shawna M Hollen, Linyou Cao, Yi Cui, Jay A Gupta, Humberto R Gutiérrez, Tony F Heinz, Seung Sae Hong, Jiaxing Huang, Ariel F Ismach, Ezekiel Johnston-Halperin, Masaru Kuno, Vladimir V Plashnitsa, Richard D Robinson, Rodney S Ruoff, Sayeef Salahuddin, Jie Shan, Li Shi, Michael G Spencer, Mauricio Terrones, Wolfgang Windl, and Joshua E Goldberger. Progress, Challenges, and Opportunities in Two-Dimensional Materials Beyond Graphene. *ACS Nano*, 7(4):2898–2926, apr 2013.

[86] Kyunghee Choi, Young Tack Lee, and Seongil Im. Two-dimensional van der waals nanosheet devices for future electronics and photonics. *Nano Today*, 11(5):626 – 643, 2016.

[87] Kin Fai Mak and Jie Shan. Photonics and optoelectronics of 2D semiconductor transition metal dichalcogenides. *Nature Photonics*, 10:216, mar 2016.

[88] Myron D Kapetanakis, Wu Zhou, Mark P Oxley, Jaekwang Lee, Micah P Prange, Stephen J Pennycook, Juan Carlos Idrobo, and Sokrates T Pantelides. Low-loss electron energy loss spectroscopy: An atomic-resolution complement to optical spectroscopies and application to graphene. *Phys. Rev. B*, 92(12):125147, September 2015.

[89] Zhongli Wang, Tao Li, Kristoffer Almdal, N Asger Mortensen, Sanshui Xiao, and Sokol Ndoni. Experimental demonstration of graphene plasmons working close to the near-infrared window. *Opt. Lett.*, 41(22):5345–5348, 2016.

[90] P R Wallace. The Band Theory of Graphite. *Phys. Rev.*, 71(9):622–634, May 1947.

[91] S. Das Sarma, Shaffique Adam, E. H. Hwang, and Enrico Rossi. Electronic transport in two-dimensional graphene. *Rev. Mod. Phys.*, 83:407–470, May 2011.

[92] Sanshui Xiao, Xiaolong Zhu, Bo-Hong Li, and N Asger Mortensen. Graphene-plasmon polaritons: From fundamental properties to potential applications. *Front. Phys.*, 11(2):117801, 2016.

[93] Bingchen Deng, Qiushi Guo, Cheng Li, Haozhe Wang, Xi Ling, Damon B Farmer, Shu-jen Han, Jing Kong, and Fengnian Xia. Coupling-Enhanced Broadband Mid-infrared Light Absorption in Graphene Plasmonic Nanostructures. *ACS Nano*, 10(12):11172–11178, December 2016.

[94] Marinko Jablan, Hrvoje Buljan, and Marin Soljačić. Transverse electric plasmons in bilayer graphene. *Opt. Express*, 19(12):11236–11241, 2011.

[95] Godfrey Gumbs, Andrii Iurov, Jhao-Ying Wu, M F Lin, and Paula Fekete. Plasmon Excitations of Multi-layer Graphene on a Conducting Substrate. *Sci. Rep.*, 6:21063, feb 2016.

[96] I Crassee, M Orlita, M Potemski, A L Walter, M Ostler, Th. Seyller, I Gaponenko, J Chen, and A B Kuzmenko. Intrinsic Terahertz Plasmons and Magnetoplasmons in Large Scale Monolayer Graphene. *Nano Lett.*, 12(5):2470–2474, May 2012.

[97] T Stauber Gómez-Santos and G. Plasmons in layered structures including graphene. *New J. Phys.*, 14(10):105018, 2012.

[98] P A D Gonçalves, E J C Dias, Sanshui Xiao, M I Vasilevskiy, N Asger Mortensen, and N M R Peres. Graphene Plasmons in Triangular Wedges and Grooves. *ACS Photonics*, 3(11):2176–2183, November 2016.

[99] E H Hwang and S Das Sarma. Plasmon modes of spatially separated double-layer graphene. *Phys. Rev. B*, 80(20):205405, November 2009.

[100] Hugen Yan, Xuesong Li, Bhupesh Chandra, George Tulevski, Yanqing Wu, Marcus Freitag, Wenjuan Zhu, Phaedon Avouris, and Fengnian Xia. Tunable infrared plasmonic devices using graphene/insulator stacks. *Nature Nanotechnology*, 7:330, apr 2012.

[101] Tobias Stauber. Plasmonics in dirac systems: from graphene to topological insulators. *J. Phys.: Condens. Matter*, 26(12):123201, 2014.

[102] Ming Liu, Xiaobo Yin, and Xiang Zhang. Double-layer graphene optical modulator. *Nano Letters*, 12(3):1482–1485, 2012.

[103] A. Tredicucci and M. S. Vitiello. Device concepts for graphene-based terahertz photonics. *IEEE J. Sel. Top. Quantum Electron.*, 20(1):130–138, Jan 2014.

[104] Yan Francescato, Vincenzo Giannini, Jingjing Yang, Ming Huang, and Stefan A. Maier. Graphene sandwiches as a platform for broadband molecular spectroscopy. *ACS Photonics*, 1(5):437–443, 2014.

[105] J S Gomez-Diaz, C Moldovan, S Capdevila, J Romeu, L S Bernard, A Magrez, A M Ionescu, and J Perruisseau-Carrier. Self-biased reconfigurable graphene stacks for terahertz plasmonics. *Nat. Commun.*, 6:6334, mar 2015.

[106] Daniel Rodrigo, Andreas Tittl, Odeta Limaj, F Javier Garcia de Abajo, Valerio Pruneri, and Hatice Altug. Double-layer graphene for enhanced tunable infrared plasmonics. *Light Sci. Appl.*, 6(6):e16277, 2017.

[107] Sergey G Menabde, Daniel R Mason, Evgeny E Kornev, Changhee Lee, and Namkyoo Park. Direct Optical Probing of Transverse Electric Mode in Graphene. *Sci. Rep.*, 6:21523, feb 2016.

[108] D. Mencarelli, L. Pierantoni, M. Stocchi, and S. Bellucci. Efficient and versatile graphene-based multilayers for em field absorption. *Appl. Phys. Lett.*, 109(9):093103, 2016.

[109] Banxian Ruan, Jun Guo, Leiming Wu, Jiaqi Zhu, Qi You, Xiaoyu Dai, and Yuanjiang Xiang. Ultrasensitive terahertz biosensors based on fano resonance of a graphene/waveguide hybrid structure. *Sensors*, 17(8):1924, 2017.

[110] Y. Huang, S. Zhong, H. Yao, and D. Cui. Tunable terahertz plasmonic sensor based on graphene/insulator stacks. *IEEE Photonics J.*, 9(1):1–10, Feb 2017.

[111] Farhan Rana. Graphene Terahertz Plasmon Oscillators. *IEEE Trans. Nanotechnol.*, 7(1):91–99, 2008.

[112] S. M. Badalyan and F. M. Peeters. Effect of nonhomogenous dielectric background on the plasmon modes in graphene double-layer structures at finite temperatures. *Phys. Rev. B*, 85(19):195444, 2012.

[113] G. Gomez-Santos and T. Stauber. Graphene plasmons and retardation: Strong light-matter coupling. *EPL (Europhysics Letters)*, 99(2):27006, 2012.

[114] Rosario E. V. Profumo, Reza Asgari, Marco Polini, and A. H. MacDonald. Double-layer graphene and topological insulator thin-film plasmons. *Phys. Rev. B*, 85:085443, Feb 2012.

[115] V. Despoja, T. Djordjevic, L. Karbunar, I. Radovic, and Z. L. Miskovic. Ab initio study of the electron energy loss function in a graphene-sapphire-graphene composite system. *Phys. Rev. B*, 96:075433, 2017.

[116] J.-J. Zhu, S. M. Badalyan, and F. M. Peeters. Plasmonic excitations in coulomb-coupled n-layer graphene structures. *Phys. Rev. B*, 87:085401, Feb 2013.

[117] T. Stauber and G. Gomez-Santos. Plasmons and near-field amplification in double-layer graphene. *Phys. Rev. B*, 85(7):075410, 2012.

[118] Pablo Alonso-Gonzalez, Alexey Y Nikitin, Yuanda Gao, Achim Woessner, Mark B Lundeberg, Alessandro Principi, Nicolo Forcellini, Wenjing Yan, Saul Velez, Andreas. J Huber, Kenji Watanabe, Takashi Taniguchi, Felix Casanova, Luis E Hueso, Marco Polini, James Hone, Frank H L Koppens, and Rainer Hillenbrand. Acoustic terahertz graphene plasmons revealed by photocurrent nanoscopy. *Nat. Nanotechnol.*, 12:31–35, oct 2016.

[119] Frank H L Koppens, Darrick E Chang, and F Javier Garcia de Abajo. Graphene Plasmonics: A Platform for Strong Light–Matter Interactions. *Nano Lett.*, 11(8):3370–3377, aug 2011.

[120] J. A. Stratton. *Electromagnetic Theory*. McGraw-Hill, New York, 1941.

[121] C.T. Tai, IEEE Antennas, Propagation Society, IEEE Microwave Theory, and Techniques Society. *Dyadic Green Functions in Electromagnetic Theory*. IEEE Press Series on Electromagnetic Waves. IEEE Press, 1994.

[122] Amit Agarwal and Giovanni Vignale. Plasmons in spin-polarized graphene: A way to measure spin polarization. *Phys. Rev. B*, 91:245407, Jun 2015.

[123] Mark B Lundeberg, Yuanda Gao, Reza Asgari, Cheng Tan, Ben Van Duppen, Marta Autore, Pablo Alonso-Gonzalez, Achim Woessner, Kenji Watanabe, Takashi Taniguchi, Rainer Hillenbrand, James Hone, Marco Polini, and Frank H L Koppens. Tuning quantum nonlocal effects in graphene plasmonics. *Science*, 357(6347):187–191, jul 2017.

[124] D. J. Mowbray, S. Segui, J. Gervasoni, Z. L. Mišković, and N. R. Arista. Plasmon excitations on a single-wall carbon nanotube by external charges: Two-dimensional two-fluid hydrodynamic model. *Phys. Rev. B*, 82:035405, Jul 2010.

[125] Andrei Nemilentsau, Tony Low, and George Hanson. Anisotropic 2d materials for tunable hyperbolic plasmonics. *Phys. Rev. Lett.*, 116:066804, Feb 2016.

[126] Boris Lukyanchuk, Nikolay I Zheludev, Stefan A Maier, Naomi J Halas, Peter Nordlander, Harald Giessen, and Chong Tow Chong. The Fano resonance in plasmonic nanostructures and metamaterials. *Nat. Mater.*, 9:707–715, aug 2010.

[127] G Y Hu and R F O'Connell. Analytical inversion of symmetric tridiagonal matrices. *Journal of Physics A: Mathematical and General*, 29(7):1511–1513, apr 1996.

[128] K. F. Allison, D. Borka, I. Radović, Lj. Hadžievski, and Z. L. Mišković. Dynamic polarization of graphene by moving external charges: Random phase approximation. *Phys. Rev. B*, 80:195405, Nov 2009.

[129] Tijana Marinkovic, Ivan Radovic, Dusko Borka, and Zoran L. Miskovic. Probing the plasmon-phonon hybridization in supported graphene by externally moving charged particles. *Plasmonics*, 10(6):1741–1749, Dec 2015.

[130] P Sigmund. *Particle Penetration and Radiation Effects, Volume 1: General Aspects and Stopping of Swift Point Charges*. Springer, New York, 2006.

[131] R Garcia-Molina, A Gras-Marti, A Howie, and R H Ritchie. Retardation effects in the interaction of charged particle beams with bounded condensed media. *J. Phys. C: Solid State Phys.*, 18:5335–5345, 1985.

[132] A Rivacoba and N Zabala. Retardation effects in the interaction of charged particle beams with bounded condensed media. *New J. Phys.*, 16:073048, 2014.

[133] S A Mikhailov and K Ziegler. New Electromagnetic Mode in Graphene. *Phys. Rev. Lett.*, 99(1):16803, jul 2007.

[134] A Principi, Marco Polini, and G Vignale. Linear response of doped graphene sheets to vector potentials. *Phys. Rev. B*, 80(7):75418, aug 2009.

[135] T Stauber and G Gómez-Santos. Dynamical current-current correlation of the hexagonal lattice and graphene. *Phys. Rev. B*, 82(15):155412, oct 2010.

[136] M Alducin, V M Silkin, and J I Juaristi. Two dimensional behaviour of friction at a metal surface with a surface state. *Nucl. Instrum. Methods Phys. Res. B*, 256:383, 2007.

[137] R Núñez, P M Echenique, and R H Ritchie. The energy loss of energetic ions moving near a solid surface. *J. Phys. C: Solid St. Phys.*, 13:4229–4246., 1980.

[138] V M Silkin, M Alducin, J I Juaristi, E V Chulkov, and P M Echenique. Two dimensional behaviour of friction at a metal surface with a surface state. *J. Phys.: Condens. Matter*, 20:304209, 2008.

[139] Y U V Bludov, Aires Ferreira, N M R Peres, and M I Vasilevskiy. A Primer on Surface Plasmon-Polaritons in Graphene. *Int. J. Mod. Phys. B*, 27(10):1341001, April 2013.

[140] K F Allison and Z L Miskovic. Friction force on slow charges moving over supported graphene. *Nanotechnology*, 21(13):134017, 2010.

[141] Giampiero Lovat, George W Hanson, Rodolfo Araneo, and Paolo Burghignoli. Semiclassical spatially dispersive intraband conductivity tensor and quantum capacitance of graphene. *Phys. Rev. B*, 87(11):115429, mar 2013.

[142] L. A. Falkovsky and S. S. Pershoguba. Optical far-infrared properties of a graphene monolayer and multilayer. *Phys. Rev. B*, 76:153410, Oct 2007.

[143] A. G. Marinopoulos, Lucia Reining, Angel Rubio, and Valerio Olevano. Ab initio study of the optical absorption and wave-vector-dependent dielectric response of graphite. *Phys. Rev. B*, 69:245419, Jun 2004.

[144] T. Stauber, N. M. R. Peres, and A. K. Geim. Optical conductivity of graphene in the visible region of the spectrum. *Phys. Rev. B*, 78:085432, Aug 2008.

[145] Yuan-Hong Song, You-Nian Wang, and Z. L. Miskovic. Energy loss of heavy ions specularly reflected from surfaces under glancing-angle incidence. *Phys. Rev. A*, 63:052902, Apr 2001.

[146] A Gutierrez-Rubio, T Stauber, and F Guinea. Transverse current response of graphene at finite temperature: plasmons and absorption. *J. Opt.*, 15(11):114005, 2013.

[147] Xiao Lin, Nicholas Rivera, Josue J Lopez, Ido Kaminer, Hongsheng Chen, and Marin Soljacic. Tailoring the energy distribution and loss of 2d plasmons. *New J. Phys.*, 18(10):105007, 2016.

[148] Fengnian Xia, Han Wang, and Yichen Jia. Rediscovering Black Phosphorus: A Unique Anisotropic 2D Material for Optoelectronics and Electronics. *Nat. Commun.*, 5:4458, jul 2014.

[149] Xiaomu Wang and Shoufeng Lan. Optical properties of black phosphorus. *Adv. Opt. Photon.*, 8(4):618–655, Dec 2016.

[150] Jimin Kim, Seung Su Baik, Sae Hee Ryu, Yeongsup Sohn, Soohyung Park, Byeong-Gyu Park, Jonathan Denlinger, Yeonjin Yi, Hyoung Joon Choi, and Keun Su Kim. Observation of tunable band gap and anisotropic dirac semimetal state in black phosphorus. *Science*, 349(6249):723–726, 2015.

[151] Barun Ghosh, Piyush Kumar, Anmol Thakur, Yogesh Singh Chauhan, Somnath Bhowmick, and Amit Agarwal. Anisotropic plasmons, excitons, and electron energy loss spectroscopy of phosphorene. *Phys. Rev. B*, 96:035422, Jul 2017.

[152] Tony Low, A. S. Rodin, A. Carvalho, Yongjin Jiang, Han Wang, Fengnian Xia, and A. H. Castro Neto. Tunable optical properties of multilayer black phosphorus thin films. *Phys. Rev. B*, 90:075434, Aug 2014.

[153] Tony Low, Rafael Roldán, Han Wang, Fengnian Xia, Phaedon Avouris, Luis Martín Moreno, and Francisco Guinea. Plasmons and screening in monolayer and multilayer black phosphorus. *Phys. Rev. Lett.*, 113:106802, Sep 2014.

[154] René Petersen, Thomas Garm Pedersen, and F. Javier García de Abajo. Nonlocal plasmonic response of doped and optically pumped graphene, mos_2, and black phosphorus. *Phys. Rev. B*, 96:205430, Nov 2017.

[155] D Correas-Serrano, J S Gomez-Diaz, A Alvarez Melcon, and Andrea Alù. Black phosphorus plasmonics: anisotropic elliptical propagation and nonlocality-induced canalization. *Journal of Optics*, 18(10):104006, 2016.

[156] Vl A Margulis, E E Muryumin, and E A Gaiduk. Optical reflection, transmission and absorption properties of single-layer black phosphorus from a model calculation. *Journal of Optics*, 18(5):055102, 2016.

[157] Vl. A. Margulis and E. E. Muryumin. Theory for surface polaritons supported by a black-phosphorus monolayer. *Phys. Rev. B*, 98:165305, Oct 2018.

[158] Desalegn T. Debu, Stephen J. Bauman, David French, Hugh O.H. Churchill, and Joseph B. Herzog. Tuning Infrared Plasmon Resonance of Black Phosphorene Nanoribbon with a Dielectric Interface. *Sci. Rep.*, 8(1):3224, 2018.

[159] E. V. Gorbar, V. A. Miransky, I. A. Shovkovy, and P. O. Sukhachov. Chiral response in lattice models of weyl materials. *Phys. Rev. B*, 96:125123, Sep 2017.

[160] Roman M. Lutchyn, Pavel Nagornykh, and Victor M. Yakovenko. Gauge-invariant electromagnetic response of a chiral $p_x + ip_y$ superconductor. *Phys. Rev. B*, 77:144516, Apr 2008.

[161] Anshuman Kumar, Andrei Nemilentsau, Kin Hung Fung, George Hanson, Nicholas X. Fang, and Tony Low. Chiral plasmon in gapped dirac systems. *Phys. Rev. B*, 93:041413, Jan 2016.

[162] Di Xiao, Ming-Che Chang, and Qian Niu. Berry phase effects on electronic properties. *Rev. Mod. Phys.*, 82:1959–2007, Jul 2010.

[163] Justin C. W. Song and Mark S. Rudner. Chiral plasmons without magnetic field. *Proceedings of the National Academy of Sciences*, 113(17):4658–4663, 2016.

[164] J. E. Sipe. New green-function formalism for surface optics. *J. Opt. Soc. Am. B*, 4(4):481–489, Apr 1987.

[165] Lars Matthes, Olivia Pulci, and Friedhelm Bechstedt. Influence of out-of-plane response on optical properties of two-dimensional materials: First principles approach. *Phys. Rev. B*, 94:205408, Nov 2016.

[166] M. Bordag. Monoatomically thin polarizable sheets. *Phys. Rev. D*, 89:125015, Jun 2014.

[167] John F. Dobson, Tim Gould, and Sébastien Lebègue. Layer response theory: Energetics of layered materials from semianalytic high-level theory. *Phys. Rev. B*, 93:165436, Apr 2016.

[168] M. Bordag and J. M. Muñoz Castañeda. Dirac lattices, zero-range potentials, and self-adjoint extension. *Phys. Rev. D*, 91:065027, Mar 2015.

[169] Valerio Di Giulio, Mathieu Kociak, and F de Abajo. Probing quantum optical excitations with fast electrons. *arXiv preprint arXiv:1905.06887*, 2019.

[170] A. P. Prudnikov, Yu. A. Brychkov, and O. I. Marichev. *Integrals and Series: Special Functions*. (in Russian), Nauka, Moscow, 1983.

APPENDICES

Appendix A

Retarded Green's Function Formalism

Macroscopic Maxwell's equations in Gaussian units are written as [63]:

$$\begin{aligned}
\boldsymbol{\nabla} \cdot \mathbf{D}(\mathbf{R}, t) &= 4\pi\rho(\mathbf{R}, t), \\
\boldsymbol{\nabla} \times \mathbf{E}\left(\mathbf{R}, t\right) &= -\frac{1}{c}\frac{\partial \mathbf{B}\left(\mathbf{R}, t\right)}{\partial t}, \\
\boldsymbol{\nabla} \cdot \mathbf{B}\left(\mathbf{R}, t\right) &= 0, \\
\boldsymbol{\nabla} \times \mathbf{H}\left(\mathbf{R}, t\right) &= \frac{4\pi}{c}\mathbf{J}\left(\mathbf{R}, t\right) + \frac{1}{c}\frac{\partial \mathbf{D}\left(\mathbf{R}, t\right)}{\partial t}.
\end{aligned} \tag{A.1}$$

Applying the Fourier transform with respect to time, for a linear dielectric medium with the constitutive relations $\mathbf{D}(\mathbf{R}, t) = \epsilon_d(\omega)\mathbf{E}(\mathbf{R}, t)$ and $\mathbf{B}(\mathbf{R}, t) = \mu_d(\omega)\mathbf{H}(\mathbf{R}, t)$, the Maxwell's equations are read as

$$\begin{aligned}
\boldsymbol{\nabla} \cdot \mathbf{E}(\mathbf{R}, \omega) &= \frac{4\pi}{\epsilon_d(\omega)}\rho(\mathbf{R}, \omega), \\
\boldsymbol{\nabla} \times \mathbf{E}\left(\mathbf{R}, \omega\right) &= \frac{i\omega}{c}\mu_d(\omega)\mathbf{H}\left(\mathbf{R}, \omega\right), \\
\boldsymbol{\nabla} \cdot \mathbf{B}\left(\mathbf{R}, \omega\right) &= 0, \\
\boldsymbol{\nabla} \times \mathbf{H}(\mathbf{R}, \omega) &= \frac{4\pi}{c}\mathbf{J}(\mathbf{R}, \omega) - \frac{i\omega}{c}\epsilon_d(\omega)\mathbf{E}(\mathbf{R}, \omega).
\end{aligned} \tag{A.2}$$

Hence, one can derive the vector wave equation for the electric field in Gaussian units as

$$\boldsymbol{\nabla} \times \boldsymbol{\nabla} \times \mathbf{E}(\mathbf{R}, \omega) - \frac{\omega^2}{c^2}\epsilon_d(\omega)\mu_d(\omega)\mathbf{E}(\mathbf{R}, \omega) = \frac{4\pi i\omega}{c^2}\mu_d(\omega)\mathbf{J}(\mathbf{R}, \omega). \tag{A.3}$$

Defining $k_0 = \frac{\omega}{c}$ and $k_d = k_0\sqrt{\epsilon_d(\omega)\mu_d(\omega)}$, we end up with

$$\boldsymbol{\nabla} \times \boldsymbol{\nabla} \times \mathbf{E}(\mathbf{R},\omega) - k_d^2 \mathbf{E}(\mathbf{R},\omega) = \frac{4\pi i}{\omega\epsilon_d(\omega)} k_d^2\, \mathbf{J}(\mathbf{R},\omega). \tag{A.4}$$

A.1 Retarded scalar Green's function for the components of electric Hertz vector potential $\boldsymbol{\Pi}$

Considering the relationship between the EM fields and the Hertz electric potential vector, expressed via

$$\begin{aligned} \mathbf{E}(\mathbf{R},\omega) &= \boldsymbol{\nabla}\boldsymbol{\nabla} \cdot \boldsymbol{\Pi}(\mathbf{R},\omega) + \omega^2 \epsilon_d(\omega)\mu_d(\omega)\boldsymbol{\Pi}(\mathbf{R},\omega)/c^2, \\ \mathbf{B}(\mathbf{R},\omega) &= -i\omega\epsilon_d(\omega)\mu_d(\omega)\boldsymbol{\nabla} \times \boldsymbol{\Pi}(\mathbf{R},\omega)/c, \end{aligned} \tag{A.5}$$

one may transform the vector wave equation in Eq. (A.4) into the vector Helmholtz equation for the Hertz electric potential $\boldsymbol{\Pi}(\mathbf{R},t)$. Applying the 2D in-plane spatial Fourier transform ($\mathbf{r} \to \mathbf{k}$), we have

$$\left(\frac{\partial^2}{\partial z^2} - q^2\right) \boldsymbol{\Pi}(\mathbf{k},z,\omega) = -\frac{4\pi i}{\omega\epsilon_d(\omega)}\, \mathbf{J}(\mathbf{k},z,\omega), \tag{A.6}$$

where $k = \sqrt{k_x^2 + k_y^2}$ and $q^2 = k^2 - k_d^2$. From the above equation one can ascertain that the Hertz electric vector potential is in the same direction of the current source. Thus, in order to solve the equation for the $\boldsymbol{\Pi}$ vector, it suffices to solve the equation for a component of the $\boldsymbol{\Pi}$ vector and hence find the retarded scalar Green's function (GF) for each component.

In order to obtain the scalar GF for each component of the Hertz vector in vacuum or free space ($\epsilon_d(\omega) = \mu_d(\omega) = 1$), we write the time domain version of Eq. (A.6) and write as scalar wave equation for each component $\psi(\mathbf{R},t)$ of the Hertz vector $\boldsymbol{\Pi}(\mathbf{R},t)$, in the form of

$$\left(\nabla^2 - \frac{1}{c^2}\frac{\partial^2}{\partial t^2}\right) \boldsymbol{\Pi}(\mathbf{k},z,\omega) = -4\pi\, f(\mathbf{R},t), \tag{A.7}$$

where $f(\mathbf{R},t)$ is a nonhomogeneous term due to the corresponding component of the current density $\mathbf{J}(\mathbf{R},t)$. A solution of the above equation due to the nonhomogeneous term is given by

$$\psi(\mathbf{R},t) = \iiint d^3\mathbf{R}' \int_{-\infty}^{\infty} dt'\, G(\mathbf{R}-\mathbf{R}', t-t')\, f(\mathbf{R}',t') \tag{A.8}$$

where the retarded scalar GF is given by [63]

$$G(\mathbf{R},t)=\frac{1}{R}\,\delta(\frac{R}{c}-t)=\int_{-\infty}^{\infty}\frac{d\omega}{2\pi}\,\mathrm{e}^{-i\omega t}\,\frac{1}{R}\mathrm{e}^{-i\frac{\omega}{c}R}, \tag{A.9}$$

with $R=\|\mathbf{R}\|=\sqrt{r^2+z^2}$ and $r=\|\mathbf{r}\|$. Hence, performing the Fourier transform of $G(\mathbf{R},t)$ with respect to time and the coordinates $\mathbf{r}=\{x,y\}$ gives an expression for the GF as

$$G(\mathbf{k},z,\omega)=\iint d^2\mathbf{r}\int_{-\infty}^{\infty}dt\,\mathrm{e}^{-i\mathbf{k}\cdot\mathbf{r}+i\omega t}\,G(\mathbf{R},t)=2\pi\int_{0}^{\infty}\frac{drr}{\sqrt{r^2+z^2}}J_0(kr)\,\mathrm{e}^{i\frac{\omega}{c}\sqrt{r^2+z^2}}, \tag{A.10}$$

where $k=\|\mathbf{k}\|$ and J_0 is the Bessel function of the first kind of zeroth order. It is important to notice that the real and imaginary parts of the last expression in Eq. (A.10) are even and odd functions of ω, respectively. Using the table integrals 8 and 9 (obtained from the Sommerfeld integrals) from Section 2.12.23 in Ref. [170] gives a result for the scalar retarded GF as

$$G(k,z,\omega)=\begin{cases}\frac{2\pi i}{\kappa(k,\omega)}\,\mathrm{e}^{i|z|\kappa(k,\omega)}, & |\omega|>ck\\ \frac{2\pi}{\alpha(k,\omega)}\,\mathrm{e}^{-|z|\alpha(k,\omega)}, & |\omega|<ck\end{cases} \tag{A.11}$$

with

$$\begin{aligned}\kappa(k,\omega)&=\frac{\omega}{c}\sqrt{1-\left(\frac{ck}{\omega}\right)^2}, \quad \text{for} \quad |\omega|>ck,\\ \alpha(k,\omega)&=\frac{|\omega|}{c}\sqrt{\left(\frac{ck}{\omega}-1\right)^2}, \quad \text{for} \quad |\omega|<ck,\end{aligned} \tag{A.12}$$

which is valid for both positive and negative frequencies.

Considering the appropriate coefficient in the right hand side of Eq. (A.6), the scalar retarded GF for the components of the Hertz vector in a homogeneous medium, listed in Chapters 2, 3, 4 and 5, is given by

$$G_{\Pi 0}(k,z,\omega)=\frac{2\pi}{\omega q\epsilon_d}\,\mathrm{e}^{-q|z|}, \tag{A.13}$$

where

$$q(k,\omega)=\begin{cases}-i\frac{\omega}{c}\sqrt{\epsilon_d-\left(\frac{ck}{\omega}\right)^2}\equiv -i\kappa(k,\omega), & |\omega|>ck/\sqrt{\epsilon_d},\\ \frac{|\omega|}{c}\sqrt{\left(\frac{ck}{\omega}\right)^2-\epsilon_d}\equiv\alpha(k,\omega), & |\omega|<ck/\sqrt{\epsilon_d}\end{cases} \tag{A.14}$$

It can be shown that, taking an inverse Fourier transform with respect to time of Eq. (A.10) gives

$$G(k,z,t) = 2\pi c\, J_0(k\sqrt{c^2t^2 - z^2})\, \Theta(t - \frac{|z|}{c}), \tag{A.15}$$

where the Heaviside unit step function Θ expresses retarded nature of the GF.

The approach mentioned so far is borrowed from the Ref. [42]. An alternative method to this approach for obtaining $G_{\Pi 0}(k,z,\omega)$ is that we consider the fully (4D space and time, $\{\mathbf{R},t\} \rightarrow \{\mathbf{K},\omega\}$) Fourier transformed version of the scalar Helmholtz equation for the components of the Hertz vector

$$\left(K^2 - k_d^2\right)\Pi_j(\mathbf{k},z,\omega) = -\frac{4\pi i}{\omega\epsilon_d(\omega)}\, J_j(\mathbf{k},z,\omega), \tag{A.16}$$

where $\mathbf{K} = k_x\hat{\mathbf{x}} + k_y\hat{\mathbf{y}} + k_z\hat{\mathbf{z}}$ is the 3D wave vector and $K = \|\mathbf{K}\|$, and then obtain the fully Fourier transformed scalar GF as $G_{\Pi 0}(K,\omega) = \frac{4\pi i}{\omega\epsilon_d(\omega)}\frac{1}{K^2 - k_d^2}$. Next, we apply the inverse Fourier transform in the z direction, i.e. $k_z \rightarrow z$, which involves contour integration in the complex plane and needs to be carefully executed, while paying attention regarding the Physics of the solution waves in different regions of the light cone.

A.2 Retarded dyadic Green's function for a homogeneous medium

Using the relation between the electric field and the Hertz potential in Eq. (A.5), one can obtain the electric dyadic GF (EDGF) via [121]

$$\overleftrightarrow{G}_{E0}(\mathbf{R},\mathbf{R}',\omega) = \left(k_d^2\,\overleftrightarrow{I} + \boldsymbol{\nabla}\boldsymbol{\nabla}\right) G_{\Pi 0}(R,R',\omega) \tag{A.17}$$

Here, considering the z dependency of the scalar GF, we can use the transformation $\boldsymbol{\nabla} \rightarrow \left(i\mathbf{k} + \frac{\partial}{\partial z}\hat{\mathbf{z}}\right)$, to express the EDGF as

$$\overleftrightarrow{G}_{E0}(\mathbf{k},z,\omega) = \left(k_d^2\,\overleftrightarrow{I} - \mathbf{k}\mathbf{k} + i\frac{\partial}{\partial z}\left(\mathbf{k}\hat{\mathbf{z}} + \hat{\mathbf{z}}\mathbf{k}\right) + \frac{\partial^2}{\partial z^2}\hat{\mathbf{z}}\hat{\mathbf{z}}\right) G_{\Pi 0}(\mathbf{k},z,\omega). \tag{A.18}$$

which may be separated into its in-plane, mix out-of-plane, and normal out-of-plane elements, for a better understanding of the utilization of each term, as

$$\overleftrightarrow{G}_{E0}(\mathbf{k},z,\omega) = \overleftrightarrow{G}^{\,||}_{E0}(\mathbf{k},z,\omega) + \overleftrightarrow{G}^{\,\times}_{E0}(\mathbf{k},z,\omega) + \left[\overleftrightarrow{G}^{\,\times}_{E0}(\mathbf{k},z,\omega)\right]^T + \hat{\mathbf{z}}\, G_{E0,zz}(\mathbf{k},z,\omega)\,\hat{\mathbf{z}}, \tag{A.19}$$

with

$$\begin{aligned}
\overleftrightarrow{G}^{||}_{E0}(\mathbf{k},z,\omega) &= \frac{2\pi i}{\omega q(k,\omega)\epsilon_d(\omega)}\left(k_d^2\overleftrightarrow{I}_{||}-\mathbf{kk}\right)\mathrm{e}^{-q(k,\omega)|z|},\\
\overleftrightarrow{G}^{\times}_{E0}(\mathbf{k},z,\omega) &= \frac{2\pi}{\omega\epsilon_d(\omega)}\,\mathrm{sign}(z)\,\mathrm{e}^{-q(k,\omega)|z|}\,\mathbf{k}\hat{\mathbf{z}},\\
G_{E0,zz}(\mathbf{k},z,\omega) &= \frac{2\pi i k^2}{\omega q(k,\omega)\epsilon_d(\omega)}\,\mathrm{e}^{-q(k,\omega)|z|}-\frac{4\pi i}{\omega\epsilon_d(\omega)}\,\delta(z),
\end{aligned} \tag{A.20}$$

and T denoting the transpose operation. Some important properties of the EDGF can be listed as:

- symmetry: $\left[\overleftrightarrow{G}_{E0}(\mathbf{k},z,\omega)\right]^T=\overleftrightarrow{G}_{E0}(\mathbf{k},z,\omega)$,
- parity: $\overleftrightarrow{G}_{E0}(-\mathbf{k},z,-\omega)=\overleftrightarrow{G}^{*}_{E0}(\mathbf{k},z,\omega)\;\rightarrow\;\overleftrightarrow{G}_{E0}(-\mathbf{k},z,-\omega)=\overleftrightarrow{G}^{H}_{E0}(\mathbf{k},z,\omega)$,
- $\overleftrightarrow{G}^{||}_{E0}(\mathbf{k},z,-\omega)=\left[\overleftrightarrow{G}^{||}_{E0}(\mathbf{k},z,\omega)\right]^*$,
- $\overleftrightarrow{G}^{\times}_{E0}(\mathbf{k},z,-\omega)=-\left[\overleftrightarrow{G}^{\times}_{E0}(\mathbf{k},z,\omega)\right]^*$,
- $G^{\times}_{E0,zz}(\mathbf{k},z,-\omega)=G^{*}_{E0,zz}(\mathbf{k},z,\omega)$,
- $\overleftrightarrow{G}^{||}_{E0}(\mathbf{k},-z,\omega)=\overleftrightarrow{G}^{||}_{E0}(\mathbf{k},z,\omega)$,
- $\overleftrightarrow{G}^{\times}_{E0}(\mathbf{k},-z,\omega)=-\overleftrightarrow{G}^{\times}_{E0}(\mathbf{k},z,\omega)$,
- $G^{\times}_{E0,zz}(\mathbf{k},-z,\omega)=G_{E0,zz}(\mathbf{k},z,\omega)$,

with $*$ being the complex conjugate sign.

The expansion of EDGF in Eq. (A.18) can always be expressed in any arbitrary coordinate system. Particularly, it is found to be quite useful to expand the EDGF in terms of the longitudinal and transverse (LT) in-plane components when the problem involves isotropic boundary conditions. Note that the LT coordinate system is composed of two in-plane unit vectors and the normal vector as $\left(\hat{\mathbf{k}},\hat{\boldsymbol{\tau}},\hat{\mathbf{z}}\right)$ with $\hat{\boldsymbol{\tau}}=\hat{\mathbf{z}}\times\hat{\mathbf{k}}$. Therefore, in the LT coordinate system, one may give the EDGF as

$$\overleftrightarrow{G}_{E0}(\mathbf{k},z,\omega)=\frac{2\pi i}{\omega q\epsilon_d}\left[-q^2\hat{\mathbf{k}}\hat{\mathbf{k}}+k_d^2\hat{\boldsymbol{\tau}}\hat{\boldsymbol{\tau}}-ikq\,\mathrm{sign}(z)\left(\hat{\mathbf{k}}\hat{\mathbf{z}}+\hat{\mathbf{z}}\hat{\mathbf{k}}\right)+\left(k^2-2q\delta(z)\right)\hat{\mathbf{z}}\hat{\mathbf{z}}\right]\mathrm{e}^{-q|z|}. \tag{A.21}$$

On the other hand, Cartesian coordinates suitably encompass most of the needs for anisotropic boundary conditions. In that case, the EDGF in Cartesian coordinate system can be identified via

$$\begin{aligned}\overleftrightarrow{G}_{E0}(\mathbf{k},z,\omega) = \frac{2\pi i}{\omega q \epsilon_d}\big[\left(k_d^2-k_x^2\right)\hat{\mathbf{x}}\hat{\mathbf{x}} - k_x k_y\left(\hat{\mathbf{x}}\hat{\mathbf{y}}+\hat{\mathbf{y}}\hat{\mathbf{x}}\right) + \left(k_d^2-k_y^2\right)\hat{\mathbf{y}}\hat{\mathbf{y}} \\ -ik_x q\,\mathrm{sign}(z)\left(\hat{\mathbf{x}}\hat{\mathbf{z}}+\hat{\mathbf{z}}\hat{\mathbf{x}}\right) - ik_y q\,\mathrm{sign}(z)\left(\hat{\mathbf{y}}\hat{\mathbf{z}}+\hat{\mathbf{z}}\hat{\mathbf{y}}\right) + \left(k^2-2q\delta(z)\right)\hat{\mathbf{z}}\hat{\mathbf{z}}\big]\,\mathrm{e}^{-q|z|}.\end{aligned} \tag{A.22}$$

One should note that the transformation of any arbitrary variable between the two coordinate systems can be easily derived by the projection of the unit basis vectors as

$$\begin{aligned}\hat{\mathbf{k}}\cdot\hat{\mathbf{x}} &= \frac{k_x}{k} = \cos\phi,\\ \hat{\mathbf{k}}\cdot\hat{\mathbf{y}} &= \frac{k_y}{k} = \sin\phi,\\ \hat{\boldsymbol{\tau}}\cdot\hat{\mathbf{x}} &= \frac{-k_y}{k} = -\sin\phi,\\ \hat{\boldsymbol{\tau}}\cdot\hat{\mathbf{x}} &= \frac{k_x}{k} = \cos\phi,\end{aligned} \tag{A.23}$$

where ϕ is the angle between the in-plane wavevector $\mathbf{k}$ and x-axis.

We may, also, need the magnetic dyadic GF (MDGF) for future easier calculations. This MDGF which is for the vector B, would be given by

$$\begin{aligned}\overleftrightarrow{G}_{B0}(\mathbf{R},\omega) &= \frac{c}{i\omega}\boldsymbol{\nabla}\times\overleftrightarrow{G}_{E0}(\mathbf{R},\omega)\\ &= \frac{c}{i\omega}\boldsymbol{\nabla}\times\left[\left(k_d^2\overleftrightarrow{I}+\boldsymbol{\nabla}\boldsymbol{\nabla}\right)G_{\Pi 0}(R,\omega)\right]\\ &= \frac{\omega\epsilon_d(\omega)\mu_d(\omega)}{ic}\boldsymbol{\nabla}\times\left[\overleftrightarrow{I}G_{\Pi 0}(R,\omega)\right]\\ &= \frac{\omega\epsilon_d(\omega)\mu_d(\omega)}{ic}\left[\boldsymbol{\nabla}G_{\Pi 0}(R,\omega)\right]\times\overleftrightarrow{I}.\end{aligned} \tag{A.24}$$

Applying the 2D in-plane spatial Fourier transform and seperating the in-plane and mixed out-of-plane elements, we have

$$\begin{aligned}\overleftrightarrow{G}_{B0}(\mathbf{k},z,\omega) &= \frac{c}{\omega}\mathbf{K}\times\overleftrightarrow{G}_{E0}(\mathbf{R},\omega)\\ &= \frac{\omega\epsilon_d(\omega)\mu_d(\omega)}{ic}\left[\left(i\mathbf{k}+\frac{\partial}{\partial z}\hat{\mathbf{z}}\right)G_{\Pi 0}(\mathbf{k},z,\omega)\right]\times\overleftrightarrow{I}\\ &= \frac{\omega\epsilon_d(\omega)\mu_d(\omega)}{c}G_{\Pi 0}(\mathbf{k},z,\omega)\mathbf{K}\times\overleftrightarrow{I}\\ &= \overleftrightarrow{G}^{\parallel}_{B0}(\mathbf{k},z,\omega)+\overleftrightarrow{G}^{\times}_{B0}(\mathbf{k},z,\omega),\end{aligned} \tag{A.25}$$

where

$$\begin{aligned}
\overleftrightarrow{G}^{||}_{B0}(\mathbf{k}, z, \omega) &= \frac{2\pi}{c}\mu_d(\omega)\,\mathrm{sign}(z)\,(\hat{\mathbf{x}}\hat{\mathbf{y}} - \hat{\mathbf{y}}\hat{\mathbf{x}})\ \mathrm{e}^{-q|z|}, \\
\overleftrightarrow{G}^{\times}_{B0}(\mathbf{k}, z, \omega) &= \frac{2\pi}{iqc}\mu_d(\omega)\ (k_y\hat{\mathbf{z}}\hat{\mathbf{x}} - k_x\hat{\mathbf{z}}\hat{\mathbf{y}})\ \mathrm{e}^{-q|z|}.
\end{aligned} \tag{A.26}$$

Appendix B

Conservation of Energy for the Loss (Transfer) Probability Densities

Using the Einstein notation convention, we may rewrite the 2D in-plane dielectric tensor as $\epsilon_{ij} = \delta_{ij} - G_{is}\sigma_{sj}$ with $G_{is} = \frac{2\pi i}{\omega q \epsilon_d}\left(k_d^2\delta_{is} - k_i k_s\right)$. Thus, inside the light cone, when $q = -i\kappa$, $G_{is} = -\frac{2\pi}{\omega\kappa\epsilon_d}\left(k_d^2\delta_{is} - k_i k_s\right)$ is real and outside the light cone, when $q = \alpha$, $G_{is} = \frac{2\pi i}{\omega\alpha\epsilon_d}\left(k_d^2\delta_{is} - k_i k_s\right)$ is pure imaginary, if we let $\epsilon_d > 0$. Knowing from the 2D in-plane constitutive relation that $\epsilon_{ij}E_{0j} = E_{\text{ext},i}$, one can start from the external joint probability density to prove the conservation of energy at the level of joint probability densities via

$$
\begin{aligned}
F_{\text{ext}}(\mathbf{k},\omega) &= \frac{1}{4\pi^3\omega}\Re\left\{\mathbf{E}^H_{\text{ext}||}(\mathbf{k},0,\omega)\cdot\overleftrightarrow{\sigma}(\mathbf{k},\omega)\cdot\mathbf{E}_0\right\}\\
&= \frac{1}{4\pi^3\omega}\Re\left\{\mathbf{E}_0^H\cdot\overleftrightarrow{\epsilon}^H\cdot\overleftrightarrow{\sigma}\cdot\mathbf{E}_0\right\}\\
&= \frac{1}{4\pi^3\omega}\Re\left\{E^*_{0j}\,\epsilon^*_{ji}\,\sigma_{il}\,E_{0l}\right\}\\
&= \frac{1}{4\pi^3\omega}\Re\left\{E^*_{0j}\,\left(\delta_{ji} - \sigma^*_{js}\,G^*_{si}\right)\,\sigma_{il}\,E_{0l}\right\}\\
&= \frac{1}{4\pi^3\omega}\Re\left\{E^*_{0i}\,\sigma_{il}\,E_{0l} - E^*_{0j}\,\sigma^*_{js}\,G^*_{si}\,\sigma_{il}\,E_{0l}\right\}\\
&= \frac{1}{4\pi^3\omega}\Re\left\{E^*_{0i}\,\sigma_{il}\,E_{0l}\right\} + \frac{1}{4\pi^3\omega}\Re\left\{E_{0j}\,\sigma^*_{js}\,\left(-G^*_{si}\right)\,\sigma_{il}\,E_{0l}\right\}\\
&= \begin{cases} \frac{1}{4\pi^3\omega}\Re\left\{E^*_{0i}\,\sigma_{il}\,E_{0l}\right\}, & \omega < ck,\\ \frac{1}{4\pi^3\omega}\Re\left\{E^*_{0i}\,\sigma_{il}\,E_{0l}\right\} + \frac{1}{4\pi^3\omega}\Re\left\{E^*_{0j}\,\sigma^*_{js}\,\left(-G^*_{e0,si}\right)\,\sigma_{il}\,E_{0l}\right\}, & \omega > ck,\end{cases}\\
&= \begin{cases} F^{<}_{\text{ohm}}(\mathbf{k},\omega), & \omega < ck,\\ F^{>}_{\text{ohm}}(\mathbf{k},\omega) + F_{\text{rad}}(\mathbf{k},\omega), & \omega > ck,\end{cases}
\end{aligned}
\tag{B.1}
$$

where H denotes the Hermitian (transpose and complex conjugate) operation. One should note that the above proof is general for any coordinate systems. Letting $i, j, l, s = \{x, y\}$ leads the proof for the case of anisotropic 2D material in Chapter 5 and $i, j, l, s = \{l, t\}$ leads the proof for the case of isotropic 2D material in Chapter 4. It is also simple to show that the proof applies for the case of multilayer structure with scalar conductivity.